Combined effects of post-growth thermal treatment and chemical substitution on physical properties of $CaFe_2As_2$

by

Sheng Ran

A dissertation submitted to the graduate faculty

in partial fulfillment of the requirements for the degree of

DOCTOR OF PHILOSOPHY

Major: Condensed Matter Physics

Program of Study Committee:

Paul C. Canfield, Major Professor

Sergey L. Bud'ko

Bruce N. Harmon

Sanjeevi Sivasankar

Ralph E. Napolitano

Iowa State University

Ames, Iowa

2014

DEDICATION

I would like to dedicate this thesis to my parents, my wife Fenping Wang and my son Jetsun.

TABLE OF CONTENTS

LIST OF TABLES

LIST OF FIGURES

ACKNOWLEDGEMENTS

I would like to take this opportunity to express my thanks to those who helped me with various aspects of conducting research and the writing of this thesis.

First and foremost, Dr. Paul Canfield, my adviser, for his guidance, patience and support throughout this research and the writing of this thesis. His insight into physics problems and his enthusiasm for pursuing research have continuously inspired my interest in physics.

I would like to thank Dr. Sergey L. Bud'ko for his invaluable guidance on experiments and many helpful suggestions on various projects.

Further, I would like to thank my past and present colleagues, Rongwei Hu, Xiao Lin, Stella Kim, Halyna Hodovanets, Valentin Taufour, Anton Jesche, Tai Kong, Udhara Kaluarachchi, Xiaoming Ma, Hyunsoo Kim and Eundeok Mun for their lively discussions and an enjoyable working atmosphere; and I especially acknowledge Alex Thaler, who taught me about the synthesis of FeAs-based materials.

I would also like to thank my collaborators, Dr. Min Gyu Kim, Dr. Andreas Kreyssig and Dr. Alan Goldman for scattering work, Dr. Lin Zhou and Dr. Matthew Kramer for transmission electron microscopy measurements, Warren Straszheim for the elemental analysis, Beas Roy and Dr. Yuji Furukawa for NMR measurement, Dr. Dominic Ryan for Mössbauer spectroscopy measurements and Dr. Michael Lang for wonderful work using He pressure cell.

Finally, I want to thank my wife Fenping Wang and my parents who have always been patient and supportive to me.

This work was supported by the U.S. Department of Energy (DOE), Office of Science, Basic Energy Sciences, Materials Science and Engineering Division. The research was performed at the Ames Laboratory, which is operated for the U.S. DOE by Iowa State University under contract DE-AC02-07CH11358.

ABSTRACT

This thesis summarizes experimental work using process of postgrowth thermal treatment and chemical substitution as tuning parameters in the study of physical properties of $CaFe_2As_2$. Details of sample preparation and characterization are given as well as various phase diagrams.

CHAPTER 1. INTRODUCTION

In February of 2008, the discovery of a new type of superconductor was published (Kamihara et al., 2008; Hosono, 2008). $LaFeAsO_{1-x}F_x$ (1111) with x $\sim$ 0.11 was found to superconduct with transition temperature as high as $T_c = 26$ K. Soon after this discovery it was found that applying a pressure of 4 GPa to the same compound increases the T_c even further to 43 K (Takahashi et al., 2008). Soon there after, it was also found that replacing the nonmagnetic La by magnetic rare earth elements, which have smaller ionic radius, could substantially increase the ambient pressure T_c (as high as $\sim$56 K) for this structure class (Chen et al., 2008; Ren et al., 2008a,b,c).

Although $LaFeAsO_{1-x}F_x$ is not the first reported superconducting compound containing iron [examples of earlier found iron-containing superconductors include U_6Fe (Chandrasekhar and Hulm, 1958), Th_7Fe_3 (Matthias et al., 1961), $Lu_2Fe_3Si_5$ (Braun, 1980), etc.], it is the first containing moment-bearing iron, which has been considered deleterious to superconductivity. This discovery attracted a lot of scientific attention leading to a remarkable flow of experimental and theoretical works for a number of reasons. Firstly, few would have anticipated that an Fe-containing material could show such an extraordinary T_c (Wang et al., 2008a; Takahashi et al., 2008; Chen et al., 2008; Ren et al., 2008a; Wu et al., 2009; Cheng et al., 2009). Secondly, this discovery has led to the discoveries of many other structure classes of Fe-containing superconducting compounds, which have, by now, formed a new class of high T_c superconductors, the so-called iron pnictides (Rotter et al., 2008; Wang et al., 2008b; Hsu et al., 2008; Ogino et al., 2009; Zhu et al., 2009; Ogino et al., 2010; Canfield and Bud'ko, 2010; Johnston, 2010; Ni et al., 2011; Stewart, 2011). Thirdly, the superconducting pairing mechanism may be unconventional and related to the close proximity to the antiferromagnetism (Chubukov, 2012).

The second key discovery in Fe-based superconductivity was the K-substituted $BaFe_2As_2$

with the body-centered-tetragonal $ThCr_2Si_2$-type (122-type) structure (Rotter et al., 2008; Canfield and Bud'ko, 2010). The 1111s and 122s share a similar structural feature: FeAs layers with Fe atoms in a square planar lattice arrangement as seen in Fig. 1.1. However, the $BaFe_2As_2$ compounds do not contain any oxygen. These two observations led to an early understanding that the FeAs layer was the key structural motif in these materials and that the superconductivity in the RFeAsO materials was not uniquely associated with oxide physics (as is the case for cuprates).

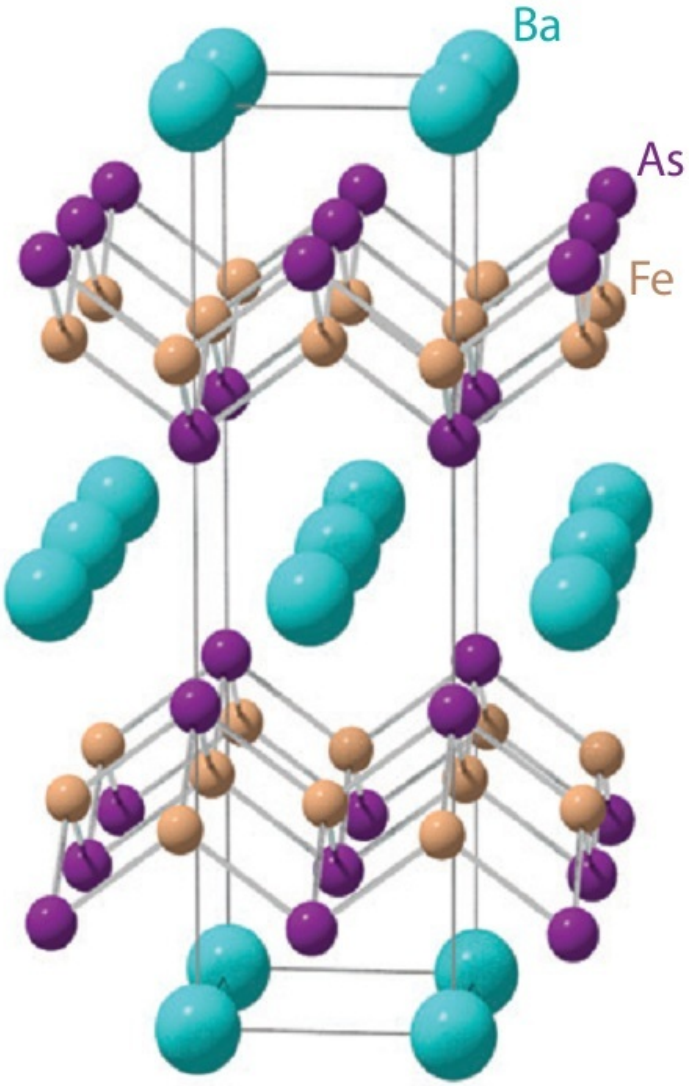

Figure 1.1 Crystal structure of $BaFe_2As_2$. (Canfield and Bud'ko, 2010)

The discovery of superconductor in K-substituted $BaFe_2As_2$ was important for another, practical, reason. Large, high-quality, homogeneous single crystals can be easily grown using conventional intermetallic solution growth technique (Ni et al., 2008a,b; Yan et al., 2008) which allows more definitive characterizations of the properties, especially by neutron scattering (Kreyssig et al., 2008; Goldman et al., 2008, 2009; Pratt et al., 2009a), compared to ≤ 1 mg size crystals of the 1111-type compounds. Therefore, research attention has largely shifted from the initially discovered 1111s to the 122-type compounds (Canfield and Bud'ko, 2010).

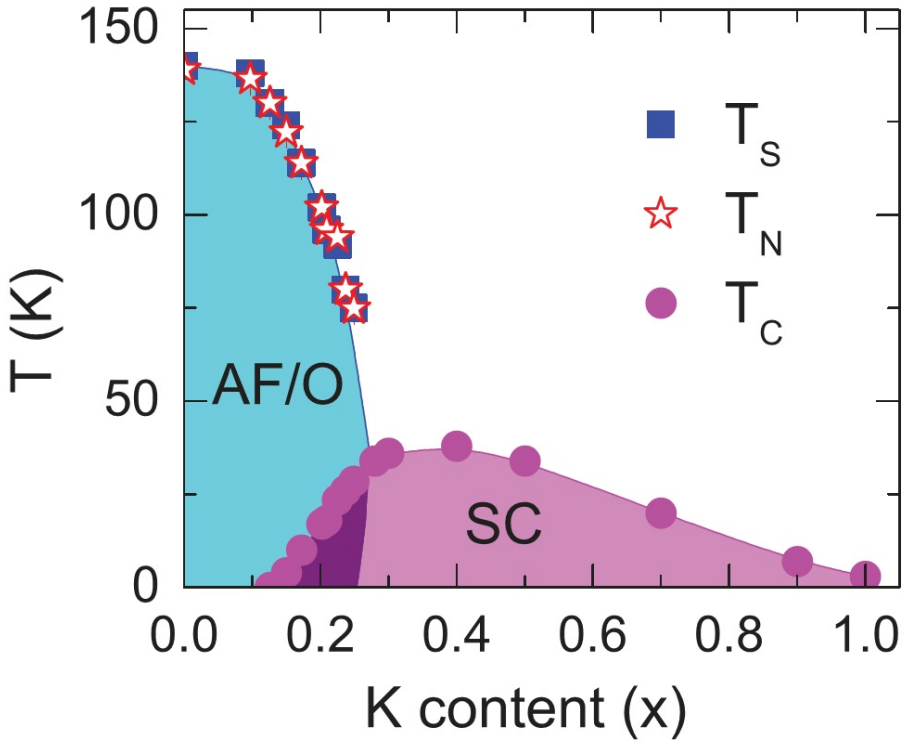

Figure 1.2 Transition temperature versus substitution level (T-x) phase diagram of $(Ba_{1-x}K_x)Fe_2As_2$ series. (Avci et al., 2012)

Soon after the discovery of $(Ba_{1-x}K_x)Fe_2As_2$ it was found that Co-substitution (and later other transition metals) for Fe could also induce superconductivity in LaFeAsO (Sefat et al., 2008a; Qi et al., 2008; Awana et al., 2009; Prakash et al., 2009; Cao et al., 2009) and $BaFe_2As_2$ (Sefat et al., 2008b; Ni et al., 2008c, 2010; Thaler et al., 2010), making Fe-based superconductors very different from cuprates, which are notoriously sensitive to perturbations of the Cu

sublattice. In both cases of K- and Co-substitution (Fig. 1.2 and Fig. 1.3), the the structural and magnetic phase transitions in the parent compound were monotonically suppressed and superconductivity was stabilized in a dome-like region centered near the critical substitution level where the antiferromagnetism is completely suppressed. For the substitution level less than this critical concentration, i.e., in the underdoped region, superconductivity and antiferromagnetism coexist (Canfield and Bud'ko, 2010).

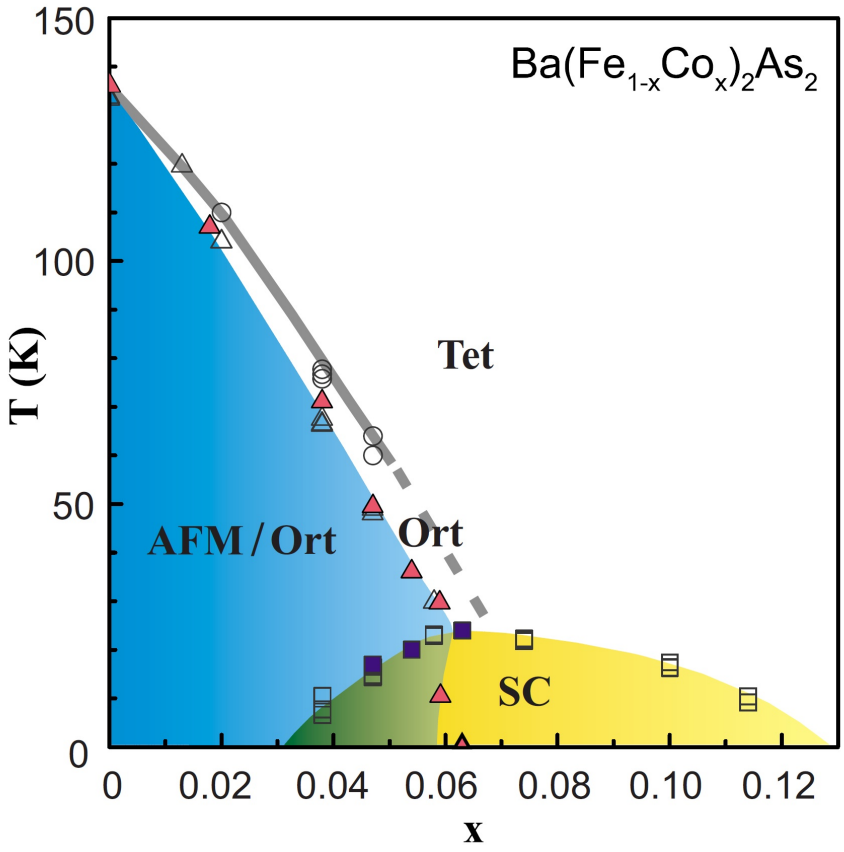

Figure 1.3 Transition temperature versus substitution level (T-x) phase diagram of $Ba(Fe_{1-x}Co_x)_2As_2$ series. (Fernandes et al., 2010)

After the reports of superconductivity in K-substituted $BaFe_2As_2$ (and $SrFe_2As_2$), a new isostructural compound was discovered; $CaFe_2As_2$ (Ni et al., 2008b; Ronning et al., 2008; Wu et al., 2008) was a previously unknown member of the $ThCr_2Si_2$ structure group. $CaFe_2As_2$ manifests an extreme example of the coupled magnetic/structural phase transition of the parent

compounds of the FeAs-based superconductors. The strongly first-order transition at ambient pressure from a high-temperature, tetragonal, paramagnetic phase to a low-temperature, orthorhombic, antiferromagnetic phase takes place near 170 K in single crystals grown from Sn flux and manifests a hysteresis of several degrees as seen in thermodynamic, transport, and microscopic measurements (Ni et al., 2008b; Goldman et al., 2008; Canfield et al., 2009a).

$CaFe_2As_2$ is also found to be the most pressure sensitive of the 122 and 1111 compounds with its magnetic/structural phase transition being initially suppressed by over 100 K per GPa (Torikachvili et al., 2008; Yu et al., 2009). As pressure increases, a non-moment bearing, collapsed tetragonal phase that is stabilized by ~ 0.4 GPa intersects and terminates the lower-pressure orthorhombic-antiferromagnetic phase line near 100 K and 0.4 GPa and rises to 300 K by ~ 1.5 GPa. In addition to this extreme pressure sensitivity, $CaFe_2As_2$ is also very sensitive to nonhydrostaticity (Torikachvili et al., 2008; Yu et al., 2009; Prokes et al., 2010). If the pressure medium solidifies before the structural phase transitions, then the anisotropic changes in the unit cell lead to nonhydrostatic stress, which in turn leads to dramatically broadened transitions and a structurally mixed phase sample at low temperatures in the 0.4 GPa pressure region. This mixed phase includes a small amount of strain-stabilized, high-temperature tetragonal phase which superconducts at low temperatures. The use of helium as a pressure medium allows for a minimization of these nonhydrostatic effects and has allowed for the determination of the transition temperature versus pressure (T-P) phase diagram (Kreyssig et al., 2008; Yu et al., 2009; Goldman et al., 2009; Canfield et al., 2009a).

$CaFe_2As_2$ samples were initially grown from Sn flux and characterized in single-crystal form (Ni et al., 2008b). Sn-grown crystals are well-formed, faceted plates that generally have planar dimensions of several millimeters and thicknesses between 0.1 and 0.5 mm. For measurements that require larger sample volumes pseudopolycrystalline or oriented single crystalline assemblies can be used (Kreyssig et al., 2008; Pratt et al., 2009b; Diallo et al., 2010). Later a FeAs based, self flux method that had been developed to grow larger single crystals of $BaFe_2As_2$ (Sefat et al., 2008b) and $SrFe_2As_2$ was adopted to grow $CaFe_2As_2$ as well. However, in order for these larger crystals to manifest a magnetic/structural phase transition similar to that seen in the smaller Sn-grown crystals, they were annealed at 500°C (a temperature similar to the

decanting temperature of the Sn-grown samples) for 24 h and quenched to room temperature (Goldman et al., 2009). Without this annealing/quenching, the larger, FeAs-grown samples had transition temperatures dramatically suppressed to below 100 K.

Given previous observations of only small shifts in the magnetic/structural transition temperatures of $BaFe_2As_2$ samples and of the superconducting transition in $Ba(Fe_{1-x}Co_x)_2As_2$, as well as of sharpenings of their signatures in thermodynamic and transport data, after postgrowth thermal treatment (Rotundu et al., 2010; Gofryk et al., 2011; Kim et al., 2012a), it is necessary to undertake a systematic study of the effects of postgrowth thermal treatment of FeAs-grown single crystals of both parent and transition metal substituted $CaFe_2As_2$. During my thesis work I have shown that the antiferromagnetic/orthorhombic phase transition can be systematically varied from 170 K down to 100 K and ultimately replaced by a non-moment bearing, collapsed tetragonal by variations of post growth annealing/quenching temperature. In addition, for transition metal substituted $CaFe_2As_2$ systems, I have found that the $CaFe_2As_2$ system offers ready access to the salient low-temperature states associated with Fe-based superconductors: antiferromagnetic/orthorhombic (AFM/ORTH), superconducting/paramagnetic/tetragonal (SC/PM/T), non superconducting/paramagnetic/tetragonal (N/PM/T) and non-moment bearing/collapsed tetragonal (cT) state. The absence of coexistence of AFM/ORTH and superconductivity (AFM/ORTH/SC) is also significant and represents an important physical point as well. Note that the results of the parent compound are highly reproducible as shown by measurements from another group (Saparov et al., 2014; Gofryk et al., 2014).

This thesis will be organized as following. A brief review of superconductivity, with focus on the parts that are related to this thesis work, will be given in chapter 2. In chapter 3, details about the growth method and postgrowth thermal treatment, as well as a brief review of the characterization techniques will be given. In chapter 4, the physical properties of $CaFe_2As_2$ grown from Sn flux under ambient and applied pressure will be reviewed. In chapter 5, a systematic study of the effects of annealing/quenching of FeAs-grown single crystals of $CaFe_2As_2$, as well as a wide variety of microscopic and spectroscopic measurements to understand the low temperature state are presented. In chapter 6, a systematic study of the combined ef-

fects of annealing/quenching and Co-substitution of FeAs-grown single crystals of $CaFe_2As_2$ is presented. This leads to the creation of a 3-D phase diagram with annealing/quenching temperature and Co substitution level as two independent control parameters are presented. In chapter 7, thermodynamic and transport properties of Ni and Rh substituted $CaFe_2As_2$ for different annealing/quenching temperature are presented. Low-temperature, 2-D phase diagrams are constructed and compared with that of the Co-substituted system. In chapter 8, a summary of the work in this thesis and some of the conclusions drawn from it are presented. In appendix A, details of sample preparation are presented. In appendix B, supplemental data of Ni- and Rh-substitution of $CaFe_2As_2$ are presented. In appendix C, the results of the magnetic susceptibility and electrical resistance measurements under He-gas pressure on single crystals of Co-substituted $CaFe_2As_2$ are presented and phase diagrams of transition temperature versus applied pressure are constructed. In appendix D, results of one of my other projects, involving the effects of substitution on low temperature physical properties of $LuFe_2Ge_2$, are presented. In appendix E, other projects and collaborations that I have been involved in are summarized. Finally, in appendix F, a list of all substitutions I studied in both $AEFe_2As_2$ (AE = Ca and Ba) and $LuFe_2Ge_2$ systems is presented.

CHAPTER 2. OVERVIEW OF SUPERCONDUCTIVITY

The phenomenon of superconductivity was first discovered by Dutch physicist Kamerlingh Onnes in 1911 (Onnes, 1911) when he cooled mercury to the temperature of liquid helium. Since then the superconductivity has become one of the major themes of research in solid state physics. Not only have the limits of superconductivity not yet been reached (Larbalestier and Canfield, 2011), but the theories that explain superconductor behavior seem to be constantly under review (Carlson et al., 2008; Schmalian, 2010; Norman, 2011). At this point in time, with more and more superconducting materials discovered, the class of superconductors extend to elements, alloys, intermetallic compounds, oxides, organic compounds and so on (Fig. 2.1). Inspite of nearly 50 years of experimental effort, the first widely-accepted microscopic theory of superconductivity was not proposed until 1957 by John Bardeen, Leon Cooper, and John Schrieffer (Bardeen et al., 1957). Their theory of Superconductivity became known as the BCS theory, which explained superconductivity at temperatures close to absolute zero for elements and simple alloys in detail. However, the discovery of superconductivity at 30 K in CuO-based materials in 1986 (Bednorz and Müller, 1986) and the following discoveries of cuprates with even higher transition temperatures (Wu et al., 1987; Sheng and Hermann, 1988; Schilling et al., 1993; Chu et al., 1993) changed this situation. Simple electron-phonon mediated BCS theory became inadequate to fully explain how superconductivity occurred in this new classes of superconductors. In a similar manner, superconductivity in the FeAs-based compounds poses challenges for electron-phonon mediated BCS theory as well.

In this chapter, I will give a brief introduction to superconductivity in both experimental and theoretical aspects.

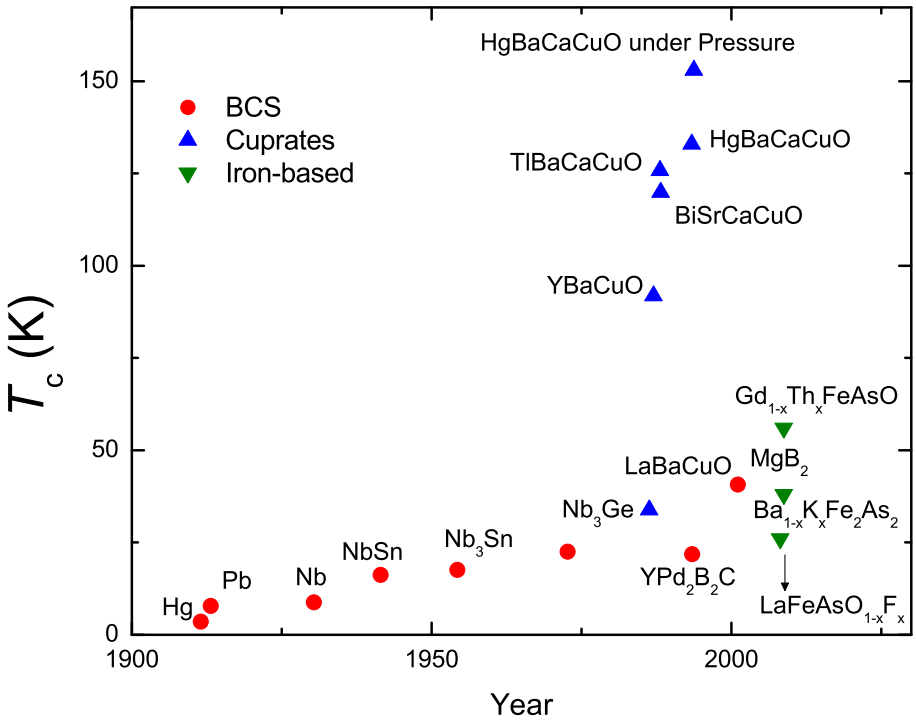

Figure 2.1 Timeline of superconductivity (Onnes, 1911; Matthias et al., 1963, 1965; Bednorz and Müller, 1986; Wu et al., 1987; Sheng and Hermann, 1988; Subramanian et al., 1988; Schilling et al., 1993; Chu et al., 1993; Cava et al., 1994a; Bud'ko et al., 2001; Kamihara et al., 2008; Rotter et al., 2008; Wang et al., 2008a).

2.1 Experimental Facts

2.1.1 Zero resistance

After leading the first group in the world to liquify Helium, Kamerlingh Onnes discovered superconductivity in 1911 (Onnes, 1911) as part of his extensive investigation of the electrical resistivity of pure metals cooled to these new lows in temperature. What he observed was that the electrical resistivity of many metals, such as mercury, tin, and lead suddenly dropped by a factor of at least 10,000 over a small temperature interval at a critical temperature called T_c, which is characteristic of the metal. Since then more sophisticated experiments have been set up to demonstrate the complete disappearance of the resistance below T_c, among which the most sensitive one is to detect the persistent current in a superconducting circuit (Smith, 1965). It has been demonstrated that currents in superconducting circuits can persist for years without any detectable decay. Theoretical estimated lifetime of a persistent current can exceed the estimated lifetime of the universe, depending on the wire geometry and the temperature. Thus zero resistance is considered the first experimental hallmark of the superconducting state.

At the time of his discovery, Onnes thought that one possible explanation of this effect would be that portion of the metal transformed to a perfect single crystal so that there would be no scattering (Finnemore, 1991). This possibility was ruled out by adding impurities in the pure metal (De Haas and Voogd, 1931; Finnemore, 1991). Such an addition of impurities greatly enhances the electrical resistivity in the normal state but only suppresses the T_c by a few hundredths of K. The phenomenon of zero resistance persists in spite of the irregularities in the crystals.

2.1.2 Meissner effect

The second hallmark of the superconductivity is the perfect, low applied magnetic field, diamagnetism in the superconducting state, which is called Meissner effect (Meissner and Ochsenfeld, 1933). Zero resistance is not adequate to describe the thermodynamic properties of superconductor. If the magnetic behavior of a sample in the superconducting state were completely determined by their zero resistance and Maxwell's equations, then the supercon-

ducting phase transition would depend on the history of magnetic field. The magnetization of the superconducting state can be measured in two different modes: field cooling (FC) mode in which a magnetic field is applied above T_c and then the sample is cooled through T_c, and zero field cooling (ZFC) mode in which a superconductor is cooled down below T_c in zero external magnetic field and then subjected to a field (Fig. 2.2a and b). In FC mode, the magnetic field penetrates the sample uniformly above T_c (Fig. 2.2a). Upon cooling down, magnetic field would be trapped inside of the sample as required by zero resistance and Maxwell equations (Fig. 2.2c) and remain even when the field is switched off (Fig. 2.2e). On the other hand, in ZFC mode, below T_c magnetic flux is zero before the field is applied (Fig. 2.2d). When the magnetic field is turned on below T_c, zero resistance and Maxwell equations would guarantee that the magnetic flux would remain unchanged (Fig. 2.2f) and be expelled from the sample. Therefore the magnetic flux of a superconducting sample would depend on the history of magnetic field. This is not consistent with the experimental facts (Fig. 2.2g to l).

In 1933, Meissner and Ochsenfeld measured the magnetic field distribution around a superconductor (Meissner and Ochsenfeld, 1933). What they observed is that the magnetic field inside the superconductor always remains zero, regardless of the magnetic field history (Fig. 2.2i to l). The magnetic flux is always expelled from the specimen, as long as the applied field is lower than the critical magnetic field H_c (Fig. 2.2i and l). This is called the Meissner effect and has been considered as one of the most fundamental properties of a superconductor, together with the phenomenon of zero resistance.

2.1.3 Critical magnetic field

As early as in 1914 Onnes discovered that the superconducting state was lost and the normal state was resumed if an applied magnetic field exceeded some critical value H_c (Onnes, 1914). The field H_c is called the critical magnetic field.

As more examples of superconductivity were discovered, it became clear that there were two clearly distinguishable kinds of magnetic response to the external magnetic field; two classes of superconductivity were defined: type I and type II. In a Type I superconductor the magnetic field is completely expelled from the interior for $H < H_c$. When the applied field exceeds the

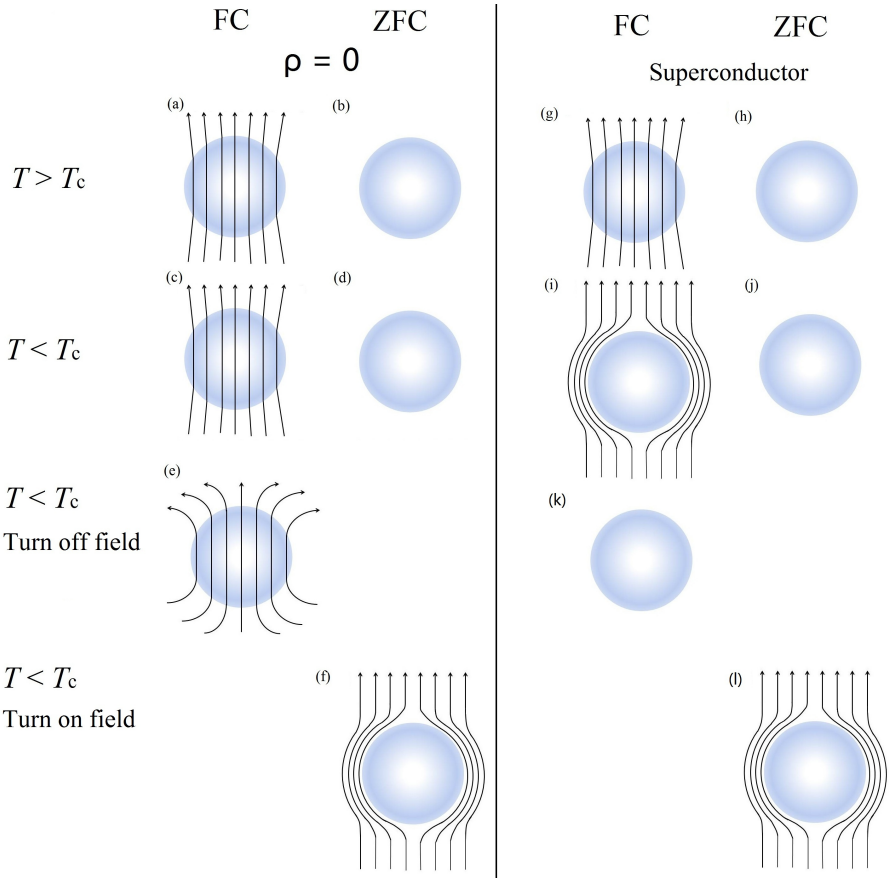

Figure 2.2 Magnetic flux distribution determined by zero resistance: (a) at $T > T_c$ in FC mode, (b) at $T > T_c$ in ZFC mode, (c) at $T < T_c$ in FC mode, (d) at $T < T_c$ in ZFC mode, (e) when the magnetic field is switched off in (c), (f) when the magnetic field is switched on in (d). Magnetic flux distribution for superconductor: (g) at $T > T_c$ in FC mode, (h) at $T > T_c$ in ZFC mode, (i) at $T < T_c$ in FC mode, (j) at $T < T_c$ in ZFC mode, (k) when the magnetic field is switched off in (i), (l) when the magnetic field is switched on in (j).

critical value H_c the entire sample reverts to the normal state and the magnetic field completely penetrates. A sample magnetization curve for a type I superconductor is plotted in Fig. 2.3a.

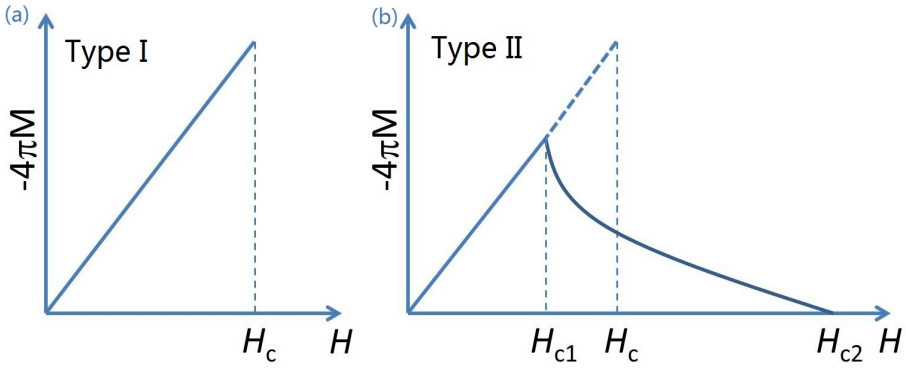

Figure 2.3 Magnetization curve for (a) type I and (b) type II superconductors for $T \ll T_c$. (Tinkham, 2004)

Type II superconductors have two critical magnetic field values. For $H < H_{c1}$ the magnetic field is completely expelled (Type-I behavior), whereas when field exceeds H_{c2} the superconductivity is completely destroyed and the field penetrates the entire sample. For $H_{c1} < H < H_{c2}$ the magnetic field partially penetrates through the material (as discussed in session 2.2.3 below, this partial penetration is associated with the vortex, or mixed, state). Fig. 2.3b presents the magnetization curve of type II superconductors. The bulk of superconductor material breaks down into two kinds of regions: superconductive regions from which the external field is completely expelled, and normal regions through which the external field penetrates. The normal regions are distributed as filaments filled with the magnetic field. The flux of magnetic field through the filaments is quantized. Electric current is induced at the interface between the normal and the superconductive regions, the surface of the filaments is wrapped in current which cancels the magnetic field in the superconductive regions. The electric current is carried by the superconductive regions of Type-II material.

2.1.4 Specific heat

The specific heat of pure Nb metal in the normal state and superconducting state is presented in Fig. 2.4a in the form of C/T versus T^2. Nb undergoes a superconducting transition at 9.2 K and has critical magnetic field H_c of 1,950 Oe. Thus, the data below T_c in the absence of a magnetic field and in a magnetic field of 10,000 Oe represent the specific heat behavior in the superconducting state and normal state, respectively. The data in the normal state fall on an essentially straight line, from which the electronic specific heat coefficient, γ, can be obtained by extrapolating the linear trend down to absolute zero.

On the other hand, the specific heat in the superconducting state jumps upward at T_c and subsequently decreases gradually toward zero with decreasing temperature. The temperature dependence of electronic specific heat in the superconducting state can be fitted to $\exp(-2\Delta/k_B T)$, indicating the presence of an energy gap in the superconducting phase. The exponential temperature dependence can be deduced from the BCS theory, which will be described below.

Alternatively, the specific heat data could also be presented in the form of C/T versus T (Fig. 2.4b), from which entropy can be integrated and represented by the area beneath the curve. The entropy difference between the normal state and the superconducting state can be related to the condensation energy through equation

$$\int_T^{T_c} (S_N - S_S) dT = V H_T^2 / 8\pi, \tag{2.1}$$

where V is volume of the sample, H_T is the critical field at a certain temperature and $V H_T^2/8\pi$ is the condensation energy. At T_c, H_c vanishes, and so does the condensation energy. Therefore the entropy at T_c is the same for both normal state and superconducting state. This is illustrated in Fig. 2.4b with the blue area above and below the normal state data being the same.

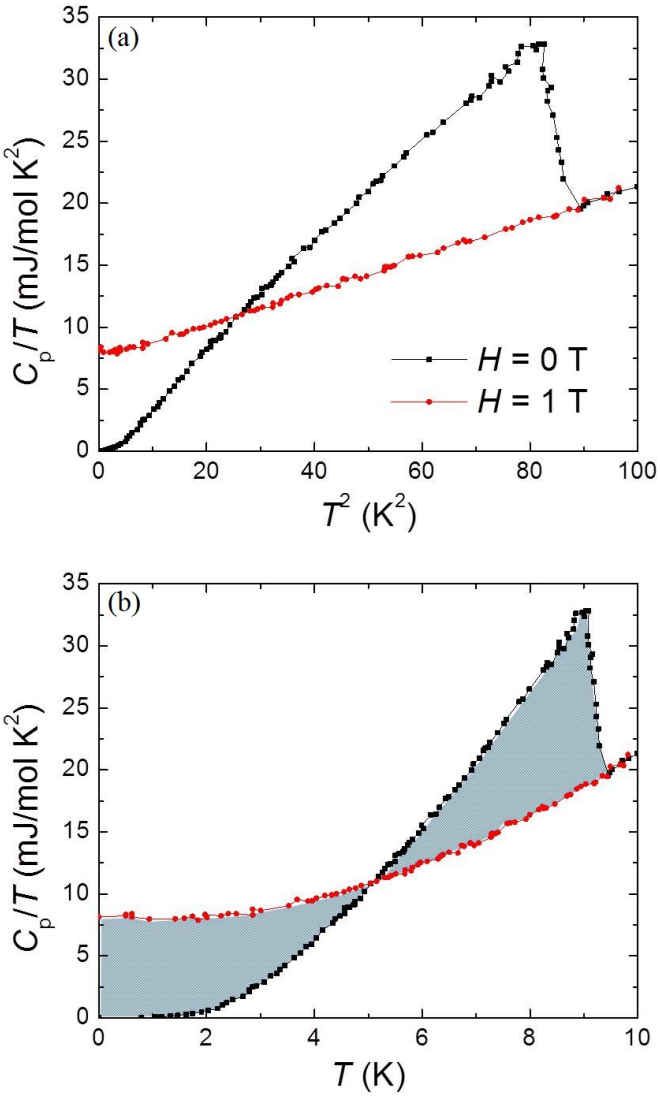

Figure 2.4 Temperature dependence of the low-temperature specific heat for pure Nb in the presence and absence of a magnetic field H (a) in the form of C/T versus T^2 and (b) in the form of C/T versus T. (Leupold and Boorse, 1964)

2.2 Theoretical Explanations

2.2.1 London equations

London equations, which were developed by the brothers F. and H. London (London and London, 1935; Tinkham, 2004), are not a microscopic theory but a phenomenological approach to describe the two basic electrodynamic properties of superconductivity: zero resistance and perfect diamagnetism. There are two equations to govern the microscopic electric and magnetic fields

$$\frac{\partial \mathbf{j}_s}{\partial t} = \frac{n_s e^2}{m}\mathbf{E} \tag{2.2}$$

$$\nabla \times \mathbf{j}_s = -\frac{n_s e^2}{mc}\mathbf{B}, \tag{2.3}$$

where j_s is the superconducting current density, E and B are, respectively, the electric and magnetic fields within the superconductor.

The first equation describes the zero resistance since the term corresponding to the friction in Ohm's law in a conductor is not present. The second equation, when combined with Maxwell equation

$$\nabla \times \mathbf{B} = \frac{4\pi \mathbf{j}}{c}, \tag{2.4}$$

leads to

$$\nabla^2 \mathbf{B} = \frac{1}{\lambda^2}\mathbf{B}, \tag{2.5}$$

where

$$\lambda \equiv \sqrt{\frac{mc^2}{4\pi n_s e^2}}. \tag{2.6}$$

Thus, the second London equation implies that external magnetic fields are exponentially suppressed inside the superconductors with a characteristic length scale, λ, which is defined as the London penetration depth.

A simple example geometry is a flat boundary between a semi-infinite superconductor and free space. If the magnetic field outside the superconductor is a constant value pointing parallel to the superconducting boundary plane in the z direction, then the field inside the superconductor is

$$\mathbf{B}_z(x) = \mathbf{B}_0 e^{-x/\lambda}. \tag{2.7}$$

as shown in Fig. 2.5. Thus we see λ measures the depth that the magnetic field penetrates the superconductor.

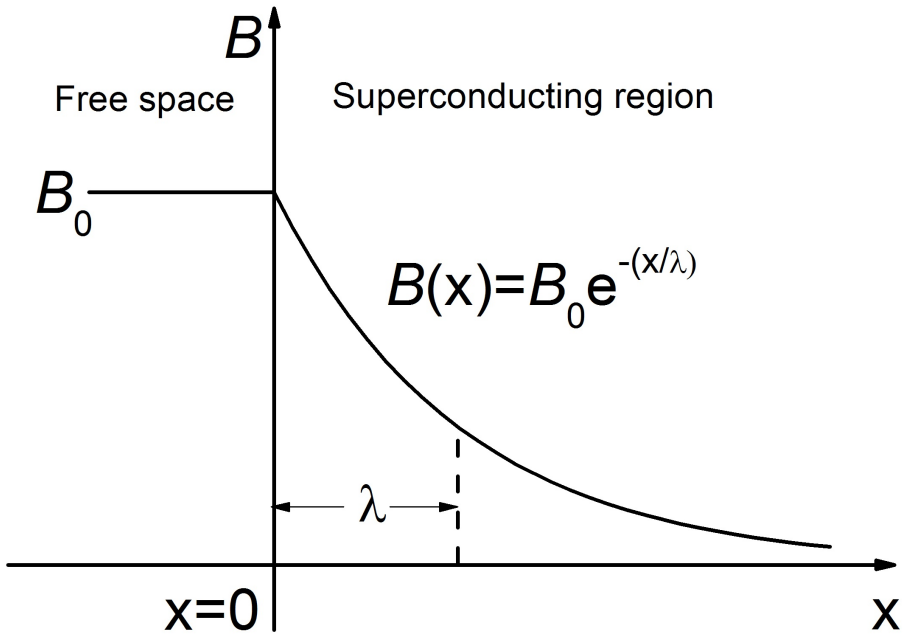

Figure 2.5 The magnetic field decays to B_0/e at a distance $x = \lambda$ in the interior of the superconductor. (Tinkham, 2004)

2.2.2 Ginzburg-Landau theory

V.L. Ginzburg and L.D. Landau developed a macroscopic theory to describe superconductivity based on the Landau mean field description of phase transitions (Ginzburg and Landau, 1950; Schmidt, 1997; Tinkham, 2004). Without knowing the microscopic mechanism, Ginzburg and Landau simply postulated the existence of a macroscopic quantum wave function $\psi(r) \equiv |\psi(r)|e^{i\phi}$, which was equivalent to an order parameter. The order parameter vanishes above T_c and measures the degree of the superconducting order below T_c.

They further proposed that the free energy a superconductor could be expressible in terms of an expansion of this quantity

$$F_s(H) = F_n + \alpha|\psi|^2 + \frac{\beta}{2}|\psi|^4 + \frac{1}{2m^*}\left|(-i\hbar\nabla - 2e^*\mathbf{A})\,\psi\right|^2 + \frac{|\mathbf{B}|^2}{2\mu_0} \tag{2.8}$$

where F_s and F_n refer to the normal and superconducting states, respectively, $\mathbf{A}$ is the magnetic vector potential, and $\mathbf{B} = \nabla \times \mathbf{A}$ is the magnetic field. α and β in the initial argument were treated as phenomenological parameters. In the region near T_c, both parameters can be taken as only the leading terms in the Taylor series expansions

$$\alpha(T) = \alpha_0(T - T_c),\ \beta(T) = \beta_0 \tag{2.9}$$

By minimizing the free energy with respect to the order parameter and the vector potential, two coupled Ginzburg-Landau equations can be obtained

$$\alpha\psi + \beta|\psi|^2\psi + \frac{1}{2m}\left(-i\hbar\nabla - 2e\mathbf{A}\right)^2\psi = 0 \tag{2.10}$$

$$\mathbf{j} = \frac{2e}{m}\mathrm{Re}\left\{\psi^*\left(-i\hbar\nabla - 2e\mathbf{A}\right)\psi\right\} \tag{2.11}$$

where $\mathbf{j}$ is the supercurrent density and $\mathrm{Re}\left\{\psi^*\left(-i\hbar\nabla - 2e\mathbf{A}\right)\psi\right\}$ the real part. The first equation determines the order parameter, $\psi(r)$ and the second equation provides the superconducting current.

The Ginzburg-Landau equations predicted two characteristic lengths in a superconductor, coherence length, ξ, and penetration depth, λ. Coherence length characterizes the distance over which the order parameter can vary without significant energy increase. Penetration depth, which was first introduced in London equations, is the distance over which the magnetic field can penetrate into the superconductor surface. Expressed in terms of the parameters of Ginzburg-Landau model the two characteristic lengths are

$$\xi = \sqrt{\frac{\hbar^2}{4m|\alpha|}} \tag{2.12}$$

$$\lambda = \sqrt{\frac{m}{4\mu_0 e^2\psi_0^2}}. \tag{2.13}$$

The ratio of these two characteristic lengths defines the Ginzburg-Landau parameter

$$\kappa = \lambda/\xi \tag{2.14}$$

which determines the energy of the interface between the normal and superconducting states. In the classical elemental superconductors, $\lambda \approx 500$ $\mathring{A}$ and $\xi \approx 3000$ $\mathring{A}$, so $\kappa \ll 1$. In this case, there is a positive surface energy associated with the domain wall between normal and

superconducting materials. If κ is large instead of small, the surface energy will be negative. As a sharp boundary between two phases is possible only if the surface energy of the interface is positive, negative surface energy will lead to radically different behavior. This type of superconductors are called type II superconductors to distinguish them from the earlier type I superconductors (Abrikosov, 1957). It was shown that the exact breakpoint between the two regimes was at $\kappa = 1/\sqrt{2}$.

For superconductors with $0 < \kappa < 1/\sqrt{2}$, type I superconductors, there is discontinuous breakdown of superconductivity in a first-order transition at H_c (Fig. 2.3a). For superconductors with $\kappa > 1/\sqrt{2}$, type II superconductors, due to the negative surface energy, it is favorable to have a mixture of the normal and superconducting phases for magnetic field between two critical values, $H_{c1} < H < H_{c2}$. There is a continuous increase in flux penetration starting at lower critical field H_{c1} and the field penetrates completely at upper critical field H_{c2} (Fig. 2.3b). The thermodynamic critical field H_c, which is defined by the thermodynamic properties of the material, be can related to these two critical values as

$$H_{c1} = H_c \frac{log\sqrt{2}}{\kappa\sqrt{2}} \tag{2.15}$$

$$H_{c2} = \kappa\sqrt{2}H_c. \tag{2.16}$$

For $\kappa \gg 1$, it follows that

$$H_{c1} \ll H_c \ll H_{c2}. \tag{2.17}$$

2.2.3 BCS theory

Since the discovery of superconductivity in mercury and other metals, there have been many theories proposed to explain the phenomenon (Schmalian, 2010). However, none of the theories successfully accounted for various observed properties inherent in the superconducting state until Bardeen, Cooper and Schrieffer put forward their historic theory in 1957 (Bardeen et al., 1957), which was proven to be the correct description and regarded as a milestone in the development of the electron theory of metals.

The BCS theory includes two basic ingredients: (i) an effective attraction between the electrons in the neighborhood of Fermi surface (Cooper, 1956) and (ii) pairing of electrons into

bosonic Cooper pairs which then form a condensate in the superconducting state (Bardeen et al., 1957).

Such a pairing of electrons seems counter-intuitive since, according to Coulombs law, interaction between electrons should be repulsive rather than attractive. BCS theory addressed this apparent contradiction by invoking an attraction mediated by phonons (the quanta of atomic ion vibration). Although this is a quantum effect, the reason for attractive interaction can be seen from a simplified classical explanation. Consider an electron moving through the metal. The other electrons in the region are repelled away from the electron and the lattice ions are drawn toward it. If the motion of the electrons and lattice have sufficient amplitude, then in the region of the moving electron there actually be a net positive charge. It is this overscreening by the lattice that provides the source of attraction for a second electron.

BCS theory points out that, if two electrons interacting with an attractive force are placed immediately above the Fermi sphere at absolute zero, the two electrons form a bound state and their total energy is lowered relative to $2E_f$, even though the attractive interaction is very weak. To maximize the number of these pairs that may be formed, the electrons in each pair must have momentum of equal magnitude but opposite direction, as well as antiparallel spin. The entity formed by such an interaction is called a Cooper pair.

BCS theory further constructs a ground state in which all electrons within the range $\Delta k = m\omega_D/\hbar k_F$ (m is the mass of electrons, ω_D is the Debye frequence and k_F is the wavevector at the Fermi surface) about k_F are coupled to form Cooper pairs. The pairs can not be thought as independent particles, but are spatially overlapped in very complicated manner. All allowed wave vectors are involved to form Cooper pairs, although the electrons in each pair should always have equal but opposite momenta. Hence, at nonzero temperature, the momenta of the paired electrons cannot be freely increased as energy is imparted to a superconductor. The only possible way to use the energy is to break up a Cooper pair. According to the BCS theory, the minimum amount of energy needed is 2Δ, which is called the superconducting energy gap.

As shown in Fig. 2.6, in the ground state at absolute zero temperature, all Cooper pairs are condensed into a single energy level. If the Cooper pair receives energies higher than the energy gap 2Δ, then the pair is broken into two independent electrons. The energy spectrum

of the resulting electrons, which are called quasiparticles, represents the excited states of a superconductor.

BCS theory makes the following major predictions:

- Critical Temperature

  In zero magnetic field, superconducting ordering sets in at a critical temperature given by

  $$k_B T_c = 1.134 \hbar \omega_D exp(-1/N(0)V), \tag{2.18}$$

  where $N(0)$ is the density of states at the Fermi level, V is the attractive interaction between electrons mediated by phonons and ω_D is the Debye frequency.

- Energy Gap

  Zero temperature energy gap is predicted by a similar formula

  $$\Delta(0) = 2\hbar \omega_D exp(-1/N(0)V). \tag{2.19}$$

  The ratio of (2.1) and (2.2) gives the relation between the critical temperature and zero temperature energy gap independent of the experimental parameters

  $$\frac{\Delta(0)}{k_B T_c} = 1.76. \tag{2.20}$$

- Critical Field

  The BCS prediction for critical magnetic field is given by

  $$\frac{H_c(T)}{H_c(0)} \approx 1 - (\frac{T}{T_c})^2, \tag{2.21}$$

- Specific Heat

  BCS theory predicts the low temperature electronic specific heat to be

  $$\frac{C_s}{\gamma T_c} = 1.34(\frac{\Delta(0)}{T})^{3/2} exp(-\Delta(0)/T), \tag{2.22}$$

  where γ is the coefficient of linear term in the specific heat of the metal in normal state.

  BCS theory also predicts a discontinuity in the specific heat at the critical temperature in zero magnetic field

  $$(\frac{C_s - C_n}{C_n})|_{T_c} = 1.43. \tag{2.23}$$

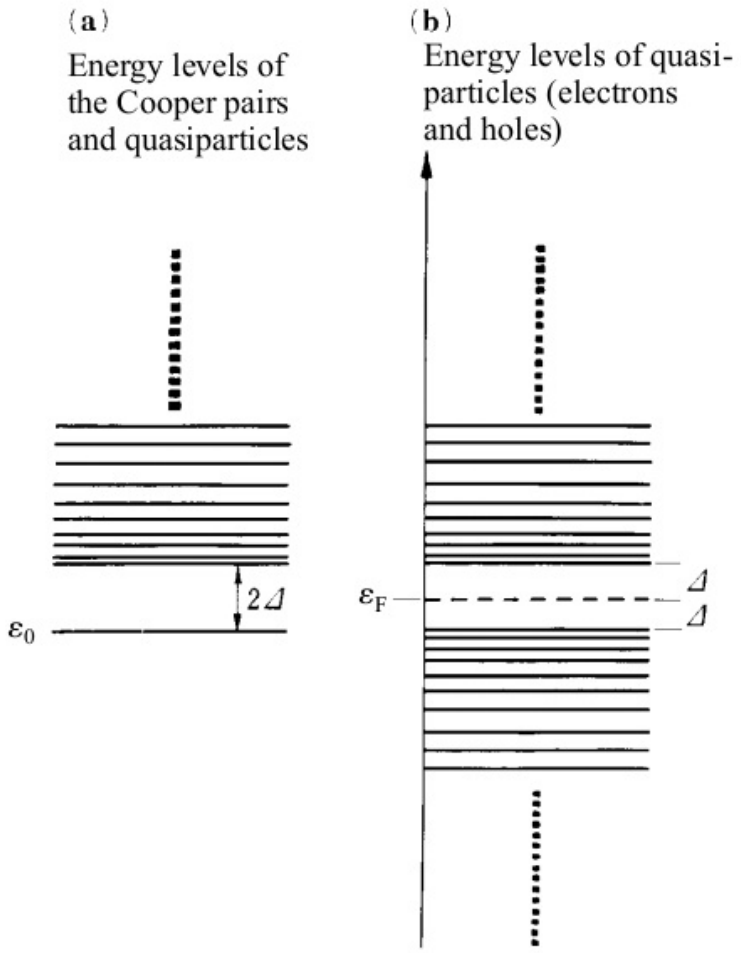

Figure 2.6 (a) All Cooper pairs in the ground state are in the energy level ϵ_0. The lowest excited energy of the two quasiparticles (electrons) is 2Δ higher than ϵ_0. Each level is filled by two electrons with spin-up and spin-down, since the quasiparticle obeys the Fermi statistics. (b) Energy levels for the excited states of a superconductor. The Fermi level for electrons is raised by Δ relative to that in the normal state. Likewise, the Fermi level for holes is lowered by Δ. Accordingly, the energy gap 2Δ is opened. (Mizutani, 2001)

2.3 Impurity Effect

The problem of impurity effects in superconductors has been of great interest for a long time. Depending on the magnetic properties of the impurities and gap symmetry of the superconductor, the effects upon critical temperature vary largely. For this section, I will confine the discussion to the s-wave superconductor and summarize the effects first for non-magnetic and then for magnetic impurities.

2.3.1 Non-magnetic impurities

One of the most important early experimental results was the robustness of the conventional superconductivity to small concentrations of non-magnetic impurities (De Haas and Voogd, 1931; Lazarev et al., 1957; Matthias et al., 1956). The theoretical underpinning of this result is now known as Anderson's theorem (Anderson, 1959a,b). Anderson noticed that, since superconductivity is due to the instability of the Fermi surface to pairing of time-reversed quasiparticle states, any perturbation that does not prevent the time-reversal transformation of these states does not affect the mean field superconducting transition temperature.

This theorem serves to explain how the earlier calculations (Suhl and Matthias, 1959) could overestimate the effect of the impurities. However, it doesn't account for changes of T_c for conventional superconductors with addition of impurities (Lynton et al., 1957; Chanin et al., 1959; Nakamura, 1959; Gayley et al., 1962; Markowitz and Kadanoff, 1963; Ginsberg, 1964; Hohenberg, 1964). Figure 2.7 presents typical data for three different impurities in tin (Lynton et al., 1957). To explain the curves in Fig. 2.7 it was proposed that the change in T_c comes from two sources (Markowitz and Kadanoff, 1963; Ginsberg, 1964): (a) the reduction in gap anisotropy due to scattering (Clem, 1966), and (b) all the changes in the gross parameters of the system. Included in (b) are the changes in the values of ω_D, V, and $N(0)$ of Eq. (2.1) plus the addition of such new events as the scattering of phonons by impurities. Included also in (b) would be any other effects excluded from (a). For low doping, the former dominates and there is a drop in T_c, which is almost linear with impurity concentration and depends primarily on the mean free path. For higher doping, the latter does. Then the material enters a region

where the further changes in T_c are determined by the specific impurity.

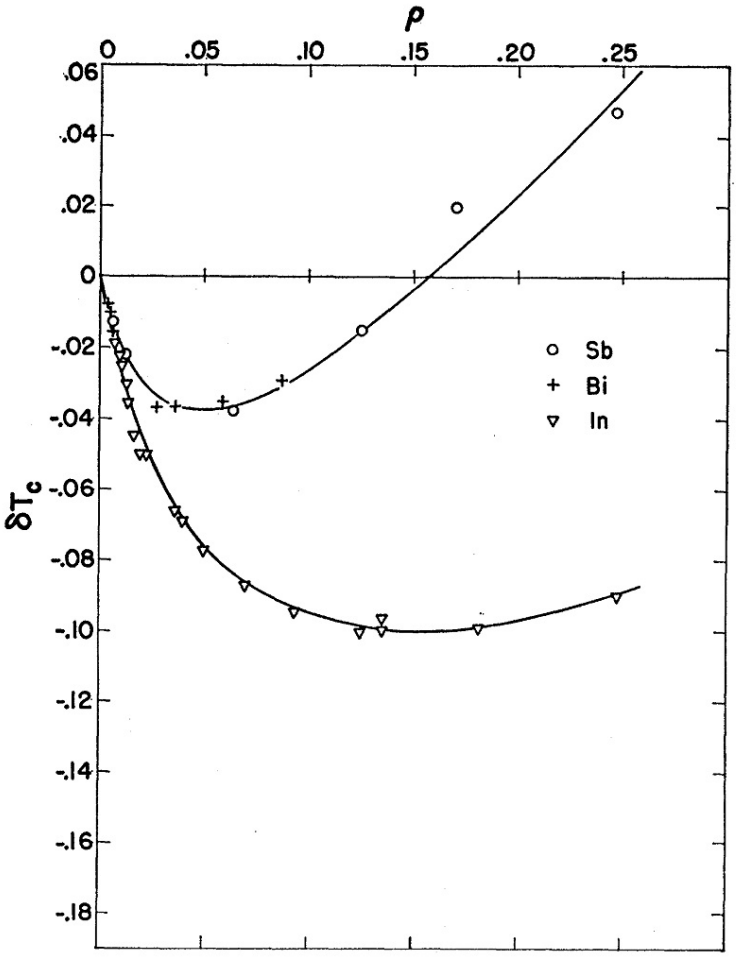

Figure 2.7 Change of T_c versus ρ for Tin with three different impurities. ρ is defined in the original paper as $R_0/[(R\text{-}R_0)(1\text{-}\alpha t_c)]$, which is proportional to the impurity concentration. (Lynton et al., 1957)

2.3.2 Magnetic impurities

The effect of magnetic impurities on superconductivity has attracted a great deal of interest since the discovery that even a small amount of magnetic impurities can strongly reduce the transition temperature or, below the transition, break the pairs and form states within the superconducting gap (Abrikosov, 1957; Matthias et al., 1958; Abrikosov and Gor'kov, 1961; Helfand and Werthamer, 1964; Finnemore et al., 1965a,b; Decker et al., 1967; Decker and

Finnemore, 1968; Maple, 1968). It was proposed that exchange interaction between conduction spin and the spin of local impurity is large enough to accout for the strong suppression of T_c (Herring, 1958; Suhl and Matthias, 1959). From simple phenomenological point, magnetic impurities give rise to spin-flip scattering and a spin-flip to a member of a spin up and down Cooper pair is, by definition, a pair breaking. Abrikosov and Gor'kov developed a theory assuming that exchange scattering of conduction electrons by impurity spins may be adequately described within the first Born approximation (Abrikosov, 1957; Matthias et al., 1958; Abrikosov and Gor'kov, 1961). This theory, which is named AG theory, has become a classic theory for superconductors containing paramagnetic impurities.

In the AG theory, superconducting properties in the presence of paramagnetic impurities are characterized by a pair breaking parameter, $\alpha = \tau_s^{-1}$, where τ_s^{-1} is the lifetime of the time-reversed single particle paired states of which the superconducting wave function is composed. τ_s^{-1} is no longer infinite with presence of paramagnetic impurities. The theory predicts a rapid decrease of T_c with α given by the universal relation

$$\frac{T_c}{T_{c0}} = \psi(\frac{1}{2}) - \psi(\frac{1}{2} + 0.14\frac{\alpha T_{c0}}{\alpha_{cr} T_c}), \tag{2.24}$$

Where T_{c0} corresponds to $\alpha = 0$, α_{cr} corresponds to $T_c = 0$ and ψ is the digamma function.

It is important to note that α is proportional to n and independent of temperature. Therefore α/α_{cr} can be replaced by n/n_{cr}, where n_{cr} is the critical concentration for the complete suppression of superconductivity. Thus, the AG theory predicts that superconducting transition temperature is a universal function of the impurity concentration

$$\frac{T_c}{T_{c0}} = \psi(\frac{1}{2}) - \psi(\frac{1}{2} + 0.14\frac{n T_{c0}}{n_{cr} T_c}). \tag{2.25}$$

For rare earth impurities, pair breaking parameter α can be calculated within the first Born approximation, which gives the result

$$\alpha = \frac{n}{\hbar}[\frac{N(E_F)}{2k_B}]\mathcal{J}^2((g_J - 1)J(J+1)), \tag{2.26}$$

where $\mathcal{J}$ is the exchange interaction parameter, g_J is the Lande g-factor for the Hund's rule ground state of the rare earth ion and J is the total angular momentum vector of the Hund's

rule ground state. Thus, the AG theory yields an initial depression of T_c with n that is linear with a rate given by

$$(\frac{dT_c}{dn})_{n=0} = -[\frac{\pi^2 N(E_F)}{2k_B}]\mathcal{J}^2(g_J-1)^2 J(J+1), \tag{2.27}$$

where the quantity $(g_J-1)^2J(J+1) = D(R)$ is called the deGennes factor. If $\mathcal{J}^2$ is assumed to be constant or decrease slightly with increasing rare earth atomic number, the depression of T_c with rare earth scales with the deGennes factor.

Fig. 2.8 presents the phase diagram of Superconducting and antiferromagnetic transition temperatures versus Gd concentration for $La_{1-x}Gd_x$ alloy (Finnemore et al., 1965a), which shows a clear suppression of T_c by Gd impurities. In Fig. 2.9, a plot of $\frac{T_c}{T_{c0}}$ vs. $\frac{n}{n_{cr}}$ for $La_{1-x}Gd_xAl_2$ system is presented (Maple, 1968; Maple et al., 2008). The solid line represents the theoretical universal curve from AG theory. As can be seen, good agreement was achieved. In Fig. 2.10, the normalized suppression rate of T_c in different rare earth element doped $La_{1-x}R_xAl_2$ and $La_{1-x}R_x$ series are presented (Finnemore et al., 1965a,b; Maple, 1970; Wollan and Finnemore, 1971; Maple et al., 2008). The solid line is the theoretical curve of de Gennes factor. Good agreements were also achieved.

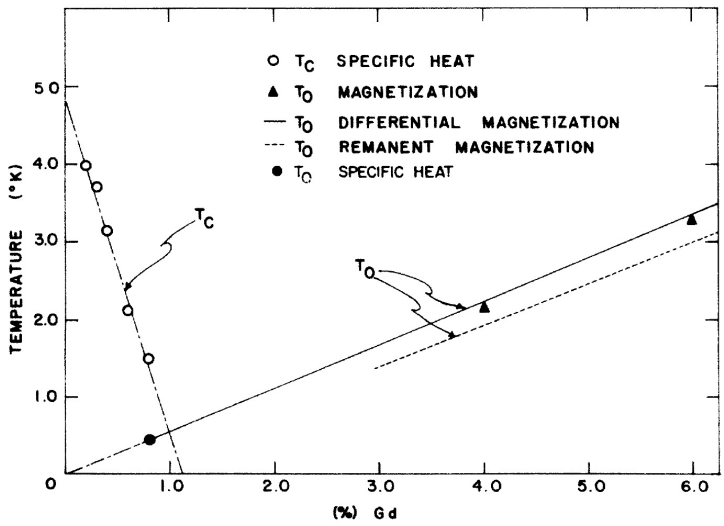

Figure 2.8 Superconducting and antiferromagnetic transition temperatures for $La_{1-x}Gd_x$ alloy. (Finnemore et al., 1965a)

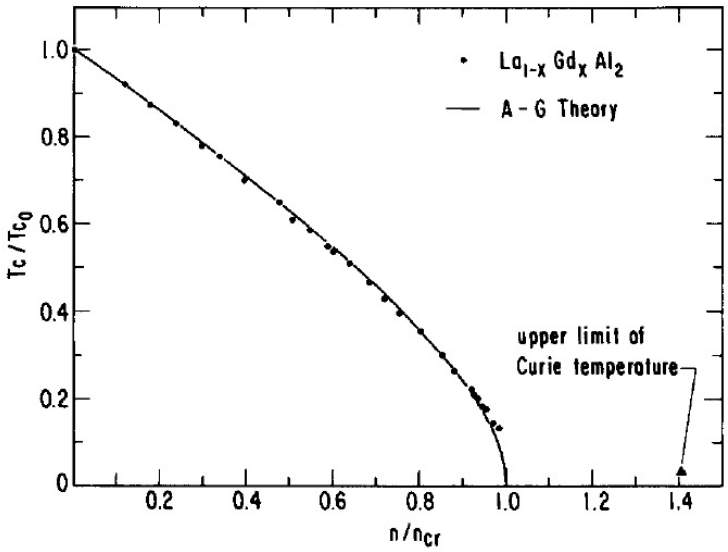

Figure 2.9 Reduced superconducting critical temperature $\frac{T_c}{T_{c0}}$ vs. reduced Gd impurity concentration $\frac{n}{n_{cr}}$ for the $La_{1-x}Gd_xAl_2$ system. Solid line: from the AG theory. Dots: experiment data. (Maple, 1968)

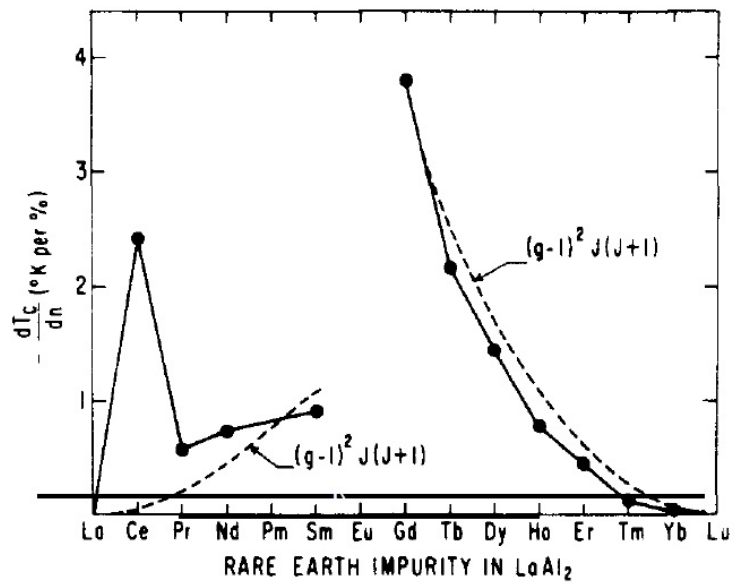

Figure 2.10 Rate of depression of T_c with paramagnetic impurity concentration n, $\frac{dT_c}{dn}$, vs. rare earth impurity for the $La_{1-x}R_xAl_2$ and $La_{1-x}R_x$ series. Solid line: from the AG theory. Dots: experiment data. (Maple, 1970)

Figure 2.11 shows the data of T_c and T_N with respect to the de Gennes factor for pure RNi_2B_2C compounds (Canfield et al., 1997; Bud'ko and Canfield, 2006). As we can see, the de Gennes factor can work as a scaling parameter for both T_c and T_N in these compounds. The fact that T_N scales well with the de Gennes factor is consistent with the RKKY interaction which gives rise to the long range ordering in these compounds. And the fact that T_c roughly scales with the de Gennes factor is consistent with AG theory.

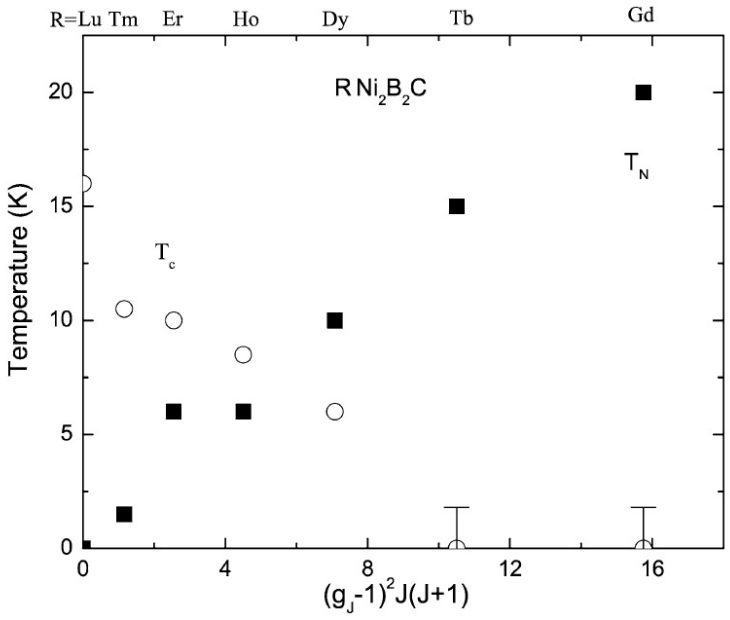

Figure 2.11 T_c and T_N vs. the de Gennes factor for pure RNi_2B_2C compounds. (Bud'ko and Canfield, 2006)

However, the simple de Gennes scaling of the suppression of T_c fails when magnetic impurities are added, as can be seen from Fig. 2.12 (Canfield et al., 1997; Bud'ko and Canfield, 2006). Whereas the T_c for $TmNi_2B_2C$ does coincide with the $(Lu_{1-x}Gd_x)Ni_2B_2C$ manifold, the data for other local moments impurities appears to manifest much higher T_c values than would be predicted for their dG factor. This deviation from simple dG scaling of T_c has been associated with the highly anisotropic nature of the local moments for R = Er - Tb (Canfield et al., 1997; Bud'ko and Canfield, 2006).

It becomes more complicated when a series of samples between $HoNi_2B_2C$ and $DyNi_2B_2C$ is

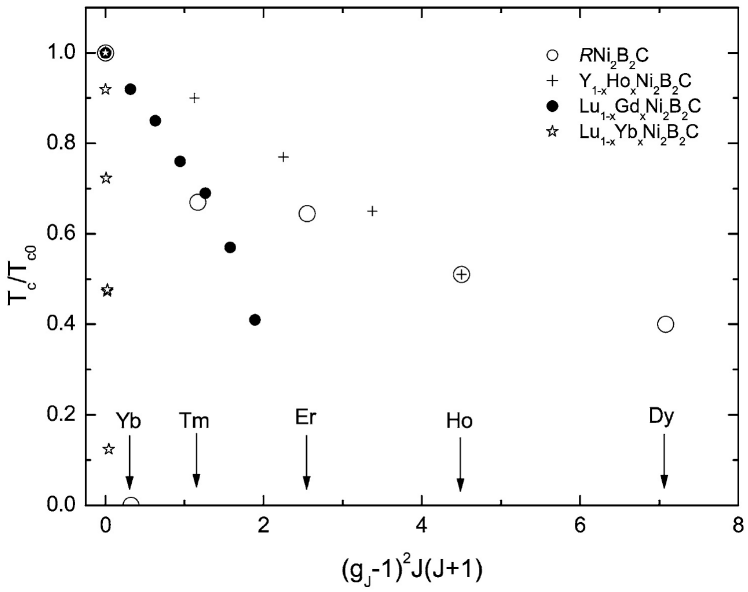

Figure 2.12 T_c vs. the de Gennes factor for pure RNi_2B_2C compounds and several series of solid solutions. (Bud'ko and Canfield, 2006)

examined, as shown in Fig. 2.13 (Cho et al., 1996; Canfield et al., 1997; Bud'ko and Canfield, 2006). As can be seen, T_c does drop until near 30% Dy, the concentration at which $T_c \approx T_N$. From that point onward, T_c is essentially independent of Dy concentration (and therefore dG factor). In order to more fully understand this behavior, detailed studies were carried on and it was suggested that there is a cross over from paramagnetic impurity scattering to an interaction between a Cooper pair and a magnon (Cho et al., 1996; Canfield et al., 1997; Bud'ko and Canfield, 2006).

2.4 Unconventional Superconductors

The focus of this section is on the three classes of unconventional superconductivity: heavy fermion f electron materials, high T_c cuprate and iron-based materials. One of the similarities of all the three classes of materials is the occurrence of superconductivity in the vicinity of the magnetic phase in the hyperspace of temperature, chemical concentration, pressure and magnetic field (Norman, 2011). This has been widely regarded as indication of the important

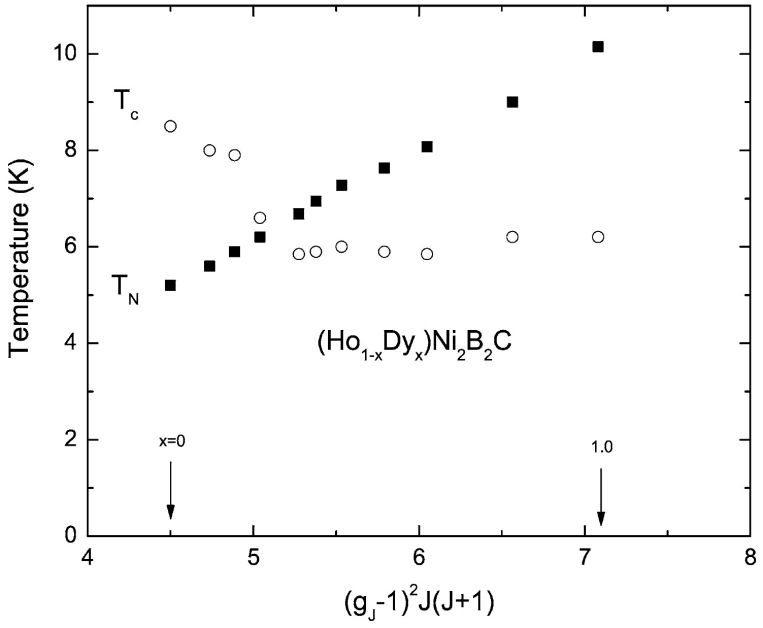

Figure 2.13 T_c and T_N vs. the de Gennes factor for $(Ho_{1-x}Dy_x)Ni_2B_2C$ compounds. (Cho et al., 1996)

role of the spin fluctuations in the paring mechanism of superconductivity in unconventional superconductors. In this section I will give brief introduction to each class.

2.4.1 Heavy fermion superconductors

The first heavy fermion superconductor, $CeCu_2Si_2$, was discovered in 1979 (Steglich et al., 1979). Since then over 30 heavy fermion superconductors were found in materials based on Ce and U (Stewart, 1984; Riseborough et al., 2008; Pfleiderer, 2009; Steglich et al., 2010, 2013).

In heavy-fermion systems, strong electronic correlations lead to a strong renormalization of the effective mass m* of the electrons (which explains the name "heavy fermions") and to a Fermi liquid behavior at low temperature (Coleman, 2007). Due to the presence of *f* electrons and conduction electrons, physics of heavy fermion materials is dominated by two mechanisms: the Kondo effect and the RKKY exchange. The Kondo effect involves the hybridization of the localized *f* states and the conduction bands and leads to the formation of a strongly renormalized Fermi liquid in the heavy fermion regime. The RKKY exchange interaction is the indirect

exchange interaction between two f electrons via the conduction electrons, which leads to a localized magnetically ordered state of f electrons. The competition between the Kondo effect and the RKKY exchange interaction causes a variety of ground states (Doniach, 1977; Stewart, 2006; Coleman, 2007).

Figure 2.14 presents the Doniach phase diagram of heavy fermion systems, which involves an antiferromagnetic phase, of a paramagnetic and Fermi-liquid regime, and of a non-Fermi-liquid regime. By adjusting $JN(E_f)$ (J is the effective interaction and $N(E_f)$ is the density of state at the Fermi level) through the control parameter, such as pressure or chemical substitution, the system can be tuned between different ground states. In some of the heavy fermion systems, superconductivity is observed in the vicinity of the quantum critical point, where the quantum phase transition takes place at $T = 0$.

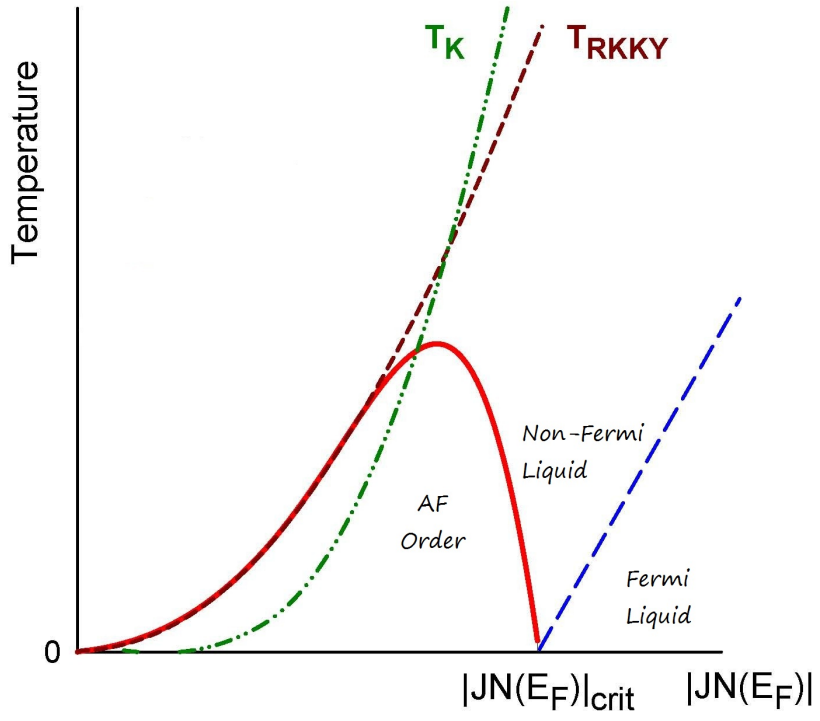

Figure 2.14 Doniach phase diagram of heavy fermion systems. In some heavy fermion systems, superconductivity is found in the vicinity of quantum critical point. (Doniach, 1977; Stewart, 2006; Coleman, 2007)

2.4.2 Cuprate superconductors

Cu-based high-temperature superconductors (or cuprates) have played an outstanding role in the scientific and technological development of superconductors since theirs discovery in 1986 (Bednorz and Müller, 1986). It still holds the world record of T_c (135 K at ambient pressure and above 150 K under applied pressure, achieved in the layered cuprate $HgBa_2Ca_2Cu_3O_{8+x}$) (Schilling et al., 1993; Chu et al., 1993). The main result of the early studies is that all members of the family have a similar phase diagram, as presented in Fig. 2.15 (Varma, 2010), of which superconductivity is only one aspect.

For many of the high-T_c cuprates, the parent compounds, with no chemical substitution, are poor conductors. They are believed to be an example of the Mott insulator, in which electronic conductivity is blocked by the electron-electron Coulomb repulsion (Anderson, 1987; Tachiki and Matsumoto, 1990; Levin et al., 1991). At low temperature there is magnetic (antiferromagnetic) ordering in the system, which can be suppressed with the increase of the chemical substitution. With adequate substitution a superconducting dome is established. A persistently mysterious part of the phase diagram of cuprates comes at intermediate temperature, after the loss of the antiferromagnetic ordering with the increase of the chemical substitution. Commonly this region is known as the "pseudogap" state (Levi, 1993; Maple et al., 2008). The discussion of pseudogap is beyond the scope of this work. Further increasing the chemical substitution in the pseudogap state eventually leads to the superconductivity. Despite substantial effort, the microscopic mechanism of the superconductivity in cuprates is still uncertain. However,the proximity of antiferromagnetism suggests superconducting electron pairing in cuprates may be mediated by AFM spin fluctuations (Scalapino, 1995; Pines, 1994).

2.4.3 Iron-based superconductors

The discovery of superconductivity in iron-based materials in 2008 (Kamihara et al., 2008; Hosono, 2008) is among the most significant breakthroughs in condensed-matter physics during the past decade. Before 2008, the term "high-temperature superconductivity (HTS)" was reserved for the cuprates. Now the term HTS equally applies to both cuprates and iron-based

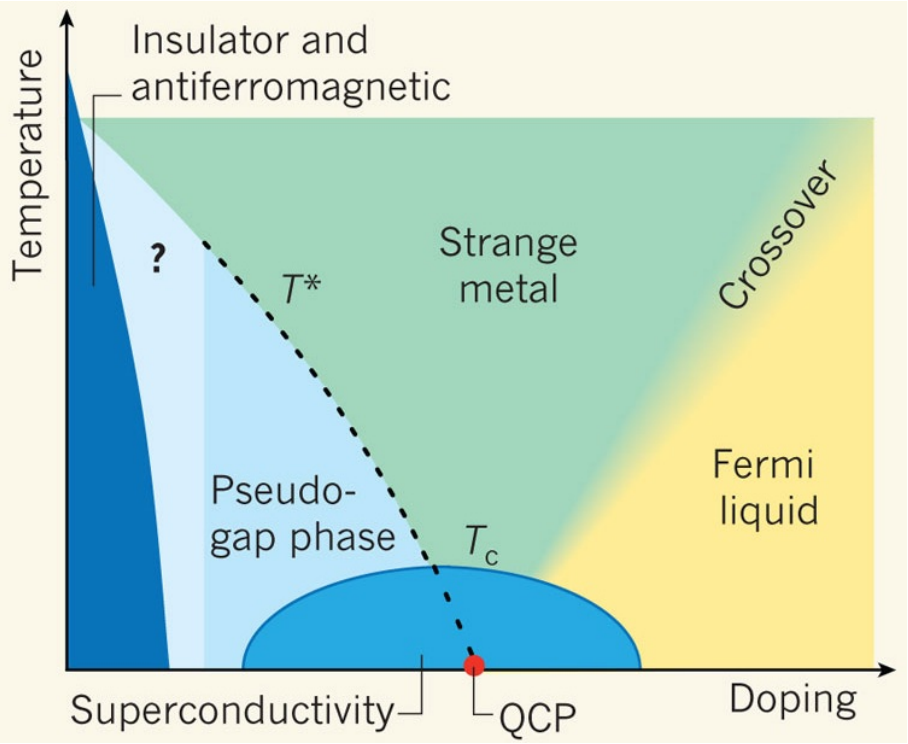

Figure 2.15 Phase diagram of cuprate superconductors. At low levels of substitution, cuprates are insulating and antiferromagnetic. At increased doping levels, they become conducting. At temperatures below T_c, they become superconducting, and at temperatures above T_c but below T^* they fall into the pseudogap phase. The boundary of the pseudogap region at low doping levels is unknown. The transition between the Fermi-liquid phase and the strange-metal phase occurs gradually (by crossover). QCP denotes the quantum critical point at which the temperature T^* goes to absolute zero. (Varma, 2010)

superconductivity. One of the reasons for the enormous excitement is the intricate interplay between magnetism and superconductivity, which is similar to heavy fermion superconductors and cuprates.

The phase diagram of iron-based superconductors looks amazingly similar to that of cuprates, as presented in Fig. 2.16 (Chubukov, 2012). The parent compound has magnetic ordering which will be suppressed with increasing chemical substitution or pressure. Unlike cuprates, in which the antiferromagnetism is associated with strong electron correlation, the relatively small and variable values of ordered moment observed for the parent compounds of iron-based superconductors suggest that the antiferromagnetic order in these materials is a spin-density-wave (SDW) arising from itinerant electrons. Superconductivity emerges when this SDW is suppressed enough, and sometimes coexists with antiferromagnetism.

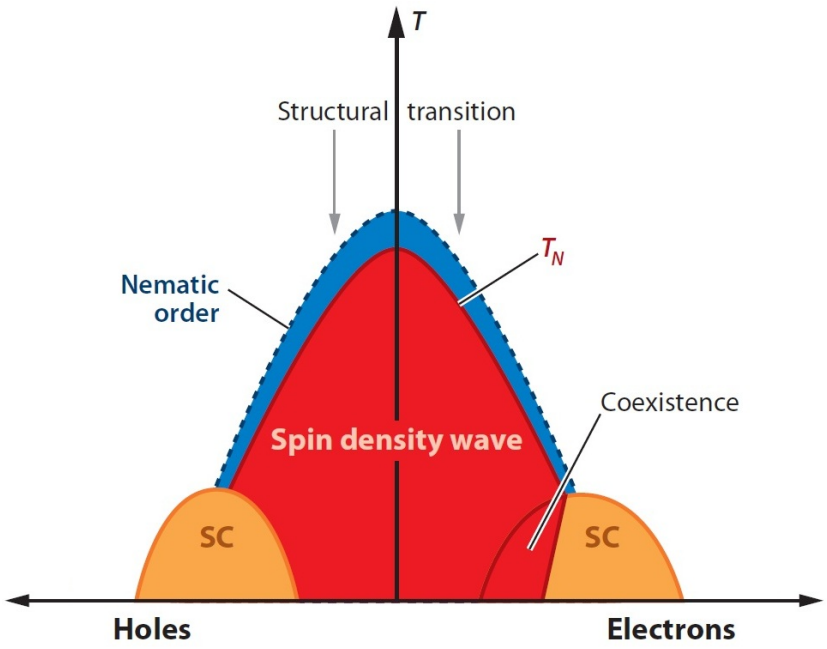

Figure 2.16 Phase diagram of iron-based superconductors. Below the temperature of structural transition, the crystal structure is orthorhombic whereas, above this transition, the crystal structure is tetragonal. Below T_N, there is antiferromagnetic order (spin-density wave state). In the shaded region, superconductivity (SC) and antiferromagnetism coexist. The nematic phase above T_N is the subject of debate. (after Chubukov (2012))

Whether superconductivity coexists with antiferromagnetic order is of particular interest as this aspect is thought to hold the clue for discriminating the unconventional s+- type of superconductivity from the conventional s++ one (Fernandes et al., 2010; Fernandes and Schmalian, 2010). Earlier work on Co-substitution of $CaFe_2As_2$ also shows coexistence of superconductivity and antiferromagnetism (Harnagea et al., 2011; Hu et al., 2012). However, due to the issues with solubility, reproducibility and inhomogeneity, the phase diagrams constructed by different groups do not match very well and, therefore, need to be clarified. In my thesis work, I constructed unambiguous phase diagrams for various transition metal substitutions of $CaFe_2As_2$ system, with substitution level and annealing/quenching temperature as two independent control parameters. I have shown that, in contrast to transition metal (TM)-substituted $BaFe_2As_2$, superconductivity in TM-substituted $CaFe_2As_2$ does not coexist with antiferromagnetism. Given the strong first order nature of the antiferromagnetic/orthorhombic (AMF/ORTH) phase transition in pure and substituted $CaFe_2As_2$, lacking superconductivity under the AFM/ORTH phase line underscores the importance of spin fluctuation for the formation of superconductivity in iron-based systems.

CHAPTER 3. EXPERIMENTAL METHODS

3.1 Crystal Growth

Crystal growth is important for modern science and technology, and is often the very first step towards understanding interesting phenomena. Bulk materials can be crystallized in either single crystalline form or polycrystalline form. Although it is usually more difficult to prepare single crystals than polycrystalline materials, the extra effort is justified because of the outstanding advantages of single crystals. Single crystals, by definition, have no grain boundaries. In polycrystalline materials, many physical properties, such as anisotropy, are obscured or complicated by the effect of grain boundaries. Other advantages of single crystals over polycrystalline materials include the ability to better detect and quantify anisotropy and in general, better uniformity of composition. Therefore, good quality single crystals are greatly preferred for both fundamental research and in some cases, applications.

Various techniques have been developed to grow single crystalline samples. Based on the phase transformation process, single crystal growth techniques are classified as solid state growth, vapor phase growth, melt growth and solution growth. The solid state growth method usually results in crystals of micron size and has issues of phase segregation and grain boundaries. The vapor phase growth method often results in very high purity crystals. But it is often difficult to grow large crystals because of multiple nucleation sites. Also finding a suitable transporting agent can be a formidable problem for this technique. The melt growth method is widely used in the semiconductor industry to produce large single crystalline Si and Ge semiconductors. However, the melt growth method is limited to the materials that melt congruently without decomposition at the melting point and do not undergo any phase transformation between the melting point and room temperature. The solution growth method can

easily grow both congruently melting and incongruently melting materials, provided that they have adequate solubility and have adequate temperature dependent variation in solubility. In this thesis, all the samples presented were grown using a high temperature solution growth method.

3.1.1 High temperature solution growth method

High temperature solution growth is one of the most powerful and widely used technique for the production of single crystals for basic and applied research (Fisk and Remeika, 1989; Canfield and Fisk, 1992; Canfield and Fisher, 2001; Canfield, 2010). It is a versatile technique, using relatively simple equipment, that allows for the growth of congruently and incongruently melting materials with equal ease.

In high temperature solution growth, all the constituent elements and a suitable solvent are heated in a container to a peak temperature so that all the solute materials dissolve to form a uniform solution. This temperature is maintained for several hours and then the temperature is lowered slowly. As the temperature decreases, the solubility of the target compound decreases, the desired compound starts to precipitate out of the solution (ideally in single crystal form) below a temperature determined by the location of the liquidus surface. As the temperature further decreases, at a constant and slow rate, crystals grow. Once the crystals are grown, they can be separated from the remaining liquid by decanting off the excess liquid using a centrifuge at a decanting temperature.

A successful single crystal synthesis via solution growth involves consideration of several factors: material, solvent, crucible, initial concentrations of components, maximum temperature, vapor pressure, cooling rate, decanting temperature, etc.

The solvent used in high temperature solution growth is also referred to as a “flux”, which is required to have a relatively low melting temperature and offer good solubility for the other components in the growth. According to whether extra elements other than the ones in the target compound are introduced, flux can be classified into two types: self-flux and non-self-flux. When using self-flux, the excess of one or more constituent elements of the desired compound is used as the solvent; while when using non-self-flux, elements other than the ones in the

desired compound are used as the solvent. It is often preferable to use a self-flux since it does not introduce any other elements into the melt, and thus no other element can enter into the desired single crystal, and the number of possible undesired phases can also be reduced. However, non-self-flux is often used as well, since it is not always practical (or even possible) to use self-flux. For example, the self-flux may require too high of a melting temperature, one that exceeds the working temperatures of ampoules or furnaces. In some other cases, self-flux may have too high of a vapor pressure which will lead to loss of stoichiometry in the resulting single crystals or even to a possible explosion. In these cases, non-self-flux, which has low vapor pressure, high solubility for the constituent elements and compatibility with the crucibles, is often used. For intermetallic compounds, the frequently used elemental fluxes (for either self-flux or non-self-flux) include Zn, Al, Ga, In, Ge, Sn, Pb, Sb and Bi.

The initial concentrations of components and maximum temperature are often chosen together based on the solubility of the constituent elements in the flux. The maximum temperature is also limited by the working temperatures of furnaces and the ampoules. Slow cooling rate, lower than 10°C per hour, is often preferred since the sample nucleation and size partially depends on the cooling rate. Often, the slower the cooling, the larger the crystal. Also slow cooling rate allows for synthesis of crystals relatively free of strains. The decanting temperature needs to be chosen carefully as well. It should be high enough so that no second phases nucleate and the flux is still liquid; on the other hand, it should be low enough so that the desired crystal has as large of a temperature window for growth as possible.

3.1.2 Single crystal growth of $Ca(Fe_{1-x}TM_x)_2As_2$

Single crystals of pure and transition metal substituted $CaFe_2As_2$ can be grown using a conventional, high temperature solution technique, using both Sn-flux and self-flux (Ni et al., 2008b; Ran et al., 2011). In this thesis, all the samples for annealing/quenching study were grown from self-flux. Single crystals of parent $CaFe_2As_2$ were also grown from Sn-flux for comparison.

3.1.2.1 Single crystal of $CaFe_2As_2$ grown from Sn-flux

$CaFe_2As_2$ was discovered when single crystal of $CaFe_2As_2$ was first synthesized using Sn as flux (Ni et al., 2008b; Ronning et al., 2008). From the binary phase diagrams (Fig.3.1-3.2), it can be seen that the solubility of Ca, Fe and As in Sn is fairly large. The low melting temperature of Sn allows growth of single crystals at relatively low temperature.

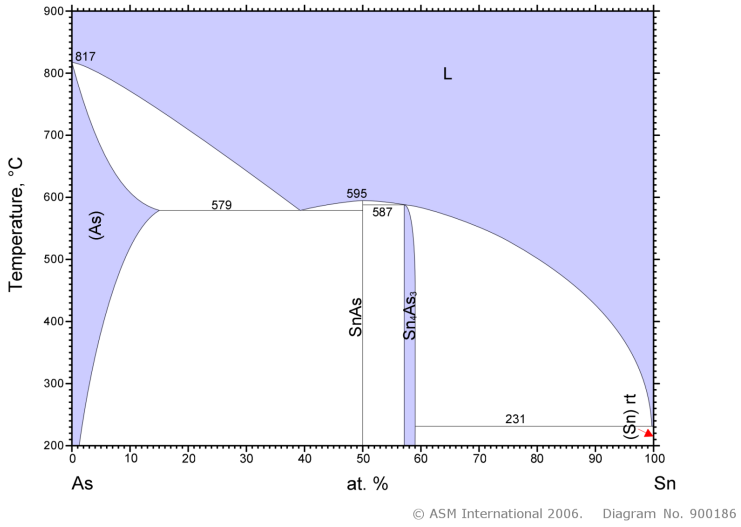

Figure 3.1 Phase diagrams of the As-Sn binary systems. (ASM alloy phase diagram database)

Elemental Ca, Fe, As and Sn were mixed together according to the ratio Ca:Fe:As:Sn = 2:3.5:4:96 and placed in a 2 ml alumina crucible. Total amount of Sn used for each growth is around 6 g. 12.5 % of Fe less than the 1:2:2 stoichiometry of $CaFe_2As_2$ is used to prevent the formation of a rod-like crystalline second phase, $CaFe_4As_3$ (Ni et al., 2008b). A second catch crucible containing silica wool was placed on top of the growth crucible and both crucibles were then sealed in a silica ampoule under approximately 1/3 atmosphere of argon gas. It should be noted that the packing and assembly of the growth ampoule was performed in a glovebox with a nitrogen atmosphere, since Ca is air sensitive. The sealed ampoule was placed in a 50 ml alumina crucible which itself was placed in a programmable box furnace. The furnace was heated up to 600°C in 3 hours and dwelled for one hour to make sure that As was completely dissolved into the melt . Then the furnace was heated up to 1150°C at a rate of 100°C/hour,

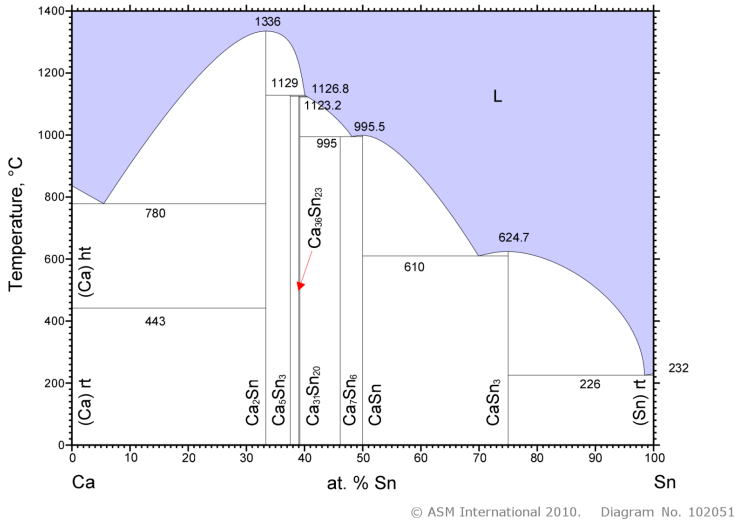

Figure 3.2 Phase diagrams of the Ca-Sn binary systems. (ASM alloy phase diagram database)

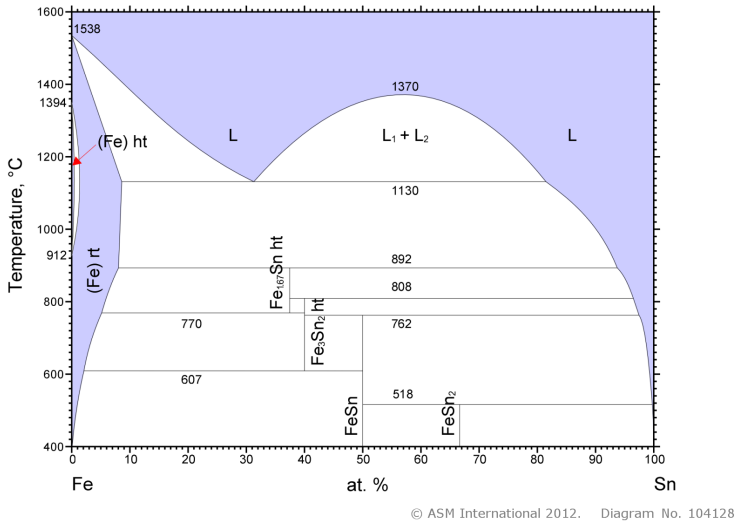

Figure 3.3 Phase diagrams of the Fe-Sn binary systems. (ASM alloy phase diagram database)

stayed at 1150°C for 2 hours so that the liquid mixed completely and cooled over 40 hours to 600°C. Once the furnace reached 600°C the liquid was decanted from the platelike $CaFe_2As_2$ crystals by using a centrifuge. The resulted single crystal can be as big as $3 \times 3 \times 0.2$ mm. Fig. 3.4a shows a picture of a single crystal of $CaFe_2As_2$ grown from Sn-flux against a 1 mm scale. The as-grown flat surface is the *ab* plane. The sample has clear [100] edges.

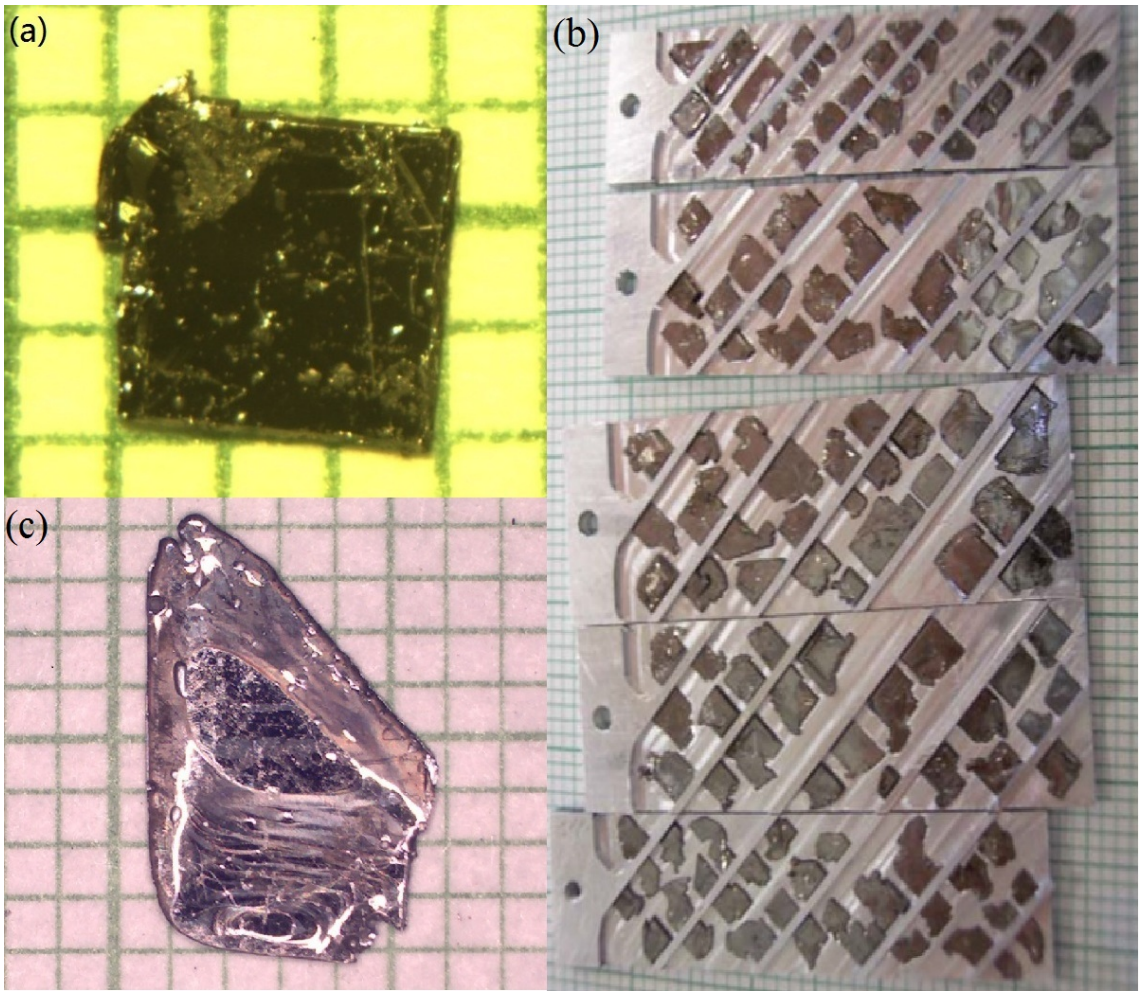

Figure 3.4 (a) Single crystal of $CaFe_2As_2$ grown from Sn-flux against 1mm scale. (b) Coaligned single crystals of $CaFe_2As_2$ grown from Sn-flux, used for an inelastic neutron scattering experiment (Pratt et al., 2009b). (c) Single crystal of $CaFe_2As_2$ grown from self-flux against 1mm scale.

3.1.2.2 Single crystal of $Ca(Fe_{1-x}TM_x)_2As_2$ grown from self-flux

Although single crystals of $AEFe_2As_2$ (AE = Ca, Sr, Ba) can be grown from Sn-flux, the size of crystals is rather small. This could lead to difficulties for some experiments which require large mass crystals, such as neutron scattering (Pratt et al., 2009b). Fig. 3.4b shows a picture of coaligned single crystals of $CaFe_2As_2$ grown from Sn-flux, used for an inelastic neutron scattering experiment. Approximately 300 crystals were mounted on both sides of five Al plates. A self-flux growth technique was also developed to grow single crystals of $AEFe_2As_2$ using FeAs as flux (Sefat et al., 2008b; Wu et al., 2008), which yields much larger size crystals. Also, when substituting other transition metals onto the Fe site, self-flux method allows for homogeneous substitution.

The single crystals of pure and transition metal substituted $CaFe_2As_2$ were grown using self-flux in two steps. First FeAs/TMAs binary compounds, which were used as flux, were synthesized by hybrid vapor phase/solid state reaction method. Single crystals of $Ca(Fe_{1-x}TM_x)_2As_2$ were then synthesized from self-flux by mixing small Ca chunks, FeAs powder, and TMAs powder together according to the ratio Ca:FeAs:TMAs =1:4(1-$x_{nominal}$):4$x_{nominal}$, where $x_{nominal}$ is the nominal TM concentration. Given the higher melting point of FeAs and some other TMAs (Fig. 3.5), the growth takes place during a cooling from 1180°C to 960°C over 40 hours. After that the excess liquid was decanted by using a centrifuge. The details of the synthesis process are presented in Appendix A. The dimension of the resulting single crystals can exceed 10 × 10 × 0.8 mm. An example is shown in Fig. 3.4c. Unlike crystals grown out of Sn-flux which have clear [100] edges, single crystals grown from self-flux do not have clear edges.

3.2 Postgrowth Thermal Treatment

The single crystals grown from self-flux, which were quenched from 960°C to room temperature, will be referred to as $T_{A/Q}$ = 960°C (or "as-grown") samples. Postgrowth thermal treatments of samples involve annealing samples at a certain temperature, $T_{A/Q}$, ranging from 350°C to 800°C, and subsequently quenching them from this temperature to room temperature. These samples will be identified as $T_{A/Q}$ = 350°C to $T_{A/Q}$ = 800°C. The postgrowth thermal

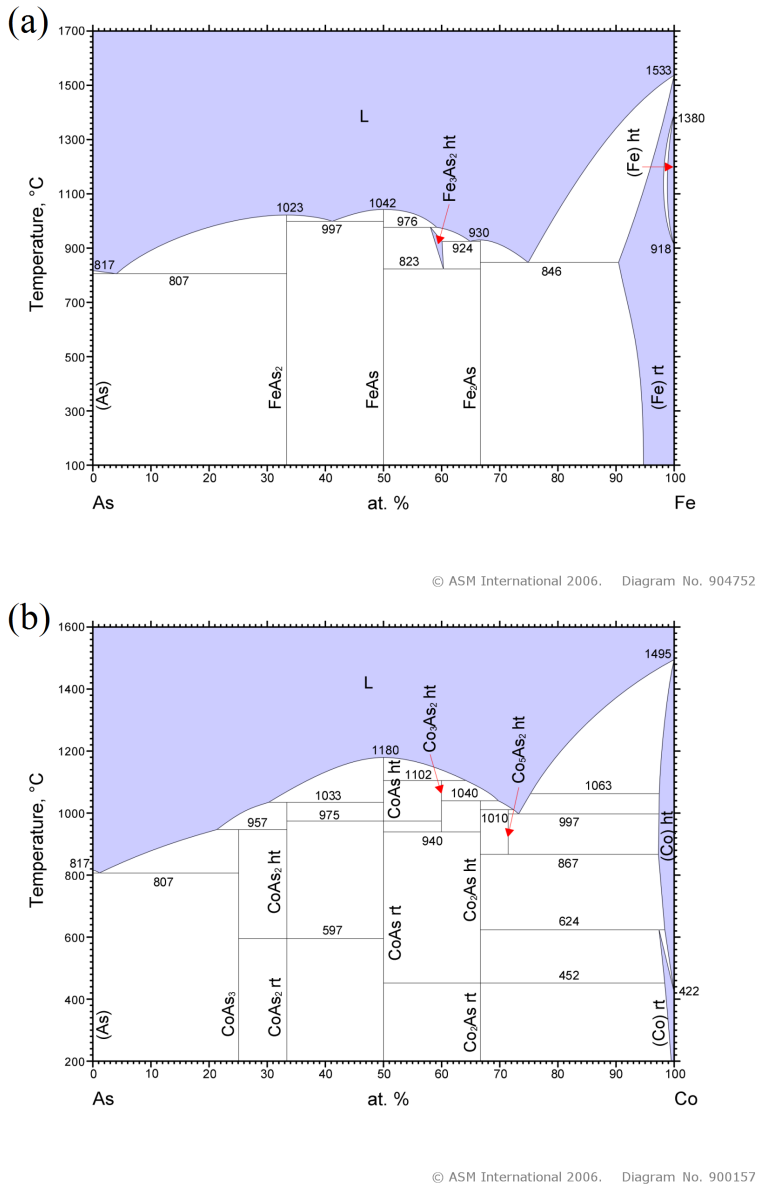

Figure 3.5 Phase diagrams of the (a) As-Fe and (b) As-Co binary systems. (ASM alloy phase diagram database)

treatments were approached in two different ways: (i) annealing a whole, unopened, decanted growth ampoule or (ii) annealing individual crystals that have been picked from a growth and resealed in evacuated silica tubes. In the second case, 3-5 pieces of crystals are chosen and sealed in silica tube under approximately 1/3 atmosphere of argon gas. To prevent samples from damage potentially caused by the H_2-O_2 flame during sealing, silica wool is placed at top of the tube (top of Fig. 3.6). In both cases, the sample was placed into a hot furnace (bottom of Fig. 3.6) stabilized at the specified temperature, $T_{A/Q}$ and, after annealing, it was taken out the furnace and quenched to room temperature in air. Although longer annealing time at the same annealing/quenching temperature was used to anneal the whole batch, the data collected on samples from these "whole batch anneals" were quantitatively similar to those collected on the individually annealed samples.

3.3 Characterization Methods

3.3.1 x-ray diffraction measurements

To measure the variation of the lattice parameters with substitution level, x-ray diffraction from the plate-like samples was performed at room temperature using a Rigaku Miniflex diffractometer with Cu $K\alpha$ radiation. Standard powder x-ray diffraction was not attempted since we have found that $CaFe_2As_2$ based compounds are exceptionally malleable and are very easily damaged by attempts to grind them. Diffraction lines broaden dramatically even compared to the Ba122 and Sr122 (Ni et al., 2008b). Of equal concern, the magnetization data from the resulting powder is dramatically different from that of intact crystals, probably due to gross deformation or partial amorphization during the process of "grinding" the samples.

When x-ray diffraction measurements were performed on the plate-like samples, only (00L) peaks were observed (c-axis is perpendicular to the sample surface), as seen in Fig. 3.7. Therefore, only the values of the c-lattice parameter can be inferred. For the standard powder x-ray diffraction, in order to make quantitative statements about the lattice parameters, Si powder, with well defined lattice parameter, is combined with ground samples as an internal standard reference. This can not be done for the plate-like sample. For the plate-like samples, the major

Figure 3.6 Top: individual crystals that have been picked from a growth and resealed in evacuated silica tubes for annealing. Bottom: annealing furnace stabilized at 350°C.

source of error is from the thickness of the samples, the effect of which on the 2θ value is a function of the 2θ value itself. By using 2θ values of two most intensive peaks, (002) and (008), the effects of thickness can be minimized and the c-lattice parameter can be calculated (this could be done in Origin).

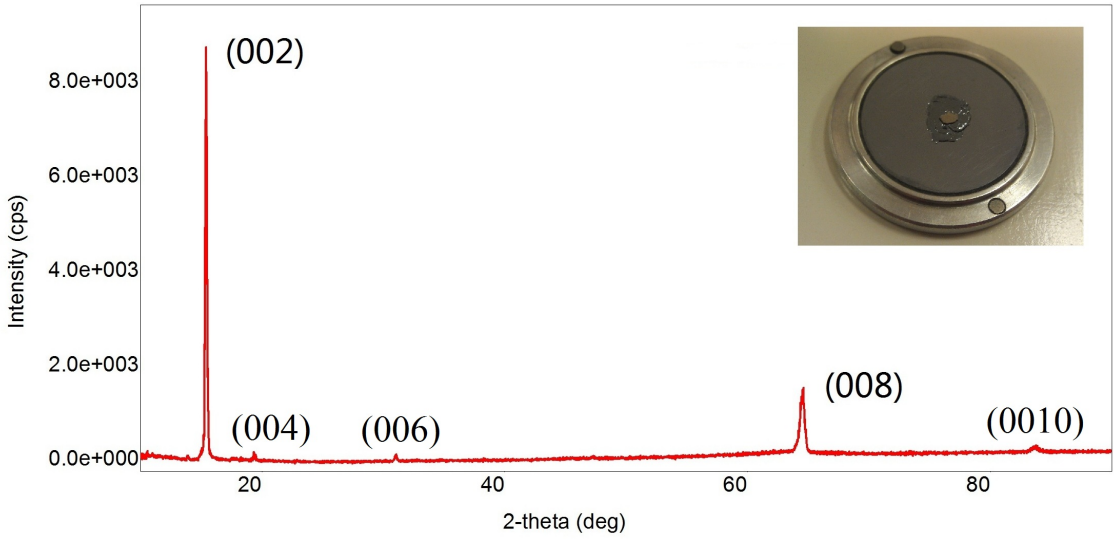

Figure 3.7 Selected X-ray pattern for a plate-like sample of Co-substituted $CaFe_2As_2$. Insert: a plate-like sample of Co-substituted $CaFe_2As_2$ mounted on the powder x-ray puck.

3.3.2 Wavelength dispersive spectroscopy

Given the nature of solution growth, the nominal transition metal substitution fraction does not have to be the actual substitution fraction in a grown crystal. In order to directly determine the actual concentration of TM in the crystals, elemental analysis of the $Ca(Fe_{1-x}TM_x)_2As_2$ samples was performed using wavelength dispersive x-ray spectroscopy (WDS) in the electron probe microanalyzer of a JEOL JXA-8200 electron-microprobe. In the WDS measurement, an electron beam with sufficient energy (20 kV is used in our measurements) is incident on the sample surface and interacts with the atoms in the sample. Characteristic spectra of x-ray is produced in this process. Since the characteristic x-ray wavelength is unique for each element, its energy can be used to identify the elements present in the sample and its intensity can be used for quantitative elemental analysis. WDS measurements were performed for all

the batches.[1] For some batches more than one piece of sample was measured to check the homogeneity within a batch. For each piece, WDS measurements were made at 12 locations on one side of the cleaved surface and the average value is used as the actual concentration of the transition metal. The error bars are taken as twice the standard deviation determined from the measurements. In this thesis, the average experimentally determined concentration values, $x = x_{WDS}$, will be used to identify all the compounds rather than the nominal concentration, $x_{nominal}$.

3.3.3 Resistivity measurement

Temperature dependent electrical resistivity measurements between 2 and 300 K were performed in a Quantum Design (QD) Magnetic Properties Measurement System (MPMS) operated in external device control (EDC) mode, in conjunction with Linear Research LR700 AC resistance bridges ($f = 16$ Hz, $I = 1$ mA) or in the QD Physical Properties Measurement System (PPMS) using the DC transport option ($I = 1$ mA). The outer layers of plate-like samples were removed by cleaving them off and the electrical contacts were placed on the samples in standard four-probe geometry, using Pt wires attached to the sample with Epotek H20E silver epoxy. The epoxy was then cured at 120°C for 30 minutes. Typical contact resistance was between 1 and 3 Ω after a DC current flow of up to 100 mA was applied. The temperature-dependent AC ($f = 16$ Hz, $I = 1$ mA) resistance was also measured in applied magnetic fields up to 14 T in a QD-PPMS so as to determine the anisotropic, upper superconducting critical field, $H_{c2}(T)$ values.

In this thesis the normalized resistivity values are plotted, but the measured resistivity values of representative samples did not vary outside the uncertainty associated with a combination of geometric error (associated with measuring dimensions of the sample) and difficulties associated with sample exfoliation. The average room temperature resistivity of $CaFe_2As_2$ samples with $T_{A/Q} = 960$°C, 700°C and 400°C was 3.75 ± 0.75 mΩ cm (a 20% variation).

[1] The measurements were done by Warren Straszheim.

3.3.4 Magnetization measurement

The temperature dependent magnetization measurements were made in QD-MPMS systems. In this thesis, magnetization measurements were made for two different reasons: (1) high field (1 T) temperature dependent magnetization between 2 and 300 K to detect the antiferromagnetic/orthorhombic (AFM/ORTH) and the non-moment bearing/collapsed tetragonal (cT) phase transitions, due to the weak magnetic signal (normally $M/H \sim 10^{-4}$ emu/mole); (2) low field temperature dependent magnetization between 2 and 20 K to detect the superconducting/paramagnetic/tetragonal (SC/PM/T) phase transitions. For high field measurement, it turns out that when the magnetic field is applied parallel to the c-axis, the size of the jump in the magnetization for the cT phase transition is significantly larger than that for the AFM/ORTH phase transition, whereas, when the magnetic field is applied perpendicular to the c-axis, the two types of transitions manifest comparable sized jumps in magnetization (Fig. 3.8). Therefore, when there is collapsed tetragonal phase, in order to allow for clearer differentiation between the two types of transition, magnetization was measured with applied magnetic field parallel to the c-axis. In cases when there is no collapsed tetragonal phase, magnetization was sometimes measured with field perpendicular to the c-axis. For superconducting samples, zero-field-cooled (ZFC) magnetization data were then taken at 10 mT with field perpendicular to the c axis (the low demagnetization direction) near and below the superconducting temperature, so that estimation of the screening could be made. To diminish the remanent field, a demagnetization sequence, 0 T $\rightarrow$ 5 T $\rightarrow$ -5 T $\rightarrow$ 2 T $\rightarrow$ -2 T $\rightarrow$ 1 mT $\rightarrow$ -1 mT $\rightarrow$ 0 T , was used before the low field measurement.

3.3.5 Specific heat measurement

Temperature-dependent heat capacity for representative samples was measured in a QD-PPMS system in both zero field and magnetic fields of either 9 or 14 T applied along the c axis down to 2 K. The heat capacity option in the QD-PPMS uses a relaxation technique (QD, 2004). The samples were attached to the heat capacity platform which contains a heater and a thermometer with a thin layer of Apiezon N grease. The platform is connected through

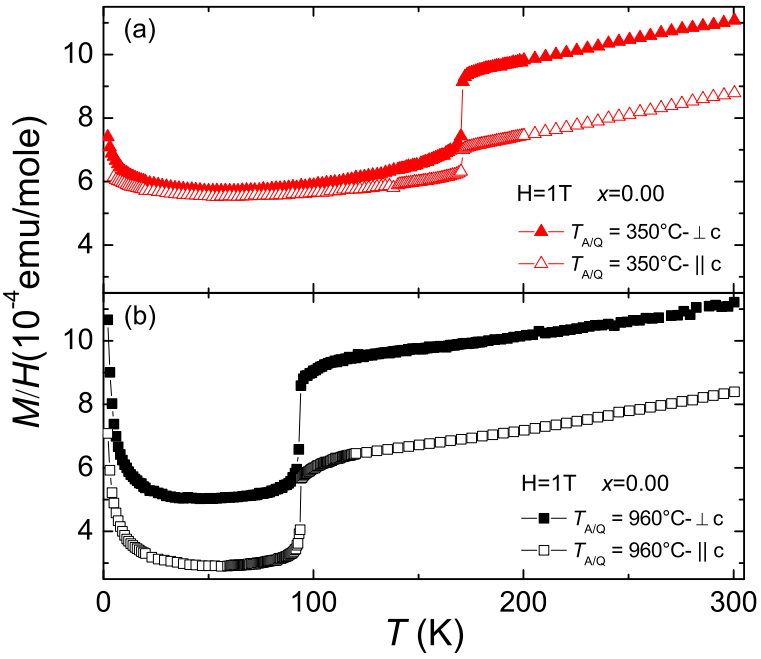

Figure 3.8 Temperature dependent anisotropic magnetization, with a magnetic field of 1 T applied perpendicular and parallel to the c-axis, for (a) the $x = 0.00/\, T_{A/Q} = 350$°C sample, as an example of the AFM/ORTH transition, and (b) the $x = 0.00/\, T_{A/Q} = 960$°C sample, as an example of the cT phase transition.

conducting wires to a reservoir. After the bath and the sample have reached the same temperature, a well defined constant heating pulse is applied to the platform for a fixed time (heating process), until a steady-state temperature is reached. The heater power is then turned off and the temperature decays for the time duration. After each measurement cycle (a heating process and a cooling process), the heat capacity values can be obtained by fitting the entire temperature response of the sample platform to a model which includes both thermal relaxation of the sample platform to the bath temperature and the thermal relaxation between the platform and sample itself.

3.3.6 Criteria for determination of the salient transition temperatures

In order to infer phase diagrams from the thermodynamic and transport data, I need to introduce criterion for determination of the salient transition temperatures. The AFM/ORTH phase was first detected in magnetization, resistance and specific heat data as seen in Fig. 3.9 (Ni et al., 2008b), and then confirmed by diffraction measurements (Goldman et al., 2008). The cT phase was initially observed in the Sn-grown samples under pressure (Torikachvili et al., 2008; Yu et al., 2009). The striking feature of the cT phase is the sudden drop in resistance data when cooling through the transition temperature as seen in Fig. 3.10. The cT phase was also confirmed by both neutron and x-ray diffraction measurements (Kreyssig et al., 2008; Goldman et al., 2009). When $CaFe_2As_2$ is grown out of FeAs-flux, the cT phase can be stabilized at ambient pressure, showing a very sharp drop in magnetization and discontinuity (or, in many cases, a loss of contacts) in resistance occurring well below 100 K. X-ray diffraction, Mössbauer spectroscopy, and NMR measurements were conducted to confirm that the ground state of the as-grown samples of $CaFe_2As_2$ grown out of FeAs-flux is the cT phase (Ran et al., 2011).

Having traced the various phases associated with $CaFe_2As_2$ to the salient diffraction and spectroscopic measurements, in this thesis work I will identify the phase and infer the transition temperature from magnetization and resistance data. The characteristic signatures of AFM/ORTH, SC/PM/T and cT phase transitions manifesting in resistivity and magnetization measurements near the transition temperatures are shown in Figs. 3.11 - 3.13.

The AFM/ORTH phase transition (when present) appears as a single (i.e., not split), sharp

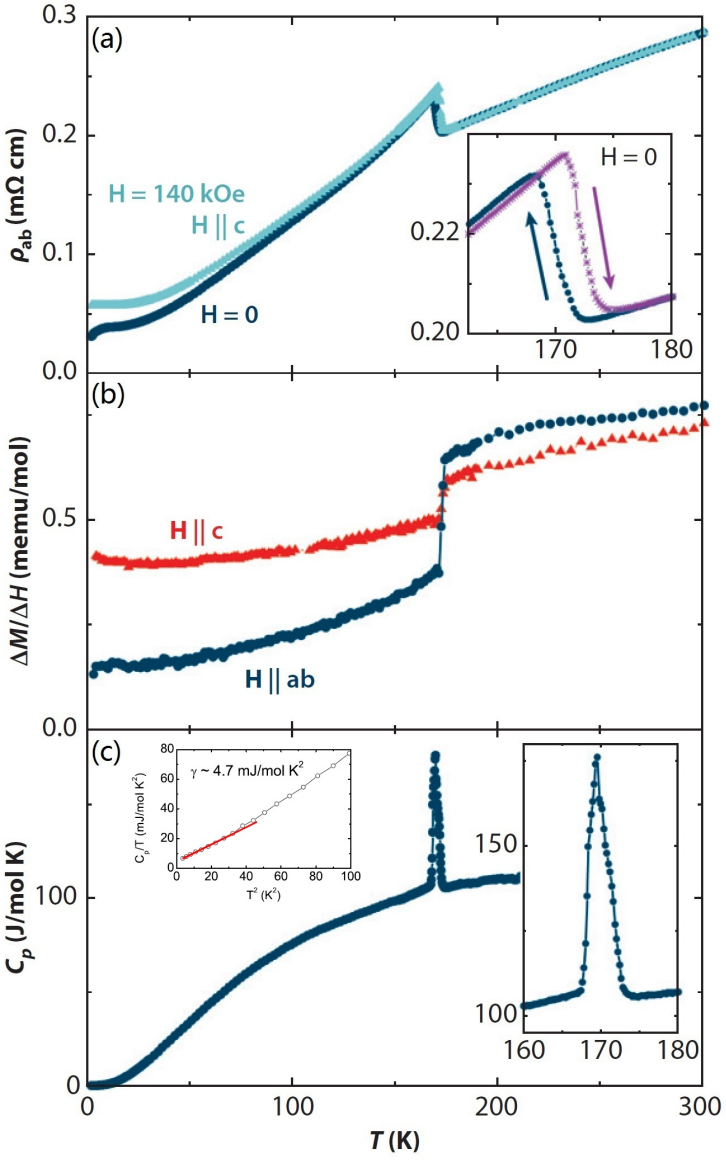

Figure 3.9 Temperature dependent (a) electrical resistivity, with current flowing within the basal plane, (b) magnetization for applied field parallel to and perpendicular to the crystallographic c-axis, and (c) specific heat of $CaFe_2As_2$. (Ni et al., 2008b)

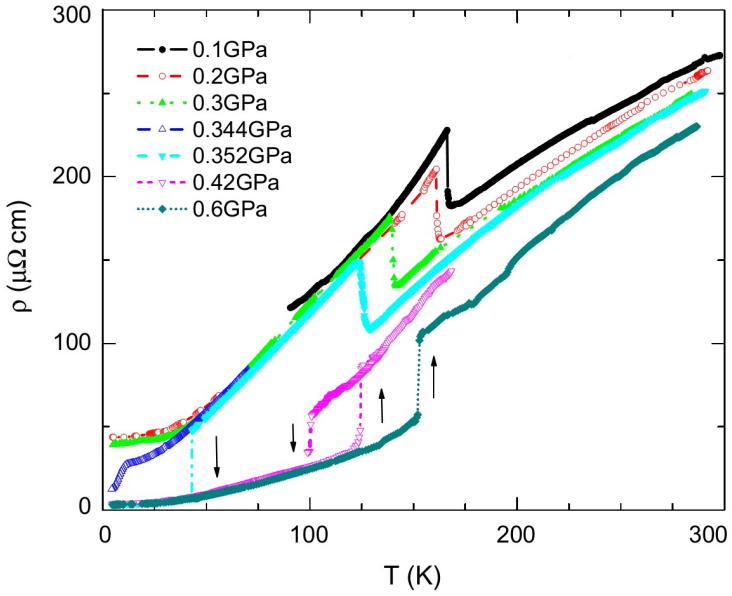

Figure 3.10 The resistivity of a $CaFe_2As_2$ single crystal at different pressures in a He-gas pressure cell. (Yu et al., 2009)

feature which is clearly identifiable in both resistance and magnetization. This is clearly seen in Fig. 3.9 for pure $CaFe_2As_2$. Figure 3.11 shows the susceptibility and resistance, as well as their temperature derivatives (insets), for a $x = 0.006/T_{A/Q} = 400°C$ Rh-substituted sample. Clear features, including a sharp drop in susceptibility and a sharp jump in the resistance, occur upon cooling through the transition temperature. The transition temperature is even more clearly determined by the extrema in the $d(M/H)/dT$ and dR/dT data.

For the superconducting transition, I only used an onset criterion for magnetic susceptibility (the temperature at which the maximum slope of the susceptibility extrapolates to the normal state susceptibility) to determine T_c. This criteria for T_c is presented in Fig.3.12a, with an example of a $x = 0.023/T_{A/Q} = 400°C$ Rh-substituted sample. Sometimes an offset criterion for resistance (the temperature at which the maximum slope of the resistance extrapolates to zero resistance) is also used in literature to determine T_c (Ni et al., 2008c). However, this leads to substantially higher T_c than ones inferred from magnetic susceptibility in $CaFe_2As_2$ which, given its profound pressure and strain sensitivities, is prone to filamentary superconductivity (Fig. 3.12b). Given that we do observe superconducting screening with zero field cooling (ZFC)

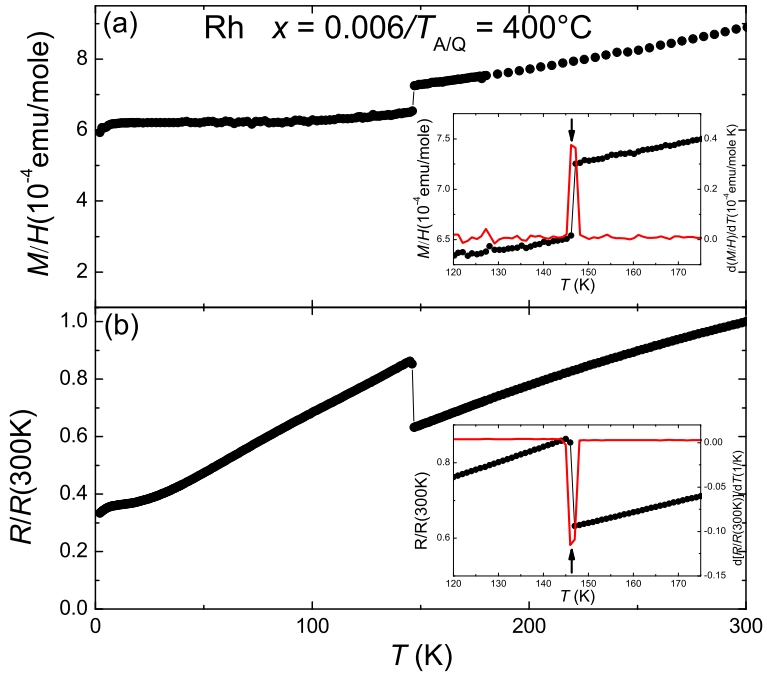

Figure 3.11 Criteria used to determine the transition temperatures of the AFM/ORTH phase transition. The data close to the transition are presented in the insets, together with the derivatives. Inferred transition temperatures are indicated by vertical arrows.

susceptibility reaching $1/4\pi$, I choose to err on the side of bulk superconductivity rather than minority phase of filamentary superconductivity (Saha et al., 2012).

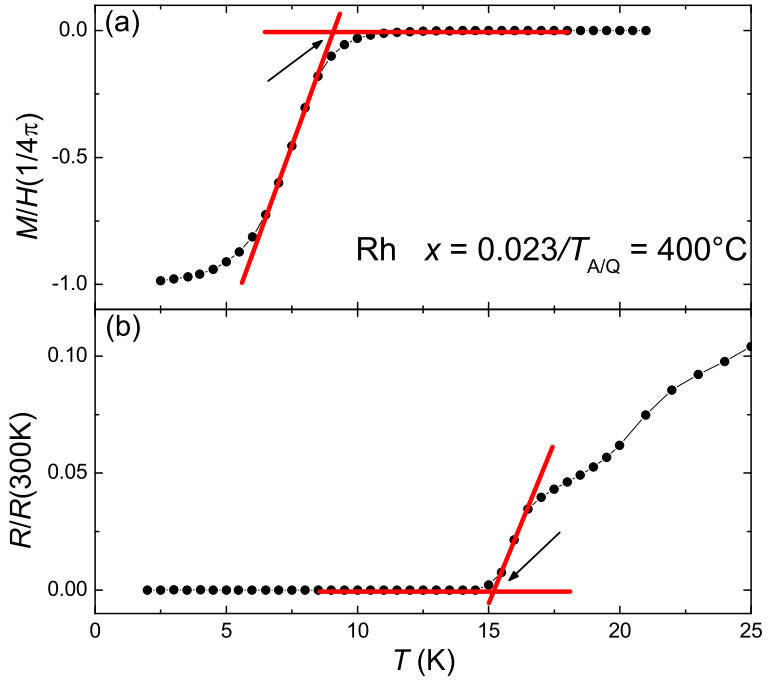

Figure 3.12 Criteria used to determine the transition temperatures of the superconducting phase transition. Inferred transition temperatures are indicated by arrows. As discussed in the text, use of resistivity data can lead to artificially high T_c values due to strain-induced filamentary superconductivity.

At ambient pressure, the cT phase is induced by higher $T_{A/Q}$. When the cT phase transition occurs, the very large, first order, changes to the unit cell dimensions often lead to cracks in the resistance bar and loss of resistance data below the transition temperature (in case the resistance bar survives upon cooling through the transition, resistance data shows downward jump and hysteresis of up to around 15 K), which is an unique fingerprint of the cT phase transition and helps us to distinguish it from AFM/ORTH phase transition. On the other hand, loss of data below the transition makes it difficult to extract an unambiguous value of the transition temperature from $R(T)$ data. Therefore only susceptibility data were used to determine the transition temperature, T_{cT}. Figure 3.13 shows the susceptibility data for two different samples. The peak in derivative of the susceptibility was employed to determine T_{cT}.

Note that the peak in derivative becomes significantly broadened for higher concentrations, as shown for the $x = 0.049/\,T_{A/Q} = 400°$C Rh-substituted sample. I capture the broadness of the transition by including error bars, which were defined here as the full width at half maximum of the peaks in derivatives of the susceptibility.

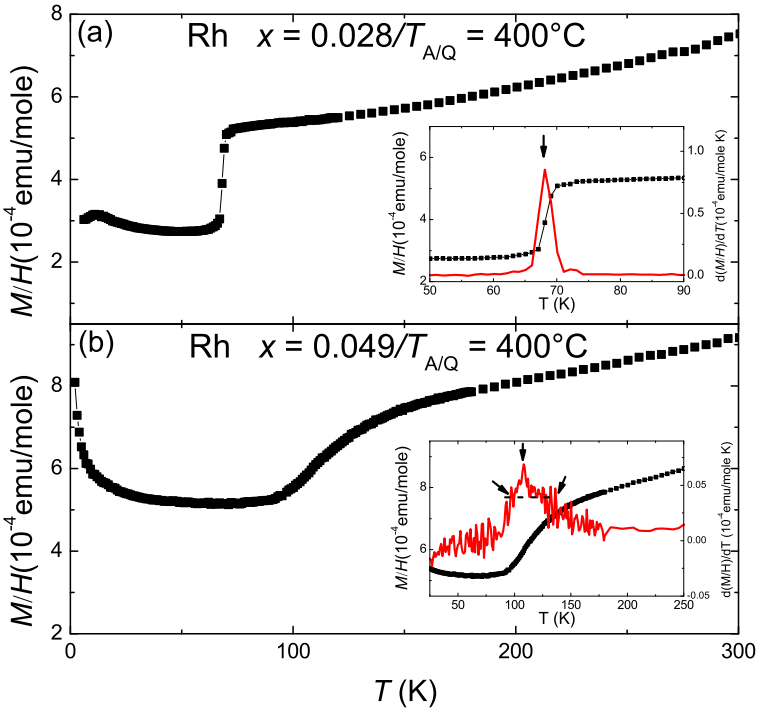

Figure 3.13 Criteria used to determine the transition temperatures of the cT phase transition shown for two different samples. The data close to the transition are presented in the insets, together with the derivatives. Inferred transition temperatures are indicated by vertical arrows.

CHAPTER 4. PHYSICAL PROPERTIES OF $CaFe_2As_2$ GROWN FROM Sn-FLUX

4.1 Introduction

Whereas $BaFe_2As_2$ and $SrFe_2As_2$ were known compounds before 2008, $CaFe_2As_2$ was not known to exist until its discovery in single crystal form (Ni et al., 2008b). Initially, single crystals of $CaFe_2As_2$ were grown out of a Sn-flux, and microscopic, thermodynamic, and transport measurements were conducted both under ambient and applied pressure. Transition metal substitution studies were also attempted using Sn-flux grown single crystals (Harnagea et al., 2011; Hu et al., 2012). Since our study of annealing/quenching effects on $CaFe_2As_2$ grown from FeAs-flux requires comparison with physical properties of $CaFe_2As_2$ grown from Sn-flux, before outlining the results of annealing/quenching and transition metal substitution study of $CaFe_2As_2$ grown from FeAs-flux, I will first review the salient physical properties $CaFe_2As_2$ grown from Sn-flux. A lot of these data were reviewed by Canfield et al. (2009a) in a 2009 overview of the first dozen papers from the Ames collaborations.

4.2 Physical Properties of $CaFe_2As_2$ at Ambient Pressure

$CaFe_2As_2$ was first successfully synthesized from Sn-flux (Ni et al., 2008b). Temperature dependent transport and thermodynamic measurements both show a clear and sharp phase transition at around 170 K, as shown in Figs. 3.9. The in-plane (ρ_{ab}) resistivity decreases with decreasing temperature from a room temperature value near 0.3 mΩ cm to near 0.05 mΩ cm at 2 K, with a discontinuous, and hysteretic jump in resistivity upon cooling through the 170 K, antiferromagnetic/orthorhombic (AFM/ORTH) transition. The magnetic susceptibility decreases very weakly with decreasing temperature (in both directions of applied field) but

manifests a dramatic decrease upon cooling through the transition temperature. Specific heat data show a sharp feature at this temperature, consistent with a latent heat that appears slightly broadened by collecting the data with a thermal excitation of 2% of the temperature (i.e., $\sim$ 4 K) in the temperature range of the anomaly. The low-temperature electronic specific heat can be evaluated from a plot of C/T vs. T^2 (Figs. 3.9c, inset) and is $\sim$4.7 mJ/mole K^2, consistent with a relatively low density of states at the Fermi-level in the low-temperature state.

The thermodynamic and transport data shown in Figs. 3.9 are consistent with a first order phase transition near 170 K. To determine the precise nature of this phase transition, single crystal x-ray diffraction study and elastic neutron diffraction study were performed (Ni et al., 2008b; Goldman et al., 2008), which showed that the phase transition near 170 K is a coupled, strongly first order, structural and magnetic phase transition, from a high-temperature tetragonal, paramagnetic state to a low-temperature orthorhombic, antiferromagnetically ordered state.

4.3 Physical Properties of $CaFe_2As_2$ under Pressure

Although the ambient pressure properties of $CaFe_2As_2$ appear to epitomize the general behavior of the $AEFe_2As_2$ (AE = Ba, Sr, Ca) materials, none of these parent compounds, at ambient pressure, allow for the study of superconductivity (Ni et al., 2008b; Yan et al., 2008; Sasmal et al., 2008; Rotter et al., 2008; Ni et al., 2008c). Given that pressure (both physical and chemical) was key to raising the T_c value of the F-substituted RFeAsO materials (Chen et al., 2008; Takahashi et al., 2008), it was reasonable to hope that given its already reduced lattice parameter relative to $BaFe_2As_2$ and $SrFe_2As_2$, $CaFe_2As_2$ should be the most promising of the $AEFe_2As_2$ materials for pressure stabilized superconductivity. Based on this premise, measurements under pressure were performed, which demonstrated that $CaFe_2As_2$ is the most pressure sensitive of the $AEFe_2As_2$ and 1111 compounds (Torikachvili et al., 2008).

Fig. 3.10 presents the temperature dependent resistivity data taken on single crystalline $CaFe_2As_2$ at representative pressures below 0.6 GPa from the He-gas pressure cell (Yu et al., 2009). There are several salient features in these data. First, the resistive signature of the

ambient pressure transition to the low temperature, AFM/ORTH state is suppressed, and it vanishes between $P \sim 0.35$ and 0.42 GPa. Secondly, there is no transition to a zero resistance state at low temperatures. Third, for higher pressures a new feature, a sharp drop of resistance upon cooling, appears and increases in temperature as pressure is further increased. This new feature is associated with a structural phase transition into a low-temperature collapsed tetragonal state, which was demonstrated by a series of scattering studies (Kreyssig et al., 2008; Goldman et al., 2009).

This collapsed tetragonal phase does not manifest any detectable magnetic order from neutron-diffraction measurements and is thought to be non-moment bearing (Kreyssig et al., 2008; Pratt et al., 2009b). Electronic structure calculations were also performed, showing a quenched magnetic-moment ground state (Kreyssig et al., 2008). Whereas details about the crystallography as well as the magnetic structure of this cT phase can be found in references (Kreyssig et al., 2008; Goldman et al., 2009), it is worth noting that the cT phase is associated with a dramatic change in the unit cell parameters of $CaFe_2As_2$. When the sample is cooled across the tetragonal - collapsed tetragonal phase transition there is a $\sim 5\%$ decrease in volume associated with an extremely anisotropic change in the unit cell dimensions: the c-axis expands by $\sim 2.5\%$ and the c-axis contracts by $\sim 9\%$.

Fig. 4.1 is the transition temperature, T versus applied pressure, P, phase diagram assembled from He-gas cell electrical resistivity and magnetic susceptibility data (Yu et al., 2009). The ambient pressure AFM/ORTH phase transition is initially suppressed by over 100 K per GPa and essentially disappears between 0.35 and 0.4 GPa. Above ~ 0.35 GPa, the cT phase is stabilized and has its transition temperature rise with further application of pressure. No superconducting phase is detected in this temperature and pressure range.

In addition to this extreme pressure sensitivity, $CaFe_2As_2$ is also very sensitive to nonhydrostaticity (Torikachvili et al., 2008; Yu et al., 2009; Canfield et al., 2009a; Pratt et al., 2009b). If the pressure medium solidifies before the structural phase transitions, then the anisotropic changes in the unit cell lead to nonhydrostatic (by definition) stress, which in turn leads to dramatically broadened transitions and a structurally mixed phase sample in the 0.4 GPa pressure region. This mixed phase includes a small amount of strain-stabilized, high-temperature

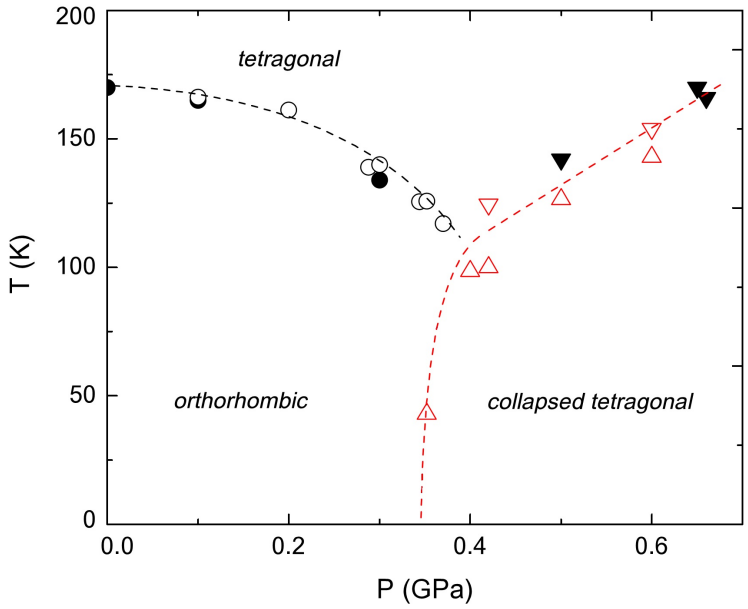

Figure 4.1 The T-P phase diagram of $CaFe_2As_2$ constructed from the transport and susceptibility measurements in a He-gas pressure cell. (Yu et al., 2009)

tetragonal phase which superconducts at low temperatures. The use of helium as a pressure medium allows for a minimization of these nonhydrostatic effects.

4.4 Effects of Co-substitution on Physical Properties of $CaFe_2As_2$

Preliminary studies of the effects of Co-substitution on physical properties of $CaFe_2As_2$ were made on samples grown out of Sn (Matusiak et al., 2010; Harnagea et al., 2011; Hu et al., 2012). It turns out that Sn-grown samples have problems with solubility, reproducibility and inhomogeneity (Harnagea et al., 2011; Hu et al., 2012). In order to obtain more homogeneous Co-substitution for Fe, single crystals of $Ca(Fe_{1-x}Co_x)_2As_2$ were grown from Sn-flux in two steps. First, polycrystalline $Ca(Fe_{1-x}Co_x)_2As_2$ was prepared by solid state reaction. Then single crystals of $Ca(Fe_{1-x}Co_x)_2As_2$ were grown from Sn-rich melt using polycrystalline $Ca(Fe_{1-x}Co_x)_2As_2$ as starting material. By following the above procedure, there was a significant amount of a needle-shaped orthorhombic phase, $CaFe_4As_3$ phase. To eliminate the $CaFe_4As_3$ phase, an excess of Ca was added to the polycrystalline $Ca(Fe_{1-x}Co_x)_2As_2$ and Sn

mixture and an optimal starting ratio was found to be $Ca_{1.5}(Fe_{1-x}Co_x)_2As_2$. Moreover, there is a solubility problem of $Ca(Fe_{1-x}Co_x)_2As_2$ in Sn. Sometimes, there was undissolved polycrystalline powder after decanting. To completely dissolve the starting polycrystals, the starting ratio of Sn had to be increased by 50% from that used to grow $CaFe_2As_2$ from Sn-flux.

For Co-substitution, the issue of solubility as well as the formation of the competing phase may change the composition of the liquid solution, thus it causes complex dependence of the substitution level of the resulted single crystals on growth conditions. Figure 4.2 shows the actual concentration of Co, x_{WDS}, as a function of the nominal $x_{nominal}$. It can be seen, x_{WDS} deviates from monotonic dependence on $x_{nominal}$. It is noteworthy that for $x_{nominal}$ greater that 0.10, the corresponding x_{WDS} decreases dramatically.

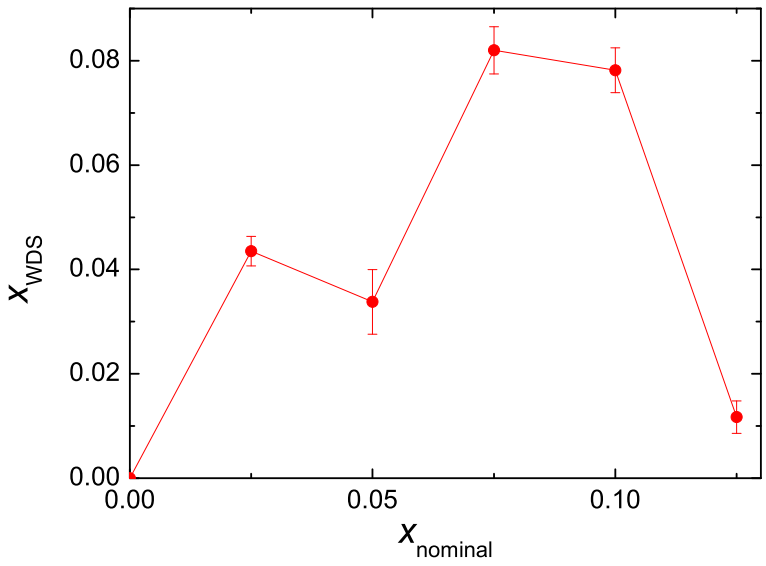

Figure 4.2 Actual Co concentration as a function of nominal one. (Hu et al., 2012)

Due to these issues with solubility, reproducibility and inhomogeneity, the phase diagrams constructed by different groups do not match very well. Figure 4.3 presents $T - x$ phase diagram for $Ca(Fe_{1-x}Co_x)_2As_2$ from Hu et al. (2012), based on the magnetic and transport measurements. The simultaneous structural and magnetic transition of the pure $CaFe_2As_2$ is monotonically suppressed by Co-substitution, and up to $x \leq 0.025$, no discernible splitting of magnetic and structural transition can be observed. For $x = 0.031$ and 0.043, the

transition broadens and appears to start to split. One possibility is that there are two distinguishable transitions, the upper structural transition and lower magnetic transition, similar to $Ba(Fe_{1-x}Co_x)_2As_2$. However, given that there can be inhomogeneity, it is well possible that the sample in this region is in mixture of different composition and therefore shows a broadening of phase transition. To compare different phase diagrams of $Ca(Fe_{1-x}Co_x)_2As_2$, the data points of phase diagram from Harnagea et al. (2011), which is constructed using the same criteria, are plotted as black asterisks. As can be seen, though superconductivity occurs roughly with the same T_c in similar region, two phase diagrams show different suppression of the magnetic and structural transitions by Co-substitution. One might imagine that inhomogeneity, and therefore different Co concentration, can shift the phase diagram.

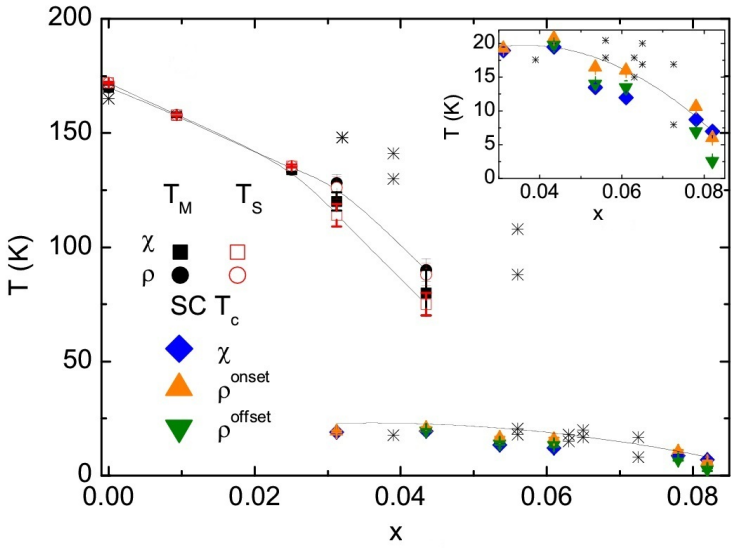

Figure 4.3 $T-x$ phase diagram of $Ca(Fe_{1-x}Co_x)_2As_2$. (Hu et al., 2012) Solid lines are guides to the eye. Inset shows the superconducting region. Black asterisk is the data from Harnagea et al. (2011) inferred from resistance.

4.5 Summary

Pure $CaFe_2As_2$ was first successfully synthesized from Sn-flux using high-temperature solution technique. Under ambient pressure, upon cooling through 170 K, $CaFe_2As_2$ undergoes

a first order phase transition, from a high-temperature tetragonal, paramagnetic phase to a low-temperature orthorhombic, antiferromagnetic phase. As pressure is applied, the ambient pressure phase transition is suppressed and essentially disappears near 0.4 GPa. At higher pressures the cT phase emerges and has its transition temperature rise with further application of pressure. Depending on the hydrostatic condition of the pressure medium, the superconducting phase may or may not be stabilized. Effects of Co-substitution was studied using Sn-grown samples. However, due to the issues with solubility, reproducibility and inhomogeneity, the phase diagrams constructed by different groups do not match very well and, therefore, need to be clarified.

CHAPTER 5. THE EFFECT OF ANNEALING/QUENCHING ON PHYSICAL PROPERTIES OF $CaFe_2As_2$

5.1 Introduction

FeAs-grown samples had dramatically suppressed transition temperatures. In order for these larger crystals to manifest a AFM/ORTH phase transition similar to that seen in the smaller Sn-grown crystal, they were annealed at 500°C (a temperature similar to the decanting temperature of the Sn-grown samples) (Goldman et al., 2009) for 24 h and then quenched to room temperature. Given previous observations of small shifts in the AFM/ORTH phase transition temperatures of $BaFe_2As_2$ samples and of the superconducting transition in doped $BaFe_2As_2$, as well as of sharpenings of their signatures in thermodynamic and transport data, after post-growth thermal treatment (Rotundu et al., 2010; Gofryk et al., 2011; Kim et al., 2012a), it is necessary to undertake a systematic study of the effects of postgrowth thermal treatment of FeAs-grown single crystals of $CaFe_2As_2$. In order to characterize and understand the effects of annealing/quenching, as well as the nature of the low-temperature state, a wide variety of thermodynamic, transport, microscopic, and spectroscopic measurements have been performed .

In this chapter, these measurements are presented in details. A phase diagram of transition temperature, T, versus annealing/quenching temperature, $T_{A/Q}$ is determined from temperature dependent electrical resistance and magnetic susceptibility measurements and the low-temperature state of the FeAs-grown $CaFe_2As_2$ without annealing is identified by the combination of the temperature-dependent single-crystal x-ray diffraction measurements, Mössbauer spectroscopy measurements and NMR measurements. Finally, a microscopic explanation is proposed based on the transmission electron microscopy (TEM) measurements.

This chapter is heavily based on the published article: Ran, S., Bud'ko, S. L., Pratt, D. K., Kreyssig, A., Kim, M. G., Kramer, M. J., Ryan, D. H., Rowan-Weetaluktuk, W. N., Furukawa, Y., Roy, B., Goldman, A. I. and Canfield, P. C. "Stabilization of an ambient-pressure collapsed tetragonal phase in $CaFe_2As_2$ and tuning of the orthorhombic-antiferromagnetic transition temperature by over 70 K via control of nanoscale precipitates" *Phys. Rev. B*, 83 (2011):144517.

5.2 Annealing/quenching Effect

5.2.1 Dramatically different physical properties of FeAs-flux as-grown $CaFe_2As_2$ single crystals

Figure 5.1 presents the resistance and magnetic susceptibility for $CaFe_2As_2$ single crystals grown from Sn and for $CaFe_2As_2$ single crystals grown from excess FeAs. Two data sets are shown for FeAs-grown crystals: one data set shows measurements on an as-grown crystal with $T_{A/Q} = 960°C$; the other data set shows measurements on a sample annealed at $T_{A/Q} = 400°C$ for 7 days. The Sn-grown single crystal and the FeAs-grown sample with $T_{A/Q} = 400°C$ are quite similar, both manifesting similar, modest increases in resistance and decreases in susceptibility associated with the phase transition near 170 K (Ni et al., 2008b; Canfield et al., 2009a). On the other hand, the FeAs-grown sample with $T_{A/Q} = 960°C$ shows a significantly larger, very sharp drop in magnetization occurring well below 100 K. The electrical resistance also drops discontinuously at this temperature, associated with the sample suddenly undergoing a violent structural phase transition that often (usually) leads to cracks along the length and width of the bar, as well as loss of contacts.

In addition to the quantitative differences shown in Fig.5.1, there is a qualitative difference between the FeAs-grown $T_{A/Q} = 960°C$ single crystals and the Sn-grown single crystals. Whereas the Sn-grown single crystals are malleable and can easily be bent and deformed, the crystals quenched from a 960°C FeAs solution are brittle and tend to shatter if bending is attempted. The FeAs-grown crystals with $T_{A/Q} = 400°C$, however, recover some of the malleability of the Sn-grown ones and can be deformed, at least, a little, without shattering.

Given the dramatic difference in transition temperature, as well as the different signatures

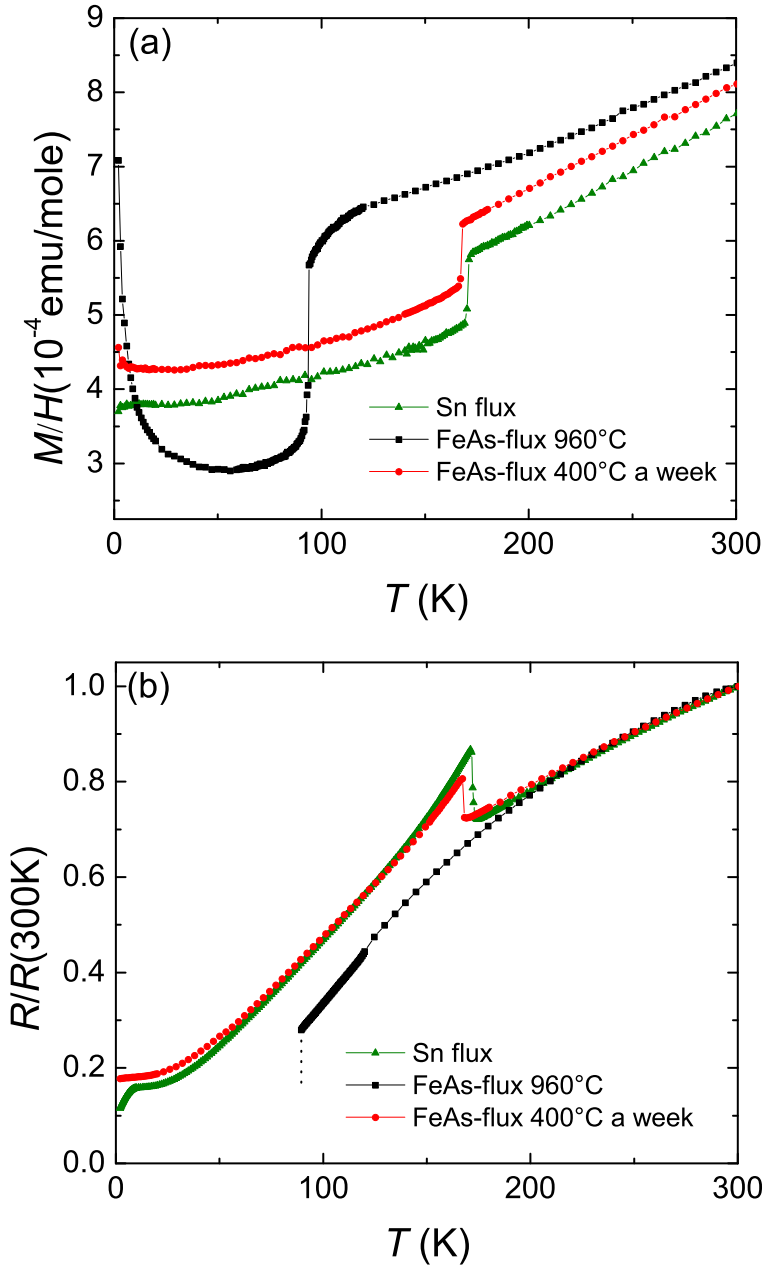

Figure 5.1 Temperature-dependent (a) magnetic susceptibility and (b) normalized electrical resistance of $CaFe_2As_2$ for three differently prepared single crystals: (green squares) Sn-grown, (black circles) FeAs-grown, $T_{A/Q} = 960°C$ (as-grown), and (red triangles) FeAs-grown, $T_{A/Q} = 400°C$. Note: when the as-grown sample from FeAs melt was cooled below the transition temperature, near 90 K it shattered, making further lower-temperature resistance measurements impossible.

of the transition in resistance and magnetization, several questions arise. Among them two are considered: (i) what is the nature of the phase transition in the FeAs-grown $T_{A/Q}$ = 960°C sample and (ii) can the transition in annealed/quenched samples be varied from near 170 K to below 100 K in a systematic manner? I will address the latter question first and return to the former after the creation of a phase diagram of transition temperature, T, vs annealing/quenching temperature, $T_{A/Q}$.

5.2.2 Effects of annealing/quenching time

Before I present the data associated with the temperature dependence of the effects of annealing, I will first address the question of what is the annealing time dependence of these effects. In other cases of clear annealing effects, both time and temperature cuts through phase space are needed to establish unambiguous annealing protocols (Miao et al., 2002). In Fig.5.2 I show the evolution of the magnetic susceptibility with annealing times, for different $T_{A/Q}$. At 350°C, it is clear that 24 h is not a sufficient amount of time to reach a well-defined state. It leads to split, broadened features with drops in susceptibility below both 170 and 100 K. 48 h leads to a less split but still broadened feature near 170 K. 5 days leads to a single sharp feature at around 168 K, which is comparable to what is seen for a 7 day anneal. This progression shows that for 350°C, the salient time scale for annealing is between 2 and 5 days. At 400°C, the salient time scale is remarkably shorter. 2 h leads to feature similar to what is seen for 1 day anneal at 350°C and 15 h is longer than the amount of time to reach a well-defined state. In a similar way, the salient time scale for annealing temperature of 450°C is between 1 and 3 h. As would be expected, for higher temperatures the salient time scale is even shorter. For 800°C, which is close to the spin temperature, 960°C, a similar behavior as seen in as-grown sample is expected. Therefore, it becomes hard to resolve the changes due to annealing/quenching time. In order to compare effects of different annealing/quenching time, I first annealed a batch for a week at 500°C, producing a transition temperature above 150 K, then annealed individual samples from this batch at 800°C for representative times. As can be seen in Fig.5.2d, even a 0.5-h anneal causes the sample to behave in a manner similar to the as-grown (quenched from 960°C) samples.

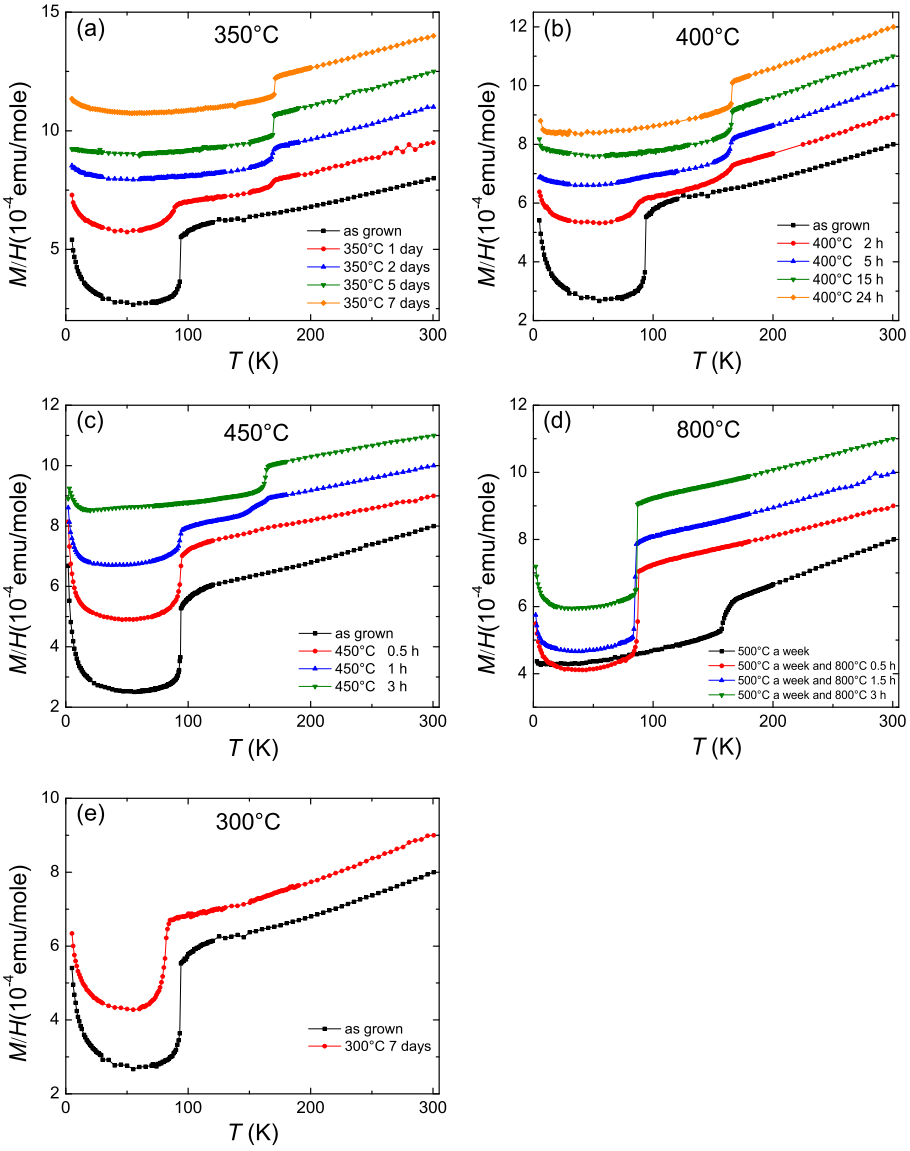

Figure 5.2 Temperature-dependent magnetic susceptibility of (a) $CaFe_2As_2$ single crystals annealed at 350°C for representative times, (b) $CaFe_2As_2$ single crystals annealed at 400°C for representative times, (c) $CaFe_2As_2$ single crystals annealed at 450°C for representative times, (d) $CaFe_2As_2$ single crystals that have been annealed for a week at 500°C and then annealed at 800°C and (e) $CaFe_2As_2$ single crystals annealed at 300°C for representative times. Data in both panels have been offset from each other by an integer multiple of 1×10^{4} or 1.5×10^{4} emu/mole for clarity.

Whereas increasing $T_{A/Q}$ from 350°C to 800°C leads to a greatly shortened time required to reach a well defined state, temperatures below 350°C require greatly lengthened time. 7-day anneals at temperatures of 300°C or lower do not change the temperature dependence of the as-grown samples significantly. The data from the sample annealed at 300°C for 7 days, as presented in Fig.5.2e shows dramatic drops in susceptibility below 85 K, similar to what was seen for as-grown sample, indicating that at 300°C 7 days is less than the salient time scale. Although longer annealing times at 300°C may lead to a sharp, single transition near 170 K (as is seen for the 400°C 24-h anneal), the time needed to achieve this state is anticipated to become exponentially long, considering that lowering the annealing temperature from 400° to 350°C requires annealing time one order of magnitude longer.

Based on the study of the effects of annealing time for different $T_{A/Q}$, the protocol of annealing/quenching I used in this thesis is the following: the lowest $T_{A/Q}$ used is 350°C, and at this temperature, samples were annealed for 5 days. (In the case where whole batches were annealed without opening, out of an abundance of caution, the annealing time used was 14 days.) For $T_{A/Q}$ at and above 400°C, samples were annealed for 24 hours. (Again, out of an abundance of caution, whole batches were annealed for 7 days.)

5.2.3 Effects of annealing/quenching temperature

In order to assess the extent to which the 170 K phase transition that occurs in Sn-grown, as well as FeAs-grown $T_{A/Q} = 400$°C samples of $CaFe_2As_2$ can be systematically shifted down to below 100 K, I measured the temperature-dependent susceptibility and resistance of samples with $T_{A/Q}$ ranging from 350° to 850°C. Figure 5.3 presents magnetic susceptibility and resistance data for representative $T_{A/Q}$. The decrease in susceptibility (or increase in resistance) can be shifted down in temperature by choosing an appropriate $T_{A/Q}$ between 350° and 800°C. For $T_{A/Q}$ between these temperatures, the transitions, particularly as seen in the resistance data, remain quite sharp and shift in a systematic manner. Whereas the size of the jump in the magnetization remains fairly constant in the samples with $T_{A/Q}$ in this temperature region, there is a monotonic increase in the magnitude of the increase in the resistance (see Fig. 5.5 below).

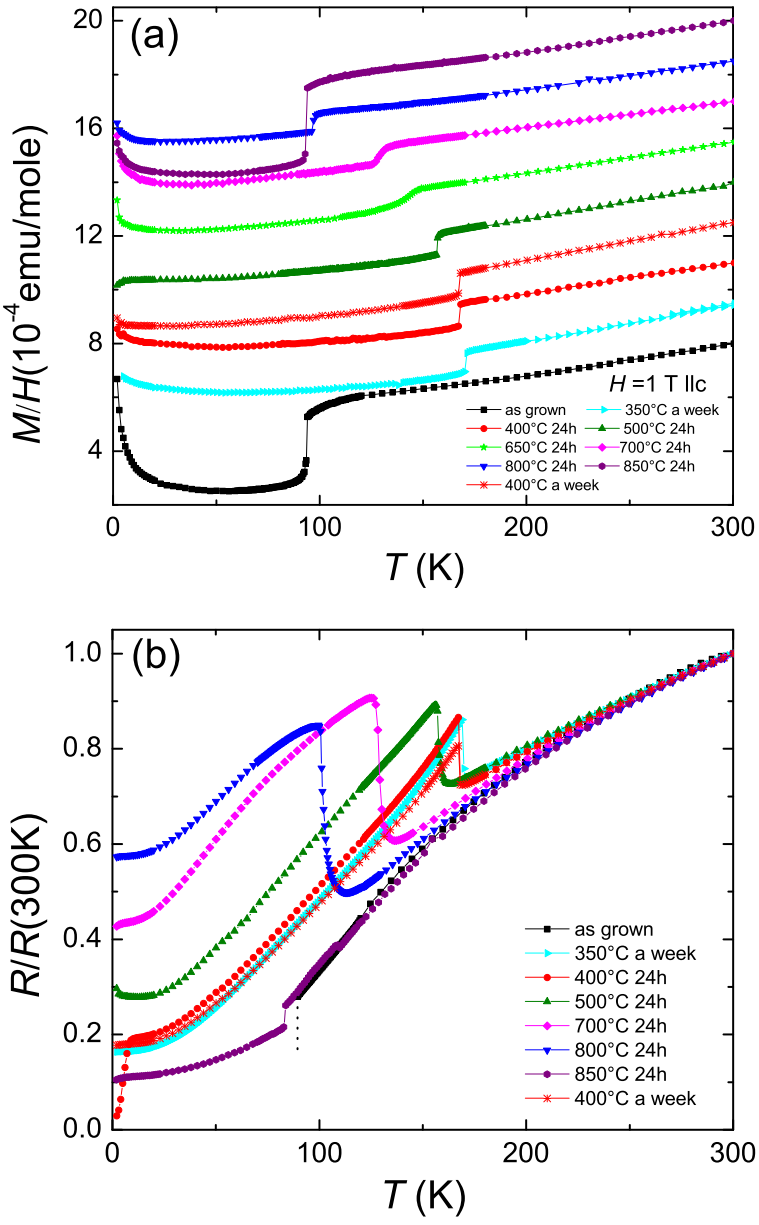

Figure 5.3 Temperature-dependent (a) magnetic susceptibility with applied magnetic field parallel to c-axis and (b) normalized electrical resistance of FeAs-grown $CaFe_2As_2$ single crystals with different $T_{A/Q}$. Susceptibility data in (a) have been offset from each other by an integer multiple of $1.5\times\ 10^{\ 4}$ emu/mole for clarity. Data for a 1-week anneal of a whole batch at 400°C is shown for comparison. The resistance data (b) for the as-grown sample could not be measured below the transition temperature due to sample breakage, but for the sample with $T_{A/Q}$ = 850°C resistance could be measured through the transition.

A 24-h anneal at 850°C does not significantly change the transition temperature from that measured for the as-grown samples with $T_{A/Q}$ = 960°C (perhaps not too surprisingly since 850°C is approaching the 960°C quench temperature); the resistance data for this sample, though, can be collected below the transition temperature, showing that the low-temperature state has a lower resistance, leading to a downward jump in resistance when cooling through the transition temperature.

In order to see if similar changes in transition temperature could be induced by annealing/quenching samples that started with transitions near 170 K (i.e., started with transitions similar to those found in Sn-grown $CaFe_2As_2$), we annealed an entire batch of crystals at 400°C for a week and quenched. The resistance and susceptibility data for these samples are also shown in Fig. 5.3 and are essentially the same as those found for the 24-h anneal of individual crystals. Single crystals from this "400°C anneal for one week" batch were then separately sealed in silica ampoules and annealed for 24 h at temperature ranging from 500° to 800°C and quenched. The temperature dependent resistance and susceptibility for these samples are shown in Fig. 5.4. As was the case for the as-grown samples, sharp features in both resistance and susceptibility systematically shift to lower temperature for the samples with higher $T_{A/Q}$. The sample with $T_{A/Q}$ = 800°C shows the larger drop in susceptibility and broke on cooling through its transition, making it appear to be similar to the as-grown samples with $T_{A/Q}$ = 960°C.

In both cases, for transition temperatures between 170 K and 100 K the magnetic signature of the transition is essentially unchanged and the resistive signature evolves gradually with the jump in resistance, $\Delta\rho$, becoming larger as transition temperature decreases. For the lowest transition temperature values, below 100 K, there is a significantly larger drop in susceptibility and, when it can be measured, the jump in resistance is downward on cooling rather than upward. These observations are quantified in Fig. 5.5. As discussed in chapter 2, as-grown samples as well as samples with $T_{A/Q}$ = 400° and 700°C all have room-temperature resistivity values of 3.75 ± 0.75 mΩ cm. This invariance, within experimental resolution, allows for conversion of these jumps to absolute resistivity as needed.

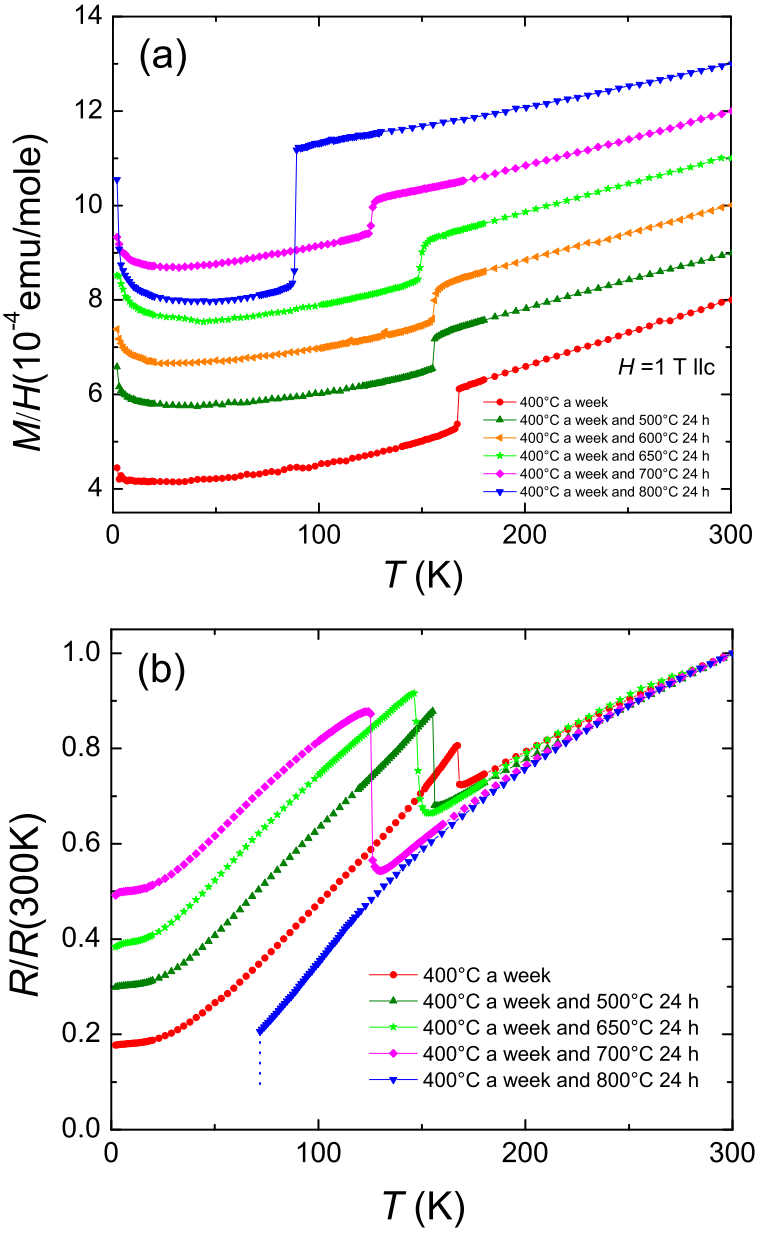

Figure 5.4 Temperature-dependent (a) magnetic susceptibility with applied magnetic field parallel to c-axis and (b) normalized electrical resistance of FeAs-grown $CaFe_2As_2$ single crystals that were first annealed/quenched for a week at 400°C and then annealed/quenched for 24 h at various $T_{A/Q}$. Susceptibility data in (a) have been offset by an integer multiple of 1×10^{-4} emu/mole from each other for clarity.

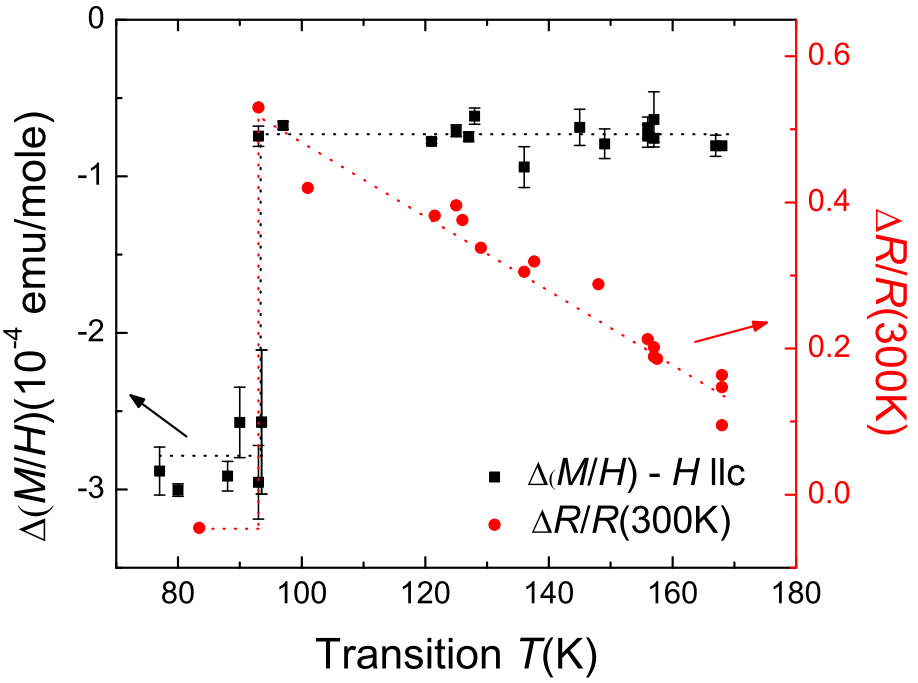

Figure 5.5 Size of jump in susceptibility and normalized resistance as a function of transition temperature for FeAs-grown $CaFe_2As_2$ crystals $T_{A/Q}$ shown in Figures 5.1 - 5.4. The magnetic field is applied in c-axis. Room-temperature resistivity of samples with transition temperature values of $\sim$ 90, 130, and 170 K all fall within the 3.75 $\pm$ 0.75 mΩ cm range.

5.2.4 T-$T_{A/Q}$ phase diagram

Based on the temperature dependent electrical resistance and magnetic susceptibility measurements, transition temperature, T, as well as the error bars, were inferred and a phase diagram of transition temperature, T, vs annealing/quenching temperature, $T_{A/Q}$ was constructed as shown in Fig. 5.6. It can be seen that there is a systematic progression of fairly sharp transitions downward for increasing $T_{A/Q}$. Figure 5.6 illustrates that (i) there is some scatter in transition temperature, T, for a given $T_{A/Q}$, but (ii) that there is also a fairly well-defined suppression of transition temperature with increasing $T_{A/Q}$, e.g., sample with $T_{A/Q} = 400°$ has a very different transition temperature from sample with $T_{A/Q} = 700°$, which itself differs from sample with $T_{A/Q} = 800°$ or the as-grown sample. In addition, annealing/quenching at a given $T_{A/Q}$ leads to a transition temperature value, regardless of whether the sample starts from a 170 K or 90 K transition state, i.e., this final annealing/quenching determines transition temperature regardless of sample history. Figure 5.6 also shows that for $T_{A/Q}$ less than 300° the sample remains unaffected by annealing on the time scale used (see section 5.2.2).

The T-$T_{A/Q}$ phase diagram presented in Fig. 5.6 shows that $CaFe_2As_2$ grown from FeAs can have the temperature of its phase transition modified in an essentially continuous manner from near 170 K to below 100 K. This evolution of the transition temperature (Fig. 5.6) as well as the evolution of the resistive and magnetic signature of the phase transition (Fig. 5.3 and Fig. 5.4) make it plausible that for transition temperature between 100 K and 170 K the transition is similar to that seen in Sn-grown $CaFe_2As_2$ under pressure (Fig. 4.1): a transition from a high-temperature, tetragonal, paramagnetic state to a lower-temperature, orthorhombic, antiferromagnetic state. On the other hand, dramatic changes in the resistive and magnetic signature associated with the as-grown sample as well as samples with $T_{A/Q} = 850°$ are consistent with our current understanding of the collapsed tetragonal phase, a phase that was associated with $CaFe_2As_2$ under pressures of 0.35 GPa or higher (Fig. 4.1). The change in the resistive signature of the transition from a sharp increase to a sharp decrease, as well as the sudden increase in the size of the drop in susceptibility upon cooling are very similar to the changes seen in Ref. (Yu et al., 2009) under hydrostatic pressure applied with

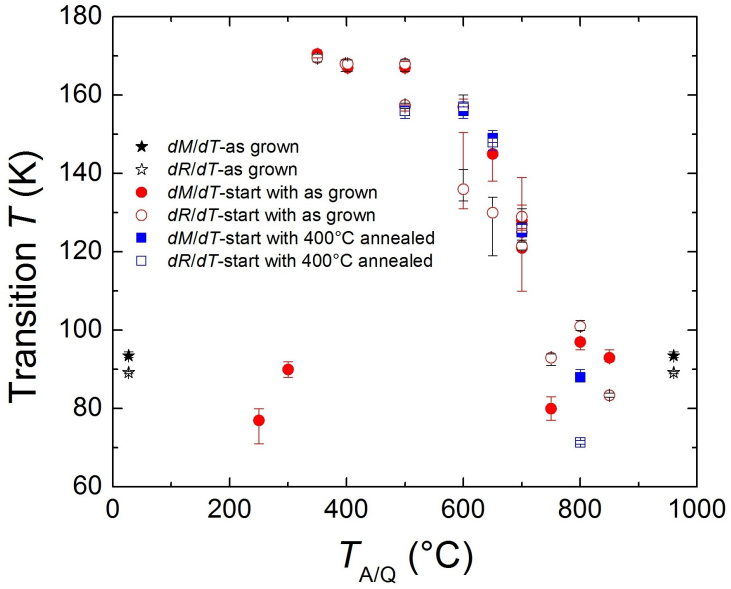

Figure 5.6 Transition temperature versus annealing/quenching temperature (T-$T_{A/Q}$) phase diagram. Open symbols are inferred from resistance data and filled symbols are inferred from susceptibility data. (Star) The as-grown samples with $T_{A/Q} = 960$°C are also shown as 20°C anneals); (squares) as-grown samples that have been annealed for 24 h at $T_{A/Q}$ and quenched to room temperature; (circles) as-grown samples that were first annealed for a week at 400°C and then annealed for 24 h at T_a and quenched to room temperature. Note that for $T_{A/Q}$ less than 300° the sample remains unaffected by annealing on the time scale used.

helium. For that matter, the basic phase diagram proposed in Refs. (Goldman et al., 2009) and (Yu et al., 2009) is remarkably similar to T-$T_{A/Q}$ phase diagram presented in Fig. 5.6, with $T_{A/Q}$ playing the role of pressure or, more precisely stated, somehow parameterizing the amount of stress in the sample. This similarity can be seen in Fig. 5.7, which directly plots transition temperature as a function of P and $T_{A/Q}$. There is a good agreement between the effects of $T_{A/Q}$ and P on transition temperature, with a scaling of $\Delta T_{A/Q} = 100°\text{C}$ being equivalent to $\Delta P = 100$ MPa, as long as the transition is from high-temperature tetragonal to low-temperature orthorhombic, antiferromagnetic. Once the low-temperature state is the cT phase the $T_{A/Q}$ does not seem to affect transition temperature in the same manner as P.

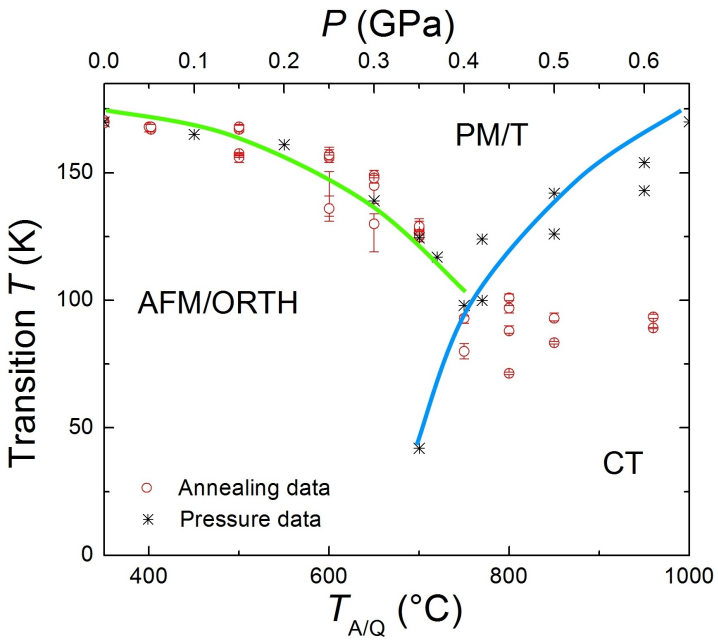

Figure 5.7 Transition temperature T as a function of pressure from Yu et al. (2009) and transition temperature T as a function of $T_{A/Q}$ for $400°\text{C} < T_{A/Q} < 960°\text{C}$. Two phase diagrams match well with a single scaling of $\Delta T_{A/Q} = 100°\text{C}$ being equivalent to $\Delta P = 100$ MPa for the AFM/ORTH region.

5.3 Low Temperature State of the FeAs As-grown $CaFe_2As_2$

5.3.1 x-ray

The transition temperature as well as the signature of the transition in the as-grown $CaFe_2As_2$ indicates that the low temperature state of the as-grown $CaFe_2As_2$ is the collapsed tetragonal, cT, phase. The cT phase was identified (Kreyssig et al., 2008; Goldman et al., 2009) in $CaFe_2As_2$ by scattering measurements made on samples under hydrostatic pressure using He as a pressure medium as part of a comprehensive effort to better understand the details of the $CaFe_2As_2$ T-P phase diagram (Torikachvili et al., 2008; Kreyssig et al., 2008; Goldman et al., 2009; Yu et al., 2009; Torikachvili et al., 2009; Canfield et al., 2009a). As $CaFe_2As_2$ transforms from the high-temperature tetragonal phase into the low-temperature, collapsed tetragonal phase the c-lattice parameter changes from $\sim$ 11.6 A to $\sim$ 10.6 A, a remarkably large ($\sim$ 10%) decrease while the a-lattice parameter increases by $\sim$ 2%, leading to an $\sim$ 4% decrease in the unit cell volume (Kreyssig et al., 2008).

In order to see if the as-grown sample manifests such a striking change in lattice parameters, high-energy single-crystal x-ray diffraction data were collected as a function of temperature. Figure 5.8 displays the results of fits to these data to extract the lattice parameters as well as the unit cell volume. The data from the original Sn-flux-grown samples, at an applied pressure of 0.63 GPa (Kreyssig et al., 2008), are also included in Fig. 5.8 for direct comparison. These data clearly indicate that, structurally, the as-grown crystals of $CaFe_2As_2$ transform into a cT phase below 100 K at ambient pressure. In particular, the inset to Fig. 5.8(b) shows the diffraction image of the (220) Bragg reflection at 6 K, the base temperature of our measurement. Within our resolution, no splitting of the peak is evident as would be expected for an orthorhombic unit cell [the two circles on the left and right of the (220) reflection show the splitting that would accompany an orthorhombic state]. Furthermore, we find that the temperature dependence of the lattice parameters and unit cell volume are consistent with what was observed for the pressure-induced, cT phase for $P = 0.63$ GPa where the tetragonal-to-collapsed tetragonal phase transition has moved above 150 K.

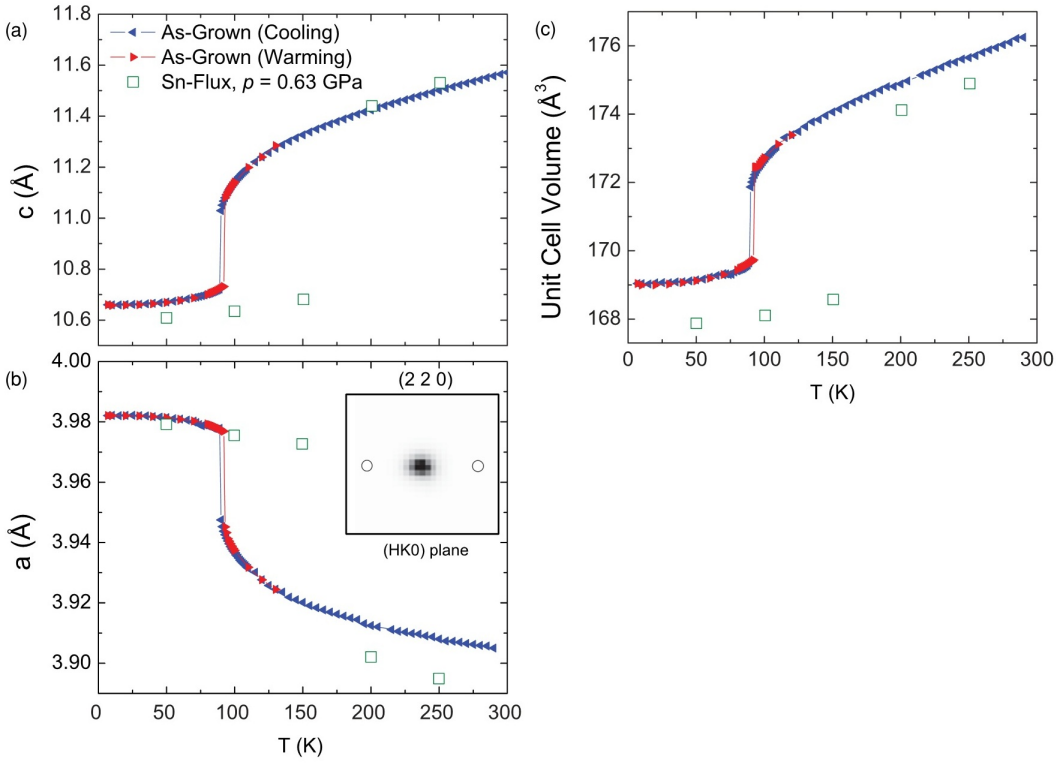

Figure 5.8 Values for (a) the c-lattice parameter, (b) a-lattice parameter, and (c) unit cell volume as a function of temperature for as-grown FeAs-flux grown $CaFe_2As_2$ sample determined from high-energy x-ray diffraction measurements. The open squares denote the results of measurements performed on a polycrystalline sample under applied hydrostatic pressure of 0.63 GPa. The inset to the middle panel is the image of the (220) diffraction peak taken from the two-dimensional x-ray detector as described in the text. Note the absence of any splitting that would signal a transition to an orthorhombic phase (the two open circles illustrate the expected distance between split Bragg peaks due to the "usual" orthorhombic distortion).

5.3.2 Mössbauer spectroscopy

Although the sharp drop in susceptibility (Fig. 5.3 and Fig. 5.4) suggests that the non-moment bearing phase is associated with the cT state, it is prudent to examine the magnetic properties of this state more closely with microscopic measurement techniques. Mössbauer spectroscopy measurements were carried out on three FeAs-grown samples at room temperature and 5 or 10 K, i.e., well into the low temperature state. Composite samples, with aligned c axes, were made from single crystals from whole batches treated in the following manner: as-grown ($T_{A/Q} = 960°$C), annealed for a week at 500°C and quenched, and annealed for a week at 700°C and quenched. As shown in Fig. 5.7, these three annealing/quenching temperatures produce samples representative of the whole range of behavior observed.

The spectra of the three samples taken at 295 K (Fig. 5.9) are essentially indistinguishable. Cooling to low temperatures makes the differences between the three samples strikingly obvious. The two lower temperature annealed/quenched samples undergo sudden transitions near 170 K ($T_{A/Q} = 500°$C) and 130 K ($T_{A/Q} = 700°$C) and by 10 K the sample with $T_{A/Q} = 500°$C has developed a clear magnetic splitting of 10.03(3) T, whereas the sample with $T_{A/Q} = 700°$C exhibits a slightly smaller hyperfine field of 9.51(3) T at 5 K. By contrast, the spectrum of the as-grown sample is almost unchanged, indicating there is no detectable internal, hyperfine, field.

5.3.3 NMR

NMR measurements were also carried out on the as-grown ($T_{A/Q} = 960°$C) and $T_{A/Q} = 400°$C samples. Figure 5.10a shows ^{75}As NMR spectra at T = 200 K for two magnetic field directions of $H \parallel c$ axis and $H \parallel ab$ plane for the samples with $T_{A/Q} = 400°$C. The blue lines in the figure show simulated spectra. Below 160 K, each NMR line for $H \parallel c$ axis splits into two lines due to internal field H_{int} (parallel or antiparallel to H) which is produced by the Fe spin-ordered moment. A typical example of the split NMR lines for $H \parallel c$ axis is shown at the bottom of Fig. 5.10a. The spectrum is reproduced well by H_{int} =2.59 T and ν_Q =12.7 MHz at $T = 50$ K. These values are in good agreement with previously reported values for ^{75}As

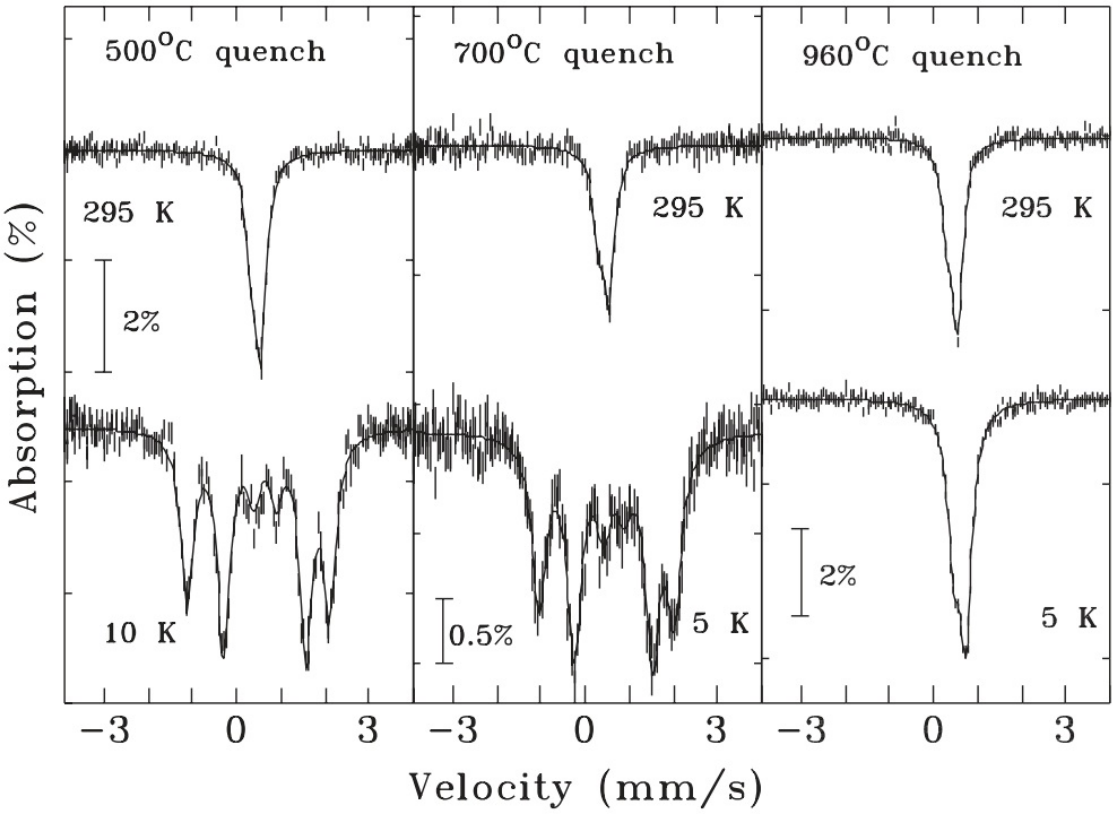

Figure 5.9 ^{57}Fe Mössbauer spectra of an *ab*-plane single-crystal mosaic of samples (from left) with $T_{A/Q} = 500$°C, with $T_{A/Q} = 700$°C, and with $T_{A/Q} = 960$°C (as-grown). In each case the upper spectrum was taken at 295 K, whereas the lower spectrum was taken at 10 K or 5 K. Only the as-grown sample shows no magnetic ordering at base temperature.

NMR of single crystals (T_N/T_S = 167 K) grown from Sn-flux (Baek et al., 2009), once again indicating that the sample with $T_{A/Q}$ = 400°C is essentially the same as previously reported ones grown from Sn.

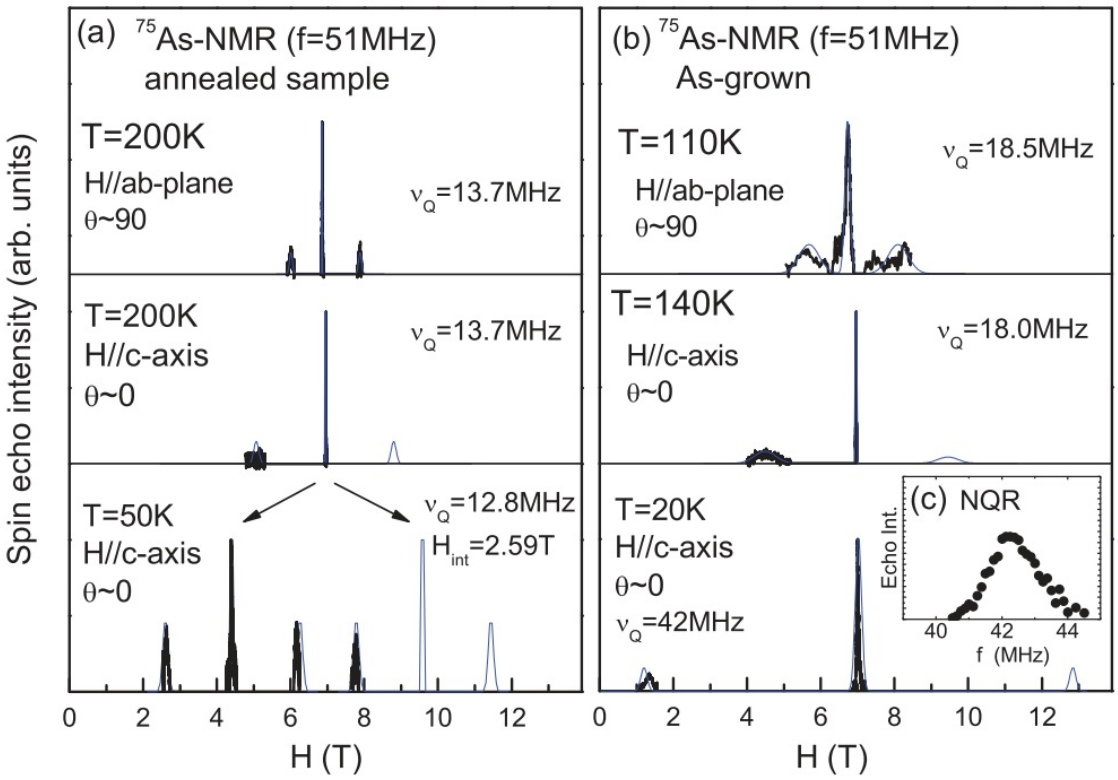

Figure 5.10 ^{75}As NMR spectra measured at f= 51 MHz for (a) annealed/quenched $CaFe_2As_2$ crystal with $T_{A/Q}$ = 400°C and (b) the as-grown $CaFe_2As_2$ crystal with $T_{A/Q}$ = 960°C. Black and blue lines are observed and simulated spectra, respectively. Expected lines above 9 T are not measured due to the limited maximum magnetic field for our SC magnet. (c)^{75}As NQR spectrum at T = 4.2 K and H = 0 T.

Similar quadrupole-split NMR spectra are observed in the as-grown $CaFe_2As_2$ sample as shown in Fig. 5.10b. The ^{75}As NMR satellite linewidth, which reflects the distribution of EFG, is significantly larger than in the annealed/quenched sample, indicative of higher degree of inhomogeneity of the local As environment due to strains, defects, or lattice distortion in the as-grown sample. Below the transition temperature, T $\sim$ 96 K, no splitting of the NMR lines is observed (indicating that there is no antiferromagnetic order) but ν_Q is found to change

dramatically: from ~ 18 to ~ 42 MHz, as is shown at the bottom in Fig. 5.10b. Such a drastic change of ν_Q (more than 230%) cannot be explained by thermal expansion of lattice (at most few percentage points) but is attributed to a structural phase transition. The combination of no splitting of the NMR lines with the large shift in ν_Q are further confirmation that, for the as-grown sample, there is only a structural phase transition without any magnetic phase transition.

The combination of x-ray diffraction, Mössbauer , and NMR data unambiguously identify the low-temperature state of the as-grown sample with $T_{A/Q} = 960°$C as being non-moment bearing and also having a collapsed tetragonal unit cell that is remarkably similar to what has been found for Sn-grown $CaFe_2As_2$ under hydrostatic pressure. For that matter, the evolution of the temperature-dependent resistance as well as magnetic susceptibility are both qualitatively similar to the evolutions found when pressure is applied as hydrostatically as possible, i.e., with He as a pressure medium (Yu et al., 2009).

5.4 Microscopic Explanation

At this point, not only having created a T-$T_{A/Q}$ phase diagram that looks a lot like the T-P phase diagram but also having clearly identified the phases associated with this phase diagram, it is appropriate to investigate the possible physical origin, or mechanism, for this apparent similarity between pressure applied to a Sn-grown crystal of $CaFe_2As_2$ and annealing/quenching of FeAs-grown crystals.

A starting point for this search for a mechanism can be found in a subset of the observations made above. The as-grown crystals from FeAs solution are far more brittle than either the Sn-grown crystals or the FeAs-grown crystals after a 400°C anneal. This qualitative observation hints at some higher concentration of defects in the as-grown crystals that leads to embrittlement. In addition, both the Mössbauer and NMR measurements find broader line shapes associated with the spectra from the as-grown samples, indicating that there may be a greater degree of disorder in them than in the crystal with $T_{A/Q} = 400(500)°$C.

In order to examine the distribution of defects at a nanoscale level, TEM measurements were carried out on both as-grown samples with $T_{A/Q} = 960°$C as well as samples with $T_{A/Q}$

= 500°C. The as-grown sample (Fig. 5.11a) shows a pervasive tweedlike pattern with ∼ 40 nm separation of features. The selected area diffraction pattern (SADP), (inset, Fig. 5.11a), shows only the [0,0,1] zone axis pattern consistent with the $CaFe_2As_2$ compound. These very long but thin features are orthogonal and are approximately parallel to the {h,0,0} planes as best can be determined in this orientation of the sample. These features were consistent throughout all the thin area of the sample, although in some regions one variant may dominate over the other and in some regions interpenetrating lamellae were observed, as shown in Fig. 5.11a. Occasional dislocations were observed, but they did not dominate the microstructure.

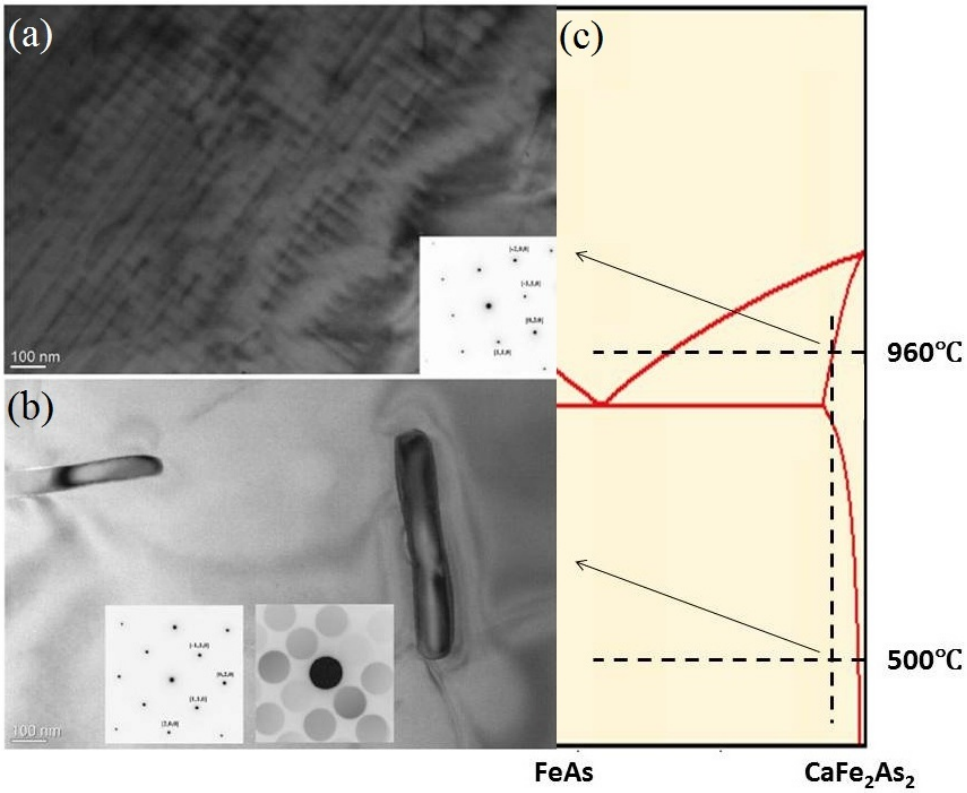

Figure 5.11 (a) TEM micrograph of the as-grown ($T_{A/Q}$ = 960°C) sample. The inset on the right is the SADP from this image area showing expected lattice reflections for a [0,0,1] zone axis for the 122 compound. (b) TEM micrograph of the $T_{A/Q} = 500$°C sample at the same magnification and zone axis orientation as the as-grown sample above. The inset on the left shows the SADP of the matrix and precipitates while the right inset is a CBED of only the precipitate phase showing nearly the same orientation and d spacing as the matrix 122 phase. (c) A schematic drawing of hypothetical width of formation with temperature dependence.

The sample with $T_{A/Q} = 500°C$ appears completely different. Here we observed a very smooth contrast across the thin region when tilting and uniformly distributed small lenticular precipitates about 25 to 100 nm in width and with a length to width aspect about 5:1 (Fig. 5.11b). These precipitates are also fairly uniformly separated, $\sim$ 500 to 1000 nm, and have their long axis parallel to the {h,0,0}, as was observed in the tweed pattern of the as-grown sample. Dislocations in the matrix are commonly observed to emanate from the interface between the precipitates and the matrix typically near the ends of the precipitate where stresses would be higher if there are differences in coefficients of thermal expansion. The SADP is nearly identical to the as-grown sample but here the precipitates are large enough for diffraction analysis. The convergent beam electron diffraction (CBED) pattern (right inset in Fig. 5.11b) produces disks rather than spots due to how the pattern is formed, but it is clear that the pattern is identical to that of the matrix. EDS indicated that the precipitate phase does not contain Ca. Subsequent efforts to identify the precise chemistry and structure of this second phase have led to a composition of FeAs and an estimate of the impurity phase fraction of less than 1% of the total sample, giving a gross idea of how much extra Fe and As is trapped in the sample when it is initially quenched from 960°C.

The similarity in the orientation and lack of distinguishing features in the diffraction between the as-grown samples and the samples that were annealed/quenched suggests that there is a similarity in chemistry and structure between the tweed strain fields and coarser precipitates in these two samples and the difference is simply one of length scale. An epitaxial relationship would lower the energy barrier for nucleation and allow a second phase to form more readily if thermodynamically stable. Annealing/quenching at moderate temperatures but within a two-phase field would promote growth of the second phase to reduce the excess energy due to interfaces (i.e., Oswald ripening). The observations here are consistent with an increase in the width of formation of $CaFe_2As_2$ with respect to excess As and Fe at elevated temperatures which decreases monotonically with temperatures below 960°C (Fig. 5.11c).

Such a temperature-dependent solid solubility of excess Fe and As leads to the following (plausible) scenario. When the FeAs-flux grown crystal is first quenched, there is little time for the excess As and Fe to come out of solution. In these single crystals, the grain dimensions

(often millimeters to centimeters) are simply too large for diffusion to allow for the expulsion of these species to the grain boundaries. Energetically, it appears easiest to exsolve excess As and Fe epitaxially along the {h,0,0} planes. Differences in their unit cell size as well as their coefficients of thermal expansion (CTE) can lead to significant stresses at the interfaces between the $CaFe_2As_2$ majority phase and the finely dispersed Fe/As-based second phase. If, as Fig. 5.11a would suggest, domains of $CaFe_2As_2$, about 40 nm on a side, are surrounded by nearly coherent second phase resulting in a significant volume fraction of interfaces or regions strained by interfaces, then the magnitude of the stress would be dependent on the volume fraction of the $CaFe_2As_2$ in these strained regions.

If there is a temperature dependence of the solubility of the excess As and Fe (Fig. 5.11c), then quenching from lower temperatures would result in a smaller fraction of finely dispersed second phase, the remaining excess As and Fe being sequestered in larger precipitates whose insignificant surface to volume ratio would have little impact on the matrix (as is the case in Fig. 5.11b). This smaller amount of finely dispersed precipitate would lead to a smaller average strain (or pressure) on the sample, leading to an effective correlation between P and $T_{A/Q}$. Since the initial quench of the large crystals from the flux essentially locks in the excess As and Fe, the subsequent processing history determines the size and distribution of the second phase and thereby determines the amount of strain in the sample.

Alternatively, if there is a temperature dependence of the solubility of excess As and Fe then quenching from lower temperatures could result in a systematic control of how much As and Fe are trapped (metastably) in a $CaFe_{2+}As_{2+}$ phase. Within this hypothesis the excess As and Fe remaining in the $CaFe_2As_2$ phase would be the parameters controlling the value of transition temperature and nature of the low-temperature ground state. Whereas this hypothesis cannot be ruled out within the current data set, the clear, tweedlike patterns seen in Fig. 5.11a may be more consistent with the strain field from a nanoprecipitate.

Returning to the initial motivations for this study: given that annealing/quenching of as-grown samples seems to lead to small changes in the transition temperatures of $BaFe_2As_2$-based compounds (Rotundu et al., 2010; Gofryk et al., 2011; Kim et al., 2012a) and given that $CaFe_2As_2$ is much more pressure or strain sensitive than $BaFe_2As_2$, it is worth exploring the

implications of our current findings. If we speculate that a similar width of formation exists in $BaFe_2As_2$ (or for that matter $SrFe_2As_2$) and that low-temperature annealing/quenching can lead to similar effects as those we present here, then, based on the existing P - T phase diagrams (Colombier et al., 2009), an effective pressure of ~ 0.4 GPa on $BaFe_2As_2$ or $SrFe_2As_2$ would lead only to shifts in transition temperature of a few K, consistent with what has been observed. Based on this analysis, TEM measurements on as-grown and annealed/quenched crystals of $BaFe_2As_2$, as well as $SrFe_2As_2$, to check for similar, annealing/quenching temperature-dependent microstructureare in order.

5.5 Summary

We have found a remarkably large response of the transition temperature of $CaFe_2As_2$ single crystals grown from excess FeAs to annealing/quenching or quenching temperature. Whereas crystals with $T_{A/Q} = 400°(500°)$C exhibit a first-order phase transition from a high-temperature tetragonal to a low-temperature orthorhombic-antiferromagnetic state near 170 K (similar to what has been found in the original Sn-grown single crystals), crystals that have been quenched from 960°C exhibit a transition from a high-temperature tetragonal phase to a low-temperature, nonmoment-bearing, collapsed tetragonal phase below 100 K. We have been able to demonstrate that the transition temperature can be reduced in a monotonic fashion by varying the $T_{A/Q}$ from 400° to 850°C with the low-temperature state remaining antiferromagnetic for transition temperatures larger than 100 K and becoming collapsed tetragonal, nonmagnetic for transition temperatures below 90 K. This suppression of the AFM/ORTH phase transition and its ultimate replacement with the cT phase is similar to what has been observed for Sn-grown single crystals of $CaFe_2As_2$ under hydrostatic pressure.

TEM studies of the as-grown (quenched from 960°C) and annealed/quenched crystals indicate that there is a temperature-dependent width of formation of $CaFe_2As_2$ with a decreasing amount of excess Fe and As being soluble in the single crystal at lower $T_{A/Q}$. On one extreme, samples quenched from 960°C have finely divided strain structure with characteristic length scales and spacings of less than 50 nm. On the other extreme, samples with $T_{A/Q} =$ 500°C have clearly identifiable Ca-free crystalline inclusions with dimensions of $\sim 70{\times}500$ nm^2

that are separated by 500 to 1000 nm. These images make it clear that when the sample as quenched from 960°C it is possible to think of some average, near uniform strain throughout the sample associated with the overlapping strain fields of this fine precipitate. It is this strain that appears to be giving rise to the dramatic suppression of the transition, in, apparently, a manner similar to that hydrostatic pressures of ~ 0.4 GPa.

CHAPTER 6. COMBINED EFFECTS OF Co-SUBSTITUTION AND ANNEALING/QUENCHING ON PHYSICAL PROPERTIES OF $CaFe_2As_2$

6.1 Introduction

Having mastered controlling the FeAs-grown $CaFe_2As_2$ we could use both chemical substitution and annealing/quenching to tune the system of $CaFe_2As_2$. Chemical substitution, such as Co-substitution, as a control parameter, has been studied extensively for members of the 122 family. For $BaFe_2As_2$, Co-substitution first suppresses the antiferromagnetic/orthorhombic (AFM/ORTH) state and then induces superconductivity, making $Ba(Fe_{1-x}Co_x)_2As_2$ a model system for the study of high-T_c superconductivity in Fe-based superconductors (Sefat et al., 2008b; Ni et al., 2008c; Canfield and Bud'ko, 2010; Ni and Bud'ko, 2011). For $CaFe_2As_2$, the effects of Co-substitution have been studied only on the samples grown out of Sn, which have issues with solubility, reproducibility and inhomogeneity (Matusiak et al., 2010; Harnagea et al., 2011; Hu et al., 2012). The phase diagrams constructed by different groups do not match very well and therefore, need to be clarified.

In this chapter, I present work on Co-substituted $CaFe_2As_2$ grown out of an FeAs-flux with different annealing/quenching temperature. As in the case of unsubstituted $CaFe_2As_2$ grown out of an FeAs-flux, we found that annealing/quenching temperature is a vital parameter to control and understand this system. I will present a systematic study of the combined effects of Co-substitution and annealing/quenching on the physical properties of $CaFe_2As_2$ and construct phase diagrams for different substitution levels and different annealing/quenching temperatures. Also, by combining the two control parameters, I am able to extend the 2-dimensional, T-x and T-$T_{A/Q}$ phase diagrams into a 3-dimensional, T-x-$T_{A/Q}$ phase diagram and reveal rich physics and better control of the system than Sn-grown samples, all at ambient pressure.

Table 6.1 WDS data for $Ca(Fe_{1-x}Co_x)_2As_2$. $x_{nominal}$ is the nominal concentration of the substitutions. x_{WDS} is the average of x values measured at 12 locations on samples from each batch. 2σ is twice the standard deviation of the 12 values measured.

$Ca(Fe_{1-x}Co_x)_2As_2$								
$x_{nominal}$	0.01	0.02	0.025	0.03	0.035	0.04	0.05	0.06
x_{WDS}	0.010	0.019	0.022	0.028	0.033	0.038	0.049	0.059
2σ	0.001	0.001	0.001	0.001	0.001	0.001	0.002	0.002

This chapter is heavily based on the published article: Ran, S., Bud'ko, S. L., Straszheim, W. E., Soh, J., Kim, M. G., Kreyssig, A., Goldman, A. I. and Canfield, P. C. "Control of magnetic, nonmagnetic, and superconducting states in annealed $Ca(Fe_{1-x}Co_x)_2As_2$" *Phys. Rev. B*, 85 (2012):224528.

6.2 Compositional and Structural Determination

A summary of the WDS measurement data is presented in Table 6.1. The table shows the nominal concentration, the measured average x value, and twice the standard deviation of the x values measured. For each sample, the measurement was done at 12 different locations on a cleaved surface. Data points of nominal versus actual concentration can be fit very well with a straight line (Fig. 6.1), with a slope of 0.96 ± 0.01, indicating a linear correlation between the measured Co concentration and the nominal concentration. The error bars are taken as twice the standard deviation determined from the measurements, and the largest deviation from the nominal value is no more than 0.002, demonstrating relative homogeneity of the substituted samples studied here. In the following, the average experimentally determined concentration values, $x = x_{WDS}$, will be used to identify all the compounds rather than the nominal concentration, $x_{nominal}$. These results are in stark contrast to the non-monotonic and scattered x_{WDS} versus $x_{nominal}$ results found for the $Ca(Fe_{1-x}Co_x)_2As_2$ grown from Sn (Fig. 4.2), for which solubility problems in Sn make systematic measurements on homogeneous samples difficult (Hu et al., 2012).

Figure 6.2a presents the c-lattice parameters of the $T_{A/Q} = 960°C$ samples, as well as selected $T_{A/Q} = 350°C$ and $400°C$ samples, determined via the diffraction from plate-like

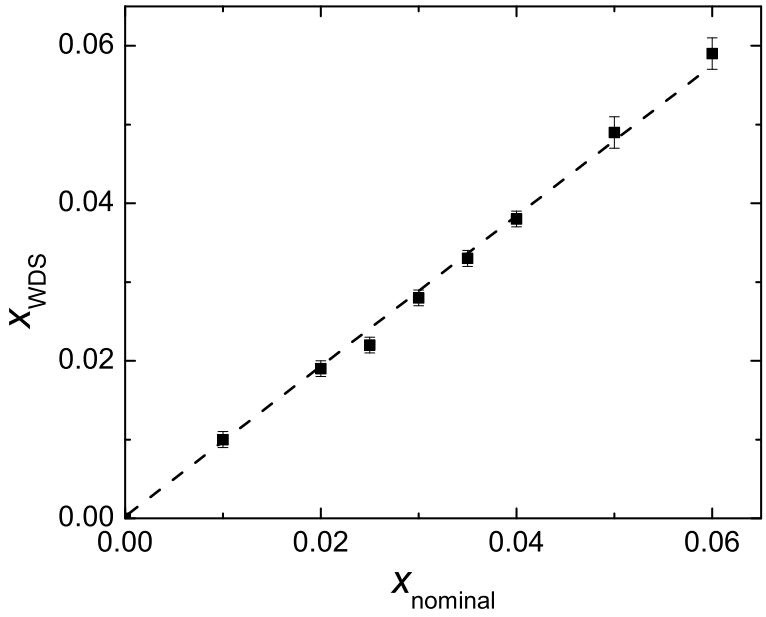

Figure 6.1 Measured Co concentration vs nominal one for the $Ca(Fe_{1-x}Co_x)_2As_2$.

samples described above, using the (002) and (008) peaks, as a function of measured Co concentration. The $x = 0.00$/ $T_{A/Q} = 400°C$ sample has c-lattice parameter similar to that of the Sn-grown sample whereas the $T_{A/Q} = 960°C$ sample manifests a reduction of almost 2% in the c-lattice parameter. Data for Sn-grown $CaFe_2As_2$ at ambient and applied pressure of $P = 0.63$ GPa demonstrate that the effects of applied pressure and annealing/quenching temperature are remarkably similar. Substituting Co decreases c-lattice parameter for both $T_{A/Q} = 350°C$ samples and $T_{A/Q} = 960°C$ samples, at roughly the same rate. Figure 6.2b presents the c-lattice parameters of the pure samples, as well as the Co-substituted samples with $x = 0.022$, 0.028 and 0.059, as a function of $T_{A/Q}$. The c-lattice parameter for both pure and Co-substituted samples decreases with increasing $T_{A/Q}$ in a monotonic, but slightly non-linear manner, which is consistent with the analogy between $T_{A/Q}$ and applied pressure that we made in last chapter. The rate at which the c-lattice parameter decreases is essentially the same for each of the different concentrations.

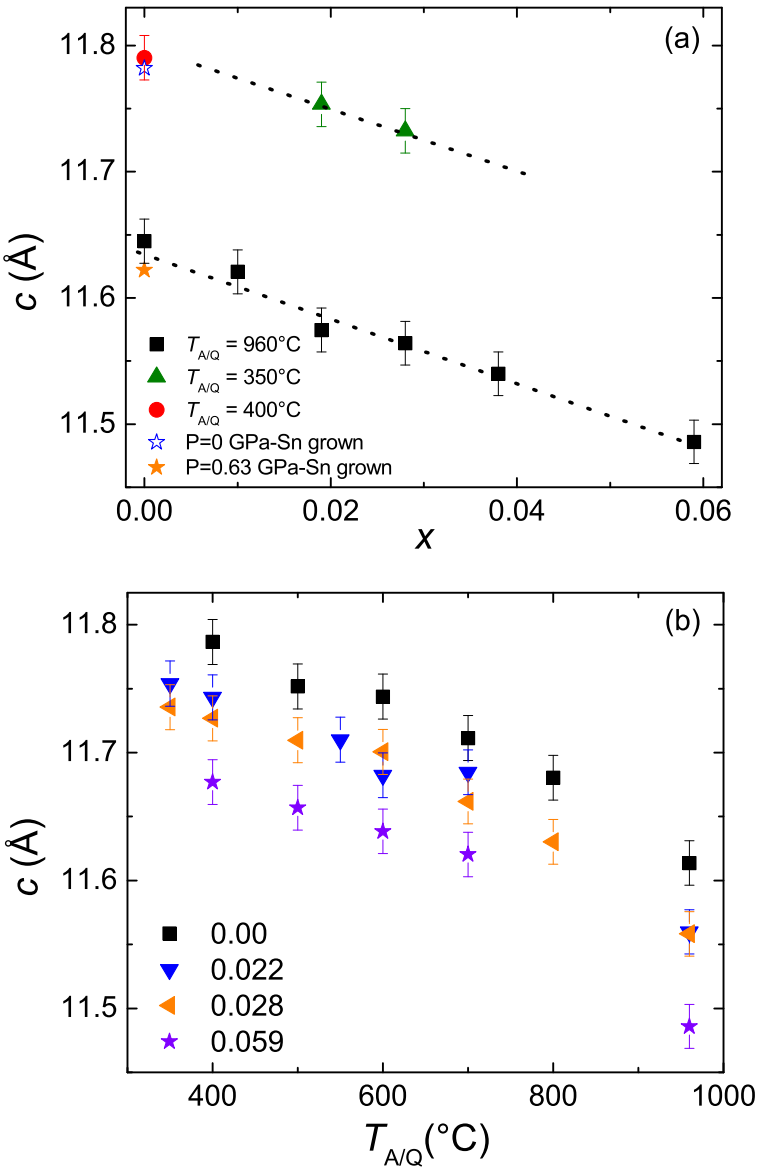

Figure 6.2 Room temperature c-lattice parameter of $Ca(Fe_{1-x}Co_x)_2As_2$, determined via the diffraction from plate-like samples described in the Experimental Methods section, (a) of $T_{A/Q} = 960°C$ samples, as well as selected $T_{A/Q} = 350°C$ and 400°C samples, as a function of measured Co concentration, x and (b) of pure samples and Co-substituted samples with $x = 0.022$, 0.028 and 0.059, as a function of annealing/quenching temperature, $T_{A/Q}$. In (a), for comparison, data of Sn-grown sample under pressure are also presented.

6.3 Physical Properties of $T_{A/Q} = 960°C$ $Ca(Fe_{1-x}Co_x)_2As_2$ Single Crystals

Figures 6.3a and 6.3b present the temperature dependent magnetic susceptibility, with magnetic field applied parallel to the c-axis, and normalized resistance for $T_{A/Q} = 960°C$ $Ca(Fe_{1-x}Co_x)_2As_2$ single crystal samples with Co substitution levels up to $x = 0.059$. For the pure compound, $CaFe_2As_2$, the susceptibility of the $T_{A/Q} = 960°C$ sample shows a sharp drop ($\sim 50\%$) below 100 K, which is associated with a phase transition from the high temperature, tetragonal, paramagnetic state to the low temperature, non-moment bearing, collapsed tetragonal (cT) state (see Chapter 5). Note that the size of the jump is almost twice as large as that of the AFM/ORTH phase transition of the Sn-grown sample (top of Fig. 6.3a) when measured with field parallel to the c-axis. This phase transition can produce a downward jump in resistance when cooling down (Yu et al., 2009), but, given that this is a first order, structural phase transition, it often leads to cracking along the length and width of the bar, as well as loss of contacts. For these reasons resistance data often stops as temperature progresses below T_{cT}.

For low Co substitution values, the magnetic susceptibility shows little change when adding Co with the signature of the phase transition appearing at roughly the same temperature. The only change in the magnetization data is the loss of the discontinuous jump in $M(T)/H$ on cooling for $x = 0.028$ and higher. In order to confirm that the low temperature state of the Co-substituted, $T_{A/Q} = 960°C$ samples is a tetragonal phase with reduced c-lattice parameter, a temperature dependent, single crystal x-ray measurement was carried out on the $x = 0.059$ sample. Figure 6.4 displays the temperature dependence of the lattice parameters as well as the unit cell volume. For the $x = 0.00$ and $x = 0.059$, $T_{A/Q} = 960°C$ samples, it is clear that there is a reduction of the c-lattice parameter and an expansion of the a-lattice parameter from high temperature to low temperature. The overall unit cell volume shrinks as a result. The lattice parameters for the $x = 0.059$ sample are almost the same as those for the pure compound at low temperature.

However, both the changes in the lattice parameters and the magnetic susceptibility of the $x = 0.059$ sample are dramatically broadened comparing with those of the pure compound.

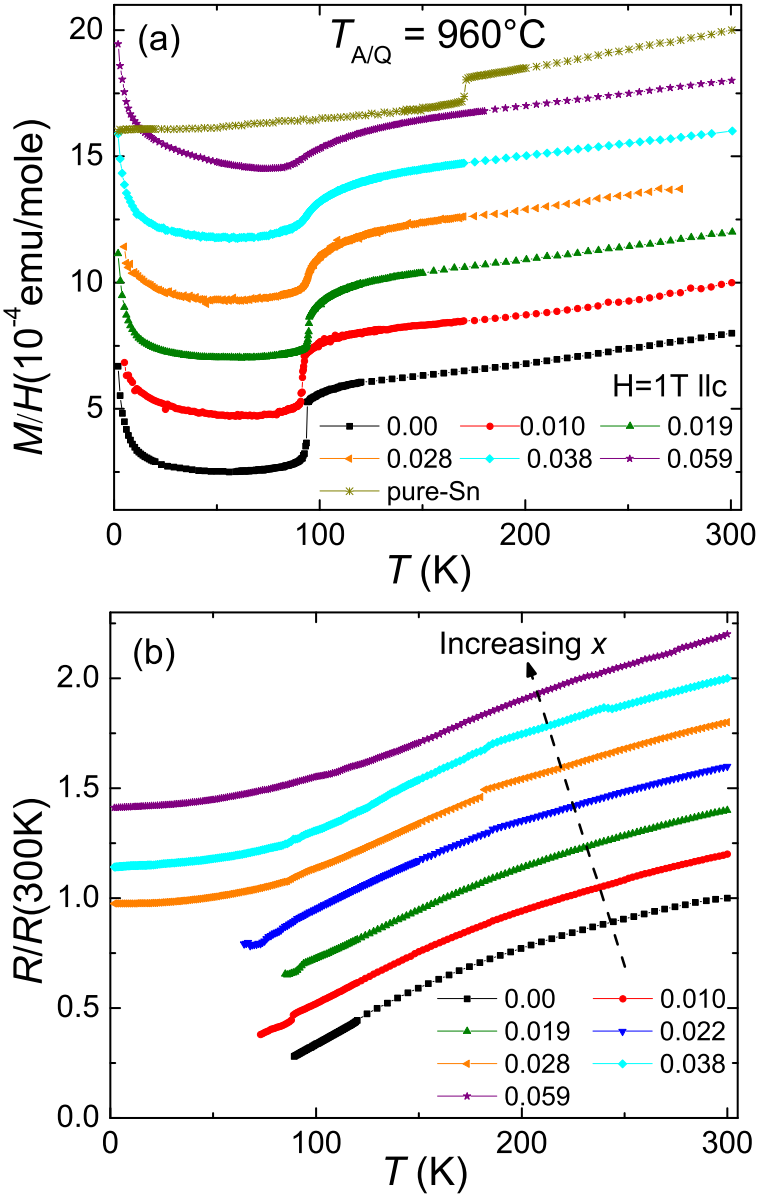

Figure 6.3 Temperature dependent (a) magnetic susceptibility with a field of 1 T applied parallel to the c-axis and (b) normalized electrical resistance of $T_{A/Q}$ = 960°C $Ca(Fe_{1-x}Co_x)_2As_2$ samples. For clarity, susceptibility data in (a) have been offset by 2×10^{-4} emu/mole from each other and resistance data in (b) have been offset by 0.2 from each other.

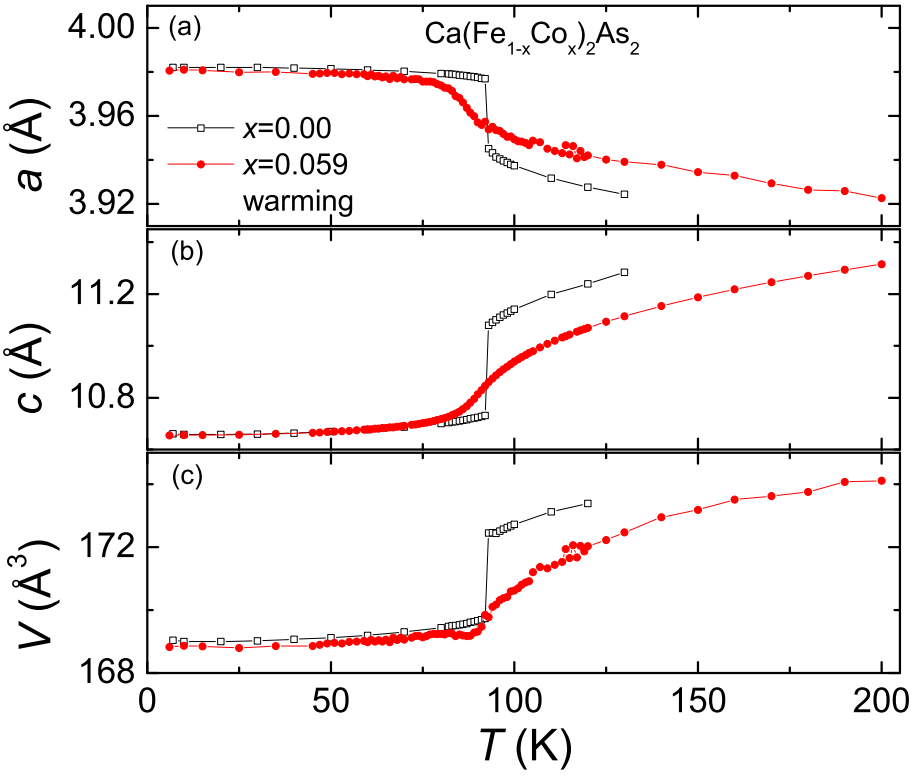

Figure 6.4 Values for (a) the a-lattice parameter, (b) the c-lattice parameter and (c) unit cell volume as a function of temperature for $Ca(Fe_{1-x}Co_x)_2As_2$ for $x = 0.00$ (square) and $x = 0.059$ (circle) $T_{A/Q} = 960°C$ samples determined from single crystal x-ray diffraction measurements.

Instead of a sharp jump at the transition temperature indicating a first order phase transition, the lattice parameters and the magnetic susceptibility change gradually over ~ 30 K. Moreover, this broadening in signatures of transition coincides with the changes in the resistance data, with the resistance bar surviving as it is cooled down to the base temperature of 1.8 K, instead of cracking and losing contact which is often an indication of a strongly first order structural phase transition. All these thermodynamic, transport and microscopic measurements suggest the possibility that a critical end point of the phase transition may exist and, at $x = 0.059$, the system has already gone beyond this critical end point resulting in a continuous thermal contraction rather than a first order phase transition. Further structural investigations of this issue are needed.

6.4 Annealing/quenching Effects on $Ca(Fe_{1-x}Co_x)_2As_2$

The results presented above for the $T_{A/Q} = 960°C$ $Ca(Fe_{1-x}Co_x)_2As_2$ samples are dramatically different from those reported for the Sn-grown samples. In the case of the pure compound, this difference is caused by stress and strain built up inside the sample during the process of quenching from 960°C (Chapter 5). Control of post growth annealing and quenching can systematically suppress the AFM/ORTH transition and stabilize the cT phase in a manner analogous to applied pressure. For $Ca(Fe_{1-x}Co_x)_2As_2$, we expect the $T_{A/Q}$ to serve as a tuning parameter in a similar way. In order to study the effect of the $T_{A/Q}$ on the Co-substituted samples, we annealed and quenched the samples with different concentrations at temperatures ranging from 350°C to 800°C and measured their thermodynamic and transport properties.

Figure 6.5a presents the in plane susceptibility data in a field of 1 T applied perpendicular to the c-axis for $T_{A/Q}$ of 350°C. After being annealed/quenched at 350°C, the pure compound manifests a AFM/ORTH phase transition at around 170 K as indicated by the sharp drop in susceptibility (and sharp increase in resistance shown in Fig. 6.5c, as will be discussed momentarily). This phase transition is progressively suppressed by Co-substitution until it is completely suppressed by $x = 0.033$. The magnetic signature of the phase transition remains quite sharp with the size of the jump fairly constant. The superconducting phase first appears in the $x = 0.033$ sample, with the superconducting transition temperature T_c around 15 K. As the

Co substitution level is further increased, T_c decreases. An upper limit of the superconducting fraction can be obtained from the zero field cooling susceptibility in the field of 0.01 T as shown in Fig. 6.5b. The screening of around 100% of $1/4\pi$ at 2 K is seen for the $x = 0.033$ and $x = 0.038$ samples without taking account of demagnetization factor. For higher Co-substitution the screening decreases and becomes essential zero for the $x = 0.059$ sample.

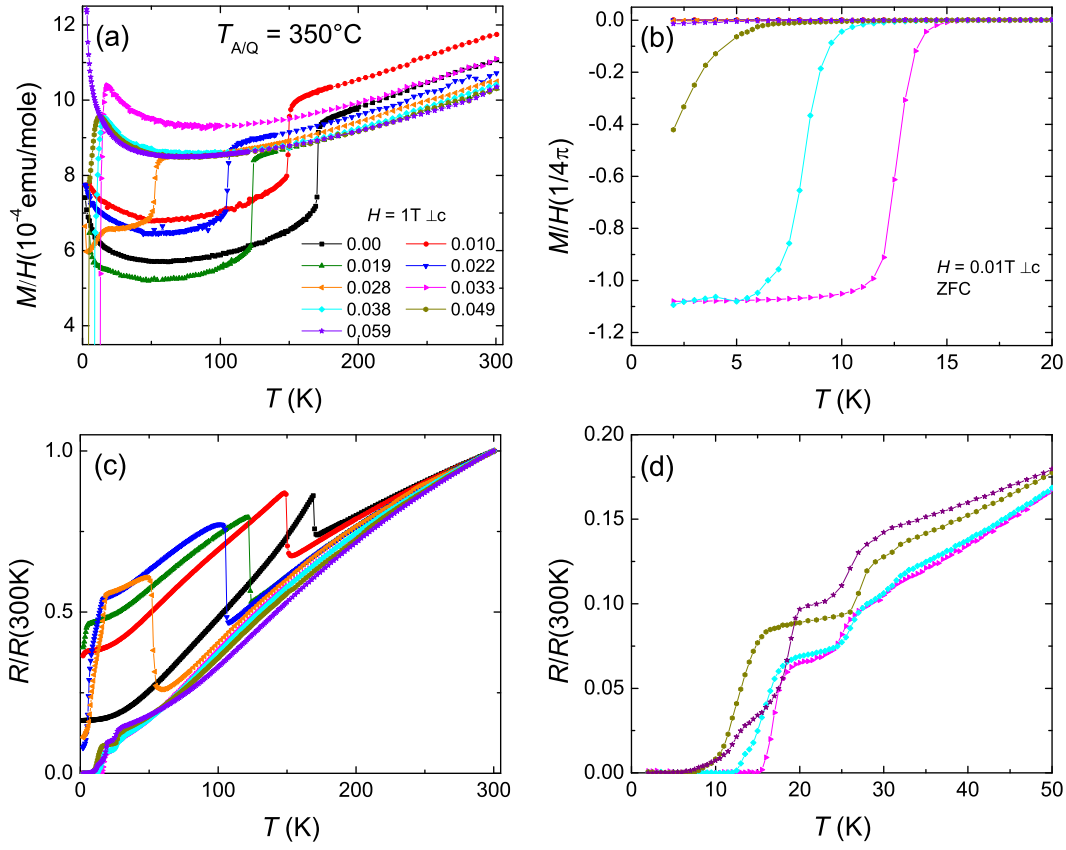

Figure 6.5 Temperature dependent (a) magnetic susceptibility with a field of 1 T applied perpendicular to the c-axis, (b) low field magnetic susceptibility measured upon zero field cooling (ZFC) with a field of 0.01 T applied perpendicular to the c-axis and (c) normalized electrical resistance of $Ca(Fe_{1-x}Co_x)_2As_2$ samples for an $T_{A/Q}$ of 350°C. Low temperature resistance of samples with $x \geq 0.033$ are presented in (d).

Figure 6.5c shows normalized, temperature dependent resistance data for the 350°C annealed/quenched samples. For substitution levels up to $x = 0.028$, the AFM/ORTH phase transition is further confirmed by the same sharp, upward jump in resistance, similar to that

found in pure $CaFe_2As_2$. As the transition temperature is suppressed, this signature remains sharp while the size of the jump increases monotonically and reaches 40% of room temperature resistance value at $x = 0.028$. The increasing size of the jump with suppressing T_N/T_S is similar to what has been seen for the pure compound grown out of an FeAs-flux, but is in contrast to the case of Sn-grown samples under pressure(Yu et al., 2009), where the size of the jump remains relatively constant. Although the resistance starts to decrease at low temperature for the samples with $x = 0.019$, 0.022 and 0.028, it does not reach instrumental zero. Considering that low field susceptibility does not show significant screening, the sudden drop in resistance for these three samples most likely indicates filamentary superconductivity (Saha et al., 2009; Colombier et al., 2009). Complete superconducting phase transitions with zero resistance are obtained for $x \geq 0.033$. The fact that resistance shows several steps before reaches instrumental zero, the highest of which has an onset near 30 K, suggest that there may be some microscopic inhomogeneity of the stress and strain. This will be discussed in detail in the Discussion section below. T_c decreases gradually with increasing Co concentration and drops to around 2.5 K for $x = 0.059$. Again, since the screening for this concentration is essentially zero, it may be a filamentary superconductor.

Before we proceed further, it is important to further explore whether that the superconductivity at optimal substitution and annealing/quenching temperature is a bulk property instead of filamentary superconductivity since zero resistance can be caused by only a thin layer or filament spanning the sample. Low field susceptibility, as a thermodynamic quantity, is normally used to confirm the bulk superconductor. However, the low field susceptibility was measured after cooling in a zero applied field, and therefore only tells the upper limit of the superconducting fraction.

One way to further establish that bulk superconductivity is present is to measure the temperature dependent specific heat and determine the size of the jump at T_c. Figure 6.6 presents the specific heat data on a representative sample, $x = 0.033/T_{A/Q} = 350°C$, which shows full diamagnetism from zero field cooled-warming susceptibility data. Specific heat was measured in both zero field and in 9 T and the size of the jump in C_P at T_c can be inferred from the difference between these two data sets. (As will be shown below, anisotropic $H_{c2}(T)$ data on an

optimal substituted/annealed $Ca(Fe_{1-x}Co_x)_2As_2$ samples show that 9 T is an adequate field for this subtraction and analysis.) Due to finite widths of the superconducting transitions, $\Delta C_P/T_c$ and T_c values were determined from C_P/T vs T data using an isoentropic construction (i.e., such that the vertical line in Fig. 6.6b delineates equal areas in the C_P/T vs T plot). A $\Delta C_P/T_c$ value of 16.1 mJ/mol K^2 is inferred from this criterion. These data fall onto a manifold of $\Delta C_P/T_c$ versus T_c^2 data (known as a BNC plot) found for many substituted $AEFe_2As_2$ materials (Bud'ko et al., 2009; Kogan, 2009; Kim et al., 2011; Stewart, 2011) (see discussion below), suggesting that there is bulk superconductivity in this sample.

Using the criteria discussed in the Experimental Methods section above, a phase diagram of transition temperature versus Co concentration can be constructed based on the magnetic susceptibility and electric resistance data. Figure 6.7 presents the T-x phase for an $T_{A/Q}$ of 350°C. The AFM/ORTH phase transition is suppressed continuously and the phase line drops to zero for a substitution level between $x = 0.028$ and $x = 0.033$, and the superconducting phase emerges by $x = 0.033$. T_c is highest when the AFM/ORTH phase has just been suppressed completely; T_c is suppressed by further Co-substitution. The superconducting region extends to around $x = 0.049$. No clear evidence of either the coexistence of the AFM/ORTH with the superconducting phases or any splitting of the magnetic and structure phase transitions is observed.

To further study the effects of the $T_{A/Q}$ on this series of compounds, we increased the $T_{A/Q}$ to 400°C. The magnetic susceptibility and resistance data, as well as specific heat data for the $x = 0.028/T_{A/Q} = 400$°C sample, are shown in Fig. 6.8 and the T-x phase diagram is shown in Fig. 6.9. As in the case of $T_{A/Q} = 350$°C, the pure compound is in the AFM/ORTH state at low temperature. Substituting Co suppresses the AFM/ORTH transition temperature and again, when it is suppressed completely, the superconducting phase appears. The major difference for this higher $T_{A/Q}$ is that the T_N/T_S line is suppressed by several K for $x = 0$ and by $x = 0.028$, the AFM/ORTH phase is already suppressed completely and the superconducting phase appears with screening of 100% of $1/4\pi$ whereas, for 350°C annealing, this only occurs for $x = 0.033$. This is consistent with the fact that increasing the $T_{A/Q}$ suppresses the AFM/ORTH transition temperature as shown for pure compound in last chapter. The

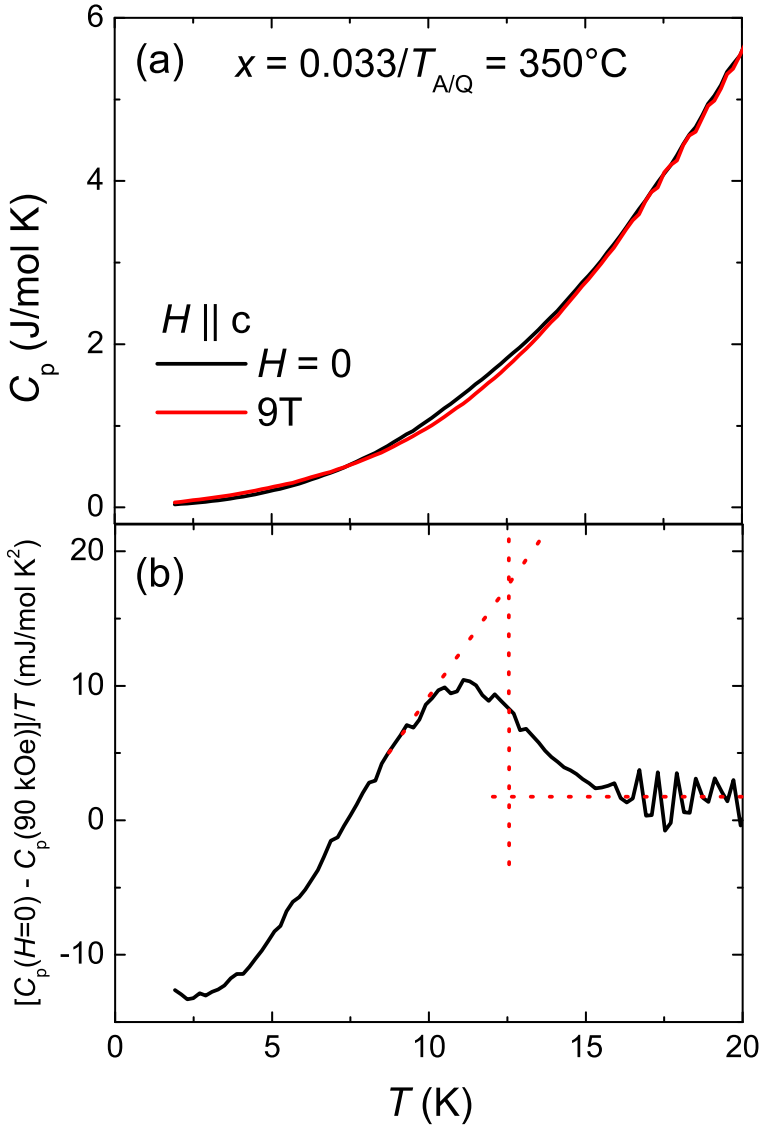

Figure 6.6 (a) Temperature dependent specific heat data of the $x = 0.033/T_{A/Q} = 350°\mathrm{C}$ sample, measured in zero field and a field of 9 T applied parallel to the c-axis and (b) the difference between of the two sets of data presented as $\Delta C_P/T$. The red dashed lines represent the isoentropic construction used to determine the jump in C_P at T_c (see text).

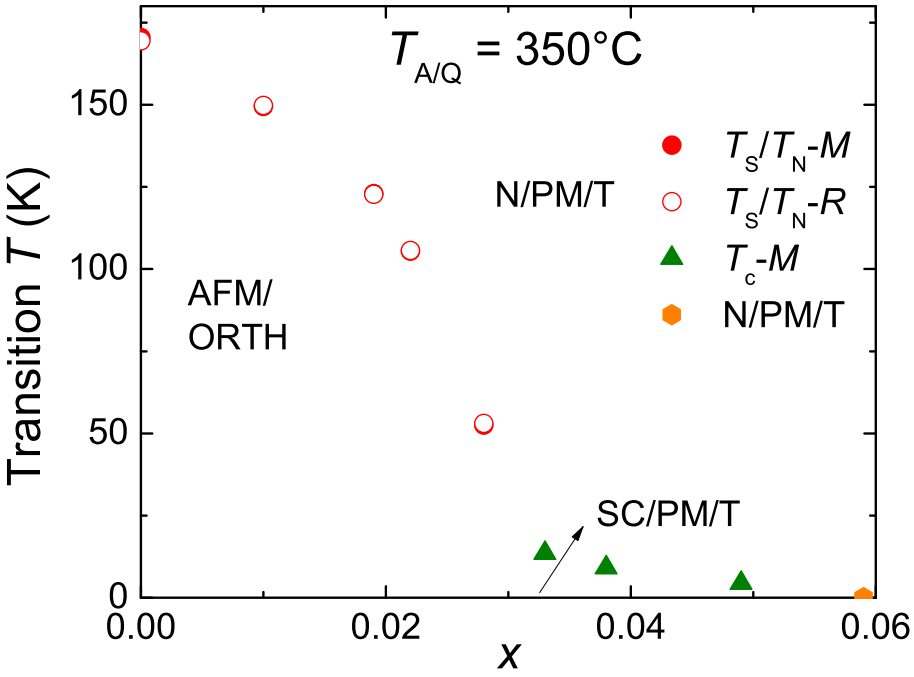

Figure 6.7 Phase diagram of transition temperature, T, versus Co concentration, x, of $Ca(Fe_{1-x}Co_x)_2As_2$ samples for an $T_{A/Q}$ of 350°C. The filled symbols are inferred from magnetization (M) data, the open symbols are inferred from resistance (R) data. Three different phases are observed: antiferromagnetic/orthorhombic (AFM/ORTH), superconducting/paramagnetic/tetragonal (SC/PM/T), and non superconducting/paramagnetic/tetragonal (N/PM/T) state.

temperature dependent specific heat for $H = 0$ and $H = 14$ T for the $x = 0.028/\,T_{A/Q} = 400°\mathrm{C}$ sample were subtracted and the $\Delta C_P/\,T_c$ data are consistent with bulk superconductivity (see discussion below). Again neither coexistence of the AFM/ORTH and the superconducting phases nor splitting of T_S and T_N were observed. Both T_c and screening are maximal right after the AFM/ORTH state is completely suppressed and then start to decrease with increasing Co concentration.

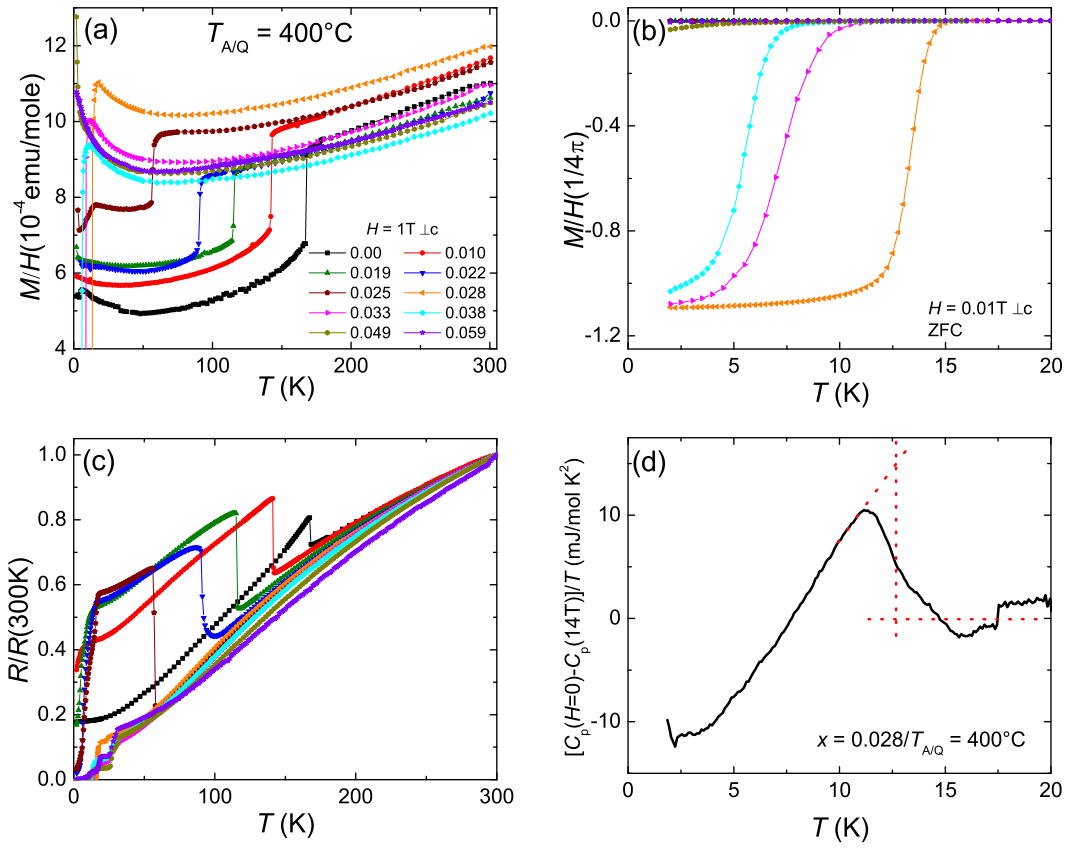

Figure 6.8 Temperature dependent (a) magnetic susceptibility with a field of 1 T applied perpendicular to the c-axis, (b) low field magnetic susceptibility measured upon ZFC with a field of 0.01 T applied perpendicular to the c-axis and (c) normalized electrical resistance of $Ca(Fe_{1-x}Co_x)_2As_2$ samples for an $T_{A/Q}$ of 400°C, together with (d) the specific heat data for the $x = 0.028/\,T_{A/Q} = 400°\mathrm{C}$ sample (see text). Low temperature resistance of superconducting samples are presented in the inset of (c).

Figure 6.10 presents the corresponding data for $T_{A/Q} = 500°\mathrm{C}$. At this $T_{A/Q}$, the AFM/ORTH

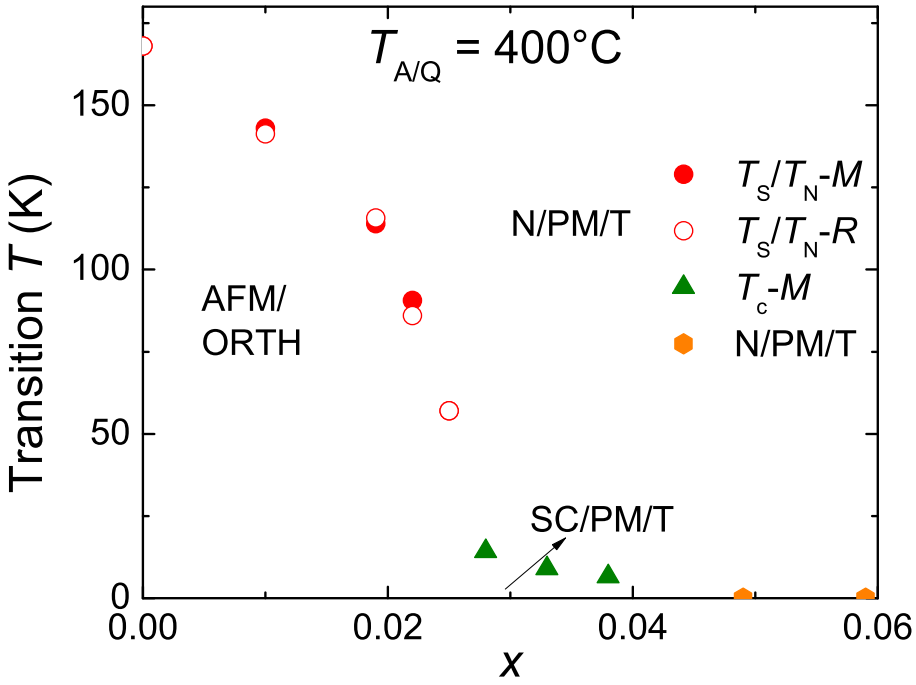

Figure 6.9 Phase diagram of transition temperature, T, versus Co concentration, x, of $Ca(Fe_{1-x}Co_x)_2As_2$ samples for an $T_{A/Q}$ of 400°C. Filled symbols are inferred from magnetization (M) data, open symbols are inferred from resistance (R) data. Three different phases are observed: antiferromagnetic/orthorhombic (AFM/ORTH), superconducting/paramagnetic/tetragonal (SC/PM/T), and non superconducting/paramagnetic/tetragonal (N/PM/T) state.

transition starts with a lower temperature for the pure compound and the switch between the AFM/ORTH and the superconducting phase occurs between $x = 0.019$ and 0.022. Only one sample, $x = 0.022$, shows significant amount of screening with T_c around 9 K.

A dramatic change is seen when the $T_{A/Q}$ is increased to 600°C, as shown in Fig. 6.11. The susceptibility is measured with the magnetic field applied parallel to the c-axis, in which direction the size of the jump in susceptibility for the cT phase transition is significantly larger than that for the AFM/ORTH phase transition, as discussed above, in the Experimental Methods section. Resistance data was also utilized to confirm the nature of the transition since it shows clearly different signature for the two types of phase transition: an upward jump for the AFM/ORTH phase transition and a downward jump or loss of signal for the cT phase transition. With the combination of these criteria, it can be seen clearly that the pure compound is in the AFM/ORTH state at low temperature, whereas the samples with $x > 0.022$ are in the cT phase. None of the sample reaches a low-temperature $R = 0$ state. Figure 6.11c presents the low field susceptibility data. It can be seen, no superconducting signal is observed for sample in either the AFM/ORTH or the cT states.

For $x = 0.010$, two samples were measured. One sample manifests broadened signatures in both susceptibility and resistance that can be associated with the AFM/ORTH phase transition. The other sample shows double transitions with the upper one consistent with the AFM/ORTH transition and the lower one consistent with the transition into the cT phase. It is likely that this sample is a mixture of two types of phases, which is reasonable noting that 600°C seems to be near the AFM/ORTH and cT phase boundary and a small degree of inhomogeneity of the local strain may separate the sample into two phases.

For x =0.019, the susceptibility data do not manifest a clear signature of either type of transition whereas resistance measured on the same piece of sample shows a downward jump with hysteresis of $\sim$ 40K between cooling and warming indicating a transition into the cT phase, as shown in the inset of Fig. 6.11c. Given that susceptibility, as a thermodynamic measurement, tells more about the bulk properties, it is possible that only part of the sample is in a cT state at low temperature.

Figure 6.11d shows the phase diagram for the $T_{A/Q}$ of 600°C reconstructed from these

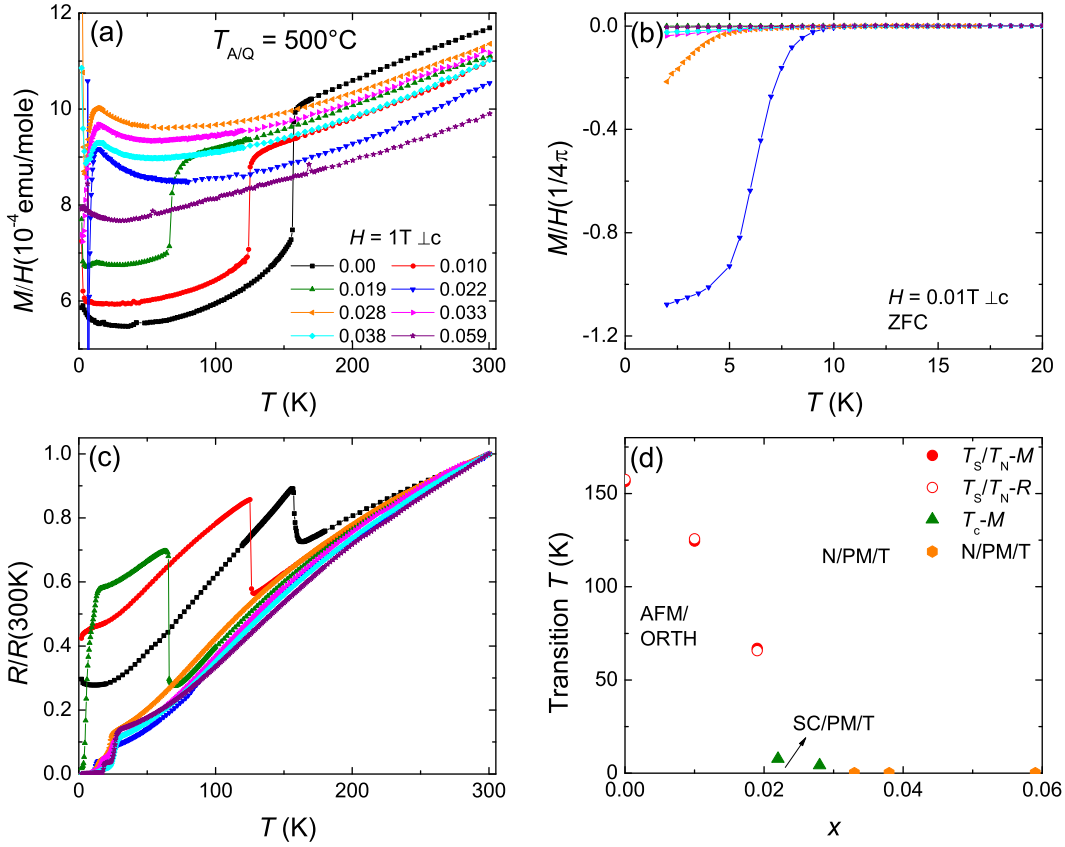

Figure 6.10 Temperature dependent (a) magnetic susceptibility with a field of 1 T applied perpendicular to the c-axis, (b) low field magnetic susceptibility measured upon ZFC with a field of 0.01 T applied perpendicular to the c-axis, (c) normalized electrical resistance and (d) phase diagram of transition temperature, T, versus Co concentration, x, of $Ca(Fe_{1-x}Co_x)_2As_2$ samples for an $T_{A/Q}$ of 500°C. Low temperature resistance of superconducting samples are presented in the inset of (c). Filled symbols are inferred from magnetization (M) data, open symbols are inferred from resistance (R) data. Three different phases are observed: antiferromagnetic/orthorhombic (AFM/ORTH), superconducting/paramagnetic/tetragonal (SC/PM/T), and non superconducting/paramagnetic/tetragonal (N/PM/T) state.

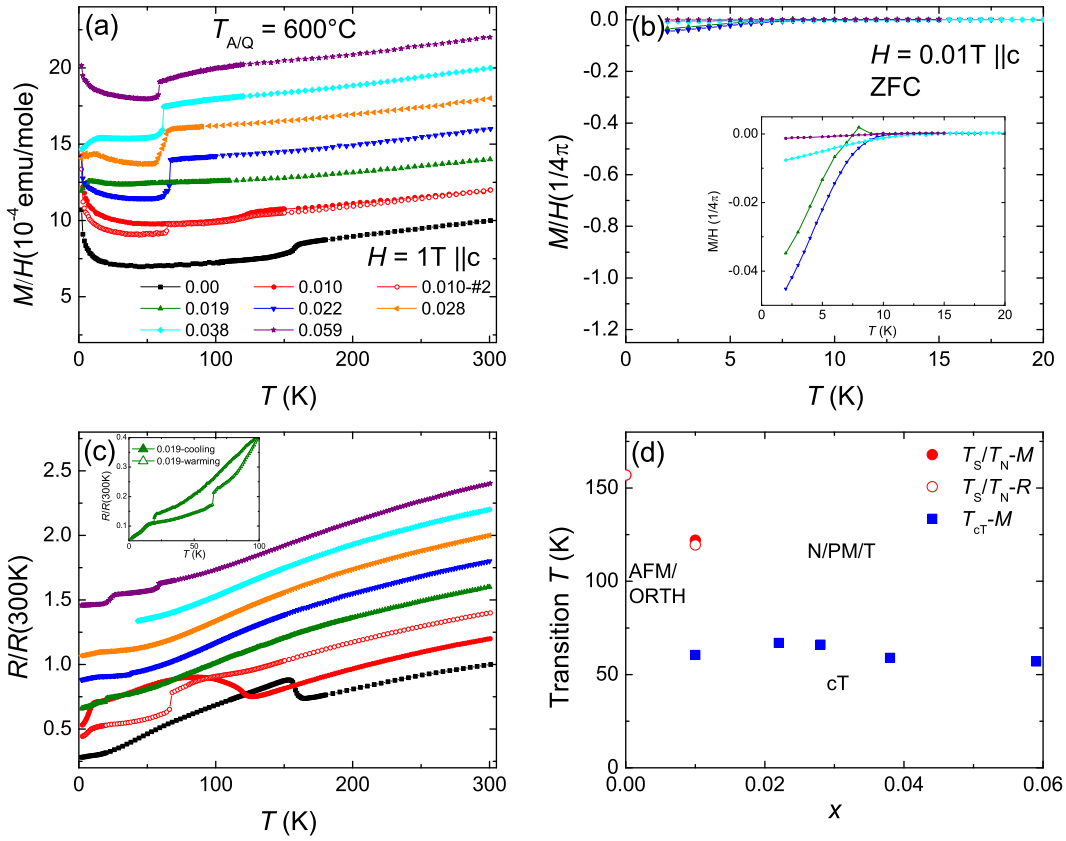

Figure 6.11 Temperature dependent (a) magnetic susceptibility with a field of 1 T applied parallel to the c-axis, (b) low field magnetic susceptibility measured upon ZFC with a field of 0.01 T applied parallel to the c-axis, (c) normalized electrical resistance and (d) phase diagram of transition temperature, T, versus Co concentration, x, of $Ca(Fe_{1-x}Co_x)_2As_2$ samples for an $T_{A/Q}$ of 600°C. The inset of (c) presents the resistance data of 1.9% sample measured upon warming up and cooling down. For clarity, susceptibility data in (a) have been offset by 2×10^{-4} emu/mole from each other and resistance data in (b) have been offset by 0.2 from each other. In figure (d), the filled symbols are inferred from magnetization (M) data, the open symbols are inferred from resistance (R) data. Three different phases are observed: antiferromagnetic/orthorhombic (AFM/ORTH), non superconducting/paramagnetic/tetragonal (N/PM/T) and non-moment bearing/collapsed tetragonal (cT) state.

data. The AFM/ORTH phase transition is suppressed by Co-substitution, but unlike the cases of the lower $T_{A/Q}$, which show a superconducting region when the AFM/ORTH phase is suppressed completely, here the cT phase line truncates the suppression of T_N/T_S and no bulk superconducting phase is observed. It is worth noting that although the transition temperature of the AFM/ORTH phase is suppressed by Co-substitution, the transition temperature of the cT phase stays fairly constant as Co concentration increases.

Figures 6.12a to 6.12c present the magnetic susceptibility and normalized resistance data for the $T_{A/Q}$ of 700°C. Again, the susceptibility is measured with field applied parallel to the c-axis. Both susceptibility and resistance data can be divided into two groups. The signatures in the data from the pure compound clearly show that it's in the AFM/ORTH state at low temperature. On the other hand, all Co-substituted samples show essentially the same signature: very sharp drop in susceptibility and a weak downward jump in resistance which is sometimes accompanied by a loss of contact or continuity due to sample breakage. No significant superconducting fraction is observed, as shown in Fig. 6.12b. Also $R(T)$ data does not show any indication of superconductivity for any substitution level.

Figure 6.12d summaries the phase diagram for this $T_{A/Q}$. Similar to the case of the 600°C annealing/quenching, the AFM/ORTH phase only exist when $T_N/T_S > T_{cT}$. The transition temperature of cT state remains roughly constant as Co concentration increases, but T_{cT} is clearly higher for the 700°C annealed/quenched samples than it is for the 600°C ones, consistent with a continued increase in stress/strain with increasing $T_{A/Q}$.

6.5 T-$T_{A/Q}$ Phase Diagram

So far, the phase diagram data have only been shown as T-x cuts for a fixed $T_{A/Q}$. The same set of data can also be presented as phase diagrams of transition temperature versus $T_{A/Q}$ (T-$T_{A/Q}$ cuts) for each Co substitution level. The T-$T_{A/Q}$ phase diagrams are presented in Fig. 6.13a to 6.13g. For the pure compound, the AFM/ORTH phase line is suppressed with increasing $T_{A/Q}$ and disappears into the cT phase line at around 800°C (Chapter 5). No superconductivity is observed. Substituting Co suppresses the AFM/ORTH phase line. Therefore, for the $x = 0.010$ sample, the AFM/ORTH phase line starts at a lower temperature

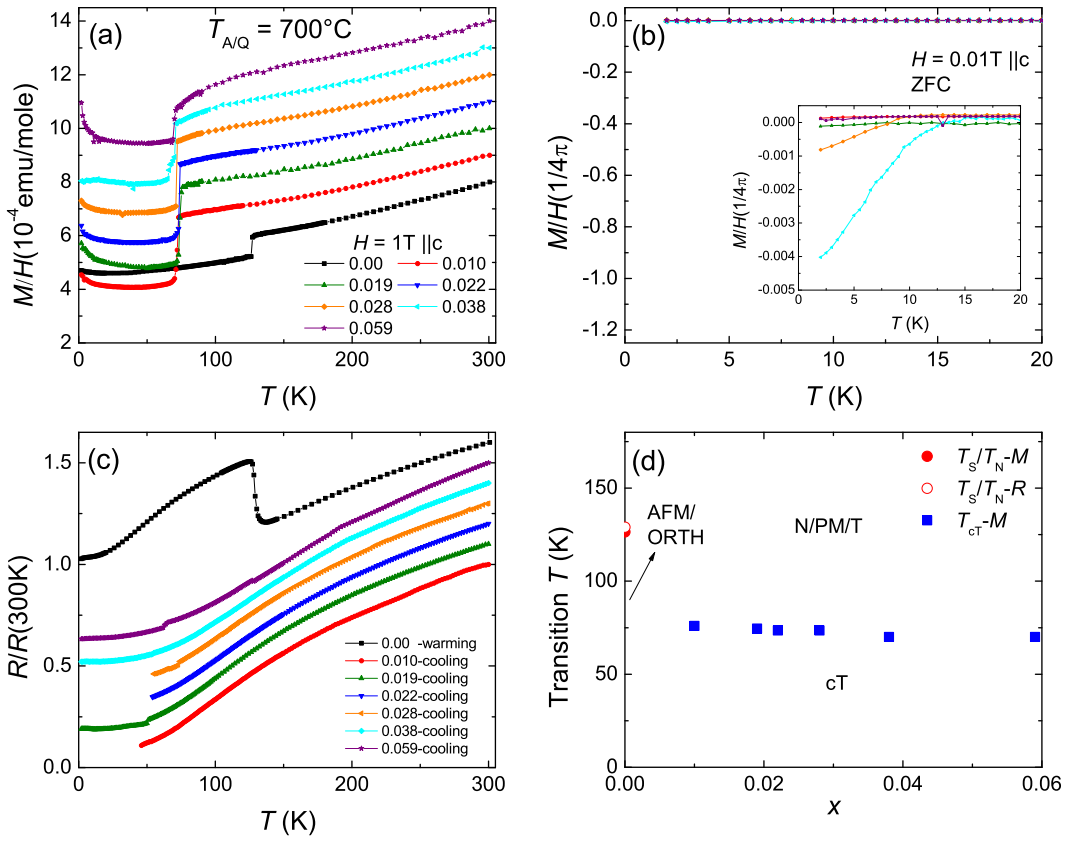

Figure 6.12 Temperature dependent (a) magnetic susceptibility with a field of 1 T applied parallel to the c-axis, (b) low field magnetic susceptibility measured upon ZFC with a field of 0.01 T applied parallel to the c-axis, (c) normalized electrical resistance and (d) phase diagram of transition temperature, T, versus Co concentration, x, of $Ca(Fe_{1-x}Co_x)_2As_2$ samples for an $T_{A/Q}$ of 700°C. For clarity, susceptibility data in (a) have been offset by 1×10^{-4} emu/mole from each other and resistance data in (b) have been offset by 0.1 from each other. In figure (d), the filled symbols are inferred from magnetization (M) data, the open symbols are inferred from resistance (R) data. Three different phases are observed: antiferromagnetic/orthorhombic (AFM/ORTH), non superconducting/paramagnetic/tetragonal (N/PM/T) and non-moment bearing/collapsed tetragonal (cT) state.

and the entire AFM/ORTH phase region shrinks. The cT phase line is further revealed with the AFM/ORTH phase line merging with it at around 600°C, which is a lower $T_{A/Q}$ for the onset of the cT phase than that for the pure compound. For the $x = 0.010$ sample, the two phase lines still intersect/overlap each other and there is no superconductivity. As the Co concentration is increased further, the AFM/ORTH phase line is further suppressed but the cT phase line remains roughly unchanged. There seems to be a minimum of $T_{A/Q}$ (internal strain) required to stabilize the cT phase (roughly $T_{A/Q} = 600$°C). Therefore, as the AFM/ORTH phase line is suppressed further, at $T_{A/Q}$ lower than 600°C, the two phase lines separate. For $x = 0.019$, and even more clearly for $x = 0.022$, the two phase lines no longer intersect each other, leaving an intermediate region where one finds the superconducting/paramagnetic/tetragonal (SC/PM/T) or the non superconducting/paramagnetic/tetragonal (N/PM/T) phase. Further increasing Co concentration, the AFM/ORTH phase line is suppressed more and more, and the space between the AFM/ORTH and the cT phase lines becomes larger and larger. By $x = 0.038$, the AFM/ORTH phase is completely suppressed and the low temperature state is divided into three phases: the SC/PM/T phase, the N/PM/T phase and the cT phase. For $x = 0.059$, no bulk superconductivity remains.

6.6 Discussion

The thermodynamic, transport and diffraction measurements of the the $x = 0.059$, $T_{A/Q} = 960$°C sample suggest that for the $T_{A/Q} = 960$°C $Ca(Fe_{1-x}Co_x)_2As_2$ samples there may be a critical end point beyond which the system has a continuous thermal contraction rather than a first order phase transition. Figure 6.14 presents the width of the transition, which is defined as full width at half maximum of the peak in temperature derivative of magnetic susceptibility. It can be seen that the broadening in transition starts from about $x = 0.022$. The resistance data shown in Fig. 6.3b can be divided into two groups according to whether the resistance bar cracks and loses contact when cooling down. Its clear that the samples with x smaller than 0.028 all lose contacts below the transition temperature indicating these samples undergo first order, structural phase transitions. On the other hand, starting from $x = 0.028$, the resistance bars survive down to the base temperature of 1.8 K although the resistive

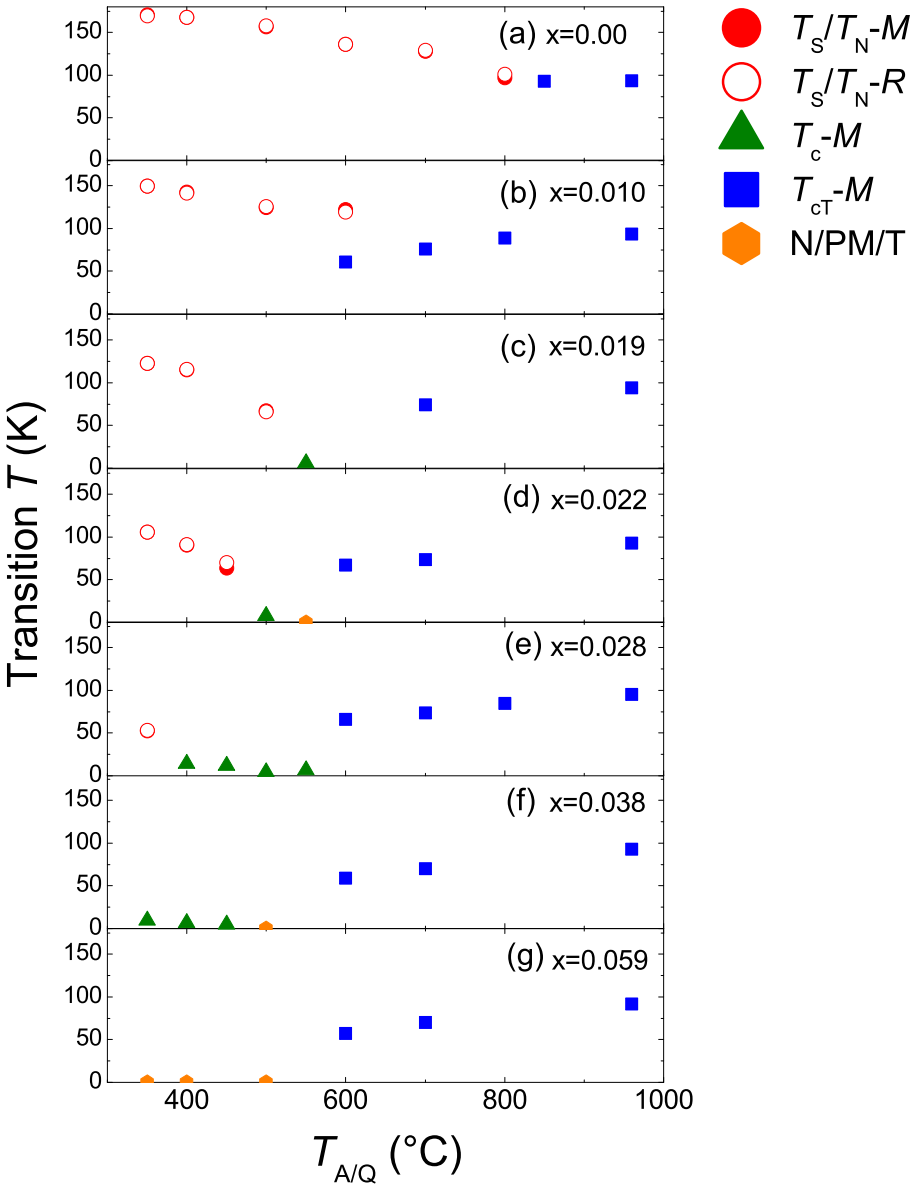

Figure 6.13 Phase diagram of transition temperature, T, versus annealing/quenching temperatue, $T_{A/Q}$, for $Ca(Fe_{1-x}Co_x)_2As_2$ for (a) $x = 0.00$, (b) $x = 0.010$, (c) $x = 0.019$, (d) $x = 0.022$, (e) $x = 0.028$, (d) $x = 0.038$ and (e) $x = 0.059$. Filled symbols are inferred from magnetization (M) data, open symbols are inferred from resistance (R) data. Four different phases are observed: antiferromagnetic/orthorhombic (AFM/ORTH), superconducting/paramagnetic/tetragonal (SC/PM/T), non superconducting/paramagnetic/tetragonal (N/PM/T) and non-moment bearing/collapsed tetragonal (cT) state.

data are not ideally smooth. Again these data are consistent with the magnetic susceptibility measurements shown in Fig. 6.3a. To fully address the question of the existence of a critical end point, detailed study of thermodynamic and microscopic properties will be needed, but, at this point the $T_{A/Q} = 960°C$ $Ca(Fe_{1-x}Co_x)_2As_2$ system appears to be a rare example of such isotructural transition that can be tuned in this manner (the volume collapse in Ce being another such example (Lashley et al., 2006)).

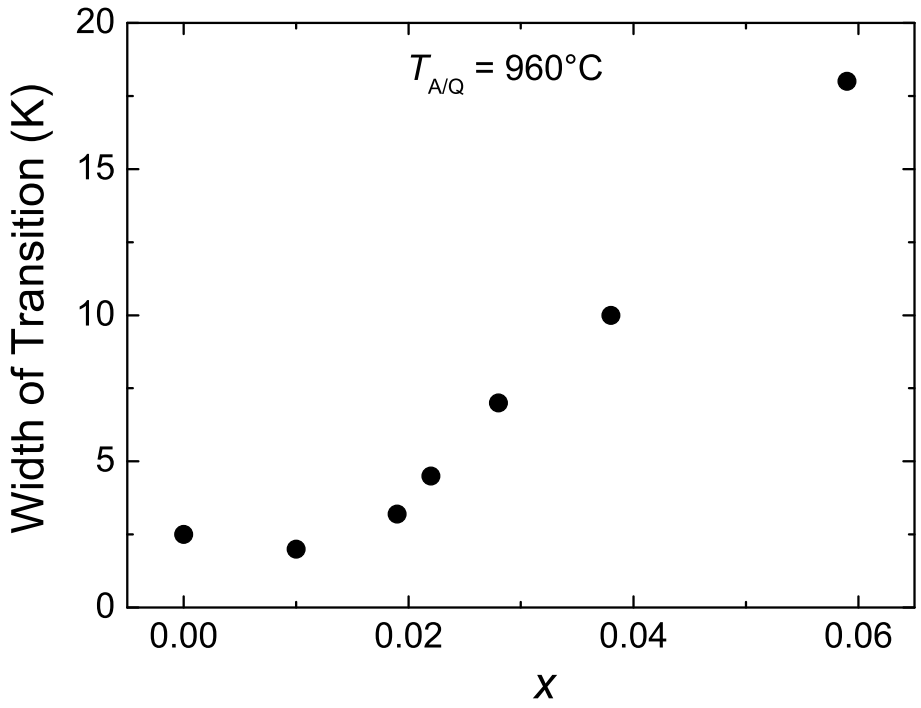

Figure 6.14 Width of transition of $T_{A/Q} = 960°C$ $Ca(Fe_{1-x}Co_x)_2As_2$ samples as a function of measured Co concentration, x.

Filamentray superconductivity is a common problem in the $AEFe_2As_2$ based materials (Saha et al., 2009; Colombier et al., 2009). In $CaFe_2As_2$ compounds great care has to be taken to identify and separate filamentray superconductivity from bulk superconductivity. The resistance data show a small superconductivity like drop at around 25 K in many samples before it reaches zero with further cooling. A magnetic field can been applied to these samples and these steps are suppressed by a field as small as 0.05 T. Figure 6.15 presents the resistance data, in applied magnetic field, for the $x = 0.033/T_{A/Q} = 350°C$ sample, as an example. In a

field of 0.05 T, the drop at higher temperature is suppressed completely whereas the final step towards zero remains sharp and is only slightly shifted to lower temperature. This indicates the final step is a rather robust signature of superconductivity, although the question of why the 25 K feature (whatever its origin is) has such an extreme field dependence is left as an unsolved puzzle for now.

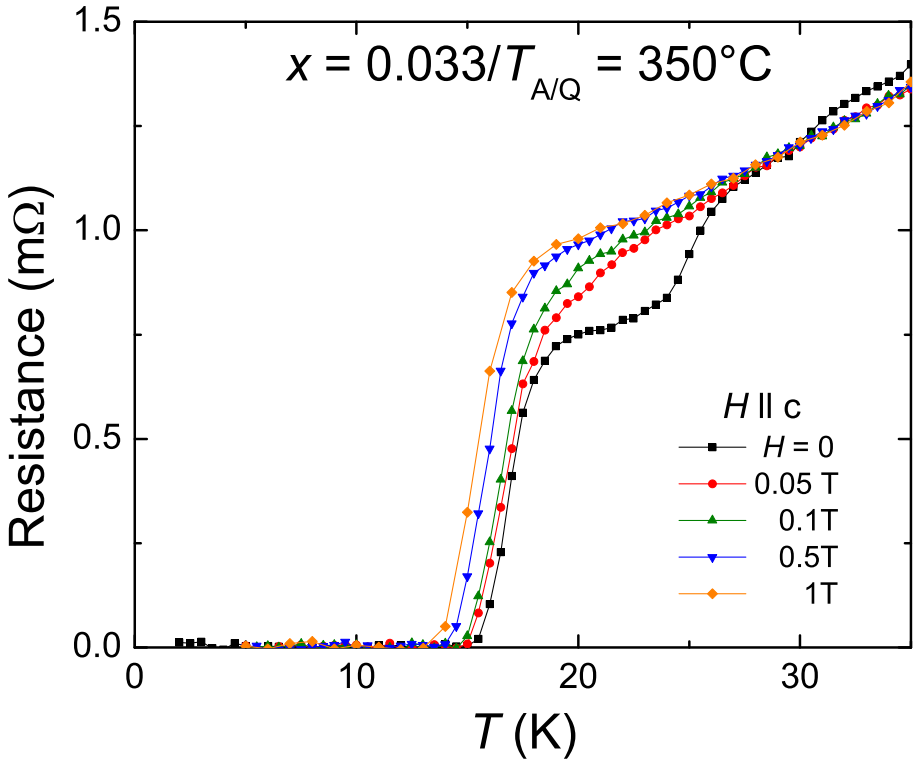

Figure 6.15 Temperature dependent resistance data of the $x = 0.033/T_{A/Q} = 350°C$ sample, measured in zero field and applied field up to 1 T.

In order to confirm bulk superconductivity, thermodynamic measurements are needed. Whereas low field magnetization data can be suggestive, specific heat data is even clearer evidence. Specific heat measurements were made on the representative samples, the $x = 0.033/T_{A/Q} = 350°C$ sample (Fig. 6.6) and the $x = 0.028/T_{A/Q} = 400°C$ sample (Fig. 6.8), both of which are located in close approximity to the suppressed T_N/T_S line and both of which show full diamagnetic fraction in zero field cooling. $\Delta C_P/T_c$ values of 16.1 mJ/mol K^2 and 15.1 mJ/mol K^2 are inferred from the data for the the $x = 0.033$ and the $x = 0.028$ samples,

respectively. These values can be placed in context of other substituted $AEFe_2As_2$ compounds on a plot of $\Delta C_P(T_c)$ (Fig. 6.16) (Bud'ko et al., 2009; Kogan, 2009; Stewart, 2011; Kim et al., 2011). Based on this comparison we can see that the signature of superconductivity found in specific heat data from these samples is comparable to that of $BaFe_2As_2$ with various substitutions and other iron-based superconducting compounds. This is in contrast to the previously reported rare earth substituted $CaFe_2As_2$, in which case no clear evidence of bulk superconductivity is observed (Saha et al., 2012).

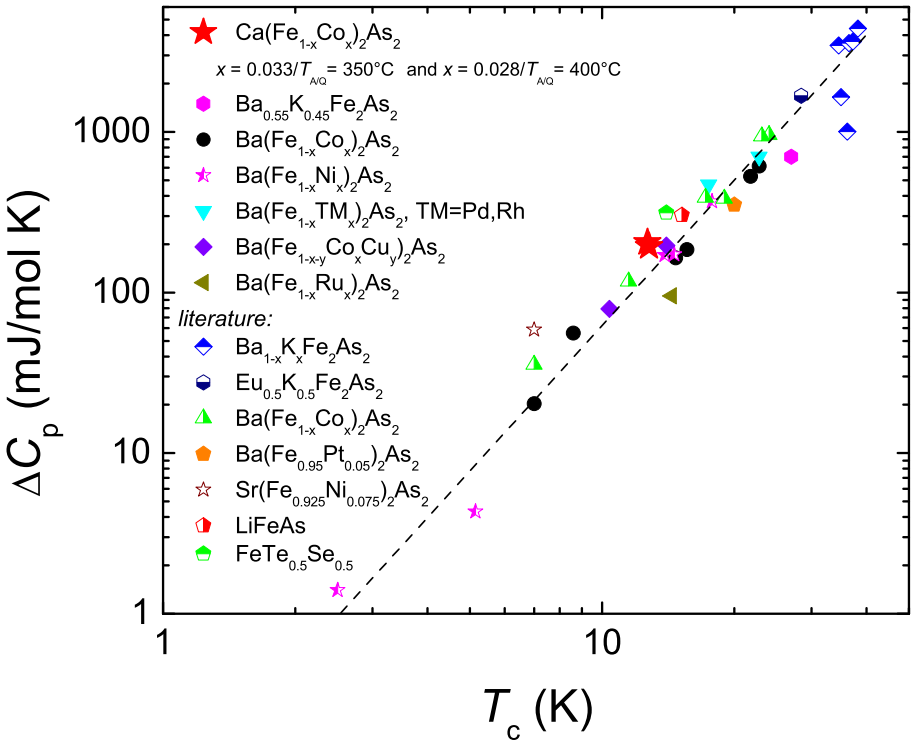

Figure 6.16 ΔC_P vs T_c for the $x = 0.033/T_{A/Q} = 350°C$ sample and the $x = 0.028/T_{A/Q} = 400°C$ sample, plotted together with literature data for various FeAs-based superconducting materials.

To more fully characterize the superconducting state, temperature dependent anisotropic H_{c2} was measured on the $x = 0.028/T_{A/Q} = 400°C$ sample up to 14 T. The $R(T)$ data for various H in the direction parallel to the c-axis are shown in Fig. 6.17a along with an example of the criterion used to infer H_{c2}, offset of the superconducting transition. Figure 6.17b presents the anisotropic H_{c2} plot inferred from the $R(T)$ data and, in the inset, the temperature dependence

of $\gamma = H_{c2}^{\perp c}/H_{c2}^{\parallel c}$. After an initial upward curvature, there is roughly a linear increase of H_{c2} with decreasing temperature. H_{c2} at zero temperature, although is not reached in our measurement, seems to be $\sim$ 20 T. As can be seen in the inset of Fig. 6.17b, the γ has values between 1.5 and 2.0. These values are consistent with those found for K-substituted, Co-substituted and Ni-substituted $BaFe_2As_2$ samples (Altarawneh et al., 2008; Ni et al., 2008c, 2010).

The progression of the T-$T_{A/Q}$ phase diagrams (Fig. 6.13) from the pure compound to the highest substitution level reveals that there is no coexistence of superconductivity with either the AFM/ORTH phase or the cT phase. The absence of the superconductivity in the cT phase region is consistent with the idea that the mechanism of iron-based superconductor depends on magnetic fluctuations (Mazin et al., 2008; Fernandes et al., 2010). Since in the cT phase magnetic moment is quenched completely, there is no spin fluctuation to drive the superconducting phase (Pratt et al., 2009b; Soh et al., 2013; Dhaka et al., 2014; Furukawa et al., 2014).

The absence of superconductivity in the AFM/ORTH phase region can be understood based on the fact that the AFM/ORTH phase transition remains quite first order even when it is suppressed to around 50 K, which is the lowest T_N/T_S we obtained in these studies. The first order nature of the AFM/ORTH phase transition is demonstrated by the sharpness of both the magnetic and resistive signatures of the transition as well as the hysteresis of the transition temperature of about 7 K, e.g. the susceptibility data of the $x = 0.025/\,T_{A/Q} = 400°$C sample are shown in Fig. 6.18. The strongly first order nature of the AFM/ORTH phase transition in $Ca(Fe_{1-x}Co_x)_2As_2$ is in stark contrast to $Ba(Fe_{1-x}Co_x)_2As_2$ which manifest split, second order magnetic and structural phase transitions (Ni et al., 2008c). For small Co substitution levels, in the case of $Ba(Fe_{1-x}Co_x)_2As_2$, a coexisting superconducting state emerges under the suppressed and separated second order phase transitions whereas for $Ca(Fe_{1-x}Co_x)_2As_2$ the superconducting state does not emerge anywhere below the strongly first order, coupled AFM/ORTH transition line. This clear difference is also consistent with magnetic fluctuations being vital for the emergence of the superconducting state.

With $T_{A/Q}$ as another tuning parameter, the phase diagram is essentially extended from two dimensions to three dimensions. We can establish a three dimensional phase diagram

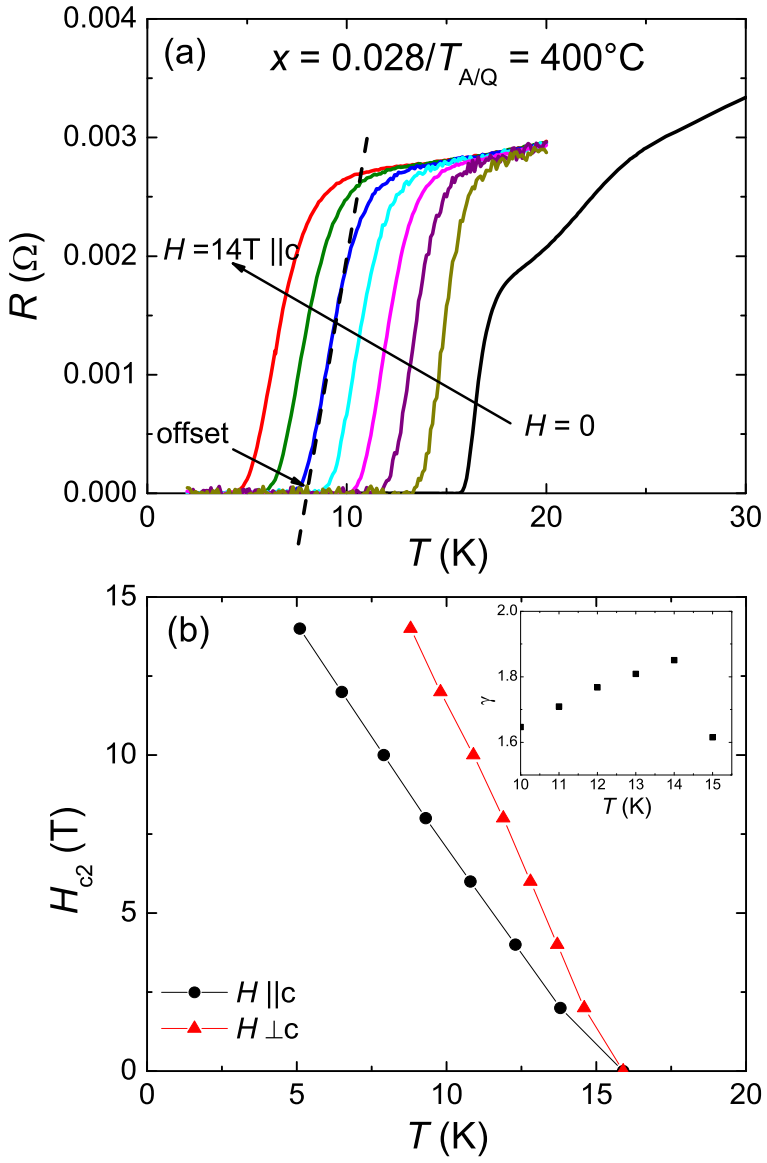

Figure 6.17 Temperature dependent (a) resistance data of the $x = 0.028/T_{A/Q} = 400°C$ sample, measured in applied field parallel to the c-axis for $H = 0$, 2 T, 4 T, 6 T, 8 T, 10 T, 12 T and 14 T and (b) anisotropic H_{c2} data determined from $R(T)$ data. Inset to (b) shows $\gamma = H_{c2}^{\perp c}/H_{c2}^{\parallel c}$ for 10 K $< T <$ 16 K.

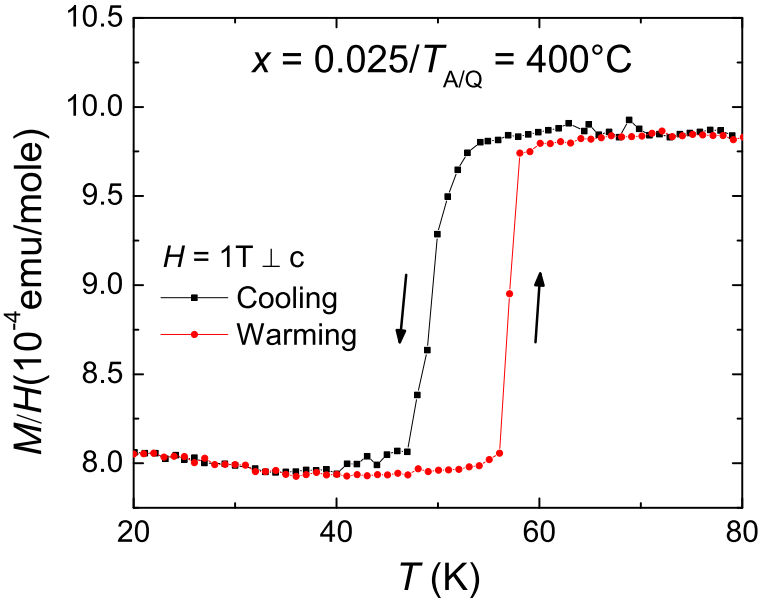

Figure 6.18 Temperature dependent magnetic susceptibility of the $x = 0.025/T_{A/Q} = 400°C$ sample, measured upon warming up and cooling down.

with substitution level, x, annealing/quenching temperature, $T_{A/Q}$, and transition temperature, T, as the three axes, as shown in Fig. 6.19. Whereas the antiferromagnetic/orthorhombic phase is clearly suppressed by increasing x and $T_{A/Q}$, the cT phase, once it emerges, varies with $T_{A/Q}$, but over this limited substitution range, does not vary significantly with x. At lowest temperatures there is no co-existence between any of these phases with superconductivity being truncated at low x and low $T_{A/Q}$ by the AFM/ORTH phase and at high $T_{A/Q}$ by the cT phase. It is clear that at ambient pressure, for modest x and $T_{A/Q}$ values, the $Ca(Fe_{1-x}Co_x)_2As_2$ system offers ready access to the salient low temperature states associated with Fe-based superconductors: antiferromagnetic/orthorhombic (AFM/ORTH), superconducting/paramagnetic/tetragonal (SC/PM/T), non superconducting/paramagnetic/tetragonal (N/PM/T) and non-moment bearing/collapsed tetragonal (cT) state.

The three dimensional T-x-$T_{A/Q}$ phase diagram we find for Co-substitution can be compared to the earlier data measured on Co-substituted samples grown out of Sn (Matusiak et al., 2010; Harnagea et al., 2011; Hu et al., 2012). The low $T_{A/Q}$ ($T_{A/Q} = 350°C$) data is qualitatively similar in that there is a suppression of the AFM/ORTH phase transition and the appearance of

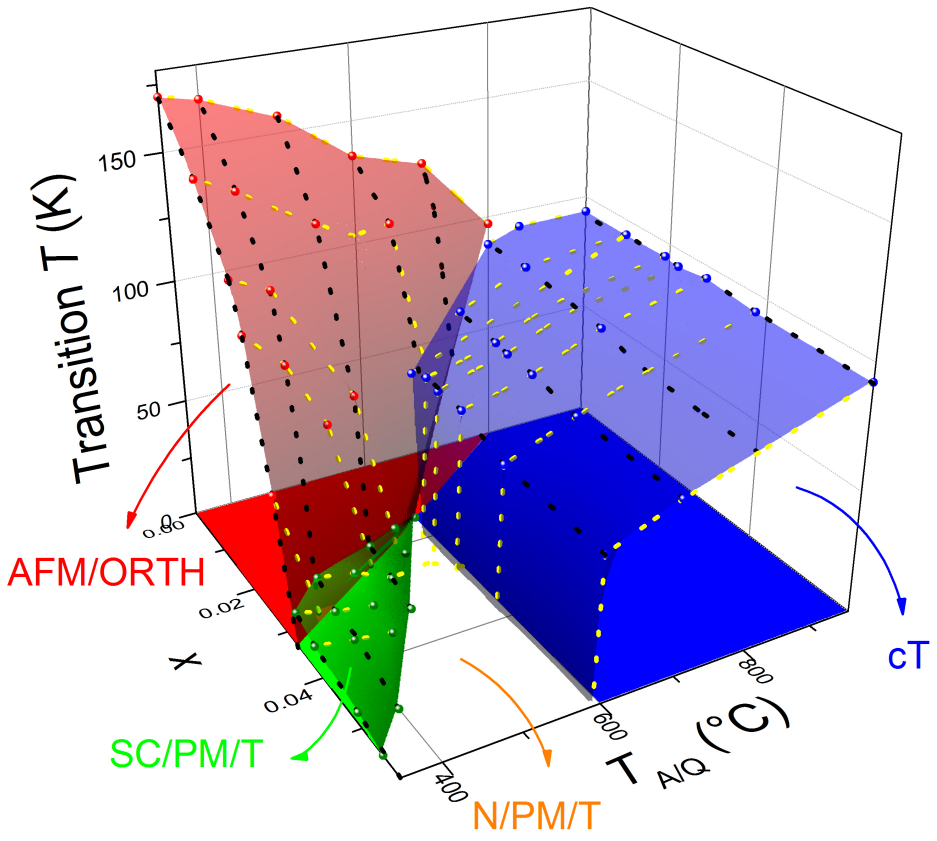

Figure 6.19 Three dimensional phase diagram with substitution level, x, annealing/quenching temperature, $T_{A/Q}$, and transition temperature, T, as three axes. Red (AFM/ORTH), green (SC/PM/T) and blue (CT) spheres represent data. Transparent, colored surfaces are guides to the eyes. Black dashed lines are T-x lines for different $T_{A/Q}$ and yellow dashed lines are T-$T_{A/Q}$ lines for different x. Solid, colored areas on the $T_{A/Q}$-x plane are low temperature ground states. Four different phases are observed: antiferromagnetic/orthorhombic (AFM/ORTH), superconducting/paramagnetic/tetragonal (SC/PM/T), non superconducting/paramagnetic/tetragonal (N/PM/T) and non-moment bearing/collapsed tetragonal (cT) state.

superconductivity. Quantitatively, we find a slightly more rapid suppression of the T_N/T_S line, and a much clearer and systematic evolution of the first order signatures of the AFM/ORTH and the cT phase transitions with substitution and $T_{A/Q}$.

Fianlly, I would like to point out that FeAs-grown $Ca(Fe_{1-x}Co_x)_2As_2$ with controlled annealing/quenching opens up a myriad of opportunities for the further research. We are able to tune the system systematically and reproducibly. Given the similar effects of pressure and $T_{A/Q}$, it is now possible for APRES (Dhaka et al., 2014; Gofryk et al., 2014) and STM (Saparov et al., 2014) to explore what were inaccessible T-P phase diagrams via use of the T-x-$T_{A/Q}$ phase diagram. Furthermore, if we extend the P-$T_{A/Q}$ analogy from our annealing work on the pure compound, then we expect that continuous tuning can be achieved for Co-substituted samples with hydrostatic pressure using He gas medium. For example, the T-$T_{A/Q}$ phase diagram of $x = 0.028$ sample presented in Fig. 6.13e suggests that it might be possible to tuning the system from the AFM/ORTH phase to the superconducting phase and then to the cT phase with applied pressures of less than 0.5 GPa. This is indeed the case as will be presented in the Appendix C. Therefore elastic and inelastic neutron scattering studies on a single sample can be used to systematically study the magnetic order and fluctuations across the whole phase space of FeAs-based superconductivity.

6.7 Summary

I have grown single crystal samples of Co-substituted $CaFe_2As_2$ out of an FeAs-flux and found that the $T_{A/Q} = 960°C$ samples are still in the cT state at low temperature at ambient pressure, similar to the pure compound. I systematically studied effects of $T_{A/Q}$ on the physical properties of these samples. The progression of the T-$T_{A/Q}$ phase diagram with increasing Co concentration shows that by substituting Co, the AFM/ORTH and the cT phase lines are separated and bulk superconductivity is revealed. I established a 3D phase diagram with Co concentration and annealing/quenching temperature as two independent control parameters. At 2 K the superconducting state exists between a low x, low $T_{A/Q}$, AFM/ORTH phase and a high $T_{A/Q}$, cT phase, in a region where magnetic fluctuations can persist to low enough temperatures.

CHAPTER 7. COMBINED EFFECTS OF Ni- AND Rh-SUBSTITUTION AND ANNEALING/QUENCHING ON PHYSICAL PROPERTIES OF $CaFe_2As_2$

7.1 Introduction

In the case of $BaFe_2As_2$ system (Ni et al., 2009; Canfield et al., 2009b; Ni et al., 2010), comparison of the phase diagrams of various transition metal substitutions reveals that while the suppression of the structural/magnetic phase transition scales, roughly, with impurity concentration, x, the superconductivity is rather controlled by extra electron count, e. Steric effect seems not to play any important role in determining the phase diagram, with Co- (Ni-) and Rh- (Pd-) substitution having exceptionally similar effect, especially on the superconducting dome on the overdoped side.

In order to compare the phase diagrams of various transition metal substitutions in $CaFe_2As_2$, we expand the exploration of transition metal substitution to Ni and Rh. Compared with Co-substitution, Ni-substitution brings one more extra electron per substituted atom, while suppressing c-lattice parameter in a very similar manner. On the other hand, Rh-substitution brings nominally the same amount of extra electrons as Co-substitution, although from a 4d-shell rather than a 3d-shell, while suppressing the c-lattice parameter much more rapidly. Therefore, comparing Co-substitution with Ni- and Rh-substitution will potentially help us understand the changes of physical properties of $CaFe_2As_2$ system caused by (i) band filling and (ii) steric effect. As we will show, this is more complicated than in the case of $Ba(Fe_{1-x}T_x)_2As_2$, not only due to the existence of one more control parameter, $T_{A/Q}$, but also because $CaFe_2As_2$ is much more sensitive to the pressure, and therefore to the steric effect.

Due to the fact that two independent control parameters ($T_{A/Q}$ and x) define this phase

space, large amounts of temperature dependent data were collected and used to assemble the various phase diagrams. In the main body of this paper only selected sets of data will be presented and the rest of data will be presented in the Appendix.

This chapter is heavily based the article submitted to *Phys. Rev. B*: Ran, S., Bud'ko, S. L., Straszheim, W. E. and Canfield, P. C. "Combined effects of transition metal (Ni and Rh) substitution and annealing/quenching on physical properties of $CaFe_2As_2$".

7.2 Results and Discussion

7.2.1 Compositional and structural determination

A summary of the WDS measurement data for both Ni- and Rh-substituted compounds is presented in Fig. 7.1. Data for the $Ca(Fe_{1-x}Co_x)_2As_2$ series (Chapter 6) are also presented for comparison. The nominal concentration versus actual concentration data for all three series can be fitted very well with straight lines, indicating a linear correlation between the measured concentration and the nominal concentration for these relatively low ($x < 0.10$) substitution levels. Whereas the slope for $Ca(Fe_{1-x}Co_x)_2As_2$ and $Ca(Fe_{1-x}Ni_x)_2As_2$ are close to 1 (0.96 ± 0.01 and 1.09 ± 0.01 respectively), it is only 0.61 ± 0.01 for $Ca(Fe_{1-x}Rh_x)_2As_2$. The error bars are taken as twice of the standard deviation determined from the 12 WDS measurements on each sample, and are no more than 0.003, demonstrating relative homogeneity of the substituted samples studied here. In the following, the average experimentally determined x values, $x = x_{WDS}$, will be used to identify all the compounds rather than the nominal concentration, $x_{nominal}$.

Figure 7.2 presents the c-lattice parameters for the $T_{A/Q} = 960°C$ samples, as well as for the $T_{A/Q} = 400°C$ samples, for both $Ca(Fe_{1-x}Ni_x)_2As_2$ and $Ca(Fe_{1-x}Rh_x)_2As_2$ series, determined via diffraction from the platelike samples using (002) and (008) peaks. Data for the $Ca(Fe_{1-x}Co_x)_2As_2$ series obtained in a similar way are also presented for comparison. It can be seen that in case of both the $T_{A/Q} = 960°C$ samples and the $T_{A/Q} = 400°C$ samples the c-lattice parameter is suppressed by all three transition metal substitutions. Whereas Ni-substitution suppresses the c-lattice parameter at roughly the same rate as Co-substitution,

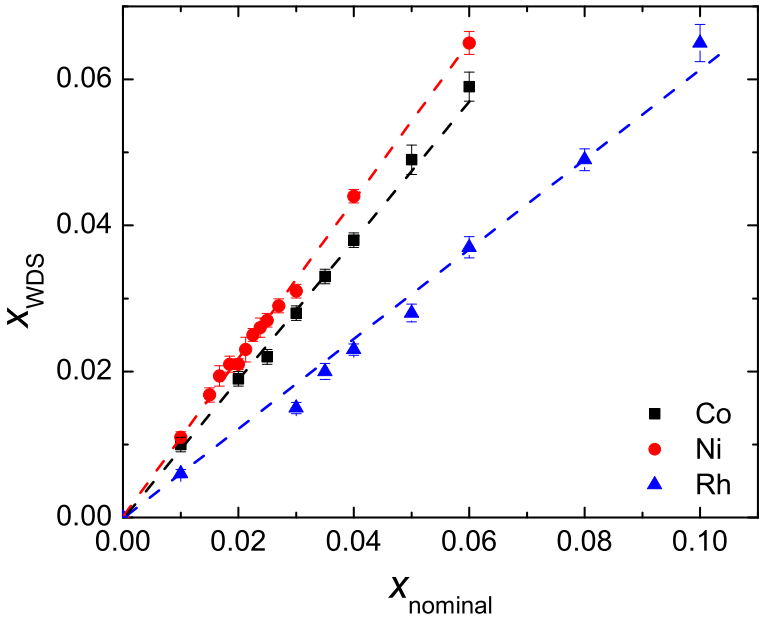

Figure 7.1 Measured Co, Ni and Rh concentration vs nominal Co, Ni and Rh concentration for the $Ca(Fe_{1-x}T_x)_2As_2$ series.

Rh-substitution suppresses the c-lattice parameter roughly twice as fast. The apparent break in slope starting from $x = 0.037$ for Rh-substitution is probably due the underestimated error bar. The suppression of the lattice similar to what has been seen for $BaFe_2As_2$ (Ni et al., 2009; Canfield et al., 2009b; Ni et al., 2010). However, in $BaFe_2As_2$ this difference in the suppression of the c-lattice parameter does not seem to matter much in terms of its effect on the T-x phase diagrams, i.e., Co- and Rh-substitutions being virtually identical but differing from Ni- and Pd-substitutions (each with an extra conduction electron). Considering that the physical properties of $CaFe_2As_2$ are much more sensitive to the stress and strain than are those of $BaFe_2As_2$, the large suppression of the lattice parameter in $Ca(Fe_{1-x}Rh_x)_2As_2$ series may have a much more dramatic effect than in the case of $Ba(Fe_{1-x}Rh_x)_2As_2$.

7.2.2 $Ca(Fe_{1-x}Ni_x)_2As_2$

Figure 7.3 presents the temperature dependent magnetic susceptibility and resistance data from $Ca(Fe_{1-x}Ni_x)_2As_2$ samples with $T_{A/Q} = 400°C$. The $x = 0$, parent compound, shows

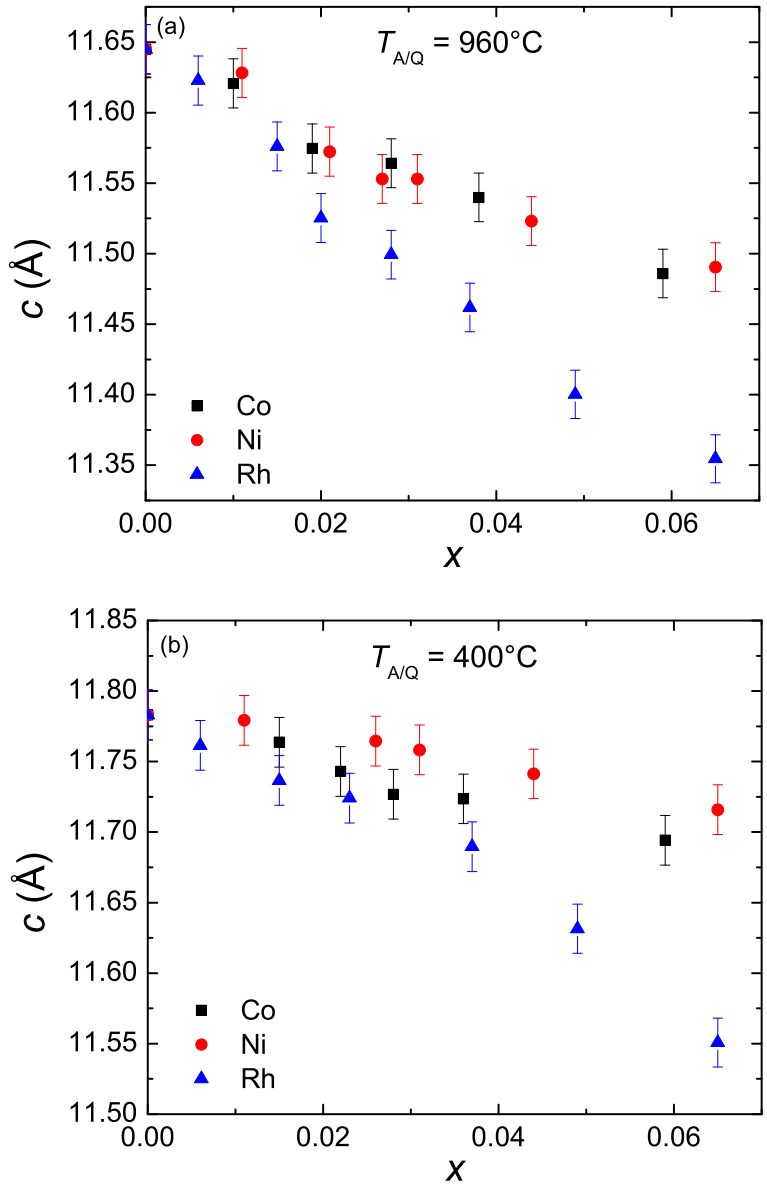

Figure 7.2 Room temperature c-lattice parameter of Ni- and Rh-substituted $CaFe_2As_2$, determined via diffraction from plate like samples, as described in the Experimental Methods section, as a function of measured Ni/Rh concentration, x for (a) $T_{A/Q} = 960°C$ samples and (b) $T_{A/Q} = 400°C$ samples. For comparison, data of $Ca(Fe_{1-x}Co_x)_2As_2$ samples are also presented.

AFM/ORTH phase transition at around 166 K as indicated by the sharp drop in susceptibility and upward jump in resistance upon cooling. The anomalies in both susceptibility and resistance are suppressed with increasing Ni substitution level, down to 55 K, at $x = 0.023$. For higher Ni concentrations, the AFM/ORTH phase transition is suppressed completely and the SC/PM/T phase is stabilized. At $x = 0.025$, low field susceptibility shows that the screening is around 60% of $1/4\pi$ at 2 K as shown in Fig. 7.3b. At $x = 0.027$, the screening increases to 100% of $1/4\pi$. Above $x = 0.027$, increasing Ni concentration suppresses T_c and the screening. For $x \geq 0.031$, the screening is suppressed to zero and the system is in a N/PM/T ground state which is neither of antiferromagnetic, superconducting or cT phase.

Based on these thermodynamic and transport measurements, we can construct a phase diagram of transition temperature versus Ni concentration for this $T_{A/Q}$ (Fig. 7.3d). The AFM/ORTH phase transition is suppressed with initial Ni-substitution and the phase line terminates at around $x = 0.025$, where the SC/PM/T phase emerges. T_c is suppressed by further increasing Ni concentration. Bulk superconductivity, as indicated by low field susceptibility, is suppressed completely for $x \geq 0.031$. No clear evidence of the coexistence of the AFM/ORTH and the SC/PM/T phases is observed and no splitting of the signature of the magnetic and structure phase transition is observed.

In a similar manner, we constructed T-x phase diagrams for other $T_{A/Q}$ values as presented in Fig. 7.4a and b (see Appendix for corresponding magnetic susceptibility and resistance data). $T_{A/Q} = 500°C$ leads to similar phase diagram, but, both the AFM/ORTH and the SC/PM/T phase regions are reduced. This is consistent with the fact that increasing $T_{A/Q}$ has the same effect as increasing pressure as shown for pure and Co-substituted compounds in Chapter 6. For $T_{A/Q} = 960°C$, $CaFe_2As_2$ transforms into a cT state at low temperature. As x is increased in the $Ca(Fe_{1-x}Ni_x)_2As_2$ series the transition temperature of this cT phase is gradually suppressed. This is in contrast to the $Ca(Fe_{1-x}Co_x)_2As_2$ series, where this phase transition occurs at roughly the same temperature throughout the whole substitution level in our study range. Around $x = 0.043$, the signature of transition is broadened and, as discussed in the experimental section, the large error bar is meant to represent this.

In order to systematically study the effect of the varying $T_{A/Q}$ for a given Ni substitution

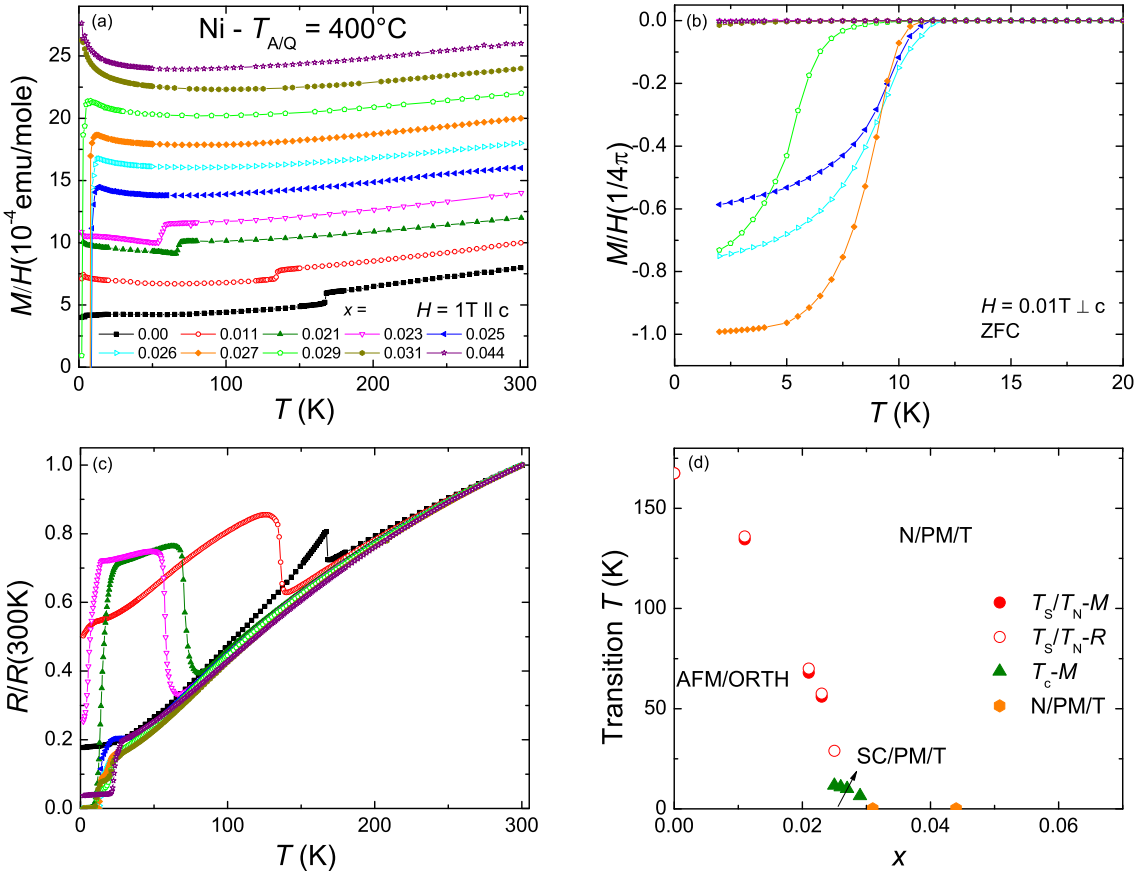

Figure 7.3 Temperature dependent (a) magnetic susceptibility with field applied parallel to the c axis, (b) low-field magnetic susceptibility measured upon zero field cooling (ZFC) with a field of 0.01 T applied perpendicular to the c axis, (c) normalized electrical resistance, and (d) phase diagram of transition temperature T vs Ni concentration x of $Ca(Fe_{1-x}Ni_x)_2As_2$ samples with $T_{A/Q}$ = 400°C. Susceptibility data in (a) have been offset from each other by an integer multiple of 1×10^{-4} emu/mole for clarity.

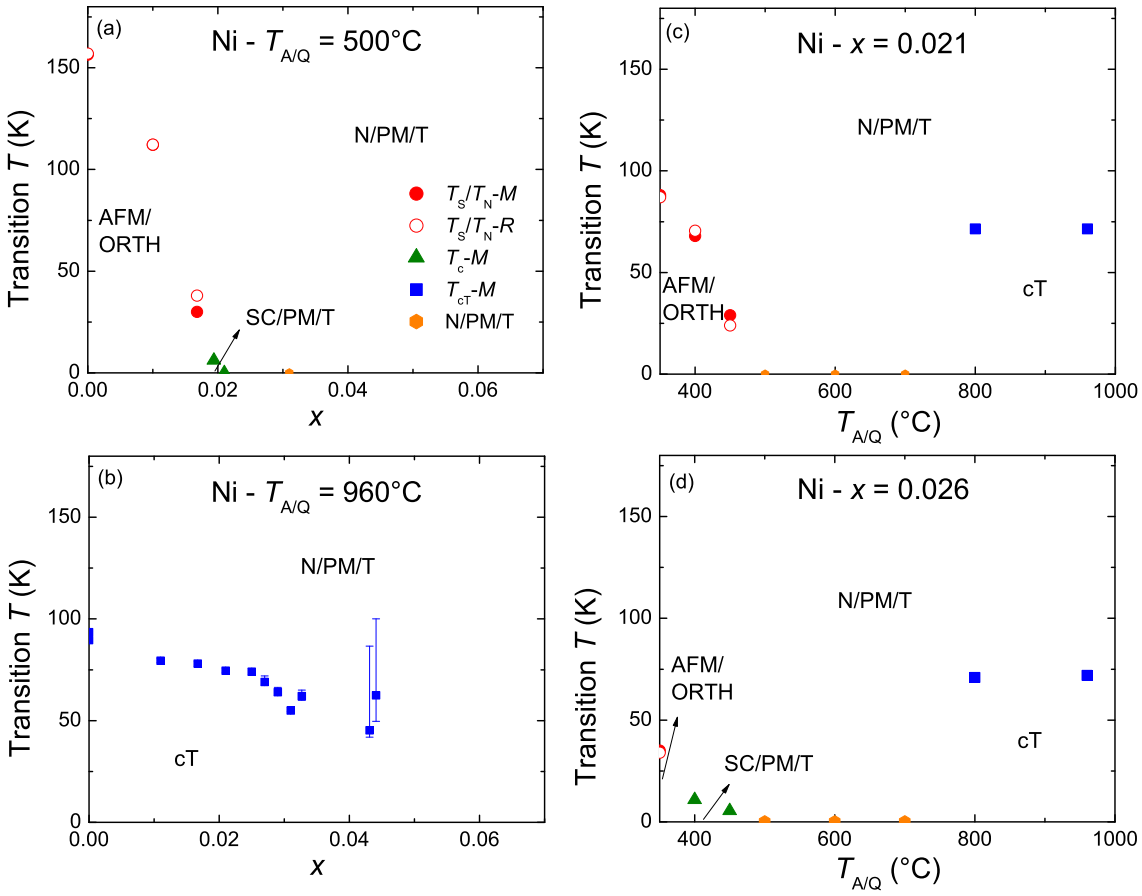

Figure 7.4 phase diagram of (a) transition temperature T vs Ni concentration x of $Ca(Fe_{1-x}Ni_x)_2As_2$ samples with $T_{A/Q} = 500°C$, (b) transition temperature T vs Ni concentration x of $Ca(Fe_{1-x}Ni_x)_2As_2$ samples with $T_{A/Q} = 960°C$, (c) transition temperature T vs annealing/quenching temperature $T_{A/Q}$ of $Ca(Fe_{1-x}Ni_x)_2As_2$ samples with Ni concentration $x = 0.021$, and (d) transition temperature T vs annealing/quenching temperature $T_{A/Q}$ of $Ca(Fe_{1-x}Ni_x)_2As_2$ samples with Ni concentration $x = 0.026$.

level, we studied $x = 0.021$ and $x = 0.026$ samples for 350°C $\leq T_{A/Q} \leq$ 960°C. The corresponding phase diagrams are presented in Fig. 7.4c and d. For both $x = 0.021$ and $x = 0.026$, the ground state of the $Ca(Fe_{1-x}Ni_x)_2As_2$ series is AFM/ORTH phase for low $T_{A/Q}$ ($\leq$ 450°C for $x =$ 0.021 and $\leq$ 350°C for $x = 0.026$) and cT phase for high $T_{A/Q}$ ($\geq$ 800°C). For intermediate values of $T_{A/Q}$, no bulk superconductivity (i.e., with significant screening) is observed for $x =$ 0.021, whereas for $x = 0.026$, bulk superconductivity with screening of more than 70% of $1/4\pi$ at 2 K is observed for $T_{A/Q} = 400$°C.

Since in this work we mainly focus on mapping out the relationship between possible low temperature states for various combinations of substitution level and annealing/quenching temperature, we can construct a 2D phase diagram, with transition metal concentration x and annealing/quenching temperature $T_{A/Q}$ as two independent variables, and mark the ground state with different symbols. This phase diagram is essentially a projection of the 3D phase diagram (Chapter 6) onto the plane of base temperature. Based on the magnetic susceptibility and resistance data, we assembled a 2D phase diagram for Ni-substitution and compare it with that of Co-substitution, as shown in Fig. 7.5.

As seen for the $Ca(Fe_{1-x}Co_x)_2As_2$ system, the $Ca(Fe_{1-x}Ni_x)_2As_2$ system also possesses the same salient low temperature states associated with Fe-based superconductors: AFM/ORTH, SC/PM/T, N/PM/T and cT. The AFM/ORTH region found for both Ni- and Co-substitution span essentially the same parameter space, whereas the SC/PM/T region for Ni-substitution is significantly reduced compared with Co-substitution, with maximum x value that supports SC/PM/T being much smaller than that for Co-substitution (for $T_{A/Q} = 350°$, the critical substitution level is roughly 3.5% for Ni and 5.5% for Co). This is consistent with what was found for Co- and Ni-substituted $BaFe_2As_2$ (Ni et al., 2009; Canfield et al., 2009b; Ni et al., 2010), where antiferromagnetism seems to be primarily controlled by the impurity concentration x whereas superconductivity was more strongly influenced by extra electron count, e. In addition, the cT phase region for Ni-substituted $CaFe_2As_2$ is also reduced. The cT phase is only stabilized for $T_{A/Q} \geq$ 800°C as opposed to $T_{A/Q} \geq$ 500°C for Co-substitution.

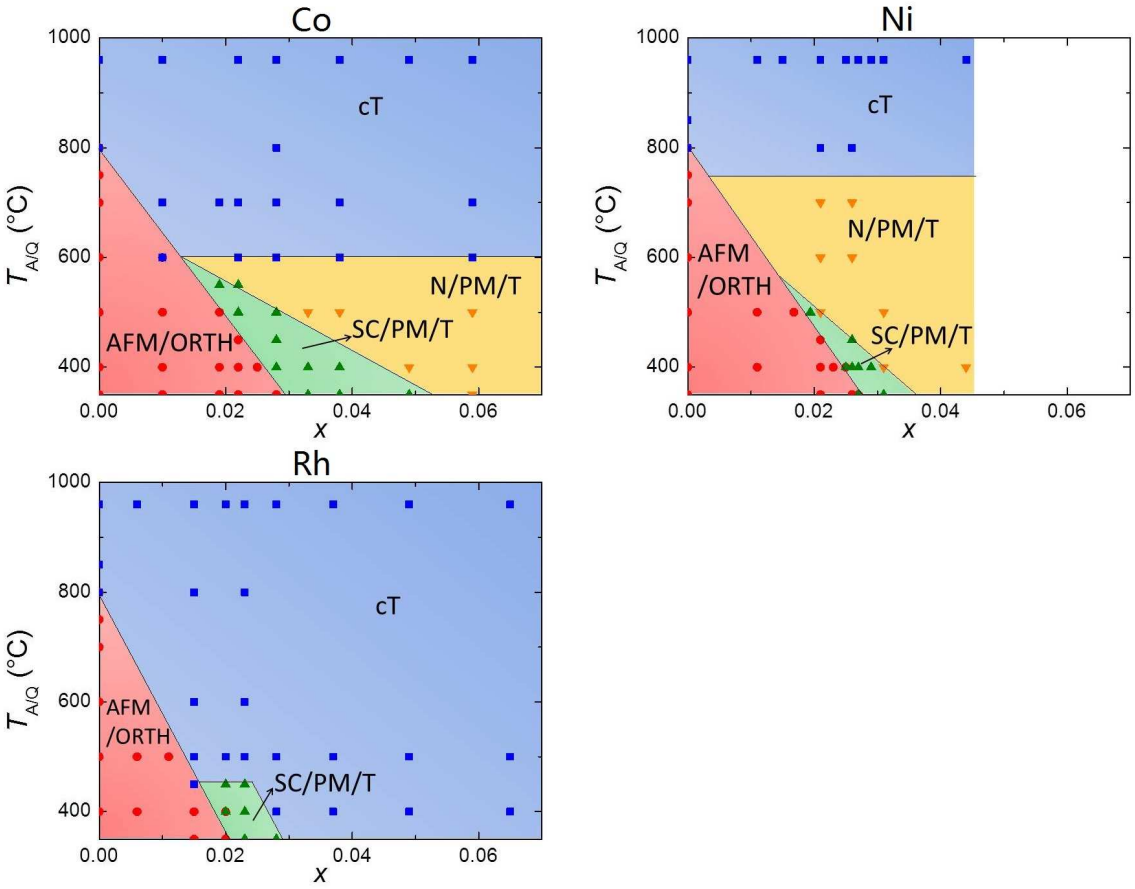

Figure 7.5 2D phase diagrams, with transition metal concentration x and annealing/quenching temperature $T_{A/Q}$ as two independent variables, for (a) $Ca(Fe_{1-x}Co_x)_2As_2$, (b) $Ca(Fe_{1-x}Ni_x)_2As_2$, and (c) $Ca(Fe_{1-x}Rh_x)_2As_2$. The red area delineates the conditions that lead to AFM/ORTH phase as ground state. The green area delineates the conditions that lead to SC/PM/T phase as ground state. The yellow area delineates the conditions that lead to N/PM/T phase as ground state. The blue area delineates the conditions that lead to cT phase as ground state.

7.2.3 $Ca(Fe_{1-x}Rh_x)_2As_2$

Rh-substitution brings the same nominal amount of extra electrons as Co-substitution does (despite the generic difference between 3d-shell and 4d-shell electrons). On the other hand, Rh-substitution brings a much more rapid change in the c lattice parameter. In the case of $Ba(Fe_{1-x}Rh_x)_2As_2$, Rh-substitution leads to a virtually identical T-x phase diagram as found for $Ba(Fe_{1-x}Co_x)_2As_2$. Given that $CaFe_2As_2$ is much more sensitive to the pressure and strain than $BaFe_2As_2$, different steric effects may well lead to differences in the $T_{A/Q}$-x phase diagrams in the case $Ca(Fe_{1-x}Co_x)_2As_2$ of $Ca(Fe_{1-x}Rh_x)_2As_2$.

Figures 7.6a to c present the magnetization and resistance data for $Ca(Fe_{1-x}Rh_x)_2As_2$ compounds with $T_{A/Q} = 400°$. Rh-substitution initially suppresses the AFM/ORTH transition to below 50 K by $x = 0.02$. Bulk superconductivity is observed in a small region of x value, as shown by screening in low field susceptibility (7.6b). Unlike the cases of Co- or Ni-substitution, both of which which have a region of $T_{A/Q}$-x values that lead to a N/PM/T ground state without bulk superconductivity (7.5a and b), Rh-substitution stabilizes the cT state much more rapidly, precluding any N/PM/T phase and abruptly terminating its SC/PM/T region in a manner similar to what is seen for application of hydrostatic pressure to superconducting samples of $Ca(Fe_{1-x}Co_x)_2As_2$ (chapter 7). Given that previous work showed that both cT and AFM/ORTH phases are much more sensitive to changes in the c-axis than to changes in the ab-axis (Bud'ko et al., 2013), this can be understood based on the fact that Rh-substitution suppresses c-lattice parameter more rapidly than either Co- or Ni-substitution. The cT phase line starts near 70 K at $x = 0.028$ and reaches 140 K at $x = 0.065$, where the transition becomes broadened as also seen for the $T_{A/Q} = 960°$C, high substitution levels. The three low temperature states can be seen in the phase diagram presented in Fig. 7.6d. Note that at $x = 0.02$, low field magnetic susceptibility shows superconducting signal with screening of more than 60% of $1/4\pi$, whereas resistance data (which was taken on the same piece of sample) shows upward turning upon cooling indicating AFM/ORTH transition. Given that $x = 0.02$ is at the phase boundary, it is very likely that part of the sample transforms into SC/PM/T phase and the other part of the sample transforms into AFM/ORTH phase. The

other possibility is the coexistence of superconductivity and antiferromagnetism. This scenario is unlikely based on our observations in $Ca(Fe_{1-x}Co_x)_2As_2$ (Chapter 6 and Appendix C). The AFM/ORTH phase transition in this compound remains quite first order even though it is suppressed to around 50 K, similar to what is seen for $Ca(Fe_{1-x}Co_x)_2As_2$. Therefore, there may not be enough magnetic fluctuations, which are vital for the emergence of the unconventional superconductivity in the iron pnictides according to the current theories (Mazin et al., 2008; Fernandes et al., 2010).

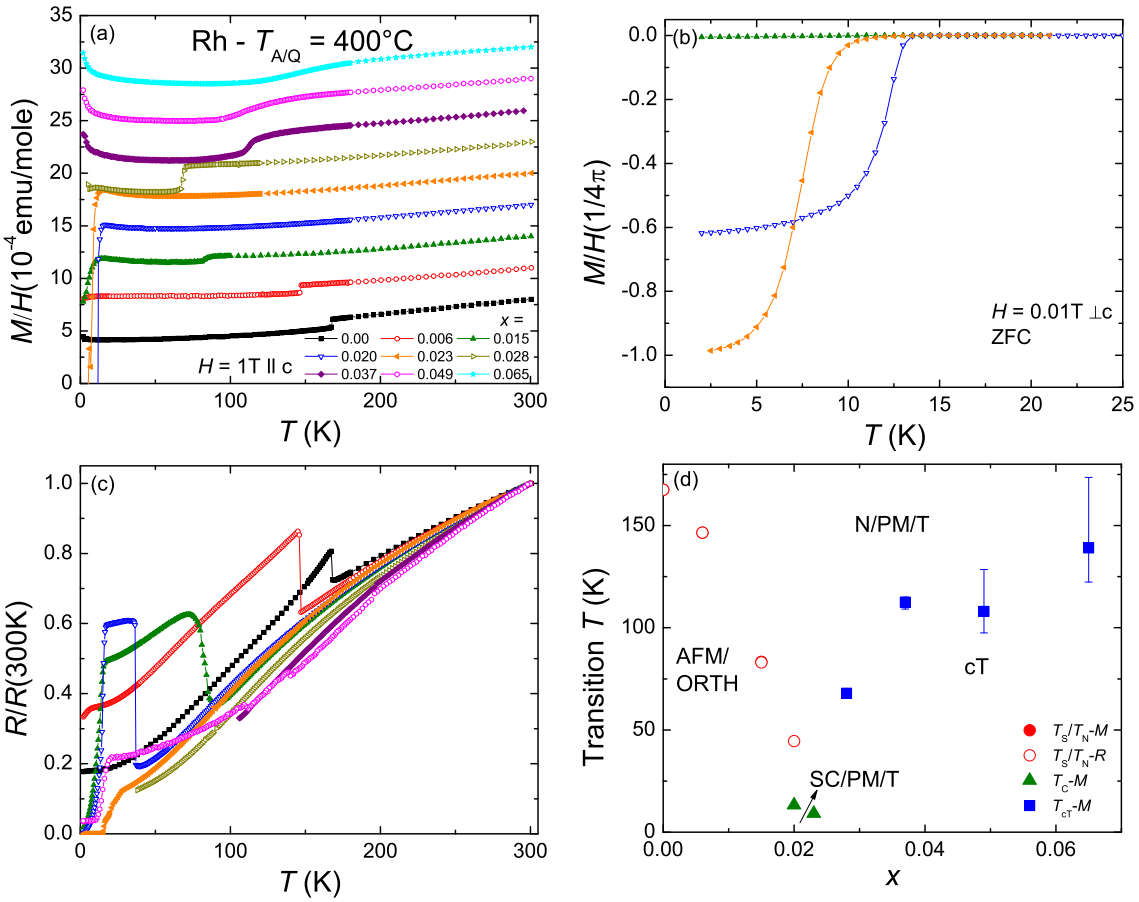

Figure 7.6 Temperature dependent (a) magnetic susceptibility with field applied parallel to the c axis, (b) low-field magnetic susceptibility measured upon ZFC with a field of 0.01 T applied perpendicular to the c axis, (c) normalized electrical resistance, and (d) phase diagram of transition temperature T vs Rh concentration x of $Ca(Fe_{1-x}Rh_x)_2As_2$ samples with $T_{A/Q}$ = 400°C. Susceptibility data in (a) have been offset from each other by an integer multiple of 3×10^{-4} emu/mole for clarity.

Figure 7.7 presents T-x phase diagrams for different annealing/quenching temperatures and T-$T_{A/Q}$ phase diagrams for different Rh concentrations. Similar to what we did for Ni-substitution, we assembled these data and constructed a 2D phase diagram for the base-temperature states of the $Ca(Fe_{1-x}Rh_x)_2As_2$ system, as presented in Fig. 7.5. The $T_{A/Q}$-x, 2D phase diagram of Rh-substitution is significantly different from that of Co-substitution. This is in contrast to the case of $Ba(Fe_{1-x}T_x)_2As_2$, where the phase diagrams for Co- and Rh-substitutions are almost identical (Ni et al., 2009; Canfield et al., 2009b; Ni et al., 2010; Canfield and Bud'ko, 2010). In the case of $Ca(Fe_{1-x}Rh_x)_2As_2$ the AFM/ORTH phase is suppressed faster than it is for Co-substitution and the cT phase is much more pervasive in case of Rh-substitution, appearing for all annealing/quenching temperatures for substitutions level above 3%. Both of these changes can be understood based on the fact that Rh-substitution suppresses the c-lattice parameter more rapidly than Co (or Ni) substitution. A consequence of the enhanced stabilization of the cT phase for low $T_{A/Q}$ values is (i) the complete absence on the N/PM/T phase and (ii) the SC/PM/T region for Rh-substitution is substantially shrunk, or truncated, compared with that for Co-substitution. Given that (i) current theories and experiments indicate that the spin fluctuations play an important role for the appearance of unconventional superconductivity in the iron pnictides; and (ii) spin fluctuations are completely suppressed in the cT phase in $CaFe_2As_2$ (Yildirim, 2009; Pratt et al., 2009b; Soh et al., 2013; Dhaka et al., 2014; Furukawa et al., 2014), it is likely that the superconductivity is limited by the pervasive cT phase in the $Ca(Fe_{1-x}Rh_x)_2As_2$ system.

7.2.4 Critical *c*-lattice parameter

The cT phase transition is driven by an increasing overlap of interlayer As orbitals (Yildirim, 2009). While it was suggested that As-As interlayer separation appears to be the key parameter controlling the volume collapse when comparing members of the $ThCr_2Si_2$ structure (Saha et al., 2012; Hoffmann and Zheng, 1985), it is conceivable that, for substitutions to $CaFe_2As_2$, there might also be a critical room temperature c-lattice parameter value. Given that As-As interlayer separation is hard to measure, a critical room temperature c-lattice parameter value can give an easy evaluation of whether the system will transform into the cT phase or not.

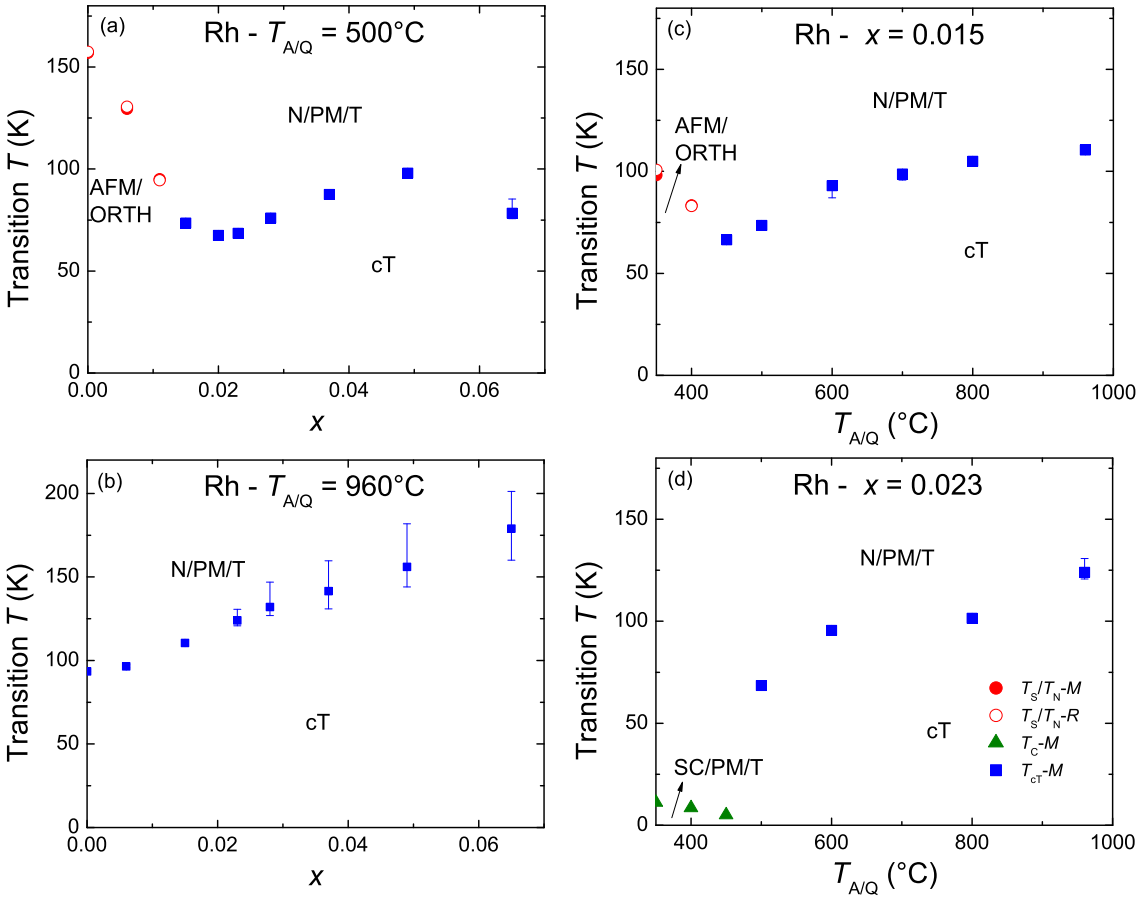

Figure 7.7 phase diagram of (a) transition temperature T vs Rh concentration x of $Ca(Fe_{1-x}Rh_x)_2As_2$ samples with $T_{A/Q}$ = 500°C, (b) transition temperature T vs Rh concentration x of $Ca(Fe_{1-x}Rh_x)_2As_2$ samples with $T_{A/Q}$ = 960°C, (c) transition temperature T vs annealing/quenching temperature $T_{A/Q}$ of $Ca(Fe_{1-x}Rh_x)_2As_2$ samples with Rh concentration $x = 0.015$, and (d) transition temperature T vs annealing/quenching temperature $T_{A/Q}$ of $Ca(Fe_{1-x}Rh_x)_2As_2$ samples with Rh concentration $x = 0.023$.

In order to assess the extent to which such a critical value can be inferred, we plotted the c-lattice parameter versus substitution level, x, for all three substitutions with various $T_{A/Q}$, as shown in Fig. 7.8. Rare earth substitution data from literature (Saha et al., 2012), as well as data for Sn-grown, $x = 0$ $CaFe_2As_2$ under pressure (Kreyssig et al., 2008), are also presented for comparison. It can be seen that the room temperature c-lattice parameter can be divided into three regions: (i) below 11.64 $\mathring{A}$, where all the samples transform into cT phase at low temperature; (ii) above 11.73 $\mathring{A}$, where all the samples have non-cT phase as low temperature ground state; (iii) between 11.64 $\mathring{A}$ and 11.73 $\mathring{A}$, where details, such as temperature dependence of thermal contraction, amount of internal strain, specific type of substitution, etc., become important for determining the low temperature structural state. Note that all the rare earth substituted samples fall into the last category which is consistent with the fact that detailed As-As interlayer separation determines the ground state. The As-As interlayer separation of the Ce-substituted samples with $x = 0.16$, when extrapolated to base temperature assuming a constant temperature dependence, is just above the claimed critical value (Saha et al., 2012). On the other hand, the room temperature c-lattice parameter, 11.65 $\mathring{A}$, is also on the edge of the last region, showing good agreement with the criteria of As-As interlayer separation. The data for Sn-grown, $x = 0$ sample also fit our criteria very well. Under the ambient pressure, the room temperature c-lattice parameter falls into the second category with the low temperature state being a AFM/ORTH phase, whereas under the pressure of 0.62 GPa, the c-lattice parameter, when extrapolated to room temperature, falls into the first category with the low temperature state being a cT phase.

7.2.5 Annealing time dependence

For earlier work on both pure $CaFe_2As_2$ and $Ca(Fe_{1-x}Co_x)_2As_2$, we performed systematic studies of effects of annealing time for various $T_{A/Q}$ and showed that the effects of annealing were established rather quickly (t < 24 h) for $T_{A/Q}$ of interest. In addition, for both pure $CaFe_2As_2$ and $Ca(Fe_{1-x}Co_x)_2As_2$ we found that longer annealing time did not significantly change the T-$T_{A/Q}$ phase diagrams indicating that there was only one salient annealing process with a single characteristic time. As an example, virtually identical phase diagrams of

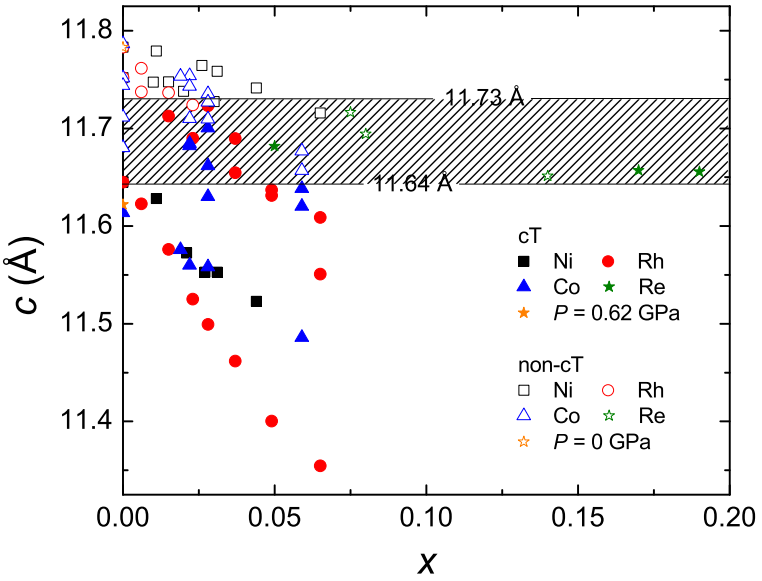

Figure 7.8 c-lattice parameter versus substitution level of all three substitutions. Data of rare earth substitution is also included for comparison.

$Ca(Fe_{1-x}Co_x)_2As_2$ for $T_{A/Q} = 500°$, assembled from two different sets of data, 1-day anneal and 7-day anneal are presented in Fig. 7.9.

Ni- and Rh-substitutions appear to be different. Although 1-day annealing gives familiar phase diagrams, they change with longer annealing times. Figure 7.10 presents the phase diagrams for Ni-substitution for $T_{A/Q} = 500°$C with different annealing time sequences. As can be seen, for samples annealed for seven days, the AFM/ORTH phase transition is suppressed more slowly and the SC/PM/T phase is only stabilized for a slightly higher Ni concentration level. However, the reproducibility with respect to annealing/quenching history seems to be preserved. We took these 7-day, 500°C annealed samples, resealed them, annealed/quenched at 800 °C trying to bring the samples back to a state that is close to $T_{A/Q} = 960°$C samples, and then annealed again at 500°C for one day and quenched. After this series of annealing, the T-x phase diagram is similar to that is seen for the initial 1-day annealing, indicating that whatever process is taking place over this longer time scale, it is reversible. These data imply that (i) there is more than one salient annealing time, but that (ii) there is clear reversibility and reproducibility.

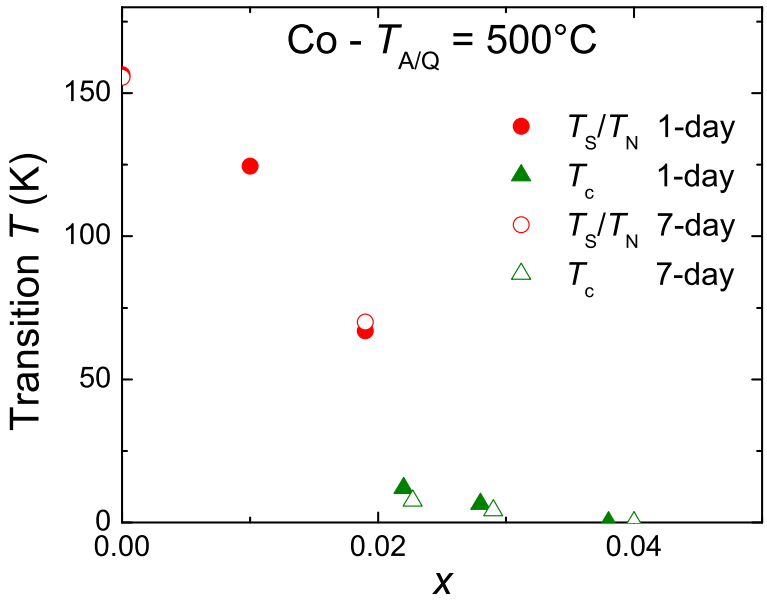

Figure 7.9 Phase diagrams of transition temperature T vs Co concentration x assembled from magnetic susceptibility data, for $Ca(Fe_{1-x}Co_x)_2As_2$ samples with $T_{A/Q} = 500°C$. Filled symbols are inferred from data from samples with 1-day annealing and open symbols are inferred from data from samples with 7-day annealing.

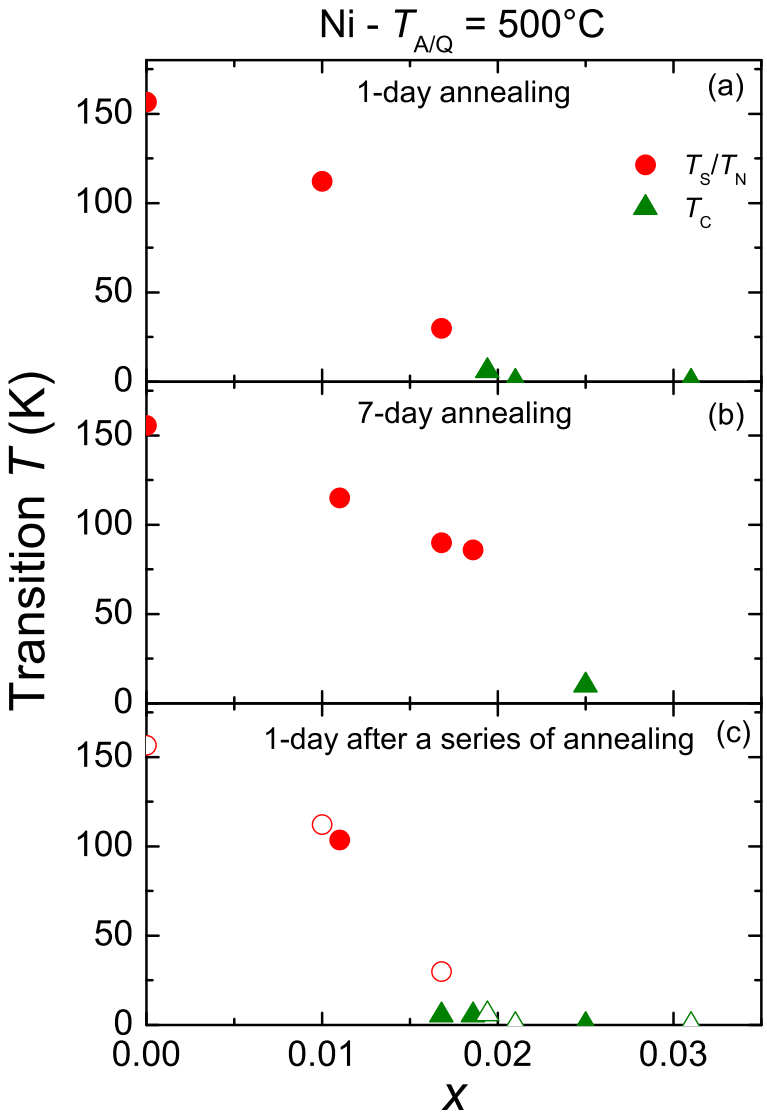

Figure 7.10 Phase diagrams of transition temperature T vs Ni concentration x assembled from magnetic susceptibility data, for $Ca(Fe_{1-x}Ni_x)_2As_2$ samples with $T_{A/Q} = 500°C$. (a) 1 day annealing, (b) 7 days annealing, (c) 1 day annealing after a series of annealing described in the text. For comparison, data in (a) are repeated in (c) with open symbols.

Even larger effects of a longer annealing time are observed for Rh-substitution as shown in Fig. 7.11. It can be seen that the AFM/ORTH phase transition is initially suppressed more slowly for the 7-day annealed/quenched samples than for the 1-day annealed/quenched samples. In addition, the SC/PM/T ground state is stabilized at low temperature for the 7-day annealed/quenched samples with substitution level of 3.7% and higher. This is in stark contrast to what has been seen for 1-day annealed/quenched $Ca(Fe_{1-x}Rh_x)_2As_2$ compounds, where the cT phase is found for high substitution level and no superconductivity is revealed. Again we resealed these 7-day annealed samples, annealed/quenched at 800 °C, and then annealed at 500°C for one day and quenched. As seen for Ni-substituted samples, after this series of annealing, the initial "1-day anneal" phase diagram is recovered, illustrating clear reversibility and reproducibility.

The clear difference between effects of 1-day and 7-day annealing, as well as the clear reversibility and reproducibility, can also be seen in the *c*-lattice parameter data from the $Ca(Fe_{1-x}Rh_x)_2As_2$ system as presented in Fig. 7.12. The *c*-lattice parameter is suppressed by Rh-substitution much less rapidly for 7-day, 500°C annealed/quenched samples, than for 1-day, 500°C annealed/quenched samples. After a series of further thermal treatment, we could bring it back to the behavior similar to what is seen for 1-day, 500°C annealed/quenched samples. Note that the apparent break in slope starting from $x = 0.040$ for 7-day annealing is probably due the underestimated error bar.

The origin of this annealing time dependence of the physical properties is still unknown. One possibility is that there are two salient time scales. One timescale for the small excess of FeAs associated with the $CaFe_2As_2$ width of formation to go in and out of the $CaFe_2As_2$ matrix, as we proposed based on our T-$T_{A/Q}$ phase diagram and TEM results (Chapter 5). Another timescale for some Fe/Ni (and Fe/Rh) segregation. Note that this is only speculation but would fit the data. As we change annealing times around the second time scale, we would change the Rh/Ni (or RhAs/NiAs) content and therefore change the phase diagram as well as the *c*-lattice parameter in a reversible manner. The fact that Co-substitution does not show the same annealing time dependence raises the question of what the differences between solubility of Co and Rh/Ni or CoAs and RhAs/NiAs in the $CaFe_2As_2$ matrix are. More detailed

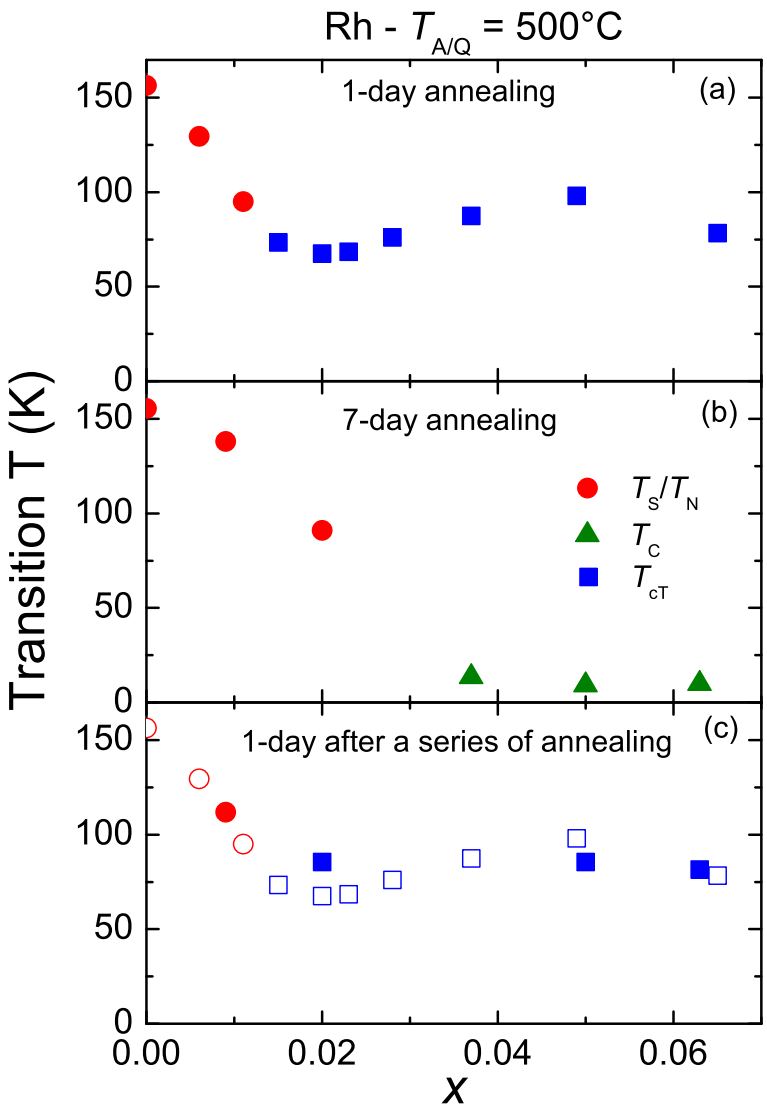

Figure 7.11 Phase diagrams of transition temperature T vs Rh concentration x assembled from magnetic susceptibility data, for $Ca(Fe_{1-x}Rh_x)_2As_2$ samples with $T_{A/Q}$ = 500°C. (a) 1 day annealing, (b) 7 days annealing, (c) 1 day annealing after a series of annealing described in the text. For comparison, data in (a) are repeated in (c) with open symbols.

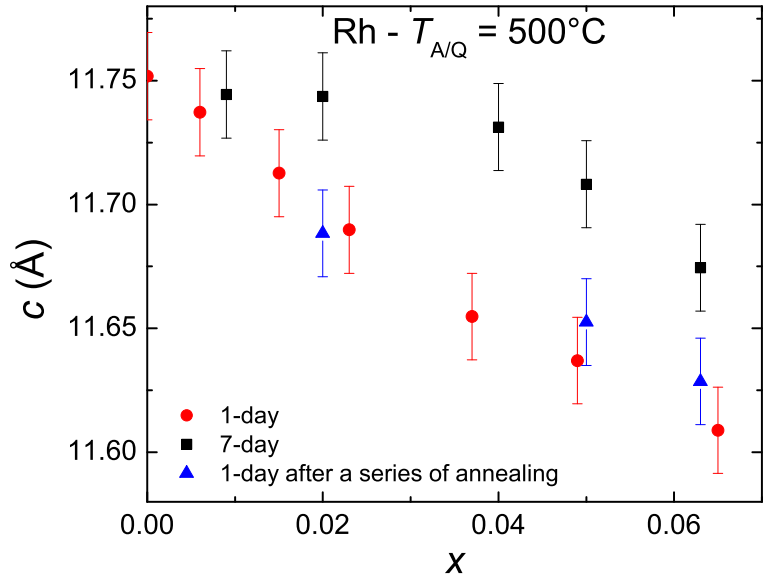

Figure 7.12 Room temperature c-lattice parameter of $Ca(Fe_{1-x}Rh_x)_2As_2$ samples with $T_{A/Q}$ = 500°C as a function of measured Rh concentration, x, for 1 day annealing (red), 7 days annealing (black) and 1 day annealing after a series of annealing described in the text (blue).

microscopic study, such as high resolution TEM, will be needed to provide further insight into this issue.

7.3 Summary

We report systematic studies of the combined effects of annealing/quenching temperature and Ni/Rh-substitution on the physical properties of $CaFe_2As_2$. We constructed two-dimensional phase diagrams for the low-temperature states for both systems to map out the relations between possible ground states and then compared with that of Co-substitution. Ni-substitution, which brings one more extra electron per substituted atom and suppresses the c-lattice parameter at roughly the same rate as Co-substitution, leads to similar changes in the $Ca(Fe_{1-x}Ni_x)_2As_2$ phase diagram as were seen when comparing the $Ba(Fe_{1-x}Co_x)_2As_2$ and $Ba(Fe_{1-x}Ni_x)_2As_2$ phase diagrams: similar suppression of the AFM/ORTH phase but a more rapid suppression of the SC/PM/T phase for Ni-substitution. On the other hand, Rh-substitution, which brings the same amount of extra electrons but suppresses the c-lattice

parameter more rapidly that Co-substitution, has a very different phase diagram from that of $Ca(Fe_{1-x}Co_x)_2As_2$: Rh-substitution suppresses the AFM/ORTH phase more rapidly than Co-substitution, but more dramatically, the cT phase is stabilized over a much greater region of the x-$T_{A/Q}$ phase space, truncating the SC/PM/T region. In addition to the differences in phase diagrams, we also found different behavior in both systems related to annealing time compared to Co-substitution. We propose that for Ni- and Rh-substitution, there is a second, reversible process taking place on a longer time scale, but at the current time we do not know its microscopic origin.

CHAPTER 8. SUMMARY

$CaFe_2As_2$ manifests an extreme example of the coupled magnetic/structural phase transition of the parent compounds of the FeAs-based superconductors (Ni et al., 2008b; Goldman et al., 2008; Kreyssig et al., 2008; Goldman et al., 2008; Torikachvili et al., 2008; Yu et al., 2009; Canfield et al., 2009a; Prokes et al., 2010; Ran et al., 2011, 2012). When grown out of Sn-flux, the magnetic and structural phase transitions are strongly coupled and first order with hysteresis of several degrees as seen in thermodynamic, transport, and microscopic measurements (Ni et al., 2008b; Goldman et al., 2008). Also, is the most pressure sensitive of the $AEFe_2As_2$ (AE = Ba, Sr, Ca) and 1111 compounds with its antiferromagnetic/orthorhombic (AFM/ORTH) phase transition being initially suppressed by over 100 K per GPa and a then non-moment bearing, collapsed tetragonal (cT) phase being stabilized by $\sim$0.4 GPa (Kreyssig et al., 2008; Goldman et al., 2008; Torikachvili et al., 2008; Yu et al., 2009; Canfield et al., 2009a; Prokes et al., 2010).

In this thesis I show that the phase transition temperatures and even ground state of can be controlled and tuned by post-growth annealing and quenching of single crystal samples grown out of FeAs-flux. I first summarized the previous results on the physical properties of $CaFe_2As_2$ grown out of Sn-flux. Both hydrostatic pressure and Co-substitution were used to tune the system.

In chapter 5, I presented the results of annealing/quenching effects on the physical properties of $CaFe_2As_2$ grown out of FeAs-flux. We found a remarkably large response of the transition temperatures of $CaFe_2As_2$ to $T_{A/Q}$. Whereas crystals that are annealed/quenched at 400°C exhibit a first order phase transition from a high temperature tetragonal to a low temperature orthorhombic and antiferromagnetic state near 170 K, crystals that have been quenched from 960°C exhibit a transition from a high temperature tetragonal phase to a low temperature, non-

moment bearing, collapsed tetragonal phase below 100 K. By use of temperature dependent electrical resistivity, magnetic susceptibility, X-ray diffraction, Mössbauer spectroscopy and nuclear magnetic resonance measurements we have been able to demonstrate that the transition temperature can be reduced in a monotonic fashion by varying the $T_{A/Q}$ from 400 to 850°C with the low temperature state remaining AFM/ORTH for $T_{A/Q}$ below 850°C and becoming cT for $T_{A/Q}$ larger than 800°C. This suppression of the AFM/ORTH phase transition and its ultimate replacement with the cT phase is similar to what has been observed for $CaFe_2As_2$ under hydrostatic pressure. Transmission electron microscopy studies suggest that there is a temperature dependent, width of formation of $CaFe_2As_2$ with a decreasing amount of excess Fe and As being soluble in the single crystal at lower annealing temperatures. For samples with $T_{A/Q} = 960$°C there is a fine (of order 10 nm), semi-uniform distribution of precipitates that can be associated with an average strain field whereas for samples annealed/quenched at 400°C the excess Fe and As form mesoscopic grains that induce little strain throughout the $CaFe_2As_2$ lattice.

In chapter 6, I studied the combined effect of annealing/quenching Co-substitution of the physical properties of $CaFe_2As_2$ grown out of FeAs-flux. Whereas the samples with $T_{A/Q} = 960$°C all enter the cT phase upon cooling, $T_{A/Q}$ between 350°C and 800°C can be used to tune the system to low temperature AFM/ORTH or SC/PM/T states as well. The progression of the transition temperature versus annealing/quenching temperature (T-T_{anneal}) phase diagrams with increasing Co concentration shows that, by substituting Co, the AFM/ORTH and the cT phase lines are separated and bulk superconductivity is revealed. We established a 3D phase diagram with Co concentration and annealing/quenching temperature as two independent control parameters. At ambient pressure, for modest x and $T_{A/Q}$ values, the $Ca(Fe_{1-x}Co_x)_2As_2$ system offers ready access to the salient low temperature states associated with Fe-based superconductors: AFM/ORTH, SC/PM/T, N/PM/T and cT phase.

I chapter 7, I presented the systematic studies of the combined effects of annealing/quenching temperature ($T_{A/Q}$) and TM = Ni, Rh substitution (x) on the physical properties of $CaFe_2As_2$. We constructed two-dimensional, $T_{A/Q}$-x phase diagrams for the low-temperature states for both substitutions to map out the relations between ground states and compared them with

that of Co-substitution. Ni-substitution, which brings one more extra electron per substituted atom and suppresses the c-lattice parameter at roughly the same rate as Co-substitution, leads to a similar parameter range of antiferromagnetic/orthorhombic in the $T_{A/Q}$-x space as that found for Co-substitution, but has the parameter range for superconductivity shrunk (roughly by a factor of two). This result is similar to what is found when Co- and Ni-substituted $BaFe_2As_2$ are compared. On the other hand, Rh-substitution, which brings the same amount of extra electrons as does Co-substitution, but suppresses the c-lattice parameter more rapidly, has a different phase diagram. The collapsed tetragonal phase exists much more pervasively, to the exclusion of the normal, paramagnetic, tetragonal phase. The range of antiferromagnetic/orthorhombic phase space is noticeably reduced, and the superconducting region is substantially suppressed, essentially truncated by the collapsed tetragonal phase. In addition, we found that whereas for Co-substitution there was no difference between phase diagrams for samples annealed for one or seven days, for Ni- and Rh- substitutions a second, reversible, effect of annealing was revealed by seven-day anneals.

At the end, I would like to point out that controlled annealing/quenching and transition metal substitution of FeAs grown $CaFe_2As_2$ has opened up a cascade of opportunities for the further research. Detailed microscopic and spectroscopic measurements were hard to collect on the collapsed tetragonal phase of $CaFe_2As_2$ as it existed only under pressure. By inducing internal strain, via the postgrowth thermal treatment of single crystals grown out of FeAs-flux, I was able to stabilize the collapsed tetragonal phase at ambient pressure and provide easy access for neutron scattering, APRES and NMR measurements (see Appendix D for details). Also Hydrostatic pressure study has revealed that it is possible to tune the system from the AFM/ORTH phase to the SC/PM/T phase and then to the cT phase with applied pressures of less than 0.3 GPa, on a single sample. Based on that, elastic and inelastic neutron scattering studies on a single sample have been proposed to systematically study the magnetic order and fluctuations across the whole phase space of FeAs-based superconductivity.

APPENDIX A. DETAILS OF SAMPLE SYNTHESIS

The single crystals of pure and transition metal substituted $CaFe_2As_2$ are grown using self flux in two steps. First FeAs/TMAs binary compounds, which are used as flux, are synthesized by a hybrid vapor phase/solid state reaction method. This process is illustrated in Fig. A.1 and was performed in a glove box with one atmosphere of nitrogen or argon gas (Fig. A.1a) because of the toxicity of As. As chunks were smashed using a home made tool and hammer (Fig. A.1b) and then roughly ground using a mortar and pestle (Fig. A.1c). Commercially produced Fe/TM powder was mixed with ground As loosely (Fig. A.1d) in a ratio of 1.05 : 1. 5% of excess Fe/TM was used to ensure that all the As would be reacted as it is both toxic and volatile. The mixed powder was placed in a silica ampoule with a small silica rod attached along the length of the inner surface (Fig. A.1e and f).

After that the ampoule was taken out the glove box and put into the torch hood where the inner surface of the ampoule was cleaned thoroughly with dry paper towel first. Two indentations are made on the wall of the ampoule (Fig. A.1g), 3 cm above the top of silica rod, using torch and a small silica tube with sealed bottom was placed into the ampoule, resting on these indentations in order to seal the ampoule later on (Fig. A.1h). One could possibly make indentations first and then fill the mixed powder to avoid heating up the As powder in the ampoule with open end. However, this causes problems in cleaning the inner surface of the ampoule for the part below the indentations, which in turn causes problems in sealing the ampoule. Therefore making indentations after cleaning is preferred. Having that said, heating up an ampoule filled with As powder could be a dangerous procedure. This is normally done within a very short time, no more than a few seconds. Practice with empty ampoule is preferred before real sealing. In addition, the indentations are at least 5 cm above the powder to reduce the heat transferred to the As powder. The silica ampoule was then sealed (Fig. A.1i) under

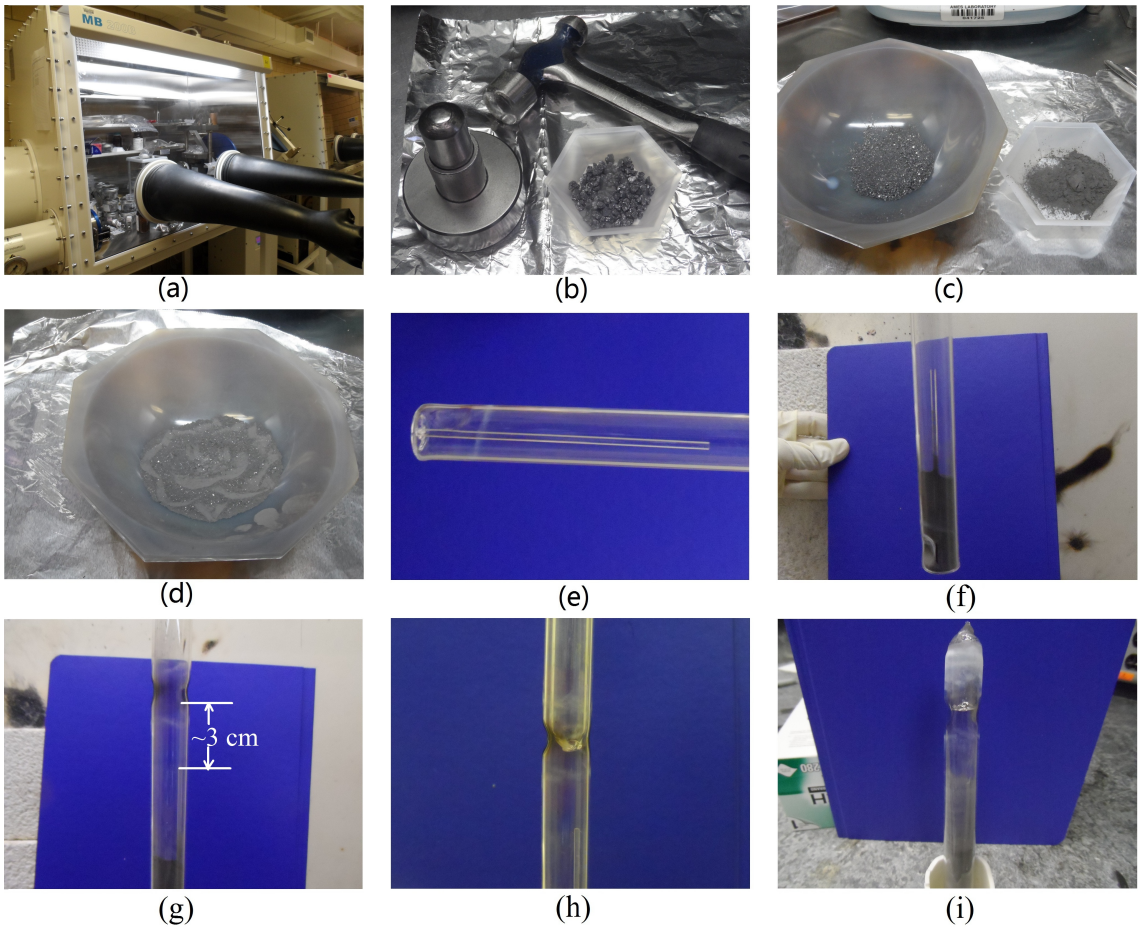

Figure A.1 Procedure of making FeAs binary compound. (a) The glove box used for sample preparation. (b) The home made tool to smash As chunks. (c) A mortar to grind As. (d) Mixture of Fe powder and ground As in the mortar. (e) A silica ampoule with a small silica rod attached along the length of the inner surface. (f) The silica ampoule filled with mixture of Fe and As. (g) The silica ampoule with indentations made using torch. (h) A small silica tube with sealed bottom placed into the ampoule. (i) The sealed silica ampoule with starting material inside.

approximately 1/5 atmosphere of argon gas.

The ampoule was heated in a horizontal furnace in conjunction with a rotating setup (Fig. A.2). A brief description and a operating procedure for the furnace are included at the end of this appendix (with permission of Kevin Dennis and Dr. William McCallum). The silica rod within the mixed powder and the rotation of the ampoule as it was being heated ensure that the As reacted thoroughly and uniformly with Fe/TM. The ampoule was heated to 580°C at a rate of 30°C/hour and held for 15 hours. For FeAs and CoAs, with melting temperature around 1100°C (Fig. 3.5), the ampoule was further heated to 900°C at the same rate and held for an additional 15 hours to obtain single phase from mixture. For other TMAs, with melting point below or close to 900°C (Fig. A.3), no further heat up was conducted. Then the furnace is turned off and the ampoule was furnace cooled to room temperature, after which the FeAs/TMAs was obtained.

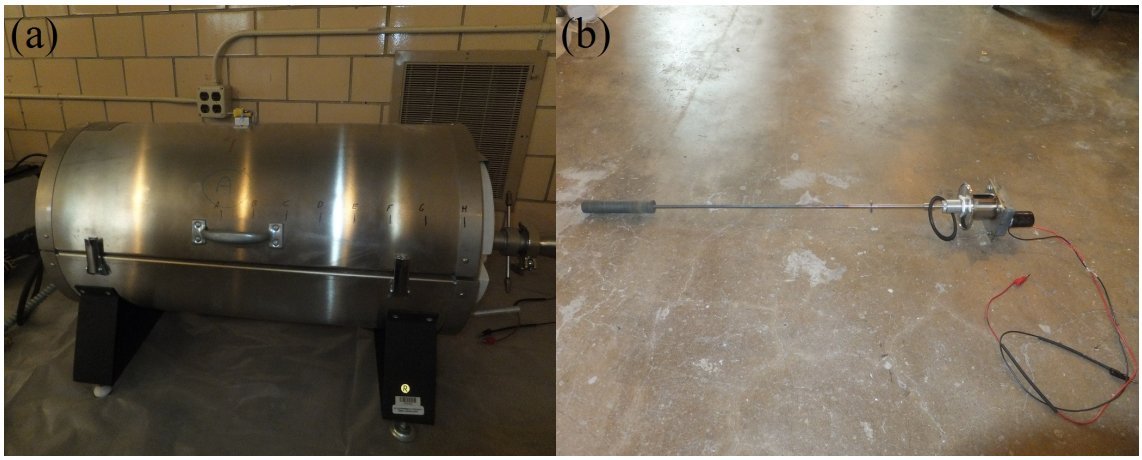

Figure A.2 (a) The horizontal furnace used to synthesis FeAs/TMAs binary compounds. (b) The rotating setup used in conjunction with the horizontal furnace.

FeAs/TMAs powder was then used as flux to synthesize single crystals of $Ca(Fe_{1-x}TM_x)_2As_2$. This step was also performed in a glove box and is illustrated in Fig. A.4. Figure A.4a shows the crucibles and silica ampoules for the growth. Single crystals of $Ca(Fe_{1-x}TM_x)_2As_2$ were synthesized from self flux by mixing small Ca chunks, FeAs powder, and TMAs powder together according to the ratio Ca:FeAs:TMAs =1:4(1-$x_{nominal}$):4$x_{nominal}$, where $x_{nominal}$ is the nominal

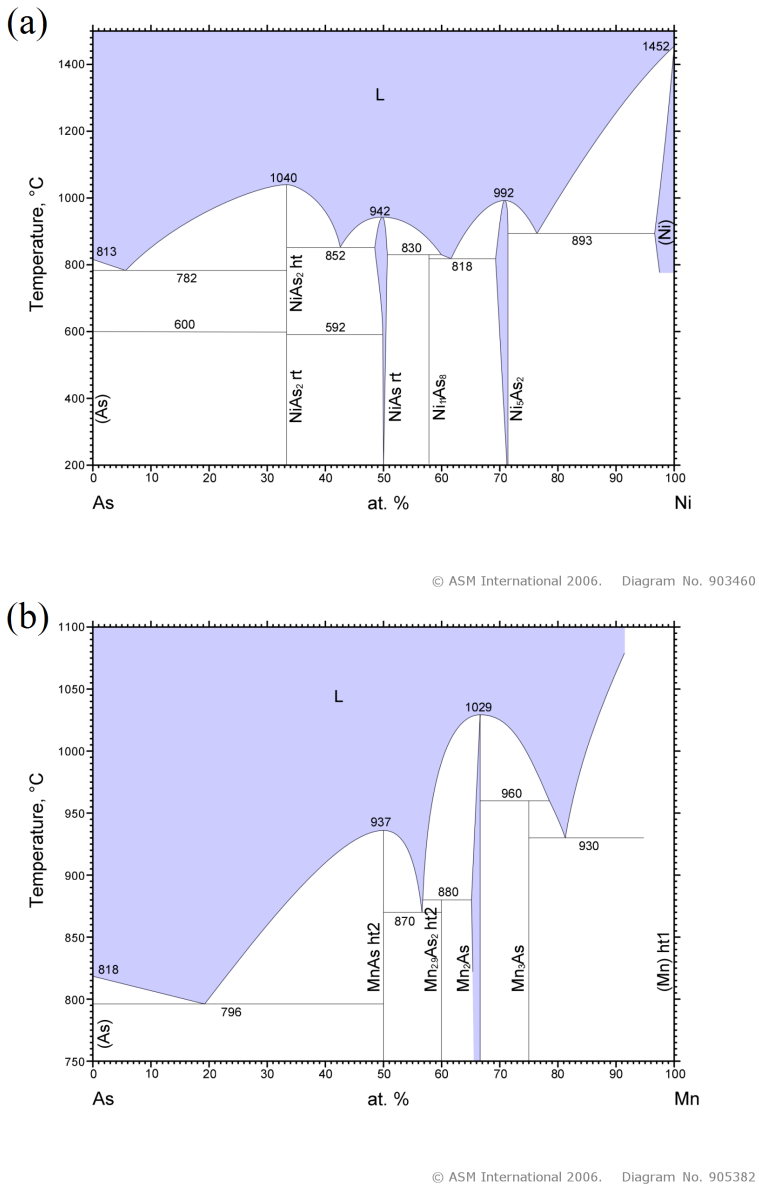

Figure A.3 Phase diagrams of the (a) As-Ni and (b) As-Mn binary systems. (ASM alloy phase diagram database)

TM concentration. First, Ca is cut into small pieces (Fig. A.4b) and FeAs powder and TMAs powder were mixed together thoroughly with a mortar and pestle (Fig. A.4c). When placing the materials (Fig. A.4d) into a crucible, layers of FeAs/TMAs powder and layers of Ca were packed alternatively to avoid contact of Ca with the crucible wall (Fig. A.4e shows a packed a crucible). Each 2 ml alumina crucible can contain roughly 0.35 g of Ca and corresponding amount of FeAs/TMAs powder. A second catch crucible containing silica wool was placed on top of the crucible containing starting materials (Fig. A.4f). A piece of quartz wool was place on top of the catching crucible and a small silica tube with sealed bottom was placed into the ampoule, resting on the quartz wool (Fig. A.4f). The silica ampoule was then connected to an adapter (Fig. A.4g), which was closed, and moved from the glove box to a hood (Fig. A.4g), where the silica ampoule was sealed under approximately 1/3 atmosphere of argon gas. The sealed ampoule was then placed in a 50 ml alumina crucible (Fig. A.4i) which itself is place in a programmable box furnace (Fig. A.4j) in a vented containment box (Fig. A.4k). The furnace was heated up to 600°C in 3 hours and dwelled for one hour to make sure that any possible remaining As could be reacted. Then the furnace was continuously heated up to 1180°C at a rate of 100°C/hour, stayed at 1180°C for 3 hours so that the liquid mixed completely. Then single crystals were grown by rapidly cooling the melt from 1180°C to 1020°C over 3 h, slowly cooling from 1020°C to 960°C over 40 h, and then decanting off the excess liquid flux by using centrifuge (Fig. A.4l). Initial attempt to grow crystals by slowly cooling the melt from 1180°C to 1000°C over 40 h (the same procedure used to grow $BaFe_2As_2$ crystals) led to a total spin (no nucleation occurred at the spin temperature). Therefore the temperature window for the growth of $CaFe_2As_2$ crystals was chosen to be from 1020°C to 960°C.

The following pages are the copy of description of the horizontal furnace used to synthesize the FeAs/TMAs binary compounds. Note that I used this furnace in conjunction with a rotating setup as described above. Therefore the sample loading is different from what is described in the last two pages of this description.

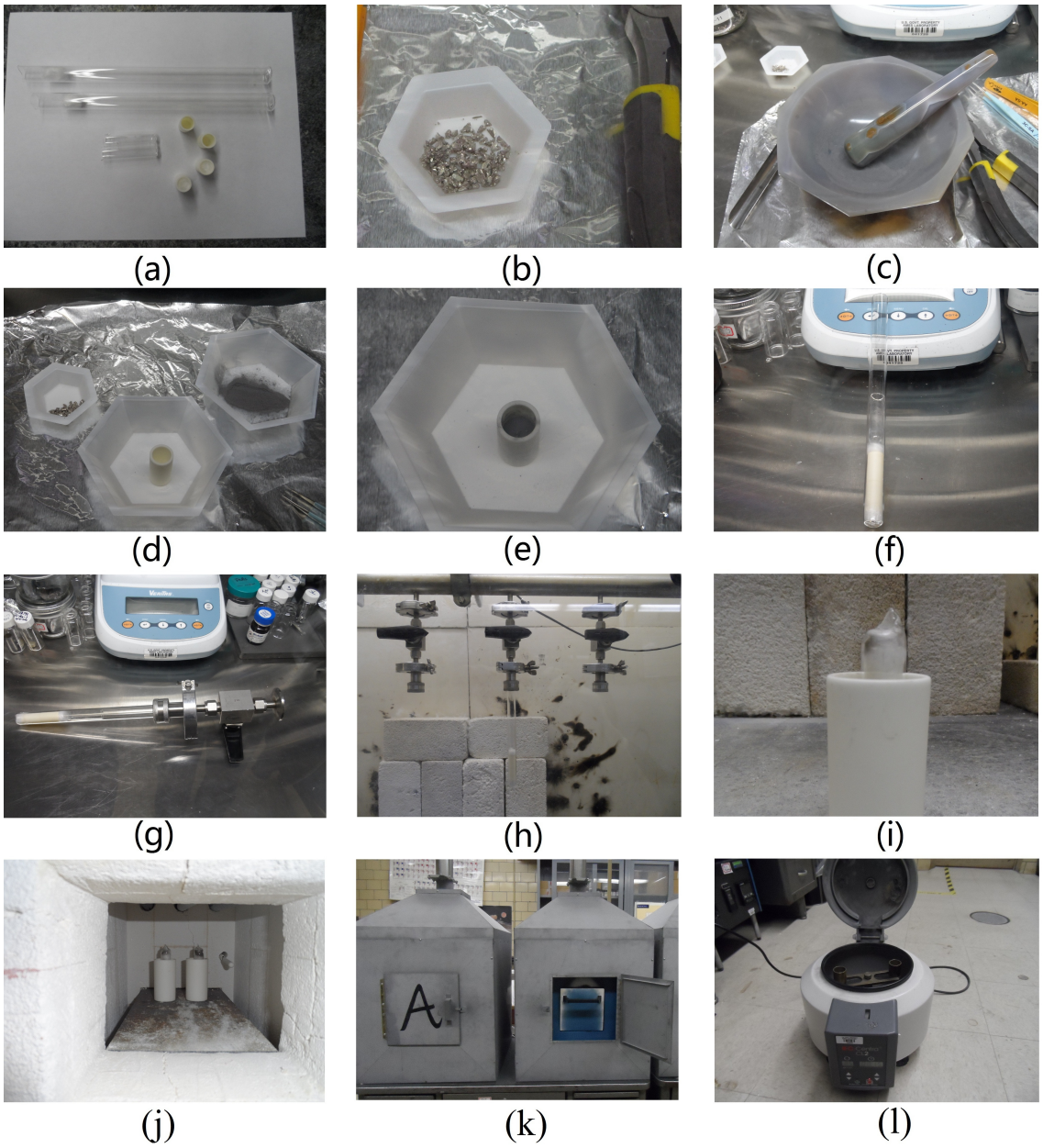

Figure A.4 Procedure of making Single crystals of $Ca(Fe_{1-x}TM_x)_2As_2$ from self flux. (a) Silica ampoules and alumina crucibles used to make growths. (b) Ca chunks that have been cut into small pieces. (c) Mixtures of FeAs powder and TMAs powder in a mortar. (d) Ca pieces and FeAs/TMAs powder to be placed into a crucible. (e) A crucible containing the starting materials. (f) A packed silica ampoule. (g) A packed silica ampoule connected to an adapter. (h) A packed silica ampoule is moved to a hood. (i) A sealed ampoule in a 50 ml alumina crucible. (j) Two growth ampoule place in the furnace. (k) Furnaces in vented containment boxes. (l) The centrifuge used to decant off the excess liquid flux.

STANDARD OPERATING PROCEDURES: FURNACES

NOTICE

Only materials approved by the Group Leader, Associate Group Leader, or Assistant Group Leader may be used with this apparatus. The master approved systems can be found in Room 39 Wilhelm Hall.

NOTICE

Operation of these apparati without proper training is a violation of Ames Laboratory safety policy. Trained persons disregarding proper procedures will lose all privileges.

WARNING
Water leaks could cause dangerous electrical shorts.

CAUTION
Lack of cooling water will cause damage to the system during operation.

Safety Precautions

1. The outside surface of a furnace can be quite hot (>100°C) during operations and will take several hours after operations to cool down fully.
2. Lack of cooling water could result in damage to the quartz tube. The cooling water should be running at all times during normal service.
3. Leaks in the cooling water lines could produce shorts in the electrical system.
4. Handling of gas cylinders should be performed in accordance with Ames Lab safety policy. Gas cylinder safety training is recommended.

Retort for the preparation of volatile and hazardous materials.

This retort is in addition to the retort previously discussed with the safety committee. Due to materials availability issues, that retort is going to take several weeks if not longer to complete. However the capabilities of that system are greater than are required in order to start the current investigation. Therefore an interim retort constructed with materials on hand is proposed.

In making the materials of current interest, the predominate safety concern is the vapor pressure of unreacted arsenic at elevated temperatures. Unreacted arsenic is only present during the preparation of the precursor materials which can be carried out between 600 and 1000 C. In these this temperature range, Inconel 600 has both the strength and corrosion resistance to be used in air. We currently have 1" diameter tubing with a 0.060" wall. This tubing is readily available an relatively inexpensive. We propose to make a small retort from existing materials so that we may rapidly enter a dynamic new area of research.

The 1" retort will be a double ended retort which passes through the tube furnace and is water cooled at both ends. Due to the fact that the volume os this retort is only about ¼ liter, an expansion volume of approximately 2 liters will be placed on one end. This volume will limit the pressure rise in the event of a quartz ampoule breach. Due to the small diameter of this retort, the quartz ampoule will be inserted directly in the retort without a sample tray. This remove the p[ossibity of examining the ampoule before opening the retort. However since the retort will only be opened at room temperature, no hazardous vapors will be present and any powder present as a result of an ampoule failure may be handled using standard chemical hygiene techniques. As before N2 will be flowing through the retort and up the exhaust system during operation.

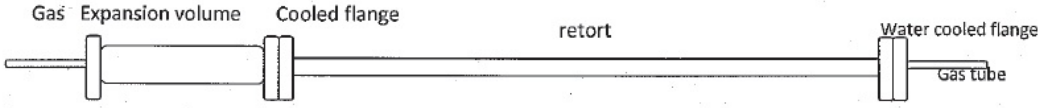

The recent discovery of the $REFeAsO_{1-x}F_x$ superconductors with T_c's in the low 40K region has highlighted the need to be able to produce high quality samples from materials containing volatile and toxic components. The standard way of producing these materials is to seal the reactants in a quartz ampoule prior to reaction. However, as recent events at Argonne have shown, this technique is susceptible to catastrophic failure if deviations from the expected behavior occur. It is therefore necessary to insure that there a secondary safeguards in place which will contain the reactants in the event of a failure of the quartz ampoule. The equipment and procedures described here are designed to allow the production of novel compounds containing volatile and/or toxic constituents. These include but are not limited to As, Cd, S, Se, Te, P, Zn, K, Rb, and Mg. As with the standard practice, the constituents of desired compound will be sealed in a suitable ampoule. This ampoule can be quartz, tantalum, molybdenum, inconel, or other suitable metals. The metal ampoules are seal using the laser welder so that they can contain any compatible gas or turbopumped vacuum. The ampoules may contain additional crucibles if required to prevent reaction with one or more of the constituents. In order to provide secondary containment, a specially designed insert will be used in a standard 3" tube furnace. Since a shock wave is expected to accompany the catastrophic failure of an ampoule, The insert will consist of an inner retort of Inconel 600 or a similar alloy. However, since the maximum temperature of the furnace is 1200 C, these allows cannot be used in air. Therefore the metal retort must have a non oxidizing gas, in this case N2, both inside and outside of the part of the retort which is heated. The control of the atmosphere inside the retort is not a problem as the sample is sealed in its' ampoule. In order to protect the outside of the metal retort, it will be inserted into one of our standard quartz retorts so that the N2 atmosphere can be maintained. The retorts are shown in the attached drawing. The sample ampoule is placed in a sample tray assembly with a support rod which can be used to insert or remove the sample from the hot zone without breaking the controlled atmosphere. Exterior to the furnace is a standard tee with a window which allows the ampoule to be inspected before opening the retort.

During use a constant low flow of N2 is maintained in both the quartz and inconel retorts. The off gas from this flow is connected to the laboratories fume hood system.

The procedure for operating the furnace is as follows.

With the furnace cold, the sample and sample tray are inserted into the furnace and the retorts are flushed with N2. The sample is then run through the appropriate temperature cycle and when the furnace is again cool, the sample rod is drawn through the quick connect so that the ampoule may be inspected. If the ampoule is intact it may be removed without special precautions. If the ampoule is not intact, approporiate procedures for dealing with the now solid, hazardous waste will be used. Since the retort is not opened until the furnace is cold, there is no exposure to toxic fumes.

There are two scenarios for the failure of the ampoule. The first is operator error. In reacting compounds with volatile components, care must be taken not to raise the temperature of the ampoule above the point where the vapor pressure of the volatile competent exceeds the burst strength of the

ampoule. For most compounds of interest, the vapor pressure of the volatile element above the compound is significantly lower than that of the pure element. Thus once the pure element is reacted the temperature can be raised for further processing. The use of a tube furnace also allows the use of a long ampoule so that one end can be maintained at a low temperature, controlling the pressure, while the non volatile elements are maintained at a high temperature to speed the reaction.

The second scenario for failure is less predictable. In this case, a volatile reaction product is created which causes the pressure to exceed the burst strength of the ampoule. This sometimes occurs when working with new systems.

Within the retorts described here, in the event of an ampoule failure, any reaction products are contained within the retort or vented up the chemical hood. As a worst case scenario, consider an ampoule containing 7 grams of unreacted As at 900 C. (Note that in reality, the ampoule would have burst at a lower temperature due to the high vapor pressure of As.) If we assume, that the As instantaneously vaporizes (not possible) we have 0.1 mole of gas at 900C. The volume of the retort is about 2.5 liters so the resulting change in pressure is 4 bar for a total pressure of 5 bar (75 psi). This pressure is easily contained by the retort and flanges. In reality the pressure can never reach this worst case value. First the retort is vented to the fume hood system. This vent has a reasonable impedance for an instantaneous pressure rise but it does cap the pressure. Second, the heat of vaporization must be supplied to the As so that in cannot vaporize instantaneously. Finally, the As vapor will condense on the cold surfaces of the retort at a rate approaching that at which it is vaporized. Given the last two considerations, the instantaneous rise in pressure in the retort will be mostly due to the sudden release of pressure from the ampoule. Since the volume of the ampoule is at most ~1/25 of the volume of the retort and the burst pressure of the ampoule is an estimated 20 bar, a 1 bar pressure rise may occur.

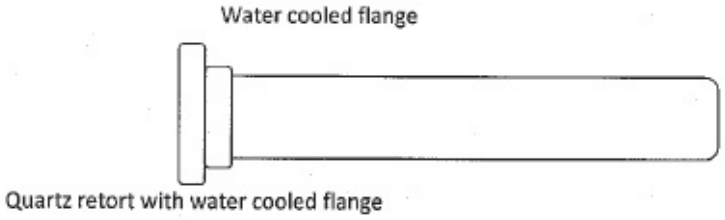

Quartz retort with water cooled flange

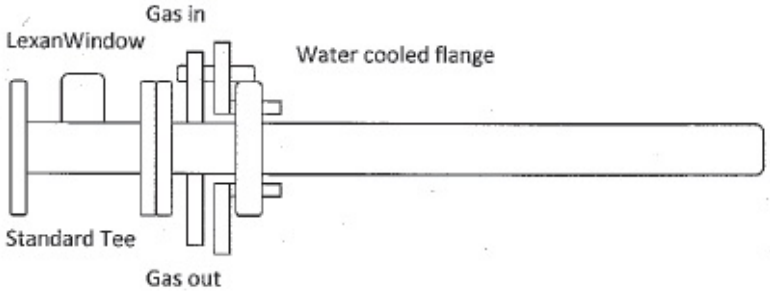

Inconel retort with water cooled flange and gas inlets and outlets

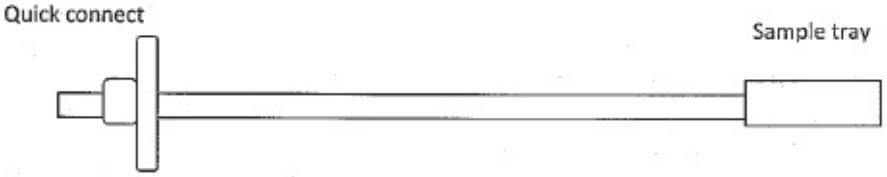

Sample tray assembly

Interim Retort for the preparation of volatile and hazardous materials.

This retort is in addition to the retort previously discussed with the safety committee. Due to materials availability issues, that retort is going to take several weeks if not longer to complete. However the capabilities of that system are greater than are required in order to start the current investigation. Therefore an interim retort constructed with materials on hand is proposed.

In making the materials of current interest, the predominate safety concern is the vapor pressure of unreacted arsenic at elevated temperatures. Unreacted arsenic is only present during the preparation of the precursor materials which can be carried out between 600 and 1000 C. In these this temperature

range, Haynes 230 has both the strength and corrosion resistance to be used in air. We currently have 1" diameter tubing with a 0.060" wall. This tubing is readily available and relatively inexpensive. We propose to make a small retort from existing materials so that we may rapidly enter a dynamic new area of research.

The 1" retort will be a double ended retort which passes through the tube furnace and is water cooled at both ends. Due to the fact that the volume os this retort is only about ¼ liter, an expansion volume of approximately 2 liters will be placed on one end. This volume will limit the pressure rise in the event of a quartz ampoule breach. Due to the small diameter of this retort, the quartz ampoule will be inserted directly in the retort without a sample tray. This remove the p[ossibity of examining the ampoule before opening the retort. However since the retort will only be opened at room temperature, no hazardous vapors will be present and any powder present as a result of an ampoule failure may be handled using standard chemical hygiene techniques. As before N2 will be flowing through the retort and up the exhaust system during operation.

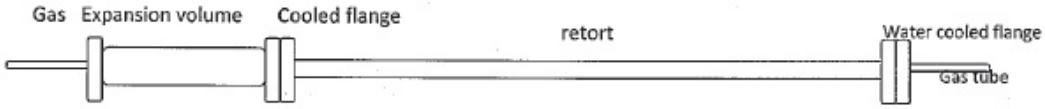

In order to produce the quantities of material reguired for work on the Fe-As superconductors we would like to increase the scale of the batches of FeAs we are producing. In our original review we presented this analysis.

Within the retorts described here, in the event of an ampoule failure, any reaction products are contained within the retort or vented up the chemical hood. As a worst case scenario, consider an ampoule containing 7 grams of unreacted As at 900 C. (Note that in reality, the ampoule would have burst at a lower temperature due to the high vapor pressure of As.) If we assume, that the As instantaneously vaporizes (not possible) we have 0.1 mole of gas at 900C. The volume of the retort is about 2.5 liters so the resulting change in pressure is 4 bar for a total pressure of 5 bar (75 psi). This pressure is easily contained by the retort and flanges. In reality the pressure can never reach this worst case value. First the retort is vented to the fume hood system. This vent has a reasonable impedance for an instantaneous pressure rise but it does cap the pressure. Second, the heat of vaporization must be supplied to the As so that in cannot vaporize instantaneously. Finally, the As vapor will condense on the cold surfaces of the retort at a rate approaching that at which it is vaporized. Given the last two considerations, the instantaneous rise in pressure in the retort will be mostly due to the sudden release of pressure from the ampoule. Since the volume of the ampoule is at most ~1/25 of the volume of the retort and the burst pressure of the ampoule is an estimated 20 bar, a 1 bar pressure rise may occur.

If we increase the batch size to contain 35 grams of As and assume that no reaction takes place during heating, until the ampoule fails at 900 C accompanied by the instantaneous vaporization of the entire As charge, we would have a pressure in the retort of 21 bar which exceeds the maximum pressure for the flanges. However, the maximum pressure quartz ampoule will sustain is 10 bar so that the ampoule will rupture at around 700 C which is above the sublimation temperature but below the melting temperature which occurs at 800 C under 28 atm pressure. Thus the majority of the As will be solid when the ampoule fails and can vaporize only as fast as the heat of vaporization is supplied. At the same time, once the ampoule fails, As will condense at the cold ends of the retort which are 300 C below the sublimation temperature and are water cooled with metallic contact. Thus vapor will actually condense faster than it is generated since there is a much larger condensing area and larger temperature gradient. Note that the volume of the ampoule is of order of a few percent of the volume of the retort so that the initial pressure rise in the retort due to the As vapor contained in the ampoule is minimal. With our current system, the only potential we see for a leak of As vapor is if a shard of not quartz from the exploding ampoule passes through a 3/16" hole and burns a hole in the decron tubing that varies the flowing N2 to the fume exhaust. We are placing a shield on the whole to insure that that cannot happen.

Note that the scenario above has assumed that we have somehow instantaneously heated the sample to high temperature and avoided reaction of the As with the Fe. This is a case that is worse than can be physically achieved. In practice several steps are taken to insure that the quartz tube does not fail and these steps limit the pressure that can occur in the event of the failure.

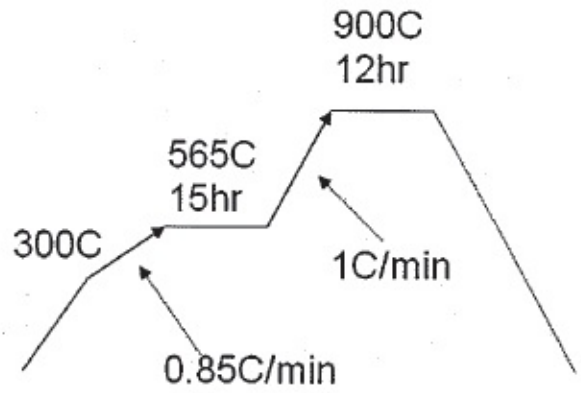

Using the heating profile above insures that all of the As is reacted before the burst pressure of the ampoule is achieved. After the 565 C soak, there is minimal free As and the sample consists of Fe, Fe2As, FeAs, and FeAs2. The purpose of the 900 C reaction is to obtain single phase FeAs from this mixture. In order to estimate the vapor pressure of Fe As at high temperature the following experiment was performed. A pellet of single phase FeAs was placed in a long sealed ampoule as in the figure below. The ampoule was placed in the gradient of the tube furnace and the FeAs was heated to 1170 C while the other end was held at about 500 C. Since the vapor pressure of As at 500 C is about 0.1 bar, if the vapor pressure of As above the FeAs is significantly higher than 0.1bar there will be a rapid removeal of the As from the and it will condense at the cold end. After 18 hours at temperature the weight loss from the sample was less than 1%. Given the 5 gram sample, if the weight loss is all As and As gas in monatomic, this is 1 cc of gas at stp. As is either diatomic or triatomic as a gas, I forget which. Given a capsule volume of ~20cc and an average temperature of 600 C we would get something like 1/20 of an atm. of As vapor.

Thus, given our protocol, the failure of an ampoule is unlikely, and should it fail, the secondary containment is more than adequate to handle the resulting as vapor.

We therefore request to raise our maximum As charge to 35 gm.

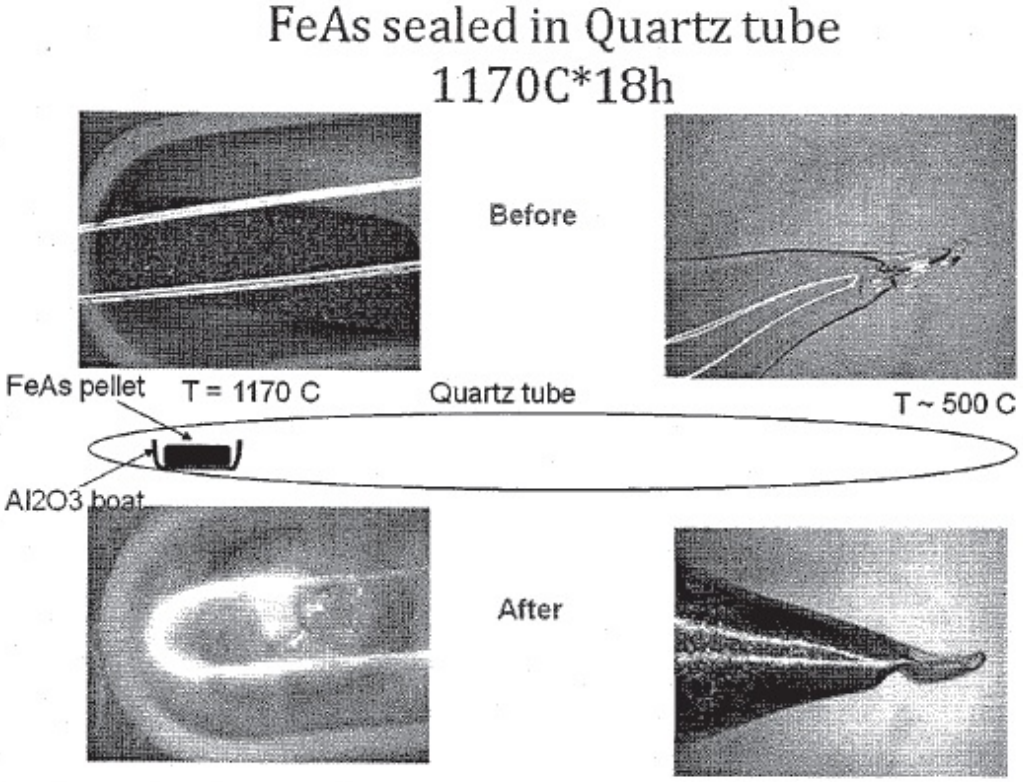
FeAs sealed in Quartz tube
1170C*18h
Before
FeAs pellet
T = 1170 C
Quartz tube
T ~ 500 C
Al2O3 boat
After

APPENDIX B. SUPPLEMENTAL DATA OF MAGNETIC SUSCEPTIBILITY AND RESISTANCE FOR BOTH Ni- AND Rh-SUBSTITUTION

This appendix includes the magnetic susceptibility and resistance data for both Ni- and Rh-substitution that were used to construct phase diagrams but not presented in the main text. For as grown samples (which were quenched from 960°C), due to the violent structure phase transition, the resistance measurement suffers from contact problems. Therefore only magnetic susceptibility data are presented.

Ni-substitution $T_{A/Q} = 500°C$

Figure B.1 presents the data used to construct the T-x phase diagram for Ni-substitution with $T_{A/Q} = 500°C$ shown in Fig. 7.4a. The AFM/ORTH transition is suppressed completely between $x = 0.017$ and 0.019. Sample with $x = 0.019$ shows significant amount of diamagnetism with T_c around 6 K.

Ni-substitution $T_{A/Q} = 960°C$

Figure B.2 presents the data used to construct the T-x phase diagram for Ni-substitution with $T_Q = 960°C$ shown in Fig. 7.4b. The drop in susceptibility is suppressed to lower temperature as Ni substitution level is increased.

Ni-substitution $x = 0.021$

Figure B.3 presents the data used to construct the T-$T_{A/Q}$ phase diagram for Ni-substitution with $x = 0.021$ shown in Fig. 7.4c. The AFM/ORTH phase transition takes place for $T_{A/Q}$

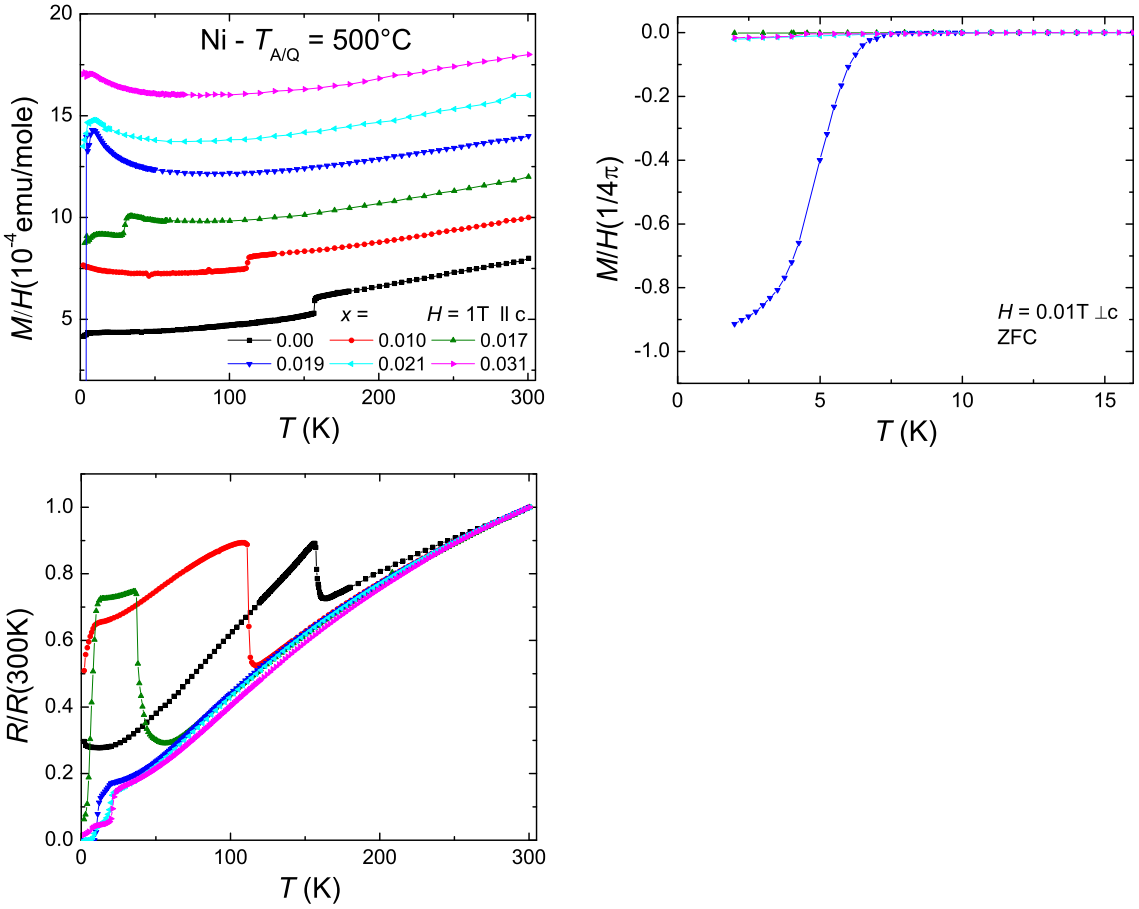

Figure B.1 Temperature dependent (a) magnetic susceptibility with field applied parallel to the c axis, (b) low-field magnetic susceptibility measured upon ZFC with a field of 0.01 T applied perpendicular to the c axis, and (c) normalized electrical resistance of samples with $T_{A/Q} = 500°C$. Susceptibility data in (a) have been offset from each other by an integer multiple of 1×10^{-4} emu/mole for clarity.

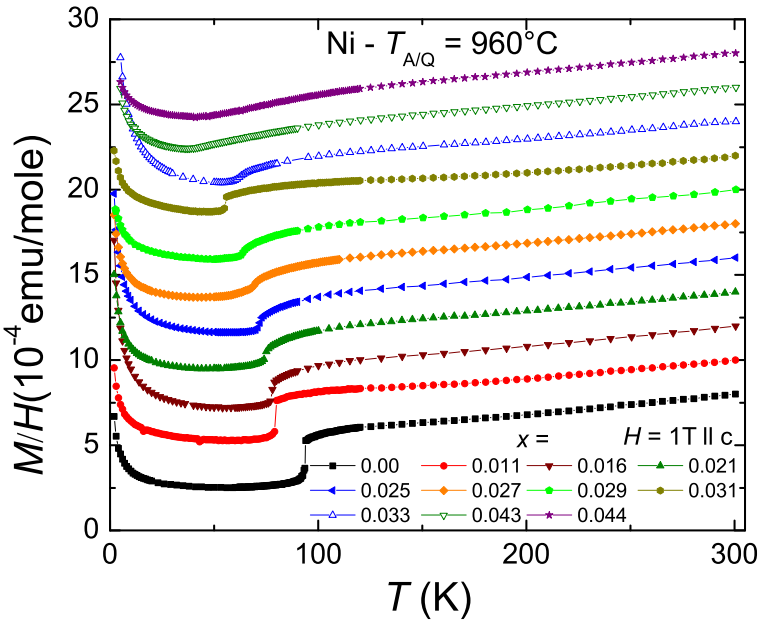

Figure B.2 Temperature dependent magnetic susceptibility with field applied parallel to the c axis of samples with $T_Q = 960$°C. Data have been offset from each other by an integer multiple of 2×10^{-4} emu/mole for clarity.

450°C and the cT phase is stabilized for $T_{A/Q}$ 800°C. No bulk superconductivity is observed for any $T_{A/Q}$.

Ni-substitution $x = 0.026$

Figure B.4 presents the data used to construct the T-$T_{A/Q}$ phase diagram for Ni-substitution with $x = 0.026$ shown in Fig. 7.4c. Sample with $T_{A/Q} = 400$°C shows superconductivity with diamagnetic fraction of 80%. The cT phase is stabilized for $T_{A/Q}$ 800°C.

Rh-substitution $T_{A/Q} = 500$°C

Figure B.5 presents the data used to construct the T-x phase diagram for Rh-substitution with $T_{A/Q} = 500$°C shown in Fig. 7.7a. The AFM/ORTH phase transition is suppressed to 95 K by $x = 0.011$ and the cT phase is stabilized by $x = 0.015$. No bulk superconductivity is observed for any Rh substitution level.

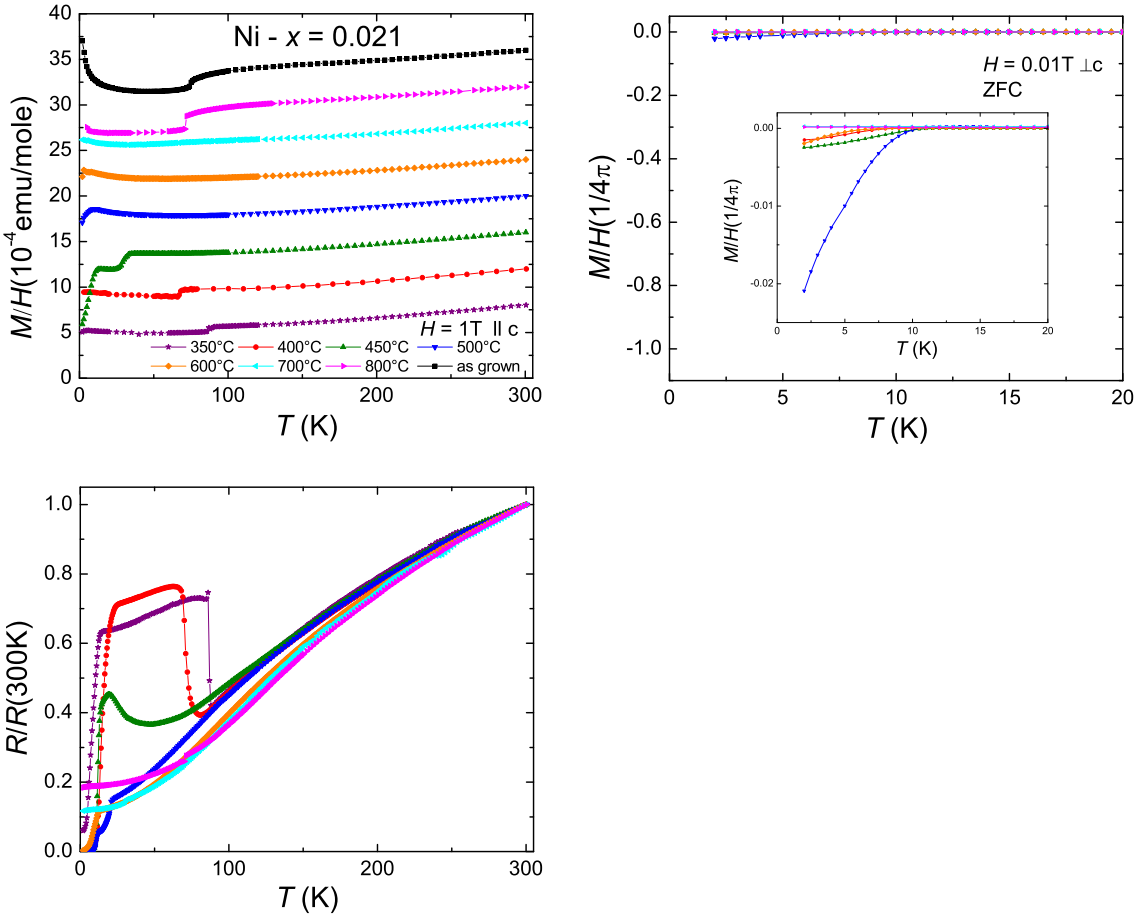

Figure B.3 Temperature dependent (a) magnetic susceptibility with field applied parallel to the c axis, (b) low-field magnetic susceptibility measured upon ZFC with a field of 0.01 T applied perpendicular to the c axis, and (c) normalized electrical resistance of samples with Ni concentration $x = 0.021$. Susceptibility data in (a) have been offset from each other by an integer multiple of 5×10^{-4} emu/mole for clarity.

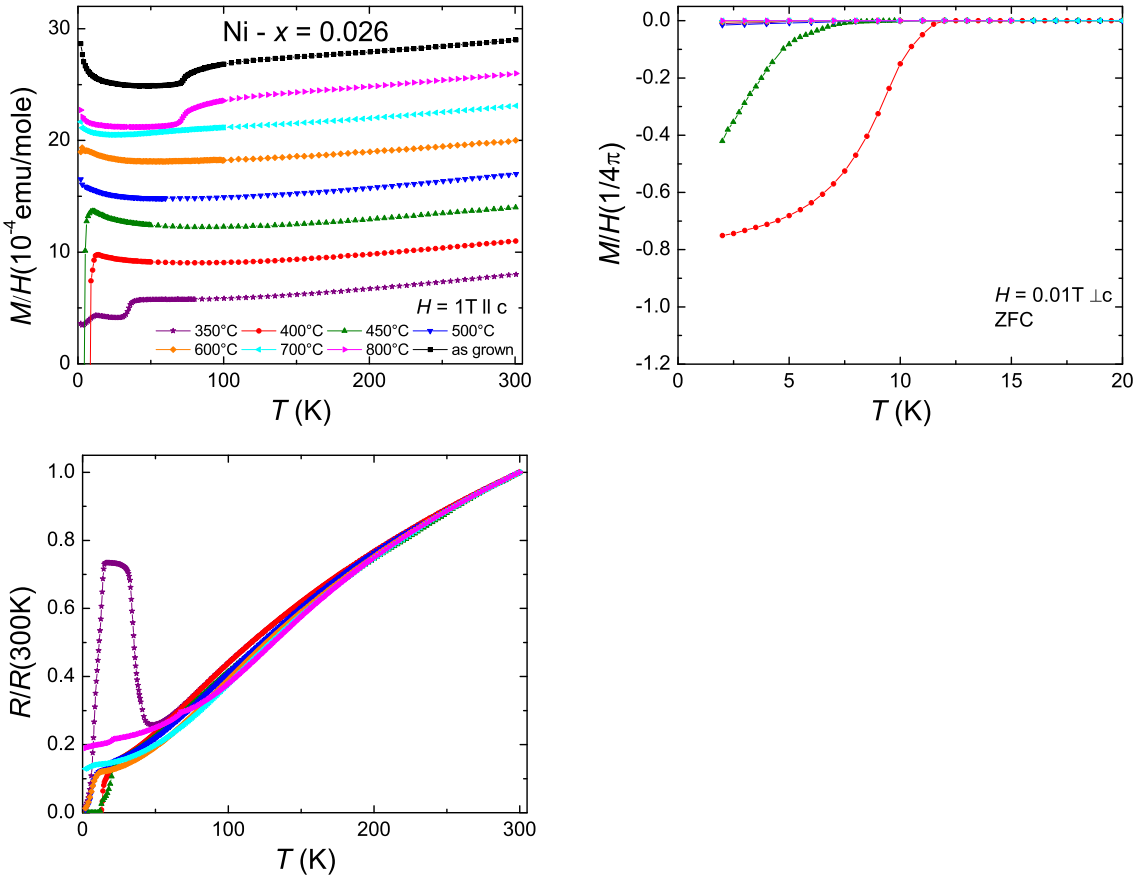

Figure B.4 Temperature dependent (a) magnetic susceptibility with field applied parallel to the c axis, (b) low-field magnetic susceptibility measured upon ZFC with a field of 0.01 T applied perpendicular to the c axis, and (c) normalized electrical resistance of samples with Ni concentration $x = 0.026$. Susceptibility data in (a) have been offset from each other by an integer multiple of 5×10^{-4} emu/mole for clarity.

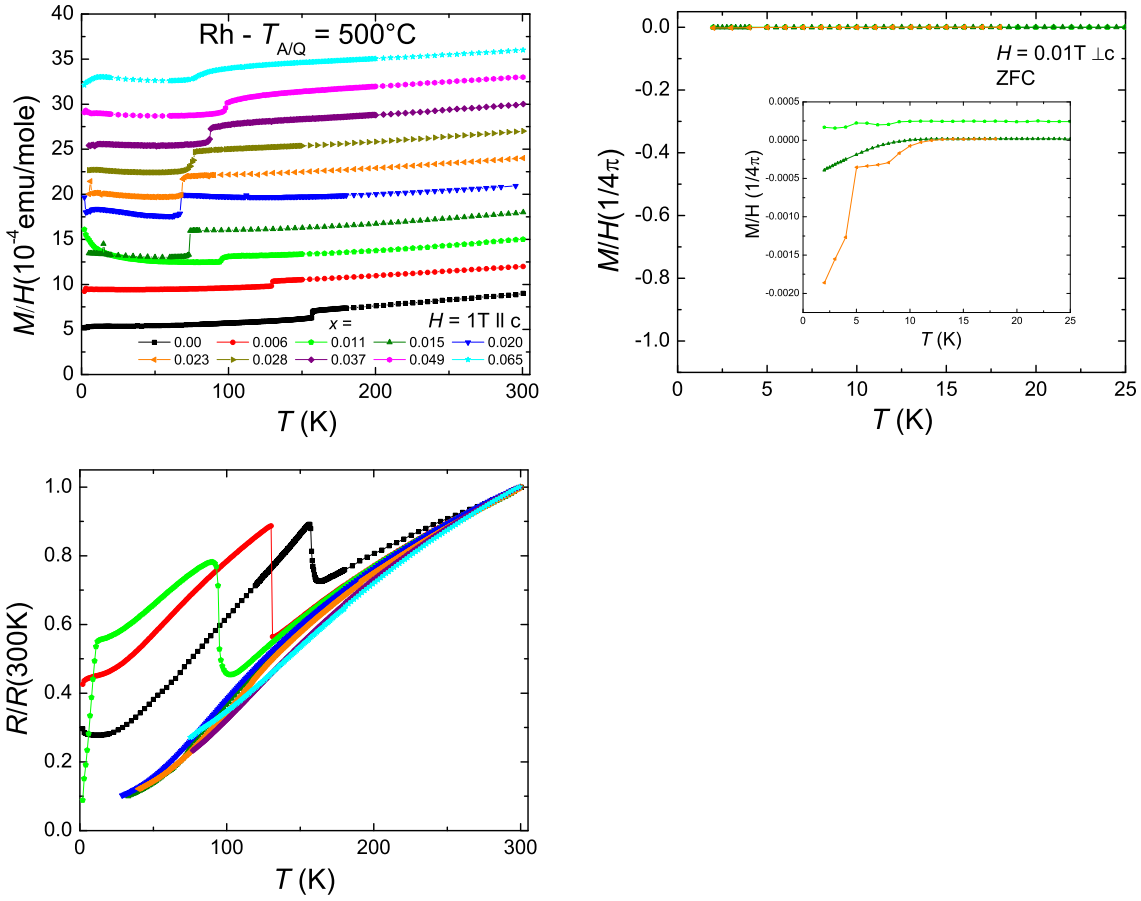

Figure B.5 Temperature dependent (a) magnetic susceptibility with field applied parallel to the c axis, (b) low-field magnetic susceptibility measured upon ZFC with a field of 0.01 T applied perpendicular to the c axis, and (c) normalized electrical resistance of samples with $T_{A/Q} = 500$°C. Susceptibility data in (a) have been offset from each other by an integer multiple of 3×10^{-4} emu/mole for clarity.

Rh-substitution $T_{A/Q} = 960°C$

Figure B.6 presents the data used to construct the T-x phase diagram for Rh-substitution with $T_Q = 960°C$ shown in Fig. 7.7b. With increasing Rh substitution level, the transition temperature of the cT phase is enhanced significantly and the feature associated with the phase transition becomes dramatically broadened.

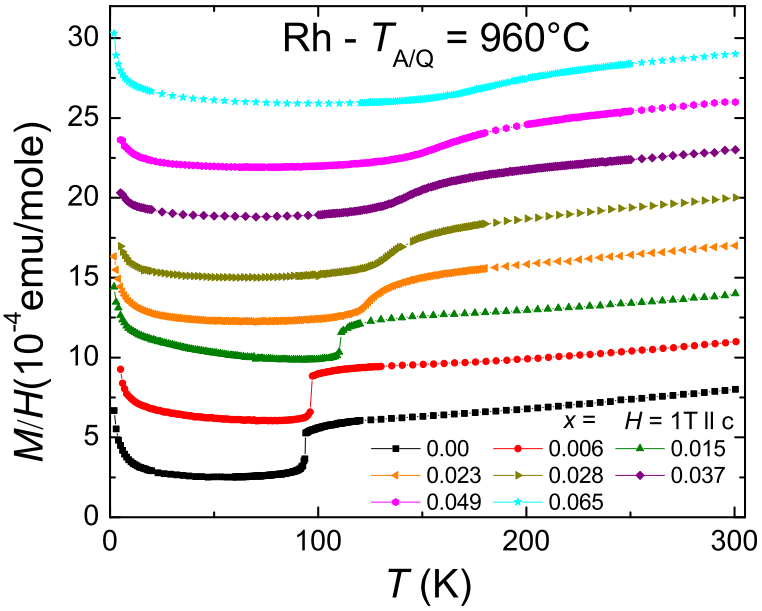

Figure B.6 Temperature dependent magnetic susceptibility with field applied parallel to the c axis of samples with $T_Q = 960°C$. Data have been offset from each other by an integer multiple of 3×10^{-4} emu/mole for clarity.

Rh-substitution $x = 0.015$

Figure B.7 presents the data used to construct the T-$T_{A/Q}$ phase diagram for Rh-substitution with $x = 0.015$ shown in Fig. 7.7c. The AFM/ORTH phase transition takes place for $T_{A/Q} <$ 450°C and the cT phase is stabilized for $T_{A/Q}$ 450°C. No bulk superconductivity is observed for any $T_{A/Q}$.

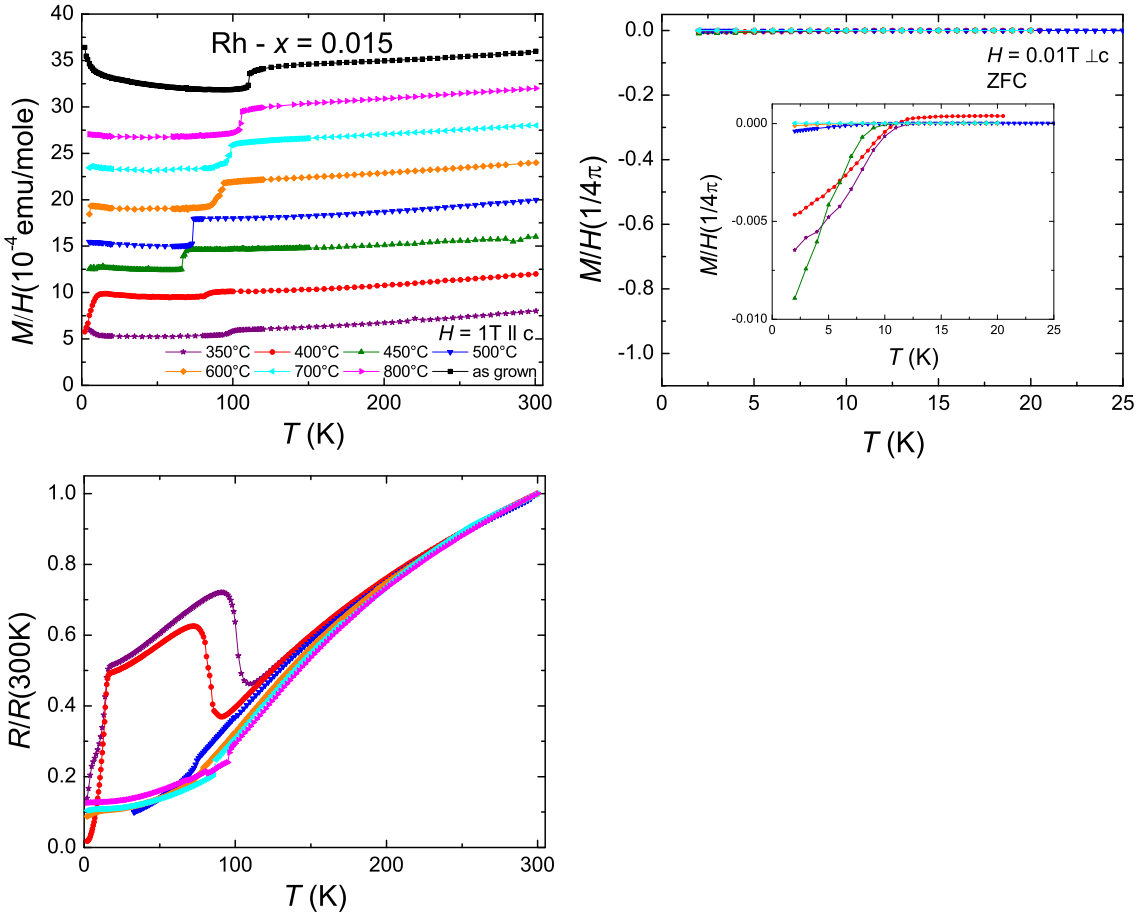

Figure B.7 Temperature dependent (a) magnetic susceptibility with field applied parallel to the c axis, (b) low-field magnetic susceptibility measured upon ZFC with a field of 0.01 T applied perpendicular to the c axis, and (c) normalized electrical resistance of samples with Rh concentration $x = 0.015$. Susceptibility data in (a) have been offset from each other by an integer multiple of 4×10^{-4} emu/mole for clarity.

Rh-substitution $x = 0.023$

Figure B.8 presents the data used to construct the T-$T_{A/Q}$ phase diagram for Rh-substitution with $x = 0.023$ shown in Fig. 7.7d. Superconductivity with full diamagnetic fraction is observed for samples with $T_{A/Q} = 350°C$ and 400°C. The cT phase is stabilized for $T_{A/Q}$ 500°C.

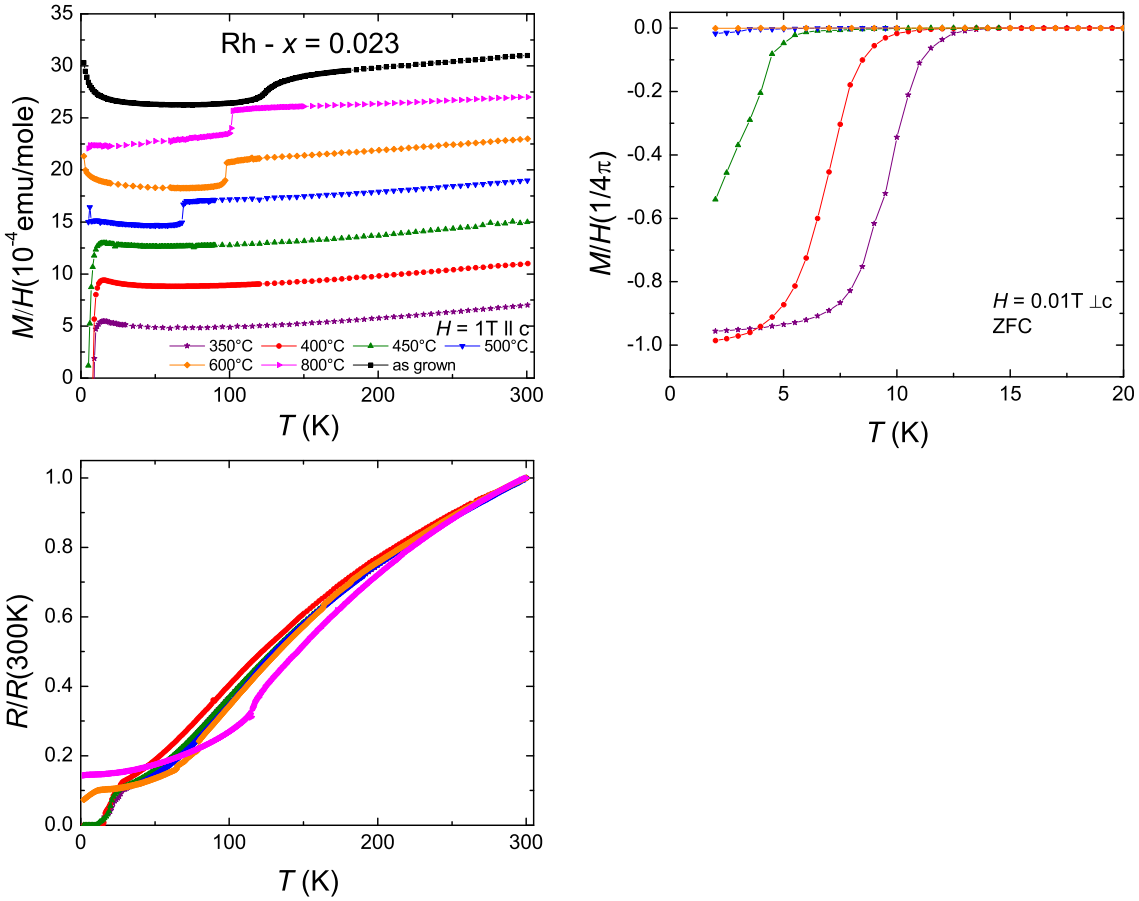

Figure B.8 Temperature dependent (a) magnetic susceptibility with field applied parallel to the c axis, (b) low-field magnetic susceptibility measured upon ZFC with a field of 0.01 T applied perpendicular to the c axis, and (c) normalized electrical resistance of samples with Rh concentration $x = 0.023$. Susceptibility data in (a) have been offset from each other by an integer multiple of 4×10^{-4} emu/mole for clarity.

APPENDIX C. HYDROSTATIC-PRESSURE TUNING OF MAGNETIC, NONMAGNETIC, AND SUPERCONDUCTING GROUND STATES IN ANNEALED $Ca(Fe_{1-x}Co_x)_2As_2$

C.1 Introduction

In previous chapters it has been shown that, for pure $CaFe_2As_2$, $T_{A/Q}$ determines the size and nature of the precipitates inside the samples, therefore the amount of strain built up in the materials. In fact, it was suggested that the effects associated with changing $T_{A/Q}$ mimic the effects of changing pressure. It is important to check if such a P-$T_{A/Q}$ analog exists in $Ca(Fe_{1-x}Co_x)_2As_2$ systems.

One other motivation for the pressure study of $Ca(Fe_{1-x}Co_x)_2As_2$ systems is related with the interplay of the various types of order in iron-based superconductors. Whether superconductivity coexists with antiferromagnetic order in the so-called "underdoped" areas of the phase diagram is of particular interest (Pratt et al., 2009a; Rotter et al., 2009; Aczel et al., 2008; Goko et al., 2009; Park et al., 2009; Julien et al., 2009) as this aspect is thought to hold the clue for discriminating the unconventional s+- type of superconductivity from the conventional s++ one (Fernandes et al., 2010; Fernandes and Schmalian, 2010). The annealing/quenching study of $Ca(Fe_{1-x}Co_x)_2As_2$ seems to reveal that superconductivity does not coexist with antiferromagnetic order for any combination of Co concentration and annealing/quenching temperature in this system. However, with finite control of both x and $T_{A/Q}$, I can not tune the system with arbitrarily small steps so as determine this unambiguously. With hydrostatic-pressure the system can be tuned with much finer steps to clarify these issues in a systematic fashion.

In this appendix, I will present the results of the magnetic susceptibility and electrical resistance measurements under He-gas pressure on single crystals of $Ca(Fe_{1-x}Co_x)_2As_2$. This

work was done in collaboration with research group of Dr. Michael Lang from Goethe University Frankfurt, Germany. It was found that with reasonably small and truly hydrostatic pressure, the salient ground states associated with iron-based superconductors, i.e., antiferromagnetic/orthorhombic (AFM/ORTH), superconducting (SC/PM/T), non superconducting (N/PM/T) and non-moment bearing/collapsed tetragonal (cT) states can be accessed all in one sample, i.e., $x = 0.028/T_{A/Q} = 350$°C. Systematic investigations of the various phase transitions and ground states via pressure tuning revealed no coexistence of bulk superconductivity with the antiferromagnetic state which we link to the strongly first-order character of the corresponding structural/magnetic transition in this compound. A P-$T_{A/Q}$ conversion was established and composite, unified phase diagrams were constructed.

Part of this appendix is based on the published article: Gati, E. and Köhler, S. and Guterding, D. and Wolf, B. and Knöner, S. and Ran, S. and Bud'ko, S. L. and Canfield, P. C. and Lang, M. "Hydrostatic-pressure tuning of magnetic, nonmagnetic, and superconducting states in annealed $Ca(Fe_{1-x}Co_x)_2As_2$" *Phys. Rev. B*, 86 (2012):220511(R), editors' suggestion.

C.2 Result

Figure C.1 shows the magnetic susceptibility and normalized electrical resistance data of $Ca(Fe_{1-x}Co_x)_2As_2$ with $x = 0.028/T_{A/Q} = 350$°C for a selection of pressure values. The data reveal distinctly different types of anomalies which are found to be representative of three distinct pressure ranges. At low pressure values, $P \leq 32$ MPa, represented by the $P = 0$ data (Figs. C.1a and C.1d), a downward jump in magnetization and upward jump in resistance were observed upon cooling, indicating the AFM/ORTH phase transition. There is a distinct hysteresis of with a few degrees.

At intermediate pressure values 32 MPa $\leq P \leq$ 180 MPa, represented by the $P = 60$ MPa data (Figs. C.1b and C.1e), a screening of around 100% of $1/4\pi$ in low field magnetization together zero resistance is observed. The superconducting transition temperature inferred from magnetization is 13.8 K. The features observed here, i.e., screening of around 100% of $1/4\pi$ accompanied by zero resistance, are similar to what has been seen for sample with $x = 0.033/T_{A/Q} = 350$°C under ambient pressure in last chapter, where the bulk character of

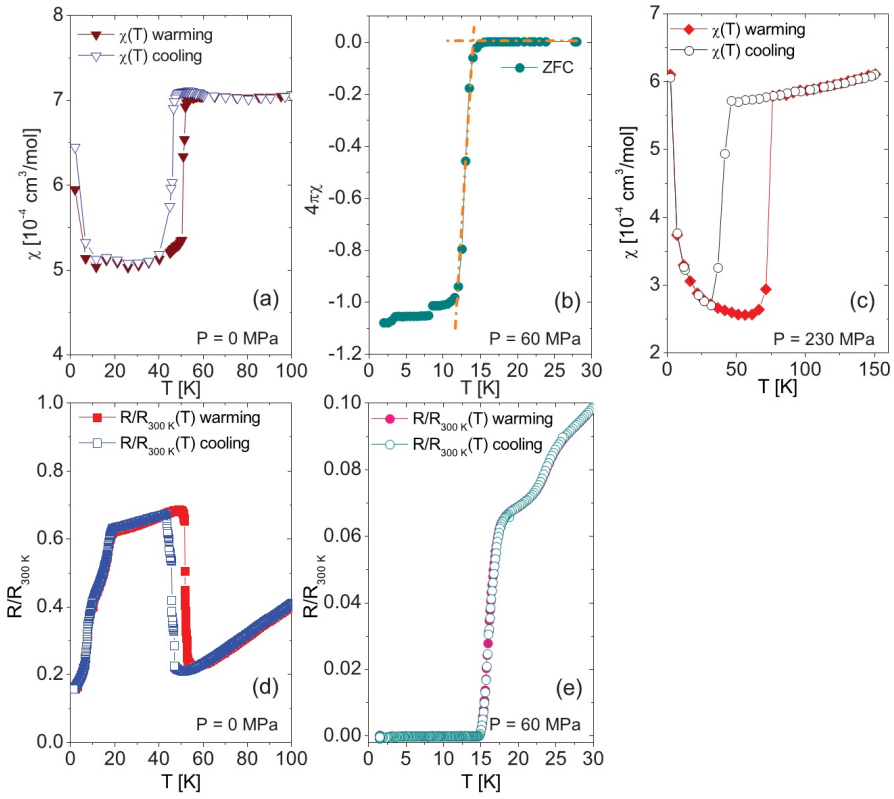

Figure C.1 Magnetization (a, b and c) and normalized electrical resistance (d and e), of $Ca(Fe_{1-x}Co_x)_2As_2$ with $x = 0.028/T_{A/Q} = 350°C$ at $P = 0$ MPa (a and d), 60 MPa (b and e), and 230 MPa (c). Magnetization data were taken in magnetic field of 1 T (a and c) and 1 mT (b) after ZFC. Small step in ($P = 60$ MPa) (b) around 8 K results from the solidification of ^{4}He, while step at 3 K marks T_c of a small In sample used as a manometer. (Gati et al., 2012)

superconductivity was further demonstrated by specific heat measurements.

At higher pressures $P \geq 210$ MPa, represented by the $P = 230$ MPa data (Fig. C.1c), no further superconductivity is observed. Instead, magnetization shows a sharper drop and an even more pronounced hysteresis than the low-P features associated with AFM/ORTH. Both the enhanced jump size and its positive pressure dependence distinguish this transition from the one at AFM/ORTH transition, characterized by a huge negative pressure coefficient (see below). The phenomenology observed here is identical to that found for $T_{A/Q} = 350$°C $CaFe_2As_2$ (chapter 5) or $Ca(Fe_{1-x}Co_x)_2As_2$ with $x \geq 0.01$ and $T_{A/Q} \geq 600$°C (chapter 6), where structural investigations have identified this feature as the transition into the cT phase. Since large lattice deformations accompany this phase transition, often leading to cracks within the sample and/or the loss of electrical contacts, no resistance data could be obtained below T_{cT} in the pressure study, consistent with the study under ambient pressure. The corresponding transition temperatures derived from cooling and warming are 39 K and 73.6 K, respectively. Since the cT phase transition is accompanied by a pronounced hysteresis as a function of P at fixed T (Goldman et al., 2009), the temperature sweeps reported here have been performed in a sequence with increasing pressure.

After having identified the nature of the various anomalies observed in magnetization and normalized electrical resistance measurements and having determined phase transition temperatures, a T - P phase diagram for x =0.028/ $T_{A/Q}$ =350°C sample is constructed (Fig. C.2). The figure highlights the extraordinarily high sensitivity of the AFM/ORTH transition to pressure: upon increasing pressure $T_{s,N}$ becomes reduced in a linear fashion from $T_{s,N} = 51$ K (0 MPa) to 29.5 K (20 MPa) and 16.5 K (30 MPa), corresponding to an unprecedentedly large pressure dependence of $\mathrm{d}T_{s,N}/\mathrm{d}P = (1100 \pm 50)$ K/GPa. The strongly hysteretic behavior revealed in the $M(T)$ and $R(T)/R(300K)$ measurements demonstrates that the AFM/ORTH transition remains first order within this pressure range. At the same time the occurrence of some filamentary superconductivity with $T_c \simeq 15$ K is observed, the screening at base temperature (2 K) of which gradually grows from 0 (0 MPa) to about 1 % of $1/4\pi$ (10 MPa) and 3 % of $1/4\pi$ (28 MPa). Upon further increasing the pressure to $P = 32$ MPa, however, no discontinuous changes accompanied by hysteretic behavior down to 2 K (1.6 K), the lowest

temperature in the magnetic (resistance) measurements, were found. This suggests that at this pressure level no phase transition line into the AFM/ORTH phase has been crossed in the T range investigated. Instead, the data show zero resistance both in cooling and warming runs and the superconducting screening at base temperature (2 K) which starts growing rapidly, reaching about 12 % (60 %) of $1/4\pi$ at $P = 32$ MPa (40 MPa). A screening of 100 % of $1/4\pi$ is revealed for P above about 50 - 60 MPa up to 156 MPa. In this pressure range T_c shows, to a good approximation, a linear reduction with P from 13.8 K (60 MPa) to 9 K (156 MPa). This corresponds to a pressure coefficient of $\mathrm{d}T_c/\mathrm{d}P = (60 \pm 3)$ K/GPa, again exceptionally large. (For comparison, $\mathrm{d}T_c/\mathrm{d}P$ values for some other superconducting materials are: between 0.7 and 1.2 K/GPa for MgB_2 (Bud'ko et al., 2005); ≈ 0 K/GPa for YNi_2B_2C and $ErNi_2B_2C$ (Matsuda et al., 2000); ≈ 0.5 K/GPa for $HoNi_2B_2C$ (Uwatoko et al., 1996) and $TmNi_2B_2C$ (Oomi et al., 1999); ≈ 0.4 K/GPa for Pb (Wittig, 1966) and ≈ 0.5 K/GPa for Sn (Jennings and Swenson, 1958).)

The progression of the transition temperature T_{cT} with pressure shown in Fig. C.2 suggests a close connection between the occurrence of the collapsed tetragonal phase and the disappearance of superconductivity: a linear extrapolation of the T_{cT}^{cool} line towards lower pressure (the broken line in Fig. C.2) truncates the T_c line around the critical pressure P_c^{sc} (~ 165 MPa) above which superconductivity disappears. The data for T_{cT}^{cool} is difficult to collect given that even the solidification of helium (shown as fine black line in Fig. C.2) is enough to give rise to non-hydrostaticity associated with the changes in the sample dimensions.

In order to further probe the pressure/$T_{A/Q}$ analogy, we have carried out an analogous pressure study on another crystal with almost identical x but different $T_{A/Q}$ (Fig. C.3). According to the study under ambient pressure (chapter 6), an enhancement of $T_{A/Q}$ leads to a suppression of the AFM/ORTH phase and the emergence of superconductivity. Thus, for these crystals one may expect to observe the P-induced change from superconductivity to the collapsed tetragonal phase already at smaller pressure values. Figure C.3 shows the results on a $Ca(Fe_{1-x}Co_x)_2As_2$ crystal with x =0.029/ $T_{A/Q}$ =400°C. At $P = 0$ the system shows a superconducting ground state with $T_c = 15.4$ K and full diamagnetic shielding. Upon increasing the pressure to 133 MPa, T_c is reduced to 7.8 K, while the shielding signal stays essentially

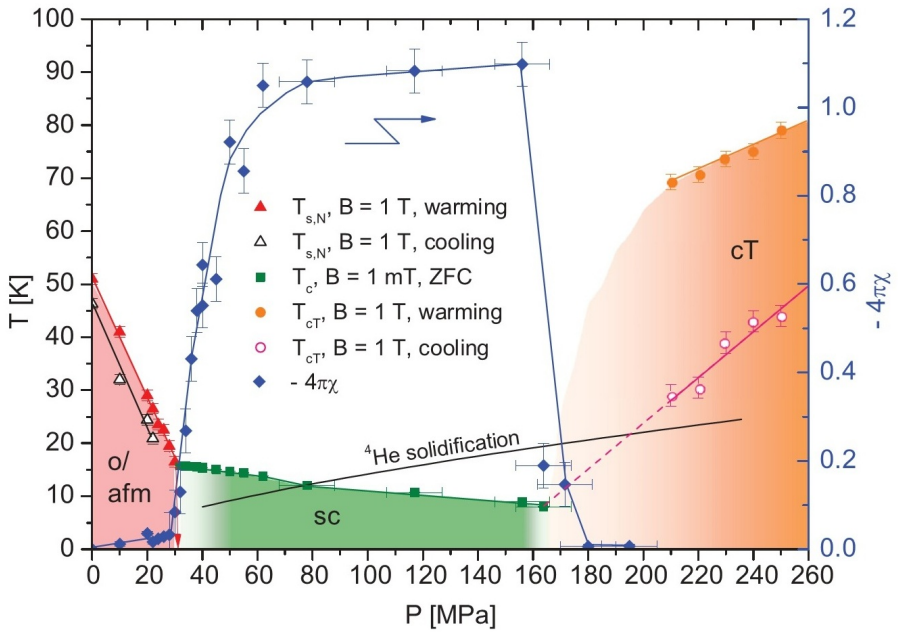

Figure C.2 T - P phase diagram of single crystalline $Ca(Fe_{1-x}Co_x)_2As_2$ with $x = 0.028/\ T_{A/Q}$ = 350°C inferred from magnetization data. Filled (open) up triangles correspond to the transition into the AFM/ORTH phase at $T_{s,N}$. Filled squares represent transition into the SC/PM/T phase at T_c inferred from ZFC measurements. For those T_c values determined below the solidification line of ^{4}He (black solid line), the P values have been corrected by a factor 0.78 to account for the P drop accompanying solidification. Closed diamonds indicate the size of the screening (right scale). Filled (open) circles correspond to transition into the cT phase. (Gati et al., 2012)

constant. Note that the corresponding pressure coefficient of $\mathrm{d}T_c/\mathrm{d}P = (60 \pm 3)$ K/GPa is identical to that obtained for the $x = 0.028/T_{A/Q} = 350°\mathrm{C}$ sample. Further similarities to the latter sample include the abrupt disappearance of superconductivity within a very narrow pressure window, here 130 - 140 MPa, and the observation of magnetic signatures of the collapsed tetragonal phase transition at somewhat higher pressures. Here too, the tracking of the magnetic signatures of T_{cT}^{cool} towards lower pressure is hampered by the limitations set by the solidification of ^{4}He. Yet, the available T_{cT} data show the same characteristics as revealed for the $x = 0.028/T_{A/Q} = 350°\mathrm{C}$ sample, i.e., a linear extrapolation of the $T_{cT}^{cool}(P)$ (the broken line in Fig. C.3) truncates superconductivity.

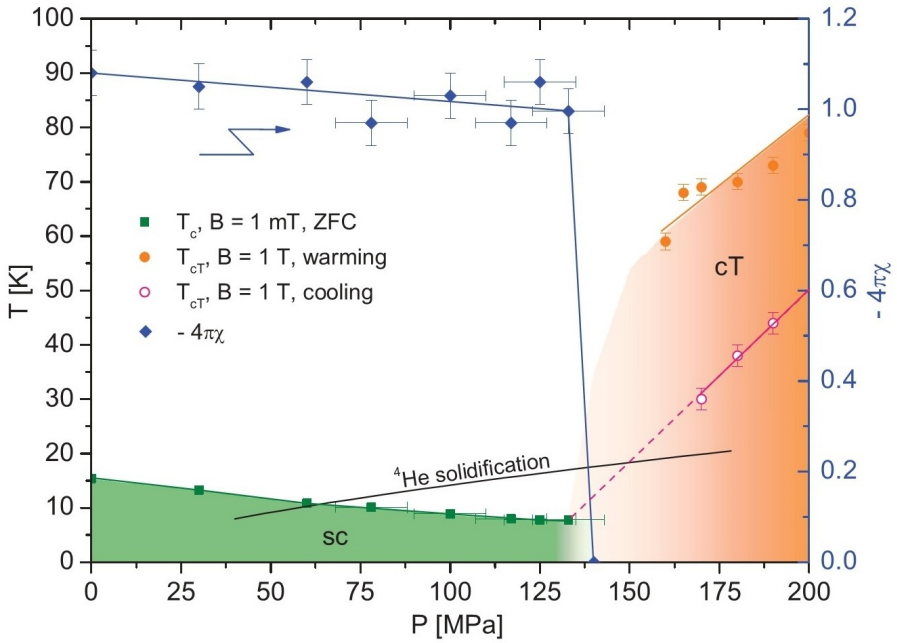

Figure C.3 T - P phase diagram of $Ca(Fe_{1-x}Co_x)_2As_2$ with x =0.029/ $T_{A/Q}$ =400°C inferred from $\chi(T)$ measurements. Filled squares represent T_c values (left scale) inferred from ZFC measurements and filled diamonds represent the corresponding diamagnetic shielding volume (right scale). Filled (open) circles correspond to T_{cT} as inferred from measurements upon warming (cooling). The black solid line indicates the solidification of ^{4}He. (Gati et al., 2012)

C.3 Discussion

The results in this study provide direct evidence for the existence of a P - $T_{A/Q}$ analogy for the present materials, indicating that here the effects associated with changing $T_{A/Q}$ mimic the effects of changing pressure as suggested in previous chapters. In fact, the various phase transition temperatures revealed for $Ca(Fe_{1-x}Co_x)_2As_2$ with $x = 0.028/\,T_{A/Q} = 350°C$ and $x = 0.029/\,T_{A/Q} = 400°C$ in the present pressure studies and those obtained from an x =0.028 sample treated with varying $T_{A/Q}$, can be combined in a composite, unified phase diagram as presented in Fig. C.4. To make the comparison, samples with $x = 0.028$ and $x = 0.029$ are considered to have the same Co concentration, which is a reasonable assumption. Therefore, these two samples are represented by different annealing/quenching temperature on the same T-$T_{A/Q}$ phase diagram at ambient pressure. By using the conversion $\Delta\,T_{A/Q} = 100°C$ being equivalent to $\Delta P = 84.6$ MPa an almost perfect matching is obtained for all the $T_{s,N}$, T_c and T_{cT} lines both as a function of $T_{A/Q}$ (data points) and of pressure (lines) for these two samples. In order to assess the extent to which this P - $T_{A/Q}$ conversion is valid, a third sample, $x = 0.038/\,T_{A/Q} = 350°C$, was also studied under pressure. It can be seen that using the same conversion a good matching is obtained for T_c and T_{cT} lines.

$CaFe_2As_2$ was known to be the most pressure sensitive of the $AEFe_2As_2$ and 1111 compounds. For $Ca(Fe_{1-x}Co_x)_2As_2$ with $x = 0.028$, the pressure coefficients of the various phase transitions lines revealed here of $\mathrm{d}\,T_{s,N}/\mathrm{d}P = (1100 \pm 50)$ K/GPa, $\mathrm{d}\,T_c/\mathrm{d}P = (60 \pm 3)$ K/GPa, and $\mathrm{d}\,T_{cT}^{cool}\,/\mathrm{d}P = +(420 \pm 70)$ K/GPa all are exceptionally large, by far the largest among all iron-based superconductors (Chu and Lorenz, 2009; Sefat, 2011).

From these observations, together with literature results, some important conclusions can be drawn as for the interplay of superconductivity with the nearby structural and antiferromagnetic orders that form in the 122 family. Most importantly, given the microscopic coexistence of competing superconducting and AFM/ORTH phases, well established for $Ba(Fe_{1-x}Co_x)_2As_2$ (Pratt et al., 2009a; Laplace et al., 2009; Julien et al., 2009; Bernhard et al., 2009), where the transition at $T_{s,N}$ is of second order, we link the noncoexistence in the present case to the strongly first-order character of the $T_{s,N}$ line. This finding, together with the absence

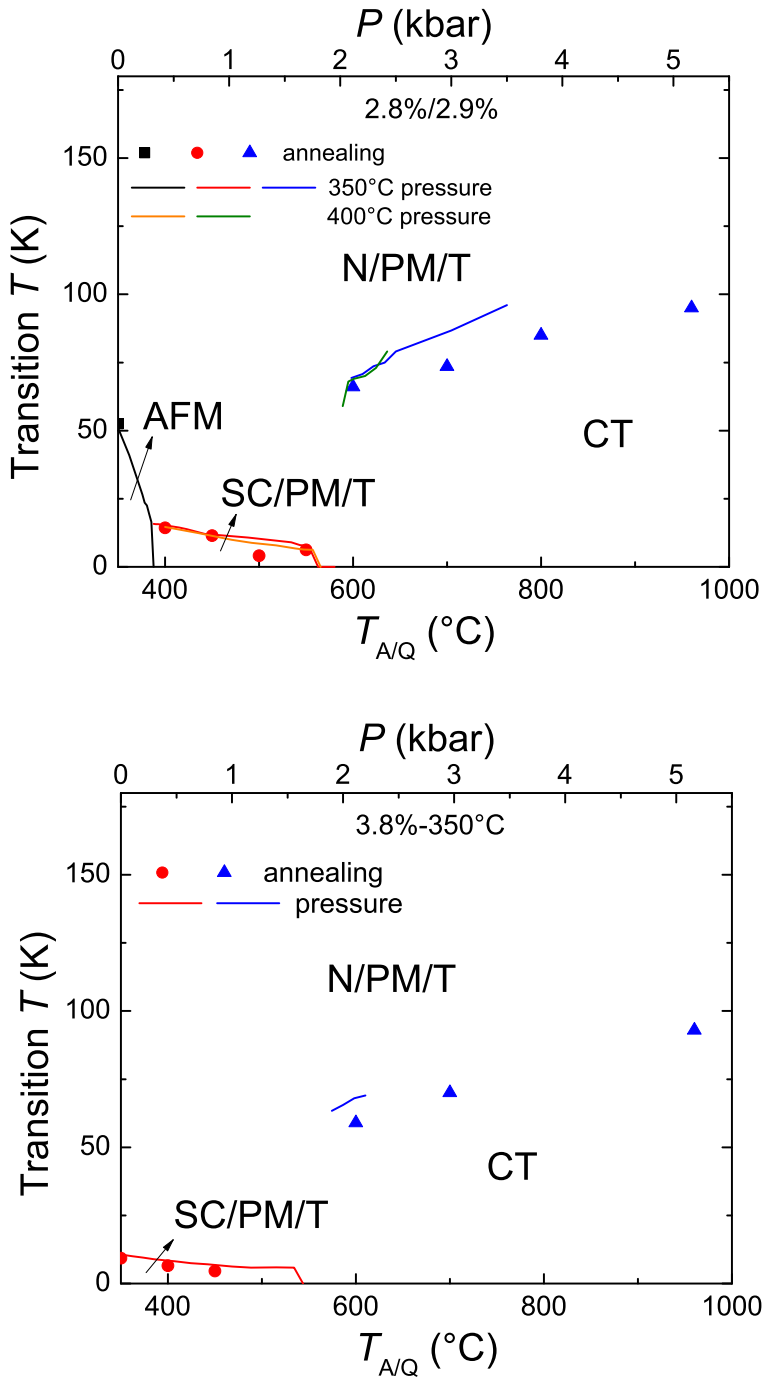

Figure C.4 Phase diagram of transition temperature versus pressure and $T_{A/Q}$ for samples with (a) $x = 0.028/T_{A/Q} = 350$°C and $x = 0.029/T_{A/Q} = 400$°C and (b) $x = 0.038/T_{A/Q} = 350$°C. Filled symbols represent data from annealing study. Lines correspond to data from pressure study.

of superconductivity in the nonmagnetic collapsed tetragonal phase, clearly indicate that preserving fluctuations associated with the AFM/ORTH transition to low enough temperatures is vital for the formation of superconductivity. It seems that in the present first-order situation, the competition between superconductivity and the AFM/ORTH order manifests itself in a separation of the two phases, i.e., a sudden drop of the $T_{s,N}$ line preceding the formation of superconductivity at higher pressures, consistent with the experimental observations.

C.4 Summary

I present the measurements of the magnetization and electrical resistance under He-gas pressure on FeAs-grown single crystals of $Ca(Fe_{1-x}Co_x)_2As_2$ with post growth thermal treatment. It was found that for $x = 0.028/T_{A/Q} = 350°C$ sample, the salient ground states associated with iron-based superconductors, i.e., antiferromagnetic/orthorhombic (AFM/ORTH), superconducting/paramagnetic/tetragonal (SC/PM/T), and non-moment bearing/collapsed tetragonal (cT) states can be accessed all in one sample with reasonably small and truly hydrostatic pressure. This is possible owing to the extreme sensitivity of the AFM/ORTH, SC/PM/T and cT states against variation of pressure. Systematic investigations of the various phase transitions and ground states via pressure tuning revealed no coexistence of bulk superconductivity with the AFM/ORTH state which is linked to the strongly first-order character of the corresponding structural/magnetic transition in this compound. The results also reveal that in the FeAs-grown $Ca(Fe_{1-x}Co_x)_2As_2$ system, P-$T_{A/Q}$ analog still exists with a well defined conversion.

C.5 Stress Sensitivity of $Ca(Fe_{1-x}Co_x)_2As_2$

As the above experimental data have shown, single crystals of $Ca(Fe_{1-x}Co_x)_2As_2$ exhibit extreme sensitivity to the pressure and strain. In addition, this sensitivity is also seen when external stress is applied in other form. For example, when preparing samples of $Ca(Fe_{1-x}Co_x)_2As_2$ with $x = 0.036/T_{A/Q} = 400°C$ for Mössbauer measurements, a thin piece (around 0.1 mm thick)of sample was glued to mylar using GE varnish. As can be seen from the T-x phase dia-

gram for 400°C (chapter 6), the $x = 0.036/T_{A/Q} = 400$°C sample has superconducting phase transition at around 6 K. However, the GE varnish glued sample shows significantly higher T_c, around 12 K, as seen in Fig. C.5. This change of T_c can be done in a reversible manner. Once the the mylar, as well as the GE varnish, is removed from the sample surface, the unglued sample resume its T_c.

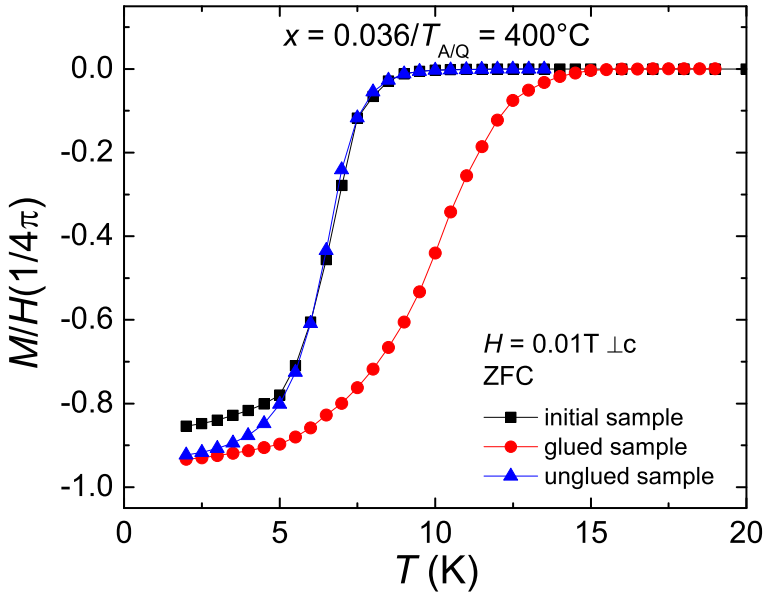

Figure C.5 Temperature dependent, low field magnetic susceptibility measured upon zero field cooling (ZFC) with a field of 0.01 T applied perpendicular to the c-axis of $Ca(Fe_{1-x}Co_x)_2As_2$ samples with $x = 0.036/T_{A/Q} = 400$°C.

Note that the screening remains close to 100% of $1/4\pi$ for the GE varnish glued sample, indicating the superconductivity is still bulk. This is further supported by specific heat measurements. As seen in Fig. C.6, the data of ΔC_P versus T_c follows the BNC scaling very well.

It is very likely that the change of T_c is due to the stress caused by the GE varnish and mylar. Upon cooling down, the sample and GE varnish and mylar might have different thermal expansion. Depending on the relative size of the thermal expansion, GE varnish and mylar can exert positive or negative stress on the sample, therefore depress or enhance T_c. Assuming the same pressure dependence of T_c as under the hydrostatic pressure, $\mathrm{d}T_c/\mathrm{d}P = (60 \pm 3)$ K/GPa,

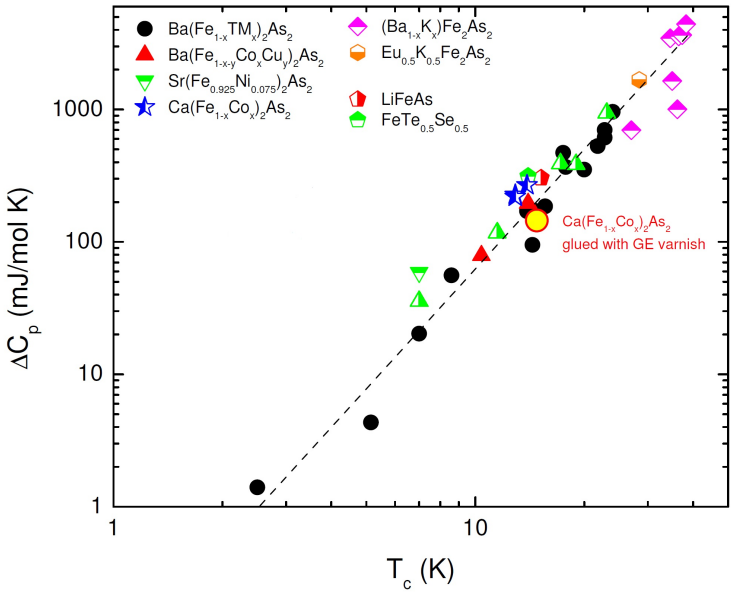

Figure C.6 ΔC_P vs T_c for a GE varnish glued $Ca(Fe_{1-x}Co_x)_2As_2$ sample with $x = 0.036/\, T_{A/Q} = 400°C$, plotted together with literature data for various FeAs-based superconducting materials.

the shift of the T_c corresponds to negative stress of roughly 0.1 GPa. In reality the stress is probably highly non-hydrostatic and, as such could be significantly less.

It is conceivable that with negative stress, a sample with higher T_c, and therefore closer to the AFM/ORTH phase region, could be driven from superconducting phase to AFM/ORTH phase. The same experiment was conducted on a $x = 0.035/\, T_{A/Q} = 350°C$ sample, which shows $T_c = 15$ K. As seen from Fig. C.7, the GE varnish glued sample exhibits the same T_c with screening reduced by half, indicating the lose of volume fraction of superconducting material. Meanwhile, the high field magnetization data of the glued sample shows a tiny, but well visible jump at around 50 K. It is very possible that part of the sample is indeed driven from the SC/PM/T phase to the AFM/ORTH phase. Again, the change can be done in a reversible manner. Once the GE varnish is removed, the sample recovers the amount of screening and the feature in high field magnetization also disappears. Note significant difference of the high temperature magnetization value in the high filed. This is very likely due to the signal from GE varnish and mylar.

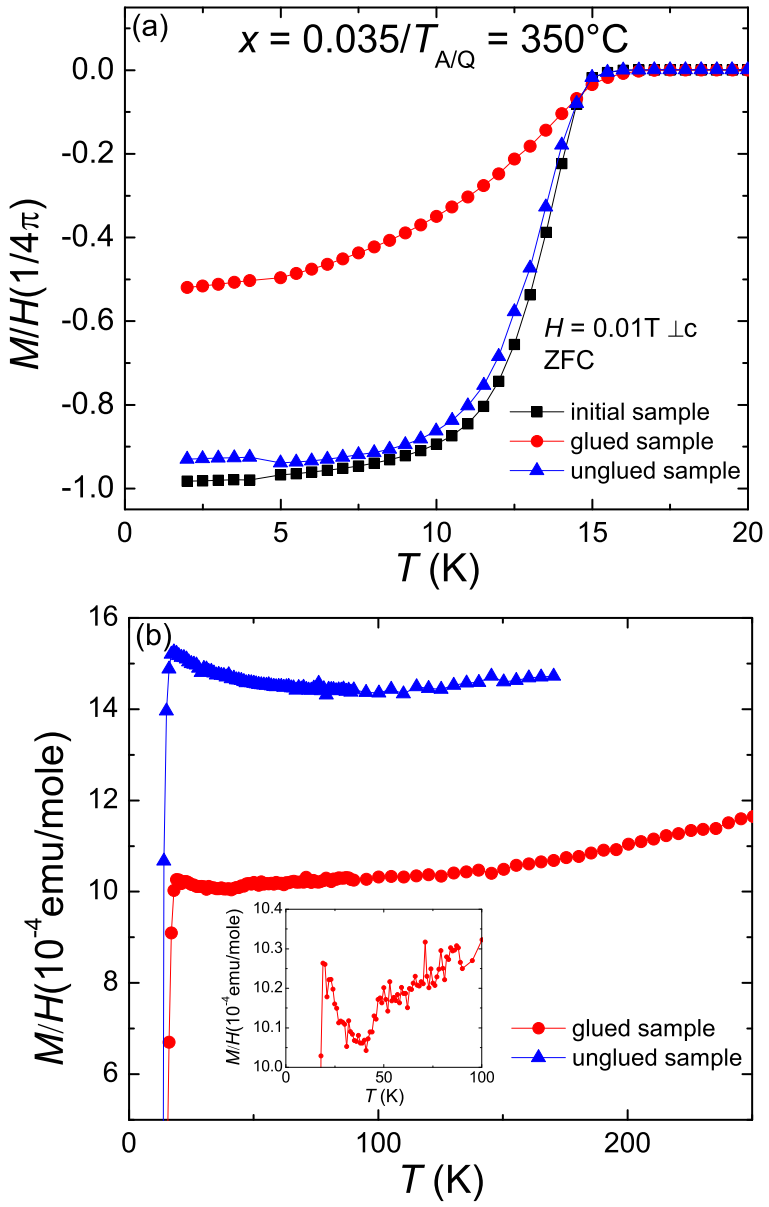

Figure C.7 Temperature dependent (a) low field magnetic susceptibility measured upon zero field cooling (ZFC) with a field of 0.01 T applied perpendicular to the c-axis, and (b) magnetic susceptibility with a field of 1 T applied perpendicular to the c-axis of $Ca(Fe_{1-x}Co_x)_2As_2$ samples with $x = 0.035/\,T_{A/Q} = 350°C$.

APPENDIX D. EFFECTS OF SUBSTITUTION ON LOW TEMPERATURE PHYSICAL PROPERTIES OF $LuFe_2Ge_2$

D.1 Introduction

In addition to the study of effects of annealing/quenching on physical properties of $CaFe_2As_2$, I also conducted one other project during my Ph.D work, to study effects of chemical substitution on low temperature physical properties of $LuFe_2Ge_2$. This project was motivated by the discovery of iron based superconductors where chemical substitutions to the parent compounds suppress the structural and magnetic phase transitions and can ultimately reveal superconductivity with a relatively high transition temperature (Ni et al., 2008a,c; Thaler et al., 2010; Canfield and Bud'ko, 2010). The proximity of the suppressed magnetic / structural phase transitions to the maximum T_c values, as well as more direct evidence, suggest the importance of magnetism, most likely itinerant magnetism, to the superconducting state.

$LuFe_2Ge_2$ forms in the same crystal structure as one of the most extensively studied families of iron based superconductors, $AEFe_2As_2$, (AE = Ca, Sr, Ba) ($ThCr_2Si_2$ crystal structure with space group I4/mmm) (Avila et al., 2004). The parent compound manifests anomalies in susceptibility, resistivity and specific heat at 9 K that have been associated with itinerant magnetic order. Although the precise nature of the magnetic ordering is still unclear, analysis of susceptibility, resistivity and specific heat data lead to the prediction of a SDW state, most likely with an ordering wave vector along a [00l] direction, a result subsequently found by neutron scattering measurements (Fujiwara et al., 2007). Two alternate hypotheses are (i) that $LuFe_2Ge_2$ (and YFe_2Ge_2) are close to the Stoner limit and easily forced into a magnetically ordered state, or (ii) that the Fe is moment bearing with a large paramagnetic effective moment (Ferstl et al., 2006), but both of these hypotheses are inconsistent with the relatively low

ordering temperatures of the other RFe_2Ge_2 members which are closer to those of RNi_2Ge_2 (Bud'ko et al., 1999) rather than RMn_2Ge_2 (Szytula and Leciejewicz, 1989) or the Stoner enhanced RFe_2Ge_{20} compounds (Jia et al., 2007a,b, 2008).

In order to better characterize this phase transition, I studied the effects of Y and Sc substitutions on the Lu site, as well as Ru and Co substitutions on the Fe site, on the low temperature properties of the parent compound and present the phase diagram for Y, Sc and Ru substitutions. All the samples were grown using Sn flux as described in the section of experimental method and the previous literature (Avila et al., 2004). The isoelectronic substitution: Y, Sc, and Ru, can be considered as chemical pressure or strain causing primarily steric effects, whereas Co substitution, can be considered (in a rigid band model) as adding electrons and thereby causing changes in the band filling as well. The goal of this work was to see how the antiferromagnetic ordering evolves with different substitutions.

This appendix is heavily based on the published article: Ran, S., Bud'ko, S. L. and Canfield, P. C. "Effects of substitution on low-temperature physical properties of $LuFe_2Ge_2$" *Philosophical Magazine*, 91 (2011):3113.

D.2 Results

A summary of the WDS measurement data is presented in Table D.1. The table shows the nominal concentration, the measured average x values, and two times the standard deviation of the x values measured. For each substitution, data points of nominal versus actual concentration can be fitted very well with straight lines, with slopes of 1.08 ± 0.03, 0.23 ± 0.005, 0.70 ± 0.01 and 1.75 ± 0.07 for Y, Sc, Ru and Co substitution, respectively. It can be seen that the difference between nominal and WDS concentration is very different for different substitutions. The nearly linear dependence indicates a close correlation between the measured substitution concentration and the nominal concentration. The error bars are taken as twice of the standard deviation determined from the measurements. The compositional spread over the sample surfaces for each concentration is no more than 0.015, demonstrating relative homogeneity of the substitution studied here. (For the lowest Sc, Ru, and Co substitution levels the 2σ values were 0.002 or less.) In the following, the average experimentally determined x values, x_{WDS}, will be used to

Table D.1 WDS data for all four series. $x_{nominal}$ is the nominal concentration of the substitutions. x_{WDS} is the average x values measured at 12 locations of samples in each batch. 2σ is two times the standard deviation of the 12 values measured.

			$Lu_{1-x}Y_xFe_2Ge_2$			
$x_{nominal}$	0.05	0.10	0.13	0.16	0.19	0.50
x_{WDS}	0.043	0.094	0.125	0.148	0.19	0.56
2σ	0.006	0.007	0.005	0.005	0.01	0.016
			$Lu_{1-x}Sc_xFe_2Ge_2$			
$x_{nominal}$	0.03	0.06	0.10	0.20		
x_{WDS}	0.008	0.015	0.024	0.045		
2σ	0.002	0.002	0.006	0.006		
			$Lu(Fe_{1-x}Ru_x)_2Ge_2$			
$x_{nominal}$	0.01	0.02	0.05			
x_{WDS}	0.008	0.014	0.035			
2σ	0.001	0.002	0.001			
			$Lu(Fe_{1-x}Co_x)_2Ge_2$			
$x_{nominal}$	0.01	0.02	0.025	0.05	0.10	0.20
x_{WDS}	0.018	0.034	0.056	0.11	0.156	0.33
2σ	0.001	0.002	0.005	0.01	0.004	0.01

identify all the compounds rather than the nominal concentration, $x_{nominal}$.

Given that the crystals were grown out of Sn flux, it is important to evaluate possible Sn substitution on the Ge site of these crystals. Table D.2 shows the WDS measurement data of Sn concentration for pure $LuFe_2Ge_2$ and selected $Lu(Fe_{1-x}Co_x)_2Ge_2$ compounds. It can be seen that (i) Sn is present and maybe substitute for Ge, but (ii) the substitution level is less than 0.4 % which is smaller than the lowest substitution levels of all the other four elements that we are interested in. In addition, as will be shown in Figure D.2 below, the residual resistivity ratio for $LuFe_2Ge_2$ is greater than 20, a result consistent with little or no Sn substitution. Finally, the Sn substitution level does not vary significantly with the Co substitution level. Therefore, the effects induced by Sn substitution should be small and can be treated as a negligible background for all compounds we studied here. In this work we focus only on the effects of substitution on Lu and Fe sites.

Figure D.1 shows the lattice parameters a and c for different substitutions as a function of x_{WDS}. For Y substitution, lattice parameter a increases in a roughly linear manner as x_{WDS}. Lattice parameter c also increases but with larger scatter in the data for low substitution

Table D.2 WDS data of Sn concentration for pure and Co-substituted $LuFe_2Ge_2$ compounds. x_{WDS} is the measured Co concentration. y_{WDS} is the measured Sn concentration based on the assumption it is substituting for Ge. $2\sigma_y$ is two times the standard deviation of Sn concentration measured at 12 points.

	$Lu(Fe_{1-x}Co_x)_2(Ge_{1-y}Sn_y)_2$				
x_{WDS}	0	0.056	0.11	0.156	0.33
y_{WDS}	0.003	0.002	0.002	0.0036	0.003
$2\sigma_y$	0.002	0.002	0.002	0.001	0.001

levels. For Sc substitution, lattice parameter a decreases with x_{WDS} whereas lattice parameter c remains constant within the error bars. For Co substitution, the lattice parameter c decreases with x_{WDS}, whereas the lattice parameter a remains almost unchanged at low substitution level then increases slightly at high substitution levels. For Ru substitution, the lattice parameter a increases whereas the lattice parameter c decreases. For all Y, Sc and Ru substitutions, it appears that the lattice parameter c is less sensitive to the substitution than lattice parameter a. In addition, the error bar in lattice parameter c is roughly twice of that in lattice parameter a, making it difficult to determine the changes in the lattice parameter c precisely.

Figure D.2a shows the temperature dependent magnetization data for H $\parallel$ ab of the Y-substituted $LuFe_2Ge_2$ which was measured in the field of 1 T. The parent compound, $LuFe_2Ge_2$, shows a weak temperature dependence that is consistent with a somewhat enhanced Pauli paramagnetic behavior (Avila et al., 2004), but that has also been fit to a Curie Weiss behavior, albeit with an unrealistically high paramagnetic θ of 800 K (Ferstl et al., 2006). Upon cooling to low temperatures there is a clear local maximum followed by a sharp drop; analysis of $d(MT/H)/dT$ gives a transition temperature of 8.2 K, a value that is similar to, but somewhat lower than, the previous report of 9 K (Avila et al., 2004). By substituting Y onto the Lu site, this transition is suppressed to lower temperatures, ultimately dropping below 2 K for $x > 0.148$. The signature of the transition evolves gradually with the substitution level. As the transition is suppressed a clear, low temperature minimum in $M(T)/H$ is revealed, followed at lowest temperatures by a sharp upturn. By $x = 0.19$ the form of $M(T)/H$ is essentially identical to that of pure YFe_2Ge_2. It is worth noting that this lowest temperature tail does not seem to be extrinsic since it essentially disappears below the tunable magnetic transition.

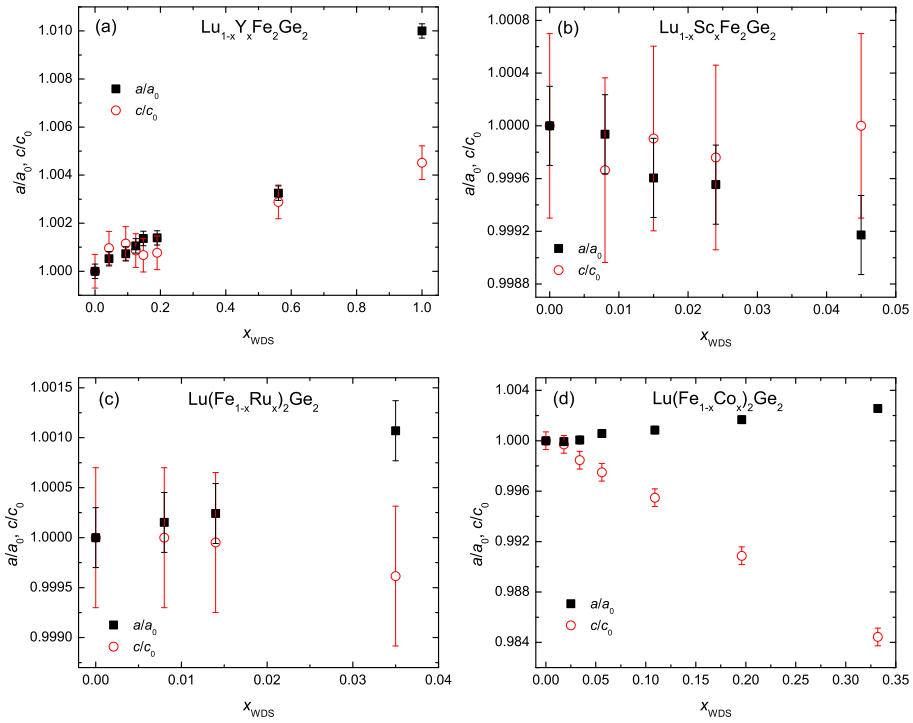

Figure D.1 Room temperature a and c lattice parameters of (a) the $Lu_{1-x}Y_xFe_2Ge_2$ series, (b) the $Lu_{1-x}Sc_xFe_2Ge_2$ series, (c) the $Lu(Fe_{1-x}Ru_x)_2Ge_2$ series and (d) the $Lu(Fe_{1-x}Co_x)_2Ge_2$series, normalized to a_0=3.9253 Å and c_0=10.405 Å of pure $LuFe_2Ge_2$ as a function of measured substitutions concentration, x_{WDS}.

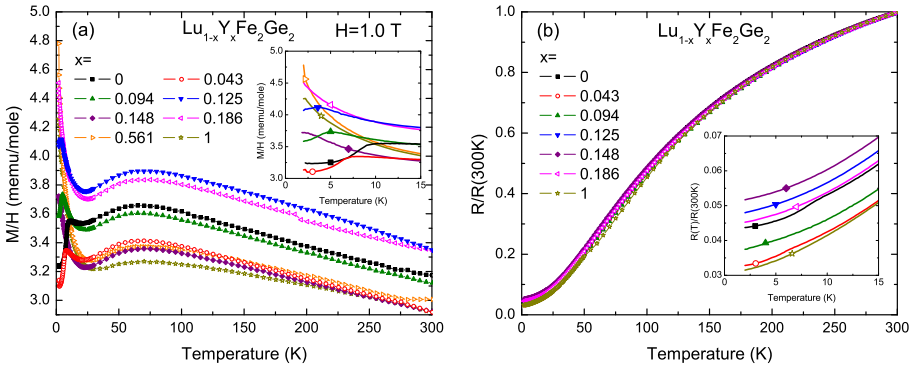

Figure D.2 Temperature dependent (a) magnetization divided by applied field with a field of 1T applied parallel to the crystallographic ab plane and (b) normalized electrical resistivity of the $Lu_{1-x}Y_xFe_2Ge_2$ series. Insets show data at low temperature. Transition temperatures are determined using the criteria described in the text.

The effect of Y substitution on the low temperature properties of $Lu_{1-x}Y_xFe_2Ge_2$ compounds can also be seen in the electrical transport data which is shown in Figure D.2b. The slope of $R(T)$ for parent compound changes slightly at around 8 K, which corresponds to the anomaly seen in the magnetization data. Upon Y substitution, the resistive feature remains weak and becomes difficult to resolve for $x = 0.125$, even though the magnetization data show a clear anomaly centered at 3.4 K. For $x \geq 0.148$, the signatures in both magnetization and resistivity are suppressed completely.

The effect of Sc substitution on the Lu site on the low temperature properties is markedly different from that of Y substitution as manifested by the temperature dependent magnetization and resistivity data as shown in Figures D.3a and D.3b. As the Sc substitution level increases, the signatures in both magnetization and resistivity are pushed up to higher temperatures instead of being suppressed. Whereas the form of the resistive signature remains essentially unchanged (a weak decrease in resistance similar to a minor reduction in scattering), the magnetic signature evolves in a way different from that of Y substituted compound. The weak local minimum in the susceptibility, seen for temperatures just above the magnetic transition disappears as the magnetic ordering temperature increases; ultimately, for the highest Sc substitution level, $x = 0.045$, the sharp drop in susceptibility associated with the magnetic transition occurs abruptly without any hint of a local minima in $M(T)/H$. The enhancement of the transition temperature is further confirmed by specific heat measurement on samples with selected substitution levels (Figure D.3c). It can be seen that the corresponding anomaly in specific heat is small but well resolved. With increasing the Sc substitution level, the anomaly shifts to higher temperature. It would be interesting to see the evolution of the transition temperature as well as the signatures of the transition at higher substitution level. Unfortunately, as the substitution level increases, a second phase with different crystal morphology begins to grow and becomes more and more pervasive. Already the nominal $x = 0.20$ growth, our highest substitution in this work, yields mostly this second phase and only a small amount of clean 122 phase that had to be carefully separated.

The enhancement of transition temperature by Sc substitution as well as the suppression of transition by Y substitution is consistent with the result of an existing pressure study of

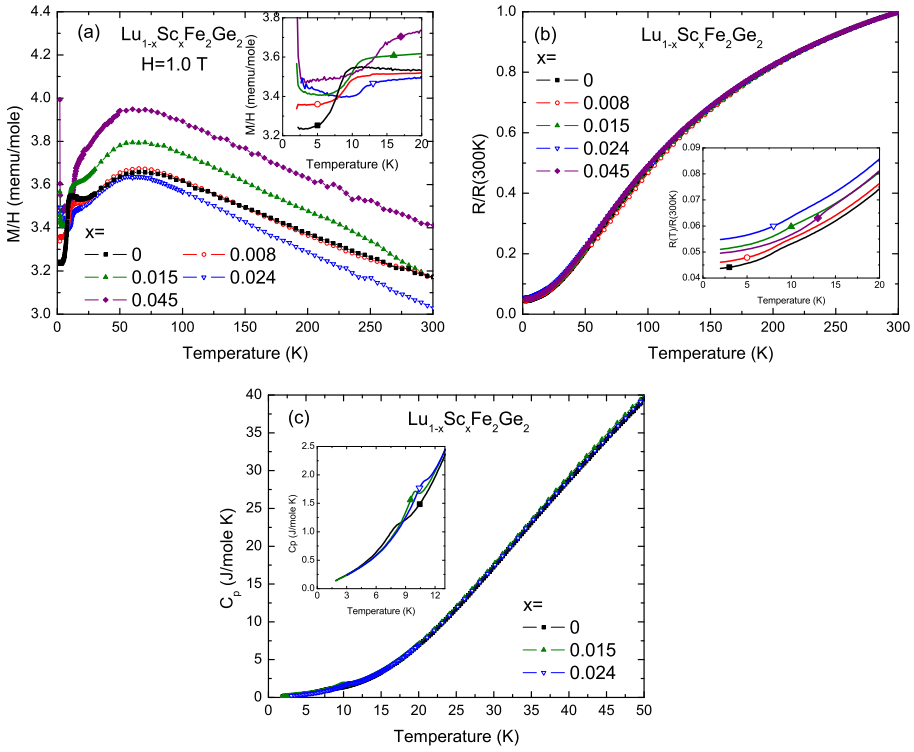

Figure D.3 Temperature dependent (a) magnetization divided by applied field with a field of 1T applied parallel to the crystallographic ab plane, (b) normalized electrical resistivity and (c) specific heat of the $Lu_{1-x}Sc_xFe_2Ge_2$ series. Insets show data at low temperature. Transition temperatures are determined using the criteria described in the text.

$LuFe_2Ge_2$ (Fujiwara et al., 2007) which shows that on applying pressure, the transition temperature monotonically increases. With Sc substitution for Lu, both lattice parameter a and c decrease, indicating that Sc substitution serves as a chemical pressure. On the other hand, Y substitution leads to increases in both a and c lattice parameters, making it similar to negative pressure.

To a first order approximation, both Y and Sc substitutions cause only steric effects without changing the band filling. Another way to modify the sample without changing the band filling is to substitute Ru for Fe. Figures D.4a and D.4b show the temperature dependent magnetization and resistivity data for the $Lu(Fe_{1-x}Ru_x)_2Ge_2$ series. It can be seen that by Ru substitution onto the Fe site the 8.2 K transition is suppressed. For $x = 0.008$, the lowest substitution level we were able to achieve, the anomaly in magnetization is suppressed to 5.2 K. The corresponding feature in resistivity is rather weak but can be seen clearly in the first derivative dR/dT (inset of Fig. D.4b) giving a transition temperature of 4.6 K. For $x = 0.014$, there is an indication of drop in magnetization just as base temperature is approached; further, lower temperature measurements would be required to determine the precise transition temperature. No indication of a transition is observed in the resistivity data for this substitution level. For $x = 0.035$, neither magnetization nor resistivity data show any signs of a transition above 2 K.

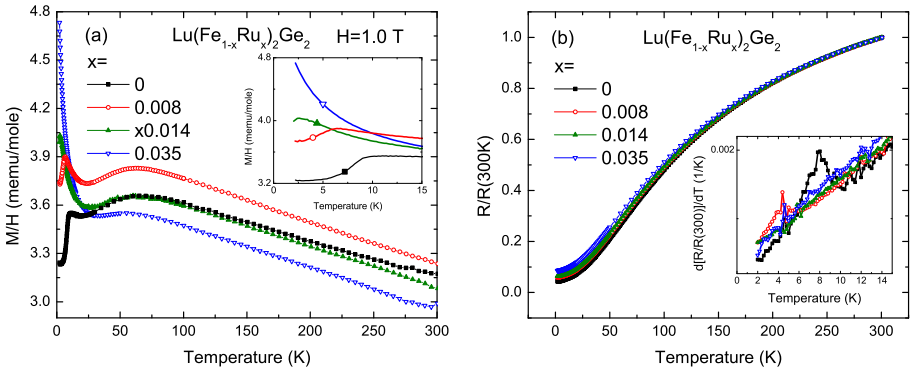

Figure D.4 Temperature dependent (a) magnetization divided by applied field with a field of 1T applied parallel to the crystallographic ab plane and (b) normalized electrical resistivity of the $Lu(Fe_{1-x}Ru_x)_2Ge_2$ series. Insets show data at low temperature. Transition temperatures are determined using the criteria described in the text.

Whereas Y, Sc and Ru substitutions are expected to primarily cause steric changes (in addition to disorder), Co substitution onto the Fe site, with one extra electron per atom, potentially affects the band filling. Figure D.5a shows the temperature dependent magnetization data for the $Lu(Fe_{1-x}Co_x)_2Ge_2$ series. By Co substitution onto the Fe site, even with our lowest substitution level, $x = 0.018$, the anomaly is suppressed completely. With the magnetic transition suppressed, the magnetization data manifests the same type of upturn at low temperature that the Y and Ru substitutions data does. As the Co substitution level is increased, the high temperature susceptibility decreases, consistent with the fact that $LuCo_2Ge_2$ has a susceptibility that is one order of magnitude smaller than that of $LuFe_2Ge_2$ (as shown in the inset to Figure D.5a). The complete suppression of the 8.2 K feature by Co substitution is further confirmed by both resistivity and specific heat data which are shown in Figures D.5b and D.5c; neither the change of slope in resistivity nor the anomaly in the specific heat are detected in Co substituted compounds for any substitution levels.

Based on the magnetization, resistivity and specific heat data, the phase diagrams for Y, Sc and Ru substitutions are presented in Figure D.6. The phase diagrams indicate a near linear suppression (enhancement) of the transition temperature for Y (Sc) substitution. Ru substitution suppresses the transition at a higher rate than Y substitution and Co substitution suppresses the transition at least as rapidly as Ru substitution.

Given the apparent similarities between the effects of Sc substitution and applied pressure as well as the effects of Y and Ru substitutions it is worthwhile seeing if there is some underlying, unifying parameter that can be used to describe the effects of isoelectronic perturbations of the low temperature magnetic transition in $LuFe_2Ge_2$. An examination of the plots in Figures D.1 and D.6 points to possible scaling of the transition temperature with either the unit cell volume or with the a-lattice parameter. Figure D.7 presents the magnetic transition temperature as a function of a/a_0, V/V_0, c/c_0 and $(c/a)/(c_0/a_0)$. Whereas changes in a and V may correlate with changes in the magnetic transition temperature, changes in c or c/a do not. Even though the changes in the a-lattice parameter (and volume) are rather small, some clear tendencies can still be extracted. It can be seen that for Y and Sc substitution, the transition temperatures can be well scaled with normalized a-lattice parameter, and to a lesser extent normalized volume

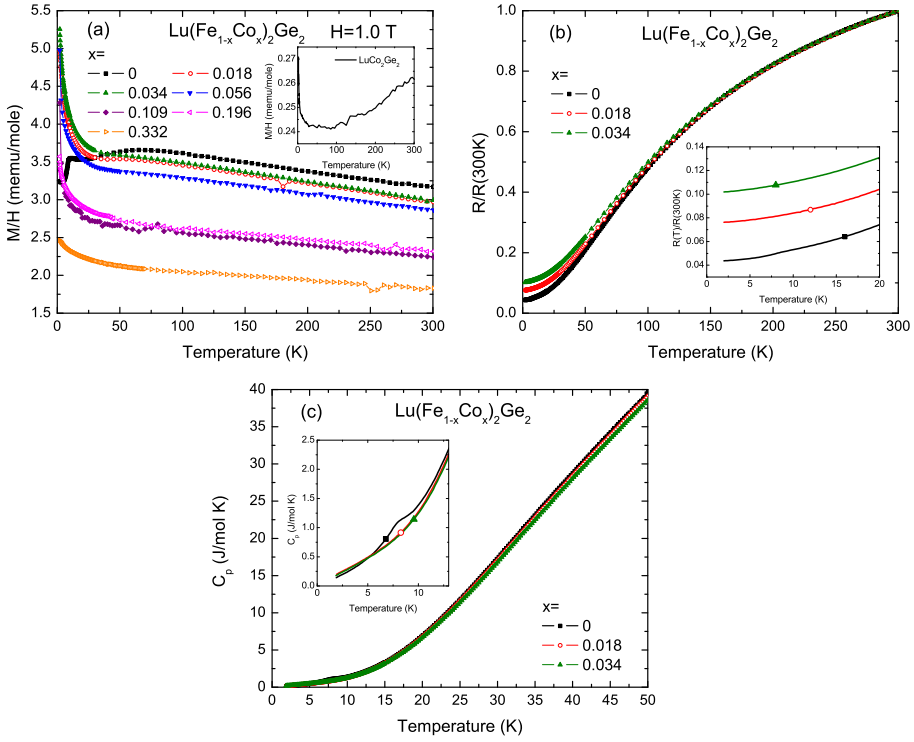

Figure D.5 Temperature dependent (a) magnetization divided by applied field with a field of 1T applied parallel to the crystallographic ab plane, (b) normalized electrical resistivity and (c) specific heat of the $Lu(Fe_{1-x}Co_x)_2Ge_2$ series. Insets show data at low temperature. Transition temperatures are determined using the criteria described in the text.

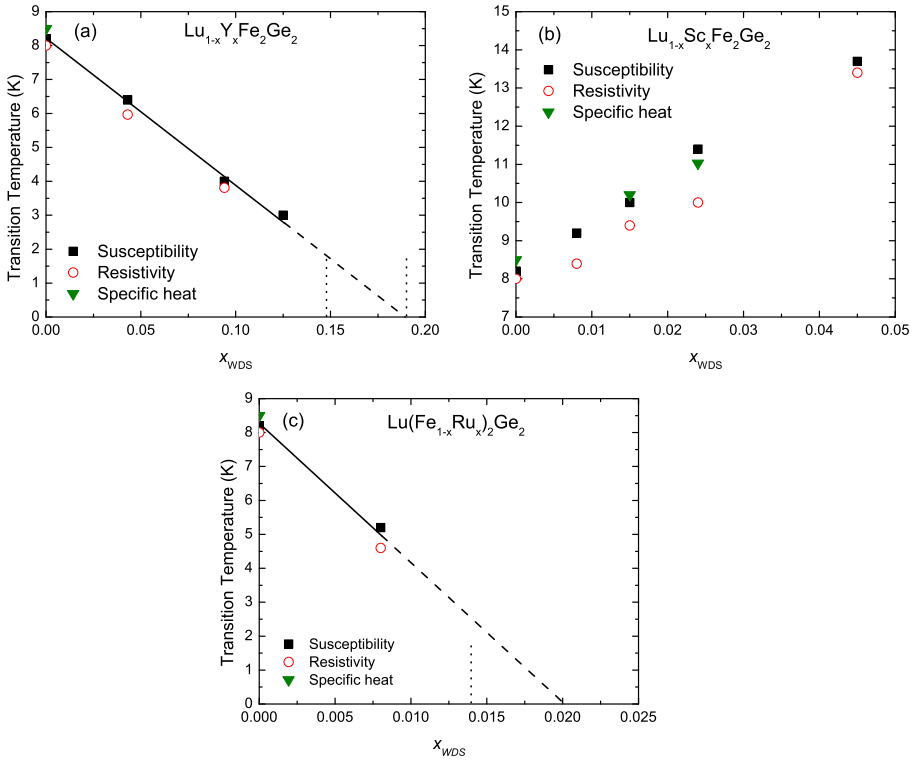

Figure D.6 T-x phase diagram for (a) $Lu_{1-x}Y_xFe_2Ge_2$, (b) $Lu_{1-x}Sc_xFe_2Ge_2$and (c) $Lu(Fe_{1-x}Ru_x)_2Ge_2$. Squares are data from susceptibility data, circles are data from resistivity data, and triangles are data from specific heat data. Solid lines are the linear fit of the data. Dashed lines are the extrapolations of data to lower temperature. Vertical dotted lines represent the possible transitions below 2 K.

(with Y substitution transition temperature values jump a little bit at first substitution level). It appears that Ru substitution with the higher rate at which it suppresses the transition temperature falls on the edge of the manifold for either normalized a-lattice parameter or normalized volume. The inset to Figure D.7b includes the transition temperature data from $LuFe_2Ge_2$ under pressure. In order to compare our data with those of the pressure study (Fujiwara et al., 2007), the change of unit cell volume under pressure was estimated by using the bulk modulus of $YbRh_2Si_2$ (Plessel et al., 2003), $B_0 = 189$ GPa, which is the closest compound that such data could be found for. Considering the possibly differences between the bulk moduli of $YbRh_2Si_2$ and $LuFe_2Ge_2$, this is only a rough estimation. It appears that Y and Sc substitutions as well as the pressure data roughly follow the same scale of volume.

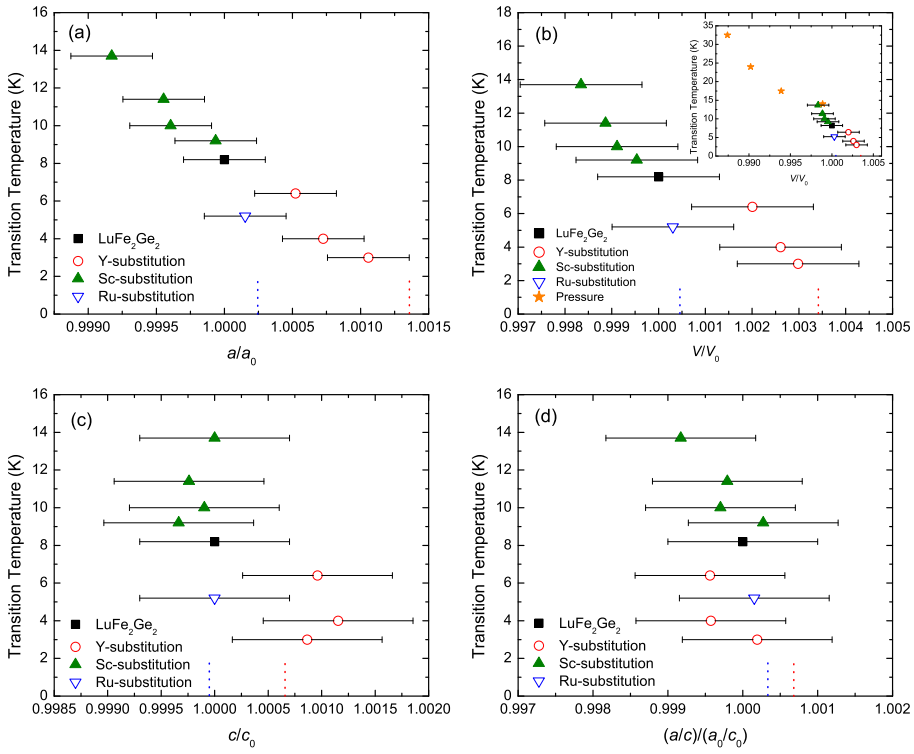

Figure D.7 Transition temperature versus normalized (a) lattice parameter a, (b) unit cell volume V, (c) lattice parameter c and (d) a/c. Stars in panel (b) are pressure data from c(Fujiwara et al., 2007) recalculated using bulk modulus from (Plessel et al., 2003) as described in the text. Vertical dotted lines represent the possible transitions below 2 K.

D.3 Summary

The effects of Y and Sc substitutions for Lu, as well as Ru and Co substitutions for Fe, on the low temperature magnetic phase transition of $LuFe_2Ge_2$ have been studied in single crystals and the phase diagrams of Y, Sc and Ru substitution have been established. The results reveal that whereas Sc substitution, which serves as chemical pressure, enhances the transition, Y and Ru substitutions which serve as negative chemical pressure or strain suppress the transition to lower temperature. This is consistent with previous report of pressure study of the parent compound $LuFe_2Ge_2$ (Fujiwara et al., 2007). In addition, for Y and Sc substitutions, there appear to be universal relations between transition temperature and both a-lattice parameter and volume so that transition temperature of these two substitutions can be scaled very well with both a-lattice parameter and volume. As this magnetic phase transition is suppressed no competing phase (such as superconductor) was revealed, at least for temperature above 2 K.

APPENDIX E. COLLABORATIONS

E.1 Introduction

Part of my Ph. D work was spent synthesizing and providing samples to other groups for specialized measurements. Some of this work was based on my own projects and provided valuable access to some new experiments. Other growths were based on results of previous members of our research group. In this second case, I learned how to synthesize the samples and use the existing data to provide samples with the requested specifications (eg. sample size or substitution level).

E.2 $CaFe_2As_2$

Before my thesis work, detailed microscopic and spectroscopic measurements were hard to collect on the collapsed tetragonal phase of $CaFe_2As_2$ as it existed only under pressure. For example, in case of inelastic neutron scattering study, the measurement was limited to narrow range in momentum transfer and energy transfer. Therefore the measurement could not exclude the presence of correlated magnetic fluctuations at other positions in reciprocal space, or a change in the energy scale of the fluctuations. In case of angle-resolved photoemission spectroscopy, which is import technique to gain information of band structure, measurements under pressure are simply not possible. By inducing internal strain, via the postgrowth thermal treatment of single crystals grown out of FeAs flux, I was able to stabilize the collapsed tetragonal phase at ambient pressure and provide easy access to those measurements.

Gati et al. (2012) reported on measurements of the magnetic susceptibility and electrical resistance under He-gas pressure on single crystals of $Ca(Fe_{1-x}Co_x)_2As_2$. They found that for properly heat-treated crystals with modest Co concentration, $x = 0.028$, the salient

ground states associated with iron-based superconductors, i.e., antiferromagnetic/orthorhombic (AFM/ORTH), superconducting, and collapsed-tetragonal states can be accessed all in one sample with reasonably small and truly hydrostatic pressure. Systematic investigations of the various phase transitions and ground states via pressure tuning revealed no coexistence of bulk superconductivity with the AFM/ORTH state which they linked to the strongly first-order character of the corresponding structural/magnetic transition in this compound. These results, together with literature results, indicate that preserving fluctuations associated with the AFM/ORTH transition to low enough temperatures is vital for superconductivity to form. Details of this work in presented in Appendix C.

Bud'ko et al. (2013) reported thermal expansion measurements on $Ca(Fe_{1-x}Co_x)_2As_2$ single crystals with different thermal treatment, with samples chosen to represent four different ground states observed in this family. This work demonstrated that for all samples, thermal expansion is anisotropic with different signs of the in-plane and c-axis thermal expansion coefficients in the high temperature, tetragonal phase. The features in thermal expansion associated with the phase transitions are of opposite signs as well, pointing to a different response of transition temperatures to the in-plane and the c-axis stress. These features, and consequently the inferred pressure derivatives, are very large, clearly and substantially exceeding those in the $Ba(Fe_{1-x}Co_x)_2As_2$ family. For all transitions the c-axis response is dominant.

Soh et al. (2013) presented unambiguous evidence of the absence of magnetic fluctuations in the nonsuperconducting, collapsed tetragonal phase of $CaFe_2As_2$ via inelastic neutron scattering time-of-flight data, which is consistent with the view that spin fluctuations are a necessary ingredient for unconventional superconductivity in the iron pnictides. The authors demonstrated that the collapsed tetragonal phase of $CaFe_2As_2$ is nonmagnetic, and discussed this result in light of recent reports of high-temperature superconductivity in the collapsed tetragonal phase of closely related compounds.

Dhaka et al. (2014) used angle-resolved photoemission spectroscopy and density functional theory calculations to study the electronic structure of $CaFe_2As_2$ in the collapsed tetragonal phase. The authors found significant differences in the Fermi surface topology and band dispersion data from the more common orthorhombic-antiferromagnetic or tetragonal-paramagnetic

phases, consistent with electronic structure calculations. Upon entering the cT phase, the top of the hole bands sinks below the Fermi level, which destroys the nesting present in parent phase. The absence of nesting in this phase, along with an apparent loss of Fe magnetic moment, are now clearly, experimentally correlated with the lack of superconductivity in this phase.

Furukawa et al. (2014) investigated the static and the dynamic spin correlations in the low-temperature collapsed tetragonal and the high-temperature tetragonal phase in $CaFe_2As_2$ by ^{75}As nuclear magnetic resonance (NMR) and nuclear quadrupole resonance (NQR) measurements. Through the temperature dependence of the nuclear spin lattice relaxation rates and the Knight shifts, they demonstrated that, although stripe-type antiferromagnetic spin correlations are realized in the high-temperature tetragonal phase, no trace of the AFM spin correlations can be found in the nonsuperconducting, low-temperature, collapsed tetragonal phase. Given that there is no magnetic splitting in ^{75}As NMR spectra, together with the T-independent behavior of magnetic susceptibility and the T dependence of $1/T_1T_\chi$, the authors conclude that Fe spin correlations are completely quenched statically and dynamically in the nonsuperconducting collapsed tetragonal phase in $CaFe_2As_2$.

E.3 $Ba(Fe_{1-x}TM_x)_2As_2$

Previous members of our research group made extensive efforts to characterize the physical properties of $Ba(Fe_{1-x}TM_x)_2As_2$ (TM = Co, Ni, Cu, Ru, Rh, Pd, Mn) and constructe phase diagrams of transition temperature versus substitution concentration. I was involved in constructing phase diagram of Mn substituted $BaFe_2As_2$. Based on these phase diagrams I could provide the requested samples for some specific measurements.

Thaler et al. (2011) grew single crystals of of $Ba(Fe_{1-x}Mn_x)_2As_2$, $0 < x < 0.148$, and characterized the samples by structural, magnetic, electrical transport, and thermopower measurements. The authors found evidence for phase separation (associated with some form of immiscibility) starting for $x > 0.1$ - 0.2. Their measurements showed that whereas the structural/magnetic phase transition found in pure $BaFe_2As_2$ at 134 K is initially suppressed by Mn substitution, superconductivity is not observed at any substitution level. Although the effect of hydrostatic pressure up to 20 kbar in the parent $BaFe_2As_2$ compound is to suppress the struc-

tural/magnetic transition at the approximate rate of 0.9 K/kbar, the effects of pressure and Mn substitution in the $x = 0.102$ compound are not cumulative. The authors constructed phase diagrams of transition temperature versus substitution concentration based on electrical transport, magnetization, and thermopower measurements compared to those of the $Ba(Fe_{1-x}TM_x)_2As_2$ (TM= Co and Cr) series.

Tucker et al. (2012) presented inelastic neutron scattering measurements single crystals of $Ba(Fe_{0.925}Mn_{0.075})_2As_2$ which manifest spin fluctuations at two different wave vectors, Q_{stripe} = (1/2,1/2,1) and $Q_{N\grave{e}el}$ = (1,0,1), corresponding to the expected stripe spin-density wave order and checkerboard antiferromagnetic order in the tetragonal I4/mmm cell, respectively. The authors demonstrated that below $T_N = 80$ K, long-range stripe magnetic ordering occurs and sharp spin wave excitations appear at Q_{stripe} while broad and diffusive spin fluctuations remain at $Q_{N\grave{e}el}$ at all temperatures. Low concentrations of Mn dopants nucleate local moment spin fluctuations at $Q_{N\grave{e}el}$ that compete with itinerant spin fluctuations at Q_{stripe} and may disrupt the development of superconductivity.

Kim et al. (2012b) compared the spin fluctuation spectra from nonsuperconducting Cu-substituted, and superconducting Co-substituted, $BaFe_2As_2$ by inelastic neutron scattering measurements and found that the spectra are indistinguishable. The authors showed that whereas diffraction studies show the appearance of incommensurate spin-density wave order in Co and Ni substituted samples, the magnetic phase diagram for Cu substitution does not display incommensurate order, demonstrating that simple electron counting based on rigid-band concepts is invalid. These results, supported by theoretical calculations, suggest that substitutional impurity effects in the Fe plane play a significant role in controlling magnetism and the appearance of superconductivity, with Cu distinguished by enhanced impurity scattering and split-band behavior.

Kim et al. (2013) presented inelastic neutron scattering measurements on single crystals of $Ba(Fe_{0.963}Ni_{0.037})_2As_2$ which manifest a neutron spin resonance in the superconducting state with anisotropic dispersion within the Fe layer. The authors demonstrated that whereas the resonance is sharply peaked at the antiferromagnetic wave vector Q_{AFM} along the orthorhombic a axis, the resonance disperses upwards away from Q_{AFM} along the b axis. In contrast to

the downward dispersing resonance and hourglass shape of the spin excitations in superconducting cuprates, the resonance in electron-doped $BaFe_2As_2$ compounds possesses a magnonlike upwards dispersion.

Dioguardi et al. (2013) presented ^{75}As nuclear magnetic resonance data from measurements of a series of $Ba(Fe_{1-x}Co_x)_2As_2$ crystals with $0.00 \leq x \leq 0.075$ that reveals the coexistence of frozen antiferromagnetic domains and superconductivity for $0.060 \leq x \leq 0.071$. Although bulk probes reveal no long range antiferromagnetic order beyond $x = 0.06$, the authors found that the local spin dynamics reveal no qualitative change across this transition. The characteristic domain sizes vary by more than an order of magnitude, reaching a maximum variation at $x = 0.06$. The authors proposed that this inhomogeneous glassy dynamics may be an intrinsic response to the competition between superconductivity and antiferromagnetism in this system.

Patz et al. (2014) used time-resolved polarimetry to reveal critical nematic fluctuations in unstrained $Ba(Fe_{1-x}Co_x)_2As_2$. The authors demonstrated that the femtosecond anisotropic response, which arises from the two-fold in-plane anisotropy of the complex refractive index, displays a characteristic two-step recovery absent in the isotropic response. The fast recovery appears only in the magnetically ordered state, whereas the slow one persists in the paramagnetic phase with a critical divergence approaching the structural transition temperature. The dynamics also reveal a gigantic magnetoelastic coupling that far exceeds electronspin and electronphonon couplings, opposite to conventional magnetic metals.

E.4 RNi_2B_2C

The rare earth nickel borocarbide compounds were discovered as a new family of magnetic superconductors in 1994 (Cava et al., 1994a,b; Siegrist et al., 1994) and attracted extensive interest in the decades-old question of how superconductivity and magnetism coexsit (Canfield et al., 1998). I learned to synthesize single crystals of these compounds and were involved in two projects related to rare earth nickel borocarbides.

Bud'ko et al. (2010) reported effects of local magnetic moment, Gd^{3+}, substitution ($x \leq 0.3$) on superconducting and magnetic properties of the closely related series, $Lu_{1-x}Gd_xNi_2B_2C$ and $Y_{1-x}Gd_xNi_2B_2C$. The authors showed that the superconducting transition temperature

decreases and the heat capacity jump associated with it drops rapidly with Gd-substitution; qualitative changes with substitution are also observed in the temperature-dependent upper critical field behavior, and a region of coexistence of superconductivity and spin-glass state is delineated on the x-T phase diagram. The authors demonstrated that the evolution of superconducting properties can be understood within Abrikosov-Gor'kov theory of magnetic impurities in superconductors taking into account the paramagnetic effect on upper critical field with additional contributions particular for the family under study.

Hodovanets et al. (2013) studied the influence of local moment magnetism on the boron isotope effect of T_c on single crystals of $ErNi_2B_2C$. The authors obtained values of the partial isotope effect exponent based on two different criteria applied to extract T_c and did not observe significant change in the partial isotope effect exponent compared to the ones obtained for $LuNi_2B_2C$. Based on this result, the authors conclude that pair-breaking due to the Er local magnetic moment appears to have no detectable influence on boron isotope effect of T_c.

APPENDIX F. LIST OF SUBSTITUTIONS AND POST GROWTH THERMAL TREATMENT

Listed here are the samples of $CaFe_2As_2$, $BaFe_2As_2$, and $LuFe_2Ge_2$ families, with various transition metal substitutions. Each table gives our internal batch growth code, nominal substitution level $x_{nominal}$, the actual substitution level x_{WDS}, as well as 2σ of the measurement (when measured). In case of $CaFe_2As_2$ family, $T_{A/Q}$ value is also given.

Table F.1 $CaFe_2As_2$

Batch	$T_{A/Q}$ (°C)
SA538	960
SA441-1	700
SA441-2	400
SA441-3	600
MC456	960
MC708-1	960
MC708-2	850
MC815	400
MC925-1	400
MC925-2	500
XH228	960
XH270-1	350
XH270-2	500
XH270-3	600
XH270-4	700

Table F.2 $Ca(Fe_{1-x}Co_x)_2As_2$

Batch	$x_{nominal}$(%)	x_{WDS}(%)	2σ(%)	$T_{A/Q}$ (°C)
SA704	6.0	5.9	0.1	960
SA954	3.0	2.8	0.1	960
SA974	1.0	1.0	0.1	960
SA975	2.0	1.9	0.1	960
SA976	4.0	3.8	0.1	960
SA977	5.0	4.8	0.2	960
SA986	3.0	2.9	0.1	960
SA987	2.5	2.2	0.1	960
SA999	3.5	3.3	0.1	960
MC063	3.0	2.9	0.1	400
MC064	2.8	2.6	0.1	960
MC102-1	2.0	1.9	0.1	350
MC102-2	2.0	1.9	0.2	500
MC103-1	3.0	2.8	0.2	350
MC103-2	3.0	2.9	0.2	500
MC486	3.5	3.2	0.2	350
MC510	15.0	12.1	0.6	960
MC511	20.0	17.7	0.6	960
MC569-1	3.0	2.7	0.1	400
MC569-2	3.0	2.5	0.1	350
MC742-1	4.0	3.7	0.1	500
MC742-2	4.0	3.8	0.1	800
MC751-1	3.0	2.8	0.1	400
MC751-2	3.0	2.8	0.1	350
MC792	2.0	2.0	0.1	400
MC793	2.8	2.7	0.1	400
MC794-1	2.5	2.3	0.1	350
MC794-2	2.5	2.3	0.1	400
MC794-3	2.5	2.2	0.1	450
MC794-4	2.5	2.3	0.1	500
MC816	3.0	2.9	0.1	400
MC827	6.0	5.8	0.1	400
MC921	1.5	1.5	0.1	400
MC922	2.4	2.2	0.1	400
MC943-2	2.8			400
MC943-3	2.8			400
MC946	1.9	1.8	0.1	350
MC947	2.6	2.3	0.1	350
XH091	4.0	3.6	0.1	400
XH241	3.0	2.7	0.1	350

Table F.3 $Ca(Fe_{1-x}Ni_x)_2As_2$

Batch	$x_{nominal}$(%)	x_{WDS}(%)	2σ(%)	$T_{A/Q}$ (°C)
MC001	2.0	2.1	0.1	960
MC624	1.0	1.1	0.1	960
MC625	3.0	3.1	0.1	960
MC666	2.5	2.7	0.1	960
MC667	6.0	6.5	0.2	960
MC692	2.3	2.5	0.1	960
MC693	4.0	4.4	0.1	960
MC730	2.1	2.3	0.1	960
MC731	2.4	2.6	0.1	960
MC762	2.8	2.9	0.1	960
MC856	2.0	2.2	0.1	960
MC857	2.5	2.7	0.1	960
MC883	1.5	1.7	0.1	960
MC884	2.3	2.6	0.1	960
MC915	1.7	1.9	0.1	960
MC916	1.9	2.1	0.1	960
XH134	1.7	1.9	0.1	500
XH135	2.3	2.4	0.1	960
XH136	2.5	2.7	0.1	400
XH137	3.0	3.3	0.1	960
XH138	4.0	4.3	0.1	960
XH143	6.0	6.4	0.1	960
XH287	3.5	3.8	0.1	960
XH288	5.0	5.4	0.2	960
XH425	1.0	1.1	0.1	500
XH426	1.6	1.7	0.2	500
Xh427	1.9	1.9	0.1	500
XH464	3.0			960
XH472	3.0			960
XH474	3.0			500
XH552	2.5			500
XH553	3.0			500
Xh554	4.0			500

Table F.4 $Ca(Fe_{1-x}Rh_x)_2As_2$

Batch	$x_{nominal}$(%)	x_{WDS}(%)	2σ(%)	$T_{A/Q}$ (°C)
MC626	1.0	0.6	0.1	960
MC627	3.0	1.6	0.1	960
MC694	3.5	2.0	0.1	960
MC668	4.0	2.3	0.1	960
MC669	5.0	2.8	0.1	960
MC695	6.0	3.7	0.2	960
MC696	8.0	4.9	0.2	960
MC729	10.0	6.6	0.3	960
MC752	2.0	1.1	0.1	960
XH139	3.0	1.6	0.1	960
XH140	4.0	2.3	0.2	400
XH141	6.0	3.5	0.1	960
XH142	10.0	6.4	0.1	960
XH289	20.0	18.9	0.3	960
XH290	30.0	38.6	3.2	960
XH291	1.5	0.9	0.1	500
XH292	3.6	2.0	0.2	500
XH293	10.0	6.3	0.9	500
XH341	4.0			960
XH342	6.0			500
Xh343	8.0			500

Table F.5 $Ca(Fe_{1-x}Cu_x)_2As_2$

Batch	$x_{nominal}$(%)	x_{WDS}(%)	2σ(%)	$T_{A/Q}$ (°C)
MC697	2.0	2.2	0.1	960
MC698	4.0	4.6	0.2	960
MC721	6.0	6.5	0.3	960
MC722	8.0	6.4	0.4	960

Table F.6 $Ca(Fe_{1-x}Ru_x)_2As_2$

Batch	$x_{nominal}$(%)	x_{WDS}(%)	2σ(%)	$T_{A/Q}$ (°C)
MC628-1	10.0	3.9	1.2	960
MC628-2	10.0	4.5	1.1	960
MC629	15.0			960

Table F.7 $Ca(Fe_{1-x}Mn_x)_2As_2$

Batch	$x_{nominal}$(%)	x_{WDS}(%)	2σ(%)	$T_{A/Q}$ (°C)
MC767	4.0			960
MC783	6.0			960
MC784	8.0			960
MC806	15.0	6.0	0.2	960
MC807	20.0			960
MC808	30.0	97.0	2.6	960

Table F.8 $Ca(Fe_{1-x}Cr_x)_2As_2$

Batch	$x_{nominal}$(%)	x_{WDS}(%)	2σ(%)	$T_{A/Q}$ (°C)
MC768	4.0			960
MC785	6.0			960
MC786	8.0			960
MC809	15.0			960
MC810	20.0			960
MC811	30.0			960
MC819	15.0	7.9	0.2	960
MC820	20.0	10.3	1.4	960

Table F.9 $Ca_{1-x}Sr_xFe_2As_2$ grown from Sn-flux

Batch	$x_{nominal}$(%)	x_{WDS}(%)	2σ(%)
MC141	10.0	17.7	1.8
MC142	20.0	31.1	1.8
MC143	40.0	52.2	1.7
MC256	3.0	3.6	1.1
MC257	6.0	10.6	0.7
MC258	9.0	15.5	1.7

Table F.10 $Ba(Fe_{1-x}Co_x)_2As_2$

Batch	$x_{nominal}$(%)	x_{WDS}(%)	2σ(%)
MC699	8.6	6.1	0.1
MC709	8.6	6.0	0.1
MC388	5.0	3.8	0.3
MC389	15.0	11.8	0.4
XH241	3.0	2.7	0.1

Table F.11 $Ba(Fe_{1-x}Rh_x)_2As_2$

Batch	$x_{nominal}(\%)$	$x_{WDS}(\%)$	$2\sigma(\%)$
MC627	3.0	1.7	0.1
MC694	3.5	2.1	0.1
MC688	4.0	2.3	0.1
MC733	13.5	8.7	0.2
MC734	6.9	4.0	0.1
MC761	11.1	6.8	0.1
XH527	10.5	6.1	0.2
XH579	15.0	10.7	0.2

Table F.12 $Ba(Fe_{1-x}Cu_x)_2As_2$

Batch	$x_{nominal}(\%)$	$x_{WDS}(\%)$	$2\sigma(\%)$
MC224	2.6	4.4	0.2
MC225	2.6	4.5	0.2
MC226	2.7	4.6	0.1
MC227	2.7	4.7	0.2
MC276	2.6	4.0	0.2
MC277	2.5	4.5	0.2
MC278	2.5	4.2	0.2
MC280	2.4	4.3	0.2
MC942-1	10.3	4.3	0.2
MC942-2	10.3	4.2	0.2
MC942-3	10.3	4.2	0.2

Table F.13 $Lu(Fe_{1-x}Co_x)_2Ge_2$

Batch	$x_{nominal}(\%)$	$x_{WDS}(\%)$	$2\sigma(\%)$
SA211	10.0	15.6	0.4
SA212	20.0	33.0	10.0
SA277	5.0	11.0	1.0
SA278	2.5	5.6	0.5
SA328	1.0	1.8	0.1
SA329	2.0	3.4	0.2

Table F.14 $Lu(Fe_{1-x}Ru_x)_2Ge_2$

Batch	$x_{nominal}(\%)$	$x_{WDS}(\%)$	$2\sigma(\%)$
SA576	5.0	3.5	0.1
SA577	10.0		
SA603	1.0	0.8	0.1
SA604	2.0	1.4	0.2

Table F.15 $Lu_{1-x}Sc_xFe_2Ge_2$

Batch	$x_{nominal}(\%)$	$x_{WDS}(\%)$	$2\sigma(\%)$
SA574	3.0	0.8	0.2
SA575	6.0	1.5	0.2
SA605	10.0	2.4	0.6
SA628	15.0		
SA629	20.0	4.5	0.6

Table F.16 $Lu_{1-x}Y_xFe_2Ge_2$

Batch	$x_{nominal}(\%)$	$x_{WDS}(\%)$	$2\sigma(\%)$
SA356	5.0	4.3	0.6
SA357	10.0	9.4	0.7
SA584	13.0	12.5	0.5
SA585	16.0	14.8	0.5
SA586	19.0	19.0	1.0
SA602	50.0	56.0	16.0

BIBLIOGRAPHY

(2004). *Quantum Design Physical Property Measurement System, Heat Capacity Option Users Manual, Part Number 1085-150, H-1.*

Abrikosov, A. (1957). On the magnetic properties of superconductors of the second group. *Zh. Eksp. Teor. Fiz.*, 32:1442.

Abrikosov, A. A. and Gor'kov, L. P. (1961). Contribution to the theory of superconducting alloys with paramagnetic impurities. *Sov. Phys. JETP*, 12:1243.

Aczel, A. A., Baggio-Saitovitch, E., Budko, S. L., Canfield, P. C., Carlo, J. P., Chen, G. F., Dai, P., Goko, T., Hu, W. Z., Luke, G. M., Luo, J. L., Ni, N., Sanchez-Candela, D. R., Tafti, F. F., Wang, N. L., Williams, T. J., Yu, W., and Uemura, Y. J. (2008). Muon-spin-relaxation studies of magnetic order and superfluid density in antiferromagnetic NdFeAsO, $BaFe_2As_2$, and superconducting $Ba_{1-x}K_xFe_2As_2$. *Phys. Rev. B*, 78:214503.

Altarawneh, M. M., Collar, K., Mielke, C. H., Ni, N., Bud'ko, S. L., Canfield, P. C., Altarawneh, M. M., Collar, K., Mielke, C. H., Ni, N., Bud'ko, S. L., and Canfield, P. C. (2008). Determination of anisotropic H_{c2} up to 60 T in $Ba_{0.55}K_{0.45}Fe_2As_2$ single crystals. *Phys. Rev. B*, 78:220505.

Anderson, P. (1959a). Theory of dirty superconductors. *Journal of Physics and Chemistry of Solids*, 11(12):26 – 30.

Anderson, P. W. (1959b). Knight shift in superconductors. *Phys. Rev. Lett.*, 3:325–326.

Anderson, P. W. (1987). The resonating valence bond state in La_2CuO_4 and superconductivity. *Science*, 235(4793):1196–1198.

Avci, S., Chmaissem, O., Chung, D. Y., Rosenkranz, S., Goremychkin, E. A., Castellan, J. P., Todorov, I. S., Schlueter, J. A., Claus, H., Daoud-Aladine, A., Khalyavin, D. D., Kanatzidis, M. G., and Osborn, R. (2012). Phase diagram of $Ba_{1-x}K_xFe_2As_2$. *Phys. Rev. B*, 85:184507.

Avila, M., Bud'ko, S., and Canfield, P. (2004). Anisotropic magnetization, specific heat and resistivity of RFe_2Ge_2 single crystals. *Journal of Magnetism and Magnetic Materials*, 270(12):51 – 76.

Awana, V., Vajpayee, A., Pal, A., Mudgel, M., Meena, R., and Kishan, H. (2009). Superconductivity at 14 K in $SmFe_{0.9}Co_{0.1}Aso$. *Journal of Superconductivity and Novel Magnetism*, 22(7):623–626.

Baek, S.-H., Curro, N. J., Klimczuk, T., Bauer, E. D., Ronning, F., and Thompson, J. D. (2009). First-order magnetic transition in single-crystalline $CaFe_2As_2$ detected by ^{75}As nuclear magnetic resonance. *Phys. Rev. B*, 79:052504.

Bardeen, J., Cooper, L. N., and Schrieffer, J. R. (1957). Theory of Superconductivity. *Phys. Rev.*, 108:1175–1204.

Bednorz, J. and Müller, K. (1986). Possible high T_c superconductivity in the Ba-La-Cu-O system. *Zeitschrift fr Physik B Condensed Matter*, 64(2):189–193.

Bernhard, C., Drew, A. J., Schulz, L., Malik, V. K., R'ossle, M., Niedermayer, C., Wolf, T., Varma, G. D., Mu, G., Wen, H.-H., Liu, H., Wu, G., and Chen, X. H. (2009). Muon spin rotation study of magnetism and superconductivity in $BaFe_{2-x}Co_xAs_2$ and $Pr_{1-x}Sr_xFeAsO$. *New Journal of Physics*, 11(5):055050.

Braun, H. F. (1980). Superconductivity of rare earth-iron silicides. *Physics Letters A*, 75(5):386 – 388.

Bud'ko, S. and Canfield, P. C. (2006). Magnetism and superconductivity in rare earth-nickel-borocarbides. *Comptes Rendus Physique*, 7(1):56 – 67. Superconductivity and magnetism Supraconductivit et magntisme.

Bud'ko, S., Islam, Z., Wiener, T., Fisher, I., Lacerda, A., and Canfield, P. (1999). Anisotropy and metamagnetism in the RNi_2Ge_2 (R=Y, La-Nd, Sm-Lu) series. *Journal of Magnetism and Magnetic Materials*, 205(1):53 – 78.

Bud'ko, S., Kogan, V. G., Hodovanets, H., Ran, S., Moser, S. A., Lampe, M. J., and Canfield, P. C. (2010). Evolution of ground state and upper critical field in $R_{1-x}Gd_xNi_2B_2C$ (R = Lu,Y): Coexistence of superconductivity and spin-glass state. *Phys. Rev. B*, 82:174513.

Bud'ko, S., Ni, N., and Canfield, P. C. (2009). Jump in specific heat at the superconducting transition temperature in $Ba(Fe_{1-x}Co_x)_2Ass_2$ and $Ba(Fe_{1-x}Ni_x)_2As_2$ single crystals. *Phys. Rev. B*, 79:220516.

Bud'ko, S., Ran, S., and Canfield, P. C. (2013). Thermal expansion of $CaFe_2As_2$: Effect of cobalt doping and postgrowth thermal treatment. *Phys. Rev. B*, 88:064513.

Bud'ko, S., Wilke, R., Angst, M., and Canfield, P. (2005). Effect of pressure on the superconducting transition temperature of doped and neutron-damaged MgB_2. *Physica C: Superconductivity*, 420(34):83 – 87.

Bud'ko, S. L., Lapertot, G., Petrovic, C., Cunningham, C. E., Anderson, N., and Canfield, P. C. (2001). Boron isotope effect in superconducting MgB_2. *Phys. Rev. Lett.*, 86:1877–1880.

Canfield, P. (2010). *Solution growth of intermetallic single crystals: a beginner's guide*, volume 2 of *Book Series on Complex Metallic Alloys*, chapter 2, pages 93–111. World Scientific.

Canfield, P. and Bud'ko, S. (2010). FeAs-Based Superconductivity: A Case Study of the Effects of Transition Metal Doping on $BaFe_2As_2$. *Annu. Rev. Cond. Mat. Phys.*, 1(1):27–50.

Canfield, P., Bud'ko, S., Cho, B., Beyermann, W., and Yatskar, A. (1997). RNi_2B_2C magnetic superconductors: An update from the front. *Journal of Alloys and Compounds*, 250(12):596 – 602.

Canfield, P., Bud'ko, S., Ni, N., Kreyssig, A., Goldman, A., McQueeney, R., Torikachvili, M., Argyriou, D., Luke, G., and Yu, W. (2009a). Structural, magnetic and superconducting phase

transitions in $CaFe_2As_2$ under ambient and applied pressure. *Physica C: Superconductivity*, 469(912):404 – 412. Superconductivity in Iron-Pnictides.

Canfield, P., Bud'ko, S. L., Ni, N., Yan, J. Q., and Kracher, A. (2009b). Decoupling of the superconducting and magnetic/structural phase transitions in electron-doped $BaFe_2As_2$. *Phys. Rev. B*, 80:060501.

Canfield, P. and Fisher, I. R. (2001). High-temperature solution growth of intermetallic single crystals and quasicrystals. *Journal of Crystal Growth*, 225(24):155 – 161. Proceedings of the 12th American Conference on Crystal Growth and Epitaxy.

Canfield, P. and Fisk, Z. (1992). Growth of single crystals from metallic fluxes. *Philos. Mag. B*, 65(6):1117–1123.

Canfield, P., Gammel, P. L., and Bishop, D. J. (1998). New magnetic superconductors: A toy box for solid-state physicists. *Phys. Today*, 51(5):40–46.

Cao, G., Jiang, S., Lin, X., Wang, C., Li, Y., Ren, Z., Tao, Q., Feng, C., Dai, J., Xu, Z., and Zhang, F.-C. (2009). Narrow superconducting window in $LaFe_{1-x}Ni_xAsO$. *Phys. Rev. B*, 79:174505.

Carlson, E., Emery, V., Kivelson, S., and Orgad, D. (2008). Concepts in high temperature superconductivity. In Bennemann, K. and Ketterson, J., editors, *Superconductivity*, pages 1225–1348. Springer Berlin Heidelberg.

Cava, R. J., Takagi, H., Batlogg, B., Zandbergen, H. W., Krajewski, J. J., Jr, W. F. P., van Dover, R. B., Felder, R. J., Siegrist, T., Mizuhashi, K., Lee, J. O., Eisaki, H., Carter, S. A., and Uchida, S. (1994a). Superconductivity at 23 K in yttrium palladium boride carbide. *Nature*, 367:146 – 148.

Cava, R. J., Takagi, H., Zandbergen, H. W., Krajewski, J. J., Peck, W. F., Siegrist, T., Batlogg, B., van Dover, R., Felder, R. J., Mizuhashi, K., Lee, J. O., Eisaki, H., and Uchida, S. (1994b). Superconductivity in the quaternary intermetallic compounds $LnNi_2B_2C$. *Nature*, 367:252–253.

Chandrasekhar, B. and Hulm, J. (1958). The electrical resistivity and superconductivity of some uranium alloys and compounds. *Journal of Physics and Chemistry of Solids*, 7(23):259 – 267.

Chanin, G., Lynton, E. A., and Serin, B. (1959). Impurity effects on the superconductive critical temperature of Indium and Aluminum. *Phys. Rev.*, 114:719–724.

Chen, X. H., Wu, T., Wu, G., Liu, R. H., Chen, H., and Fang, D. F. (2008). Superconductivity at 43 K in $SmFeAsO_{1-x}F_x$. *Nature*, 453:761–762.

Cheng, P., Shen, B., Mu, G., Zhu, X., Han, F., Zeng, B., and Wen, H.-H. (2009). High-T_c superconductivity induced by doping rare-earth elements into CaFeAsF. *EPL (Europhysics Letters)*, 85(6):67003.

Cho, B. K., Canfield, P. C., and Johnston, D. C. (1996). Breakdown of de gennes scaling in $(R_{1-x}R'_x)Ni_2B_2C$ compounds. *Phys. Rev. Lett.*, 77:163–166.

Chu, C. and Lorenz, B. (2009). High pressure studies on Fe-pnictide superconductors. *Physica C: Superconductivity*, 469(912):385 – 395. Superconductivity in Iron-Pnictides.

Chu, C. W., Gao, L., Chen, F., Huang, Z. J., Meng, R. L., and Xue, Y. Y. (1993). Superconductivity above 150 K in $HgBa_2Ca_2Cu_3O_{8+\delta}$ at high pressures. *Nature*, 365:323–325.

Chubukov, A. (2012). Pairing mechanism in Fe-based superconductors. *Annual Review of Condensed Matter Physics*, 3(1):57–92.

Clem, J. R. (1966). Effects of nonmagnetic impurities upon anisotropy of the superconducting energy gap. *Phys. Rev.*, 148:392–401.

Coleman, P. (2007). Heavy fermions: Electrons at the edge of magnetism. In Kronmuller, H. and Parkin, S., editors, *Handbook of Magnetism and Advanced Magnetic Materials*, volume 1, chapter 2, pages 95–148. John Wiley & Sons, Ltd.

Colombier, E., Bud'ko, S. L., Ni, N., and Canfield, P. C. (2009). Complete pressure-dependent phase diagrams for $SrFe_2As_2$ and $BaFe_2As_2$. *Phys. Rev. B*, 79:224518.

Cooper, L. N. (1956). Bound electron pairs in a degenerate fermi gas. *Phys. Rev.*, 104:1189–1190.

De Haas, W. J. and Voogd, J. (1931). *Commun. Phys. Lab. Univ. Leiden*, 214.

Decker, W. R. and Finnemore, D. K. (1968). Critical-field curves for gapless superconductors. *Phys. Rev.*, 172:430–436.

Decker, W. R., Peterson, D. T., and Finnemore, D. K. (1967). Meissner effect for superconductors with magnetic impurities. *Phys. Rev. Lett.*, 18:899–901.

Dhaka, R. S., Jiang, R., Ran, S., Bud'ko, S. L., Canfield, P. C., Harmon, B. N., Kaminski, A., Tomić, M., Valentí, R., and Lee, Y. (2014). Dramatic changes in the electronic structure upon transition to the collapsed tetragonal phase in $CaFe_2As_2$. *Phys. Rev. B*, 89:020511.

Diallo, S. O., Pratt, D. K., Fernandes, R. M., Tian, W., Zarestky, J. L., Lumsden, M., Perring, T. G., Broholm, C. L., Ni, N., Bud'ko, S. L., Canfield, P. C., Li, H.-F., Vaknin, D., Kreyssig, A., Goldman, A. I., and McQueeney, R. J. (2010). Paramagnetic spin correlations in $CaFe_2As_2$ single crystals. *Phys. Rev. B*, 81:214407.

Dioguardi, A. P., Crocker, J., Shockley, A. C., Lin, C. H., Shirer, K. R., Nisson, D. M., Lawson, M. M., apRoberts Warren, N., Canfield, P. C., Bud'ko, S. L., Ran, S., and Curro, N. J. (2013). Coexistence of cluster spin glass and superconductivity in $Ba(Fe_{1-x}Ni_x)_2As_2$ for 0.060 x 0.071. *Phys. Rev. Lett.*, 111:207201.

Doniach, S. (1977). The Kondo lattice and weak antiferromagnetism. *Physica B+C*, 91(0):231 – 234.

Fernandes, R. M., Pratt, D. K., Tian, W., Zarestky, J., Kreyssig, A., Nandi, S., Kim, M. G., Thaler, A., Ni, N., Canfield, P. C., McQueeney, R. J., Schmalian, J., and Goldman, A. I. (2010). Unconventional pairing in the iron arsenide superconductors. *Phys. Rev. B*, 81:140501.

Fernandes, R. M. and Schmalian, J. (2010). Competing order and nature of the pairing state in the iron pnictides. *Phys. Rev. B*, 82:014521.

Ferstl, J., Rosner, H., and Geibel, C. (2006). Evidence for fluctuating fe-moments in RFe_2Ge_2. *Physica B: Condensed Matter*, 378-380(0):744 – 745. Proceedings of the International Conference on Strongly Correlated Electron Systems {SCES} 2005 Proceedings of the International Conference on Strongly Correlated Electron Systems.

Finnemore, D. (1991). *A child's guide to BCS*. Nova Science Publishers, Inc.

Finnemore, D. K., Hopkins, D. C., and Palmer, P. E. (1965a). Coexistence of antiferromagnetism and superconductivity. *Phys. Rev. Lett.*, 15:891–893.

Finnemore, D. K., Johnson, D. L., Ostenson, J. E., Spedding, F. H., and Beaudry, B. J. (1965b). Superconductivity in pure La and La-Gd. *Phys. Rev.*, 137:A550–A556.

Fisk, Z. and Remeika, J. P. (1989). *Handbook on the Physics and Chemistry of Rare Earths*, volume 12 of *Book Series on Complex Metallic Alloys*, page 53. Elsevier, Amsterdam.

Fujiwara, T., Aso, N., Yamamoto, H., Hedo, M., Saiga, Y., Nishi, M., Uwatoko, Y., and Hirota, K. (2007). Pressure effect on magnetic short range ordering of $LuFe_2Ge_2$. *Journal of the Physical Society of Japan*, 76(Suppl.A):60–61.

Furukawa, Y., Roy, B., Ran, S., Bud'ko, S. L., and Canfield, P. C. (2014). Suppression of electron correlations in the collapsed tetragonal phase of $CaFe_2As_2$ under ambient pressure demonstrated by ^{75}As NMR/NQR measurements. *Phys. Rev. B*, 89:121109.

Gati, E., Köhler, S., Guterding, D., Wolf, B., Knöner, S., Ran, S., Bud'ko, S. L., Canfield, P. C., and Lang, M. (2012). Hydrostatic-pressure tuning of magnetic, nonmagnetic, and superconducting states in annealed $Ca(Fe_{1-x}Co_x)_2As_2$. *Phys. Rev. B*, 86:220511.

Gayley, R. I., Lynton, E. A., and Serin, B. (1962). Specific heats of tin alloys and their relation to the superconducting transition temperature. *Phys. Rev.*, 126:43–49.

Ginsberg, D. M. (1964). Effect of impurities on the critical temperature of superconductors. *Phys. Rev.*, 136:A1167–A1170.

Ginzburg, V. and Landau, L. (1950). To the theory of superonductivity. *Zh. Eksp. Teor. Fiz.*, 20:1064.

Gofryk, K., Saparov, B., Durakiewicz, T., Chikina, A., Danzenbächer, S., Vyalikh, D. V., Graf, M. J., and Sefat, A. S. (2014). Fermi-surface reconstruction and complex phase equilibria in $CaFe_2As_2$. *Phys. Rev. Lett.*, 112:186401.

Gofryk, K., Sefat, A. S., McGuire, M. A., Sales, B. C., Mandrus, D., Imai, T., Thompson, J. D., Bauer, E. D., and Ronning, F. (2011). Effect of annealing on the specific heat of optimally doped $Ba(Fe_{0.92}Co_{0.08})_2As_2$. *Journal of Physics: Conference Series*, 273(1):012094.

Goko, T., Aczel, A. A., Baggio-Saitovitch, E., Bud'ko, S. L., Canfield, P. C., Carlo, J. P., Chen, G. F., Dai, P., Hamann, A. C., Hu, W. Z., Kageyama, H., Luke, G. M., Luo, J. L., Nachumi, B., Ni, N., Reznik, D., Sanchez-Candela, D. R., Savici, A. T., Sikes, K. J., Wang, N. L., Wiebe, C. R., Williams, T. J., Yamamoto, T., Yu, W., and Uemura, Y. J. (2009). Superconducting state coexisting with a phase-separated static magnetic order in (Ba, K)Fe_2As_2, (Sr, Na)Fe_2As_2 and $CaFe_2As_2$. *Phys. Rev. B*, 80:024508.

Goldman, A. I., Argyriou, D. N., Ouladdiaf, B., Chatterji, T., Kreyssig, A., Nandi, S., Ni, N., Bud'ko, S. L., Canfield, P. C., and McQueeney, R. J. (2008). Lattice and magnetic instabilities in $CaFe_2As_2$: A single-crystal neutron diffraction study. *Phys. Rev. B*, 78:100506.

Goldman, A. I., Kreyssig, A., Prokeš, K., Pratt, D. K., Argyriou, D. N., Lynn, J. W., Nandi, S., Kimber, S. A. J., Chen, Y., Lee, Y. B., Samolyuk, G., Leão, J. B., Poulton, S. J., Bud'ko, S. L., Ni, N., Canfield, P. C., Harmon, B. N., and McQueeney, R. J. (2009). Lattice collapse and quenching of magnetism in $CaFe_2As_2$ under pressure: A single-crystal neutron and x-ray diffraction investigation. *Phys. Rev. B*, 79:024513.

Harnagea, L., Singh, S., Friemel, G., Leps, N., Bombor, D., Abdel-Hafiez, M., Wolter, A. U. B., Hess, C., Klingeler, R., Behr, G., Wurmehl, S., and Büchner, B. (2011). Phase diagram of the iron arsenide superconductors $Ca(Fe_{1-x}Co_x)_2As_2$. *Phys. Rev. B*, 83:094523.

Helfand, E. and Werthamer, N. R. (1964). Temperature and purity dependence of the superconducting critical field, H_{c2}. *Phys. Rev. Lett.*, 13:686–688.

Herring, C. (1958). Spin exchange in superconductors. *Physica*, 24, Supplement 1(0):S184.

Hodovanets, H., Ran, S., Canfield, P. C., and Bud'ko, S. L. (2013). Boron isotope effect in single crystals of superconductor. *Philosophical Magazine*, 93(14):1748–1754.

Hoffmann, R. and Zheng, C. (1985). Making and breaking bonds in the solid state: the thorium chromium silicide ($ThCr_2Si_2$) structure. *The Journal of Physical Chemistry*, 89(20):4175–4181.

Hohenberg, P. (1964). Anisotropic superconductors with nonmagnetic impurities. *Sov. Phys. JETP*, 18:834.

Hosono, H. (2008). Layered Iron Pnictide Superconductors: Discovery and Current Status. *J. Phys. Soc. Jpn.*, 77SC(Supplement C):1–8.

Hsu, F.-C., Luo, J.-Y., Yeh, K.-W., Chen, T.-K., Huang, T.-W., , Wu, P. M., Lee, Y.-C., Huang, Y.-L., Chu, Y.-Y., Yan, D.-C., and Wu, M.-K. (2008). Superconductivity in the PbO-type structure FeSe. *Proc. Natl. Acad. Sci. U.S.A.*, 105(38):14262.

Hu, R., Ran, S., Straszheim, W. E., Bud'ko, S. L., and Canfield, P. C. (2012). Single crystal growth and superconductivity of $Ca(Fe_{1-x}Co_x)_2Ass_2$. *Philosophical Magazine*, 92(24):3113–3120.

Jennings, L. D. and Swenson, C. A. (1958). Effects of pressure on the superconducting transition temperatures of Sn, In, Ta, Tl, and Hg. *Phys. Rev.*, 112:31–43.

Jia, S., Bud'ko, S. L., Samolyuk, G. D., and Canfield, P. C. (2007a). Nearly ferromagnetic fermi-liquid behaviour in YFe_2Zn_{20} and high-temperature ferromagnetism of $GdFe_2Zn_{20}$. *Nat. Phys.*, 3:334 – 338.

Jia, S., Ni, N., Bud'ko, S. L., and Canfield, P. C. (2007b). Magnetic properties of $Gd_xY_{1-x}Fe_2Zn_{20}$: Dilute, large-S moments in a nearly ferromagnetic fermi liquid. *Phys. Rev. B*, 76:184410.

Jia, S., Ni, N., Samolyuk, G. D., Safa-Sefat, A., Dennis, K., Ko, H., Miller, G. J., Bud'ko, S. L., and Canfield, P. C. (2008). Variation of the magnetic ordering in GdT_2Zn_{20} (T=Fe, Ru, Os,

Co, Rh and Ir) and its correlation with the electronic structure of isostructural YT_2Zn_{20}. *Phys. Rev. B*, 77:104408.

Johnston, D. C. (2010). The puzzle of high temperature superconductivity in layered iron pnictides and chalcogenides. *Advances in Physics*, 59(6):803–1061.

Julien, M.-H., Mayaffre, H., Horvati, M., Berthier, C., Zhang, X. D., Wu, W., Chen, G. F., Wang, N. L., and Luo, J. L. (2009). Homogeneous vs. inhomogeneous coexistence of magnetic order and superconductivity probed by NMR in Co- and K-doped iron pnictides. *EPL (Europhysics Letters)*, 87(3):37001.

Kamihara, Y., Watanabe, T., Hirano, M., and Hosono, H. (2008). Iron-Based Layered Superconductor La[$O_{1-x}F_x$]FeAs (x = 0.05-0.12) with T_c = 26 K. *J. Am. Chem. Soc.*, 130(11):3296–3297.

Kim, J. S., Faeth, B. D., and Stewart, G. R. (2012a). Specific-heat discontinuity δC vs T_c in annealed $Ba(Fe_{1-x}Co_x)_2As_2$. *Phys. Rev. B*, 86:054509.

Kim, J. S., Stewart, G. R., Kasahara, S., Shibauchi, T., Terashima, T., and Matsuda, Y. (2011). Specific heat discontinuity, δC, at T_c in $BaFe_2(As_{0.7}P_{0.3})_2$-consistent with unconventional superconductivity. *Journal of Physics: Condensed Matter*, 23(22):222201.

Kim, M. G., Lamsal, J., Heitmann, T. W., Tucker, G. S., Pratt, D. K., Khan, S. N., Lee, Y. B., Alam, A., Thaler, A., Ni, N., Ran, S., Bud'ko, S. L., Marty, K. J., Lumsden, M. D., Canfield, P. C., Harmon, B. N., Johnson, D. D., Kreyssig, A., McQueeney, R. J., and Goldman, A. I. (2012b). Effects of transition metal substitutions on the incommensurability and spin fluctuations in $BaFe_2As_2$ by elastic and inelastic neutron scattering. *Phys. Rev. Lett.*, 109:167003.

Kim, M. G., Tucker, G. S., Pratt, D. K., Ran, S., Thaler, A., Christianson, A. D., Marty, K., Calder, S., Podlesnyak, A., Bud'ko, S. L., Canfield, P. C., Kreyssig, A., Goldman, A. I., and McQueeney, R. J. (2013). Magnonlike dispersion of spin resonance in Ni-doped $BaFe_2As_2$. *Phys. Rev. Lett.*, 110:177002.

Kogan, V. G. (2009). Pair breaking in iron pnictides. *Phys. Rev. B*, 80:214532.

Kreyssig, A., Green, M. A., Lee, Y., Samolyuk, G. D., Zajdel, P., Lynn, J. W., Bud'ko, S. L., Torikachvili, M. S., Ni, N., Nandi, S., Leão, J. B., Poulton, S. J., Argyriou, D. N., Harmon, B. N., McQueeney, R. J., Canfield, P. C., and Goldman, A. I. (2008). Pressure-induced volume-collapsed tetragonal phase of $CaFe_2As_2$ as seen via neutron scattering. *Phys. Rev. B*, 78:184517.

Laplace, Y., Bobroff, J., Rullier-Albenque, F., Colson, D., and Forget, A. (2009). Atomic coexistence of superconductivity and incommensurate magnetic order in the pnictide $Ba(Fe_{1-x}Co_x)_2As_2$. *Phys. Rev. B*, 80:140501.

Larbalestier, D. and Canfield, P. C. (2011). Superconductivity at 100-where we've been and where we're going. *MRS Bulletin*, 36:590–593.

Lashley, J. C., Lawson, A. C., Cooley, J. C., Mihaila, B., Opeil, C. P., Pham, L., Hults, W. L., Smith, J. L., Schmiedeshoff, G. M., Drymiotis, F. R., Chapline, G., Basu, S., and Riseborough, P. S. (2006). Tricritical phenomena at the $\gamma \rightarrow \alpha$ transition in $Ce_{0.9-x}La_xTh_{0.1}$ alloys. *Phys. Rev. Lett.*, 97:235701.

Lazarev, B., Sudovtsev, A., and Smirnov, A. (1957). *Journal of Experimental and Theoretical Physics*, 33:1059.

Leupold, H. A. and Boorse, H. A. (1964). Superconducting and normal specific heats of a single crystal of niobium. *Phys. Rev.*, 134:A1322–A1328.

Levi, B. G. (1993). In high-T_c superconductors, is D-wave the new wave? *Phys. Today*, 46(5):17–20.

Levin, K., Kim, J. H., Lu, J., and Si, Q. (1991). Normal state properties in the cuprates and their fermi liquid based interpretation. *Physica C: Superconductivity*, 175(56):449 – 522.

London, F. and London, H. (1935). The Electromagnetic Equations of the Supraconductor. *Proc. Roy. Soc. A*, 149(866):71–88.

Lynton, E., Serin, B., and Zucker, M. (1957). The superconductive critical temperature and the electronic specific heat of impure tin. *Journal of Physics and Chemistry of Solids*, 3(34):165 – 174.

Maple, M. (1968). The superconducting transition temperature of $La_{1-x}Gd_xAl_2$. *Physics Letters A*, 26(10):513 – 514.

Maple, M. (1970). Dependence of s-f exchange on atomic number in rare earth dialuminides. *Solid State Communications*, 8(22):1915 – 1917.

Maple, M. B., Bauer, E. D., Zapf, V. S., and Wosnitza, J. (2008). *Superconductivity: Volume 1, Conventional and unconventional superconductors*. Springer.

Markowitz, D. and Kadanoff, L. P. (1963). Effect of impurities upon critical temperature of anisotropic superconductors. *Phys. Rev.*, 131:563–575.

Matsuda, N., Setoguchi, H., Kagayama, T., Oomi, G., Cho, B., and Canfield, P. (2000). Effect of pressure on the antiferromagnetism and superconductivity of $ErNi_2B_2C$. *Physica B: Condensed Matter*, 281-282(0):1001 – 1003.

Matthias, B., Compton, V., and Corenzwit, E. (1961). Some new superconducting compounds. *Journal of Physics and Chemistry of Solids*, 19(12):130 – 133.

Matthias, B., Wood, E., Corenzwit, E., and Bala, V. (1956). Superconductivity and electron concentration. *Journal of Physics and Chemistry of Solids*, 1(3):188 – 190.

Matthias, B. T., Geballe, T. H., and Compton, V. B. (1963). Superconductivity. *Rev. Mod. Phys.*, 35:1–22.

Matthias, B. T., Geballe, T. H., Willens, R. H., Corenzwit, E., and Hull, G. W. (1965). Superconductivity of Nb_3Ge. *Phys. Rev.*, 139:A1501–A1503.

Matthias, B. T., Suhl, H., and Corenzwit, E. (1958). Spin exchange in superconductors. *Phys. Rev. Lett.*, 1:92–94.

Matusiak, M., Bukowski, Z., and Karpinski, J. (2010). Nernst effect in single crystals of the pnictide superconductor $CaFe_{1.98}Co_{0.02}As_2$ and parent compound $CaFe_2As_2$. *Phys. Rev. B*, 81:020510.

Mazin, I. I., Singh, D. J., Johannes, M. D., and Du, M. H. (2008). Unconventional superconductivity with a sign reversal in the order parameter of $LaFeAsO_{1-x}F_x$. *Phys. Rev. Lett.*, 101:057003.

Meissner, W. and Ochsenfeld, R. (1933). Ein neuer Effekt bei Eintritt der Supraleitfhigkeit. *Naturwissenschaften*, 21:787–788.

Miao, X., Bud'ko, S., and Canfield, P. (2002). Effects of annealing temperature and time on the electrical resistivity of single crystal RNi_2B_2C (R=Gd-Lu, Y). *Journal of Alloys and Compounds*, 338(12):13 – 19. Special Issue to Honor Professor H. Fritz Franzen.

Mizutani, U. (2001). *Introduction to the electron theory of metals*. Cambridge university press.

Nakamura, K.-i. (1959). Impurity effect in superconductors. *Progress of Theoretical Physics*, 21:3.

Ni, N., Allred, J. M., Chan, B. C., and Cava, R. J. (2011). High T_c electron doped $Ca_{10}(Pt_3As_8)(Fe_2As_2)_5$ and $Ca_{10}(Pt_4As_8)(Fe_2As_2)_5$ superconductors with skutterudite intermediary layers. *Proceedings of the National Academy of Sciences*, 108(45):E1019–E1026.

Ni, N. and Bud'ko, S. L. (2011). Tuning the ground state of $BaFe_2As_2$: Phase diagrams and empirical trends. *MRS Bulletin*, 36:620–625.

Ni, N., Bud'ko, S. L., Kreyssig, A., Nandi, S., Rustan, G. E., Goldman, A. I., Gupta, S., Corbett, J. D., Kracher, A., and Canfield, P. C. (2008a). Anisotropic thermodynamic and transport properties of single-crystalline $Ba_{1-x}K_xFe_2As_2$ (x = 0 and 0.45). *Phys. Rev. B*, 78:014507.

Ni, N., Nandi, S., Kreyssig, A., Goldman, A. I., Mun, E. D., Bud'ko, S. L., and Canfield, P. C. (2008b). First-order structural phase transition in $CaFe_2As_2$. *Phys. Rev. B*, 78:014523.

Ni, N., Thaler, A., Kracher, A., Yan, J. Q., Bud'ko, S. L., and Canfield, P. C. (2009). Phase diagrams of $Ba(Fe_{1-x}M_x)_2As_2$ single crystals (M = Rh and Pd). *Phys. Rev. B*, 80:024511.

Ni, N., Thaler, A., Yan, J. Q., Kracher, A., Colombier, E., Bud'ko, S. L., Canfield, P. C., and Hannahs, S. T. (2010). Temperature versus doping phase diagrams for $Ba(Fe_{1-x}TM_x)_2As_2$(TM = Ni, Co, Cu/Co) single crystals. *Phys. Rev. B*, 82:024519.

Ni, N., Tillman, M. E., Yan, J.-Q., Kracher, A., Hannahs, S. T., Bud'ko, S. L., and Canfield, P. C. (2008c). Effects of Co substitution on thermodynamic and transport properties and anisotropic H_{c2} in $Ba(Fe_{1-x}Co_x)_2As_2$ single crystals. *Phys. Rev. B*, 78:214515.

Norman, M. R. (2011). The challenge of unconventional superconductivity. *Science*, 332(6026):196–200.

Ogino, H., Matsumura, Y., Katsura, Y., Ushiyama, K., Horii, S., Kishio, K., and ichi Shimoyama, J. (2009). Superconductivity at 17 K in $(Fe_2P_2)(Sr_4Sc_2O_6)$: a new superconducting layered pnictide oxide with a thick perovskite oxide layer. *Superconductor Science and Technology*, 22(7):075008.

Ogino, H., Shimizu, Y., Ushiyama, K., Kawaguchi, N., Kishio, K., and ichi Shimoyama, J. (2010). Superconductivity above 40 K observed in a new iron arsenide oxide $(Fe_2As_2)(Ca_4(Mg,Ti)_3O_y)$. *Applied Physics Express*, 3(6):063103.

Onnes, H. K. (1911). The resistance of pure mercury at helium temperatures. *Commun. Phys. Lab. Univ. Leiden*, 12.

Onnes, H. K. (1914). *Commun. Phys. Lab. Univ. Leiden*, 66.

Oomi, G., Matsuda, N., Honda, F., Kagayama, T., Honda, K., Cho, B., and Canfield, P. (1999). Effect of pressure on the critical temperature and magnetic field of $TmNi_2B_2C$. *Physica B: Condensed Matter*, 259-261(0):601 – 603.

Park, J. T., Inosov, D. S., Niedermayer, C., Sun, G. L., Haug, D., Christensen, N. B., Dinnebier, R., Boris, A. V., Drew, A. J., Schulz, L., Shapoval, T., Wolff, U., Neu, V., Yang, X.,

Lin, C. T., Keimer, B., and Hinkov, V. (2009). Electronic phase separation in the slightly underdoped iron pnictide superconductor $Ba_{1-x}K_xFe_2As_2$. *Phys. Rev. Lett.*, 102:117006.

Patz, A., Li, T., Ran, S., Fernandes, R. M., Schmalian, J., Budko, S. L., Canfield, P. C., Perakis, I. E., and Wang, J. (2014). Ultrafast observation of critical nematic fluctuations and giant magnetoelastic coupling in iron pnictides. *Nat. Commun.*, 5.

Pfleiderer, C. (2009). Superconducting phases of f-electron compounds. *Rev. Mod. Phys.*, 81:1551–1624.

Pines, D. (1994). Understanding high-temperature superconductivity: a progress report. *Physica B: Condensed Matter*, 199200(0):300 – 309.

Plessel, J., Abd-Elmeguid, M. M., Sanchez, J. P., Knebel, G., Geibel, C., Trovarelli, O., and Steglich, F. (2003). Unusual behavior of the low-moment magnetic ground state of $YbRh_2Si_2$ under high pressure. *Phys. Rev. B*, 67:180403.

Prakash, J., Singh, S., Patnaik, S., and Ganguli, A. (2009). Superconductivity at 11.3 K induced by cobalt doping in CeFeAsO. *Solid State Communications*, 149(56):181 – 183.

Pratt, D. K., Tian, W., Kreyssig, A., Zarestky, J. L., Nandi, S., Ni, N., Bud'ko, S. L., Canfield, P. C., Goldman, A. I., and McQueeney, R. J. (2009a). Coexistence of competing antiferromagnetic and superconducting phases in the underdoped $Ba(Fe_{0.953}Co_{0.047})_2As_2$ compound using x-ray and neutron scattering techniques. *Phys. Rev. Lett.*, 103:087001.

Pratt, D. K., Zhao, Y., Kimber, S. A. J., Hiess, A., Argyriou, D. N., Broholm, C., Kreyssig, A., Nandi, S., Bud'ko, S. L., Ni, N., Canfield, P. C., McQueeney, R. J., and Goldman, A. I. (2009b). Suppression of antiferromagnetic spin fluctuations in the collapsed phase of $CaFe_2As_2$. *Phys. Rev. B*, 79:060510.

Prokes, K., Kreyssig, A., Ouladdiaf, B., Pratt, D. K., Ni, N., Bud'ko, S. L., Canfield, P. C., McQueeney, R. J., Argyriou, D. N., and Goldman, A. I. (2010). Evidence from neutron diffraction for superconductivity in the stabilized tetragonal phase of $CaFe_2As_2$ under uniaxial pressure. *Phys. Rev. B*, 81:180506.

Qi, Y., Gao, Z., Wang, L., Wang, D., Zhang, X., and Ma, Y. (2008). Superconductivity in Co-doped SmFeAsO. *Superconductor Science and Technology*, 21(11):115016.

Ran, S., Bud'ko, S. L., Pratt, D. K., Kreyssig, A., Kim, M. G., Kramer, M. J., Ryan, D. H., Rowan-Weetaluktuk, W. N., Furukawa, Y., Roy, B., Goldman, A. I., and Canfield, P. C. (2011). Stabilization of an ambient-pressure collapsed tetragonal phase in $CaFe_2As_2$ and tuning of the orthorhombic-antiferromagnetic transition temperature by over 70 K via control of nanoscale precipitates. *Phys. Rev. B*, 83:144517.

Ran, S., Bud'ko, S. L., Straszheim, W. E., Soh, J., Kim, M. G., Kreyssig, A., Goldman, A. I., and Canfield, P. C. (2012). Control of magnetic, nonmagnetic, and superconducting states in annealed $Ca(Fe_{1-x}Co_x)_2As_2$. *Phys. Rev. B*, 85:224528.

Ren, Z.-A., Che, G.-C., Dong, X.-L., Yang, J., Lu, W., Yi, W., Shen, X.-L., Li, Z.-C., Sun, L.-L., Zhou, F., and Zhao, Z.-X. (2008a). Superconductivity and phase diagram in iron-based arsenic-oxides $ReFeAsO_{1-\delta}$ (Re = rare-earth metal) without fluorine doping. *Europhys. Lett.*, 83(1):17002.

Ren, Z. A., Yang, J., Lu, W., Yi, W., Che, G. C., Dong, X. L., Sun, L. L., and Zhao, Z. X. (2008b). Superconductivity at 52 K in iron based F doped layered quaternary compound $Pr[O_{1-x}F_x]FeAs$. *Mater. Res. Innovations*, 12(3):105–106.

Ren, Z.-A., Yang, J., Lu, W., Yi, W., Shen, X.-L., Li, Z.-C., Che, G.-C., Dong, X.-L., Sun, L.-L., Zhou, F., and Zhao, Z.-X. (2008c). Superconductivity in the iron-based F-doped layered quaternary compound $Nd[O_{1-x}F_x]FeAs$. *Europhys. Lett.*, 82(5):57002.

Riseborough, P. S., Schmiedeshoff, G. M., and Smith, J. L. (2008). *Superconductivity: Volume 1, Conventional and unconventional superconductors*. Springer.

Ronning, F., Klimczuk, T., Bauer, E. D., Volz, H., and Thompson, J. D. (2008). Synthesis and properties of $CaFe_2As_2$single crystals. *Journal of Physics: Condensed Matter*, 20(32):322201.

Rotter, M., Tegel, M., and Johrendt, D. (2008). Superconductivity at 38 K in the iron arsenide $(Ba_{1-x}K_x)Fe_2As_2$. *Phys. Rev. Lett.*, 101:107006.

Rotter, M., Tegel, M., Schellenberg, I., Schappacher, F. M., Pttgen, R., Deisenhofer, J., Gnther, A., Schrettle, F., Loidl, A., and Johrendt, D. (2009). Competition of magnetism and superconductivity in underdoped $Ba_{1-x}K_xFe_2As_2$. *New Journal of Physics*, 11(2):025014.

Rotundu, C. R., Freelon, B., Forrest, T. R., Wilson, S. D., Valdivia, P. N., Pinuellas, G., Kim, A., Kim, J.-W., Islam, Z., Bourret-Courchesne, E., Phillips, N. E., and Birgeneau, R. J. (2010). Heat capacity study of $CaFe_2As_2$: Effects of annealing. *Phys. Rev. B*, 82:144525.

Saha, S. R., Butch, N. P., Drye, T., Magill, J., Ziemak, S., Kirshenbaum, K., Zavalij, P. Y., Lynn, J. W., Paglione, J., Saha, S. R., Butch, N. P., Drye, T., Magill, J., Ziemak, S., Kirshenbaum, K., Zavalij, P. Y., Lynn, J. W., and Paglione, J. (2012). Structural collapse and superconductivity in rare-earth-doped $CaFe_2As_2$. *Phys. Rev. B*, 85:024525.

Saha, S. R., Butch, N. P., Kirshenbaum, K., Paglione, J., and Zavalij, P. Y. (2009). Superconducting and Ferromagnetic Phases Induced by Lattice Distortions in Stoichiometric $SrFe_2As_2$ Single Crystals. *Phys. Rev. Lett.*, 103:037005.

Saparov, B., Cantoni, C., Pan, M., Hogan, T. C., II, W. R., Wilson, S. D., Fritsch, K., Gaulin, B. D., and Sefat, A. S. (2014). Complex structures of different $CaFe_2As_2$ samples. *Scientific Reports*, 4:4120.

Sasmal, K., Lv, B., Lorenz, B., Guloy, A. M., Chen, F., Xue, Y.-Y., and Chu, C.-W. (2008). Superconducting Fe-based compounds $(A_{1-x}Sr_x)Fe_2As_2$ with A = K and Cs with transition temperatures up to 37 K. *Phys. Rev. Lett.*, 101:107007.

Scalapino, D. (1995). The case for $d_{x^2-y^2}$ pairing in the cuprate superconductors. *Physics Reports*, 250(6):329 – 365.

Schilling, A., Cantoni, M., Guo, J. D., and Ott, H. R. (1993). Superconductivity above 130 K in the HgBaCaCuO system. *Nature*, 363:56–58.

Schmalian, J. (2010). Failed theories of superconductivity. *Modern Physics Letters B*, 24(27):2679–2691.

Schmidt, V. V. (1997). *The physics of superconductors*. Springer.

Sefat, A. S. (2011). Pressure effects on two superconducting iron-based families. *Reports on Progress in Physics*, 74(12):124502.

Sefat, A. S., Huq, A., McGuire, M. A., Jin, R., Sales, B. C., Mandrus, D., Cranswick, L. M. D., Stephens, P. W., and Stone, K. H. (2008a). Superconductivity in $LaFe_{1-x}Co_xAsO$. *Phys. Rev. B*, 78:104505.

Sefat, A. S., Jin, R., McGuire, M. A., Sales, B. C., Singh, D. J., and Mandrus, D. (2008b). Superconductivity at 22 K in Co-Doped $BaFe_2As_2$ Crystals. *Phys. Rev. Lett.*, 101:117004.

Sheng, Z. Z. and Hermann, A. M. (1988). Bulk superconductivity at 120 K in the TlCa/BaCuOsystem. *Nature*, 332:138 – 139.

Siegrist, T., Zandbergen, H. W., Cava, R. J., Krajewski, J. J., and Jr, W. F. P. (1994). The crystal structure of superconducting $LuNi_2B_2C$ and the related phase LuNiBC. *Nature*, 367:254–256.

Smith, T. I. (1965). Observation of persistent currents in a superconducting circuit containing a josephson junction. *Phys. Rev. Lett.*, 15:460–462.

Soh, J. H., Tucker, G. S., Pratt, D. K., Abernathy, D. L., Stone, M. B., Ran, S., Bud'ko, S. L., Canfield, P. C., Kreyssig, A., McQueeney, R. J., and Goldman, A. I. (2013). Inelastic neutron scattering study of a nonmagnetic collapsed tetragonal phase in nonsuperconducting $CaFe_2As_2$: Evidence of the impact of spin fluctuations on superconductivity in the iron-arsenide compounds. *Phys. Rev. Lett.*, 111:227002.

Steglich, F., Aarts, J., Bredl, C. D., Lieke, W., Meschede, D., Franz, W., and Schäfer, H. (1979). Superconductivity in the presence of strong pauli paramagnetism: $CeCu_2Si_2$. *Phys. Rev. Lett.*, 43:1892–1896.

Steglich, F., Arndt, J., Friedemann, S., Krellner, C., Tokiwa, Y., Westerkamp, T., Brando, M., Gegenwart, P., Geibel, C., Wirth, S., and Stockert, O. (2010). Superconductivity versus quantum criticality: what can we learn from heavy fermions? *Journal of Physics: Condensed Matter*, 22(16):164202.

Steglich, F., Stockert, O., Wirth, S., Geibel, C., Yuan, H. Q., Kirchner, S., and Si, Q. (2013). Routes to heavy-fermion superconductivity. *Journal of Physics: Conference Series*, 449(1):012028.

Stewart, G. R. (1984). Heavy-fermion systems. *Rev. Mod. Phys.*, 56:755–787.

Stewart, G. R. (2006). Addendum: Non-Fermi-liquid behavior in d- and f-electron metals. *Rev. Mod. Phys.*, 78:743–753.

Stewart, G. R. (2011). Superconductivity in iron compounds. *Rev. Mod. Phys.*, 83:1589–1652.

Subramanian, M. A., Torardi, C. C., Calabrese, J. C., Gopalakrishnan, J., Morrissey, K. J., Askew, T. R., Flippen, R. B., Chowdhry, U., and Sleight, A. W. (1988). A new high-temperature superconductor: $Bi_2Sr_{3-x}Ca_xCu_2O_{8+y}$. *Science*, 239(4793):1015–1017.

Suhl, H. and Matthias, B. T. (1959). Impurity scattering in superconductors. *Phys. Rev.*, 114:977–988.

Szytula, A. and Leciejewicz, J. (1989). *Magnetic properties of ternary intermetallic compounds of the RT_2X_2 type*, chapter 2, page 133. Elsevier Science.

Tachiki, M. and Matsumoto, H. (1990). Metal-insulator transition in oxide superconductors. *Progress of Theoretical Physics*, 101:353.

Takahashi, H., Igawa, K., Arii, K., Kamihara, Y., Hirano, M., and Hosono, H. (2008). Superconductivity at 43 K in an iron-based layered compound $LaO_{1-x}F_xFeAs$. *Nature*, 453:376–378.

Thaler, A., Hodovanets, H., Torikachvili, M. S., Ran, S., Kracher, A., Straszheim, W., Yan, J. Q., Mun, E., and Canfield, P. C. (2011). Physical and magnetic properties of $Ba(Fe_{1-x}Mn_x)_2As_2$ single crystals. *Phys. Rev. B*, 84:144528.

Thaler, A., Ni, N., Kracher, A., Yan, J. Q., Bud'ko, S. L., and Canfield, P. C. (2010). Physical and magnetic properties of $Ba(Fe_{1-x}Ru_x)_2As_2$ single crystals. *Phys. Rev. B*, 82:014534.

Tinkham, M. (2004). *Introduction to Superconductivity*. Dover Publications.

Torikachvili, M. S., Bud'ko, S. L., Ni, N., and Canfield, P. C. (2008). Pressure induced superconductivity in $CaFe_2As_2$. *Phys. Rev. Lett.*, 101:057006.

Torikachvili, M. S., Bud'ko, S. L., Ni, N., Canfield, P. C., and Hannahs, S. T. (2009). Effect of pressure on transport and magnetotransport properties in $CaFe_2As_2$ single crystals. *Phys. Rev. B*, 80:014521.

Tucker, G. S., Pratt, D. K., Kim, M. G., Ran, S., Thaler, A., Granroth, G. E., Marty, K., Tian, W., Zarestky, J. L., Lumsden, M. D., Bud'ko, S. L., Canfield, P. C., Kreyssig, A., Goldman, A. I., and McQueeney, R. J. (2012). Competition between stripe and checkerboard magnetic instabilities in Mn-doped $BaFe_2As_2$. *Phys. Rev. B*, 86:020503.

Uwatoko, Y., Oomi, G., Canfield, P., and Cho, B. (1996). Effect of pressure on the superconductivity of $HoNi_2B_2C$. *Physica B: Condensed Matter*, 216(34):329 – 332. Proceedings of the International Workshop on Advances in High Magnetic Fields.

Varma, C. (2010). High-temperature superconductivity: Mind the pseudogap. *Nature*, 468:184185.

Wang, C., Li, L., Chi, S., Zhu, Z., Ren, Z., Li, Y., Wang, Y., Lin, X., Luo, Y., Jiang, S., Xu, X., Cao, G., and Xu, Z. (2008a). Thorium-doping induced superconductivity up to 56 K in $Gd_{1-x}Th_xFeAsO$. *EPL (Europhysics Letters)*, 83(6):67006.

Wang, X., Liu, Q., Lv, Y., Gao, W., Yang, L., Yu, R., Li, F., and Jin, C. (2008b). The superconductivity at 18 K in LiFeAs system. *Solid State Communications*, 148(1112):538 – 540.

Wittig, J. (1966). Superconductivity of tin and lead under very high pressure. *Zeitschrift für Physik*, 195(2):228–238.

Wollan, J. J. and Finnemore, D. K. (1971). Superconductivity and magnetic scattering in La-Ce. *Phys. Rev. B*, 4:2996–3002.

Wu, G., Chen, H., Wu, T., Xie, Y. L., Yan, Y. J., Liu, R. H., Wang, X. F., Ying, J. J., and Chen, X. H. (2008). Different resistivity response to spin-density wave and superconductivity at 20 k in $Ca_{1-x}Na_xFe_2As_2$. *Journal of Physics: Condensed Matter*, 20(42):422201.

Wu, G., Xie, Y. L., Chen, H., Zhong, M., Liu, R. H., Shi, B. C., Li, Q. J., Wang, X. F., Wu, T., Yan, Y. J., Ying, J. J., and Chen, X. H. (2009). Superconductivity at 56 K in samarium-doped SrFeAsF. *Journal of Physics: Condensed Matter*, 21(14):142203.

Wu, M. K., Ashburn, J. R., Torng, C. J., Hor, P. H., Meng, R. L., Gao, L., Huang, Z. J., Wang, Y. Q., and Chu, C. W. (1987). Superconductivity at 93 K in a new mixed-phase Y-Ba-Cu-O compound system at ambient pressure. *Phys. Rev. Lett.*, 58:908–910.

Yan, J.-Q., Kreyssig, A., Nandi, S., Ni, N., Bud'ko, S. L., Kracher, A., McQueeney, R. J., McCallum, R. W., Lograsso, T. A., Goldman, A. I., and Canfield, P. C. (2008). Structural transition and anisotropic properties of single-crystalline $SrFe_2As_2$. *Phys. Rev. B*, 78:024516.

Yildirim, T. (2009). Strong coupling of the Fe-spin state and the As-As hybridization in iron-pnictide superconductors from first-principle calculations. *Phys. Rev. Lett.*, 102:037003.

Yu, W., Aczel, A. A., Williams, T. J., Bud'ko, S. L., Ni, N., Canfield, P. C., and Luke, G. M. (2009). Absence of superconductivity in single-phase $CaFe_2As_2$ under hydrostatic pressure. *Phys. Rev. B*, 79:020511.

Zhu, X., Han, F., Mu, G., Cheng, P., Shen, B., Zeng, B., and Wen, H.-H. (2009). Transition of stoichiometric $Sr_2VOFeAs$ to a superconducting state at 37.2 K. *Phys. Rev. B*, 79:220512.